Modellierung und Design einer quecksilbergetriebenen Vakuumpumpe zum Pumpen der Abgase eines Fusionskraftwerks

Modeling and Design of a Mercury-driven Vacuum Pump for Fusion Power Plant Exhaust Pumping

Zur Erlangung des akademischen Grades eines
DOKTORS DER INGENIEURWISSENSCHAFTEN (Dr.-Ing.)
von der KIT-Fakultät für Maschinenbau des
Karlsruher Instituts für Technologie (KIT)
genehmigte
DISSERTATION
von
Tim Teichmann, M.Sc.

Tag der mündlichen Prüfung: 23.10.2024
Hauptreferent: Prof. Dr.-Ing. Daniel Banuti
Korreferent: Prof. Dr. Aldo Frezzotti

Danksagung / Preface

Die vorliegende Dissertation entstand in den letzten fünf Jahren während meiner Tätigkeit als Wissenschaftlicher Mitarbeiter am Institut für Technische Physik (ITEP) des Karlsruher Instituts für Technologie (KIT). Auf dem langen Weg haben mich viele Freunde, Kollegen und Mentoren begleitet, denen ich allen zu großem Dank verpflichtet bin.

Zunächst möchte ich meinem ehemaligen Doktorvater Professor Dr. Robert Stieglitz danken. Sein plötzlicher und unerwarteter Tod im Dezember 2023 war ein großer persönlicher und wissenschaftlicher Verlust. Ich danke Ihnen für Ihre zahlreichen Hinweise, kritischen Nachfragen und Denkanstöße. Die INR Seminare mit den abendlichen Diskussionsrunden werde ich in guter Erinnerung behalten.

Für die spontane Übernahme des Hauptreferats möchte ich Professor Dr. Daniel Banuti danken. Herzlichen Dank für Ihre Offenheit sich mit dem unbekannten Thema auseinanderzusetzen und für die hilfreichen Kommentare. Furthermore, I would like to thank Dr. Aldo Frezzotti for acting as second assessor of the thesis, for your interest in the topic and our helpful discussions.

Besonders bedanken möchte ich mich bei Dr. Christian Day, meinem bisherigen und zukünftigen Chef. Aus meiner Sicht spricht die Tatsache, dass einige ehemalige Kollegen sich bei mir beschwert haben, dass „ich ihnen den Chef klauen würde“, Bände. Vielen Dank für die Integration in die Vakuumgruppe am ITEP, dein offenes Ohr bei Fragen und Problemen und deine konstruktiven Hinweise, die wesentlich zum Erfolg der vorliegenden Arbeit beigetragen haben.

Danken möchte ich auch den Kollegen mit denen ich am ITEP zusammenarbeiten durfte. Für die Unterstützung beim Aufbau, Betrieb und Abbau der experimentellen Anlage bedanke ich mich bei Martin Jäger, Alan Kumb, Thomas Johann, Peter Pfeil, Jürgen Jung, Hartmut Stump und Ralf Müller. Dank geht auch an Dr. Thomas Giegerich für die Hilfe bei der Koordination und Voker Hauer für unsere bereichernden Diskussionen. Additionally, I would like to thank Dr. Christos Tantos for the fruitful discussions about rarefied gas dynamics and our collaborations.

Bei meinen Mitdoktoranden Jonas Schwenzer, Annika Uihlein, Yannick Kathage und Alejandro Vazquez Cortes möchte ich mich für eure Unterstützung und die zahlreichen erheiternden Momente bedanken.

Zuletzt möchte ich mich für die anhaltende Unterstützung, Rücksichtnahme und mitunter aufbauenden Worte bei meinen Eltern, meinem Bruder und Nicole bedanken.

Kurzfassung

Für den Betrieb zukünftiger Kernfusionskraftwerke werden Vakuumsysteme von bisher unerreichter Größe und Komplexität benötigt. Gegenwärtig ist der Tokamak der am weitesten fortgeschrittene Reaktortyp. Dessen gepulster Betrieb stellt besondere Herausforderungen an die Auslegung der Vakuumsysteme, da diese einerseits hohe Gaslasten während der Brennphase prozessieren müssen und andererseits sehr niedrige Drücke zwischen den Pulsen gewährleisten müssen. Zusätzliche Anforderungen entstehen durch die Deuterium-Tritium-Reaktion, welche zurzeit als vielversprechendste Option für die Energieerzeugung durch Kernfusion auf der Erde gilt. Für diese Reaktion werden die zwei Wasserstoffisotope Deuterium und Tritium benötigt. Deuterium stellt hier kein Problem dar, da es langzeitstabil und als Ressource hinreichend verfügbar ist. Tritium ist hingegen radioaktiv und aufgrund seiner kurzen Halbwertszeit nicht natürlich verfügbar; es muss daher künstlich hergestellt werden. Aufgrund der beschränkten Verfügbarkeit und kerntechnischer Rechtsvorschriften ist es notwendig, das Tritiuminventar von Fusionskraftwerken so gering wie möglich zu halten. Aus diesen Gründen müssen Vakuumpumptechnologien entwickelt werden, die einerseits hohe Saugvermögen und niedrige Enddrücke bereitstellen und andererseits geringe Tritiuminventare aufweisen. Eine Pumptechnologie, die diesen Anforderungen gerecht wird, ist die quecksilbergetriebene Diffusionspumpe. Diffusionspumpen sind eine bereits etablierte Technologie, allerdings erfordert ihre Anwendung in neuartigen Abgaspumpsystemen eines Tokamaks eine dedizierte Untersuchung. Ziel der vorliegenden Arbeit ist, Modelle dieser Pumpen zu entwickeln und diese für die Anwendung im Abgasstrang eines Tokamaks auszulegen und zu optimieren.

Zu diesem Zweck werden zunächst die Betriebsbedingungen und Anforderungen, die der gepulste Tokamakbetrieb an das Hochvakuumpumpsystem stellt, hergeleitet. Basierend auf der Funktionsweise wird die Gas-Dampf-Interaktion in der Diffusionspumpe als Hauptwirkmechanismus identifiziert. Um ein Austreten des Quecksilberdampfes aus der Pumpe in vorgeschaltete Systeme zu verhindern wird die quecksilbergetriebene Diffusionspumpe mit einer vorgeschalteten Quecksilberfalle betrieben. Die Quecksilberfalle basiert auf gekühlten Prallplatten (englisch *Baffle*). Durch dieses Baffle kann die effektive Saugleistung der Pumpe erheblich reduziert werden, sodass während des Auslegungsprozesses die Kombination aus Pumpe und Baffle berücksichtigt wird.

Da Diffusionspumpen im verdünnten Gasströmungsbereich arbeiten, erfolgt ihre Beschreibung auf Basis der kinetischen Gastheorie. Basierend darauf werden nachfolgend zwei Modelle für die Gas-Dampf-Wechselwirkung entwickelt. Das erste, einfachere, Modell liegt in Form einer dimensionslosen Gleichung vor und ist daher geeignet, die Einflussfaktoren auf die Pumpwirkung zu untersuchen und zu vergleichen. Ergänzend wird ein zweites, numerisches Modell auf der Basis des *Direct Simulation Monte Carlo (DSMC)* Verfahrens entwickelt, das die Simulation von realistischen Pumpenentwürfen ermöglicht. Die Kombination beider Modelle ermöglicht eine effiziente, modell-basierte Auslegung von Diffusionspumpen.

Als Validierungsgrundlage für die theoretische Modellentwicklung ist im Rahmen dieser Arbeit ein Experiment entworfen, aufgebaut und betrieben worden. Ziel ist die Charakterisierung eines Quecksilberdampfstrahles, wie er in Diffusionspumpen zum Einsatz kommt, und seine Wechselwirkung mit dem gepumpten Gas. Das DSMC-Modell wird durch detaillierten Vergleich mit den experimentellen Messdaten validiert.

Der gepulste Tokamakbetrieb erschwert die Auslegung einer effizienten Quecksilberfalle, die einen Kompromiss zwischen niedrigem Strömungswiderstand und hohem Quecksilberabscheidegrad finden muss. Um eine effiziente Auslegung zu ermöglichen, wird ein numerisches Modell

entwickelt, das die Gasströmung durch das Baffle über den gesamten Gasverdünnungsbereich beschreibt und mit Hilfe des DSMC Verfahrens gelöst.

Zuletzt werden die verifizierten Modelle zur erstmaligen Auslegung der quecksilberbetriebenen Diffusionspumpen und zugehörigen Quecksilberfallen für das europäische Fusionsdemonstrationskraftwerk EU-DEMO angewendet. Die Simulationsergebnisse werden im Hinblick auf die vorher identifizierten Betriebsbedingungen und Anforderungen diskutiert. Außerdem wird aufgezeigt, welche Anforderungen an nachgeschaltete Systeme gestellt werden und wo künftige Optimierungspotentiale liegen.

Abstract

Future nuclear fusion power plants will require vacuum pumping systems of unprecedented size and complexity. Presently, the most advanced fusion reactor concept is the pulsed Tokamak. Its pulsed operation poses unique challenges to the vacuum system design, as it has to process high gas loads during the burn phase on the one hand and reach very low pressures between the pulses on the other hand. Further challenging requirements are introduced by the pursued deuterium-tritium reaction, which is currently considered to be the most viable fusion reaction candidate for terrestrial energy production. This reaction involves the hydrogen isotopes deuterium and tritium. While deuterium is stable and abundantly available on earth, tritium is radioactive with a short half-life and thus has to be created artificially. Its limited supply as well as nuclear regulation require that the tritium inventory of fusion power plants is kept as low as possible. For these reasons vacuum pumping technologies have to be developed that feature high pumping speeds, low terminal pressures and minimal tritium inventories. One potential high vacuum pumping technology that fulfills these requirements is the mercury-driven vapor diffusion pump. While diffusion pumps are an established technology, their application in the novel context of a fusion power plant's vacuum systems requires special consideration. The aim of the present work is to develop models of these pumps and to design and optimize them for the application in Tokamak exhaust pumping.

For this purpose the requirements imposed on the high vacuum pumps by the pulsed Tokamak operation are derived. The gas-vapor interaction in the diffusion pump is identified as the main design driving process. Diffusion pumps have to be complemented by a vapor trap to prevent migration of the mercury vapor to upstream systems. The vapor trap is based on cooled baffle plates. As baffles can reduce the effective performance of the diffusion pump significantly, it is important to consider the combination of both during the design process.

As diffusion pumps operate in the rarefied gas flow regime the theoretical modeling is based on the kinetic gas theory. Building on this, two models describing the gas-vapor interaction responsible for the pumping principle are derived. The simpler model is purely analytical and constructed in dimensionless form, thus allowing to identify the main contributing factors to the pumping principle. This is complemented by a more complex, numerical model based on the *Direct Simulation Monte Carlo (DSMC)* method, which can be employed to simulate realistic designs. The combination of both models allows for an efficient model-based design of diffusion pumps.

In order to support and validate the theoretical modeling an experimental setup has been designed, assembled and operated. The experimental objective is the characterization of a mercury vapor jet as used in diffusion pumps and its interaction with the pumped gas. The DSMC pump model is validated by performing a detailed comparison with the experimental results.

The pulsed operation of Tokamaks complicates the design of an efficient baffle, which has to compromise between a low flow resistance and high mercury vapor containment efficiency. In order to facilitate the design process a numerical model of the baffle, which is valid over the entire range of flow regimes, is developed and solved using the DSMC method.

Finally, the verified models are exploited to establish preliminary designs for the mercury-driven diffusion pumps and baffles for the EU-DEMO Tokamak exhaust pumping system. The simulation results are discussed with respect to the previously identified operating conditions and requirements. Additionally, the impact on downstream systems is considered, and future optimization potentials are pointed out.

Contents

Nomenclature

Symbols

A	Area	m^2
b	Distance of closest approach	m
C	Conductance	$\mathrm{m}^3\,\mathrm{s}^{-1}$
$C(f)$	Collision operator	$\mathrm{s}^2\,\mathrm{m}^{-6}$
c_r	Relative speed	$\mathrm{m\,s}^{-1}$
$\vec{c}$	Relative velocity	$\mathrm{m\,s}^{-1}$
D	Diffusion coefficient	$\mathrm{m}^2\,\mathrm{s}^{-1}$
d	Diameter	m
E_{rot}	Rotational energy	J
f	Phase space particle distribution function	$\mathrm{s}^3\,\mathrm{m}^{-6}$
f_{b}	Burn fraction	1
f_M	Maxwell-Boltzmann phase space particle distribution function	$\mathrm{s}^3\,\mathrm{m}^{-6}$
F_N	DSMC weight	1
$\vec{F}$	Force	N
$\vec{g}$	Gravitational acceleration	$\mathrm{m\,s}^{-2}$
h	Height	m
I	Measurement current	A
Kn	Knudsen number	1
L	Length	m
l	Liquid level	%
m	Mass	kg
Ma	Mach number	1
$\dot{m}$	Mass flow rate	$\mathrm{kg\,s}^{-1}$
m_r	Reduced mass	kg
$\dot{N}$	Number flow rate / reaction rate	s^{-1}

n	Number density	m^{-3}
$\dot{n}$	Number flux	$\mathrm{m}^{-2}\,\mathrm{s}^{-1}$
$O(x)$	Computational complexity scales with x	1
P	Probability	1
p	Pressure	Pa
Pe	Péclet number for mass transfer	1
Q	Throughput	$\mathrm{Pa}\,\mathrm{m}^3\,\mathrm{s}^{-1}$
q	Throughput (normalized to 273.15 K)	$\mathrm{Pa}\,\mathrm{m}^3\,\mathrm{s}^{-1}$
$\mathfrak{R}$	(Pseudo) random number	1
S	Pumping speed	$\mathrm{m}^3\,\mathrm{s}^{-1}$
Sc	Schmidt number	1
T	Temperature	K
t	Thickness	m
t	Time	s
$\vec{u}$	Bulk velocity	$\mathrm{m}\,\mathrm{s}^{-1}$
$\dot{V}$	Volumetric flow rate	$\mathrm{m}^3\,\mathrm{s}^{-1}$
V	Volume	m^3
$\vec{v}$	Velocity	$\mathrm{m}\,\mathrm{s}^{-1}$
v_x, v_y, v_z	Cartesian velocity components	$\mathrm{m}\,\mathrm{s}^{-1}$
w	Transmission probability	1
x	Molar / number fraction	1
$\vec{x}$	Position	m
x, y, z	Cartesian position components	m
Z	Atomic number	1
z	Number of excited internal degrees of freedom	1
Z_{rot}	Rotational relaxation number	1
α	Angle	°
α	Scattering coefficient (VSS model)	1
α_c	Condensation coefficient	1
γ	Heat capacity ratio	1

δ	Overlap	m
ϵ	Azimuthal collision angle	1
ϵ_{LJ}	Depth of potential well (LJ model)	J
ε	Uncertainty	various
ζ^*	Hagena condensation parameter	1
η_{DIR}	Direct internal recycling efficiency	1
η_{f}	Fueling efficiency	1
η_ς	Pump efficiency	1
κ	Compression ratio	1
Λ	Relative sensitivity	1
λ	Mean free path	m
μ	Viscosity (dynamic)	Pa s
ξ	Sticking coefficient	1
ρ	Mass density	$\mathrm{kg\,m^{-3}}$
σ	Differential cross section	$\mathrm{m^2}$
σ_{LJ}	Inversion distance (LJ model)	m
σ_T	Total cross section	$\mathrm{m^2}$
ς	Capture coefficient	1
τ	Mean collision time	s
$\boldsymbol{\Phi}$	Speed ratio	1
φ	Speed ratio	1
χ	Deflection collision angle	1
ψ	Mercury containment efficiency	1
ω	Viscosity coefficient (VHS/VSS model)	1
$\Omega^{(i,j)*}$	Collision integral (LJ model)	1

Constants

k_B	Boltzmann constant	$1.380\,649 \times 10^{-23}\,\mathrm{J\,K^{-1}}$

Frequently used subscripts

$\square_{\mathrm{eff}}$	Effective

$\square_{G}$ Gas property

$\square_{in}$ Inlet

$\square_{max}$ Maximum

$\square_{mix}$ Mixture property

$\square_{mp}$ Most probable

$\square_{out}$ Outlet

$\square_{p}$ Property of a particle

$\square_{+/-}$ Positive or negative direction

$\square_{ref}$ Reference property

$\square_{sat}$ Saturation state

$\square_{V}$ Vapor property

$\square_{x/y/z}$ In x, y or z direction

Abbreviations

ADC Analog-to-digital converter

CAD Computer aided design

DIPAK Direct Internal Recycling Integrated Development Platform Karlsruhe

DIR Direct internal recycling

DIRL Direct internal recycling loop

DIV Divertor

DSMC Direct Simulation Monte Carlo

DVM Discrete Velocity Method

EU-DEMO European demonstration fusion power plant

FT Fore-vacuum tolerance

FV Fore-vacuum

HS Hard Sphere

HV High vacuum

INTL Inner tritium plant loop

ITER International Thermonuclear Experimental Reactor

KALPUREX Karlsruhe liquid metal based pumping process for fusion reactor exhaust gases

LDP Linear diffusion pump

LJ Lennard-Jones

LRP Liquid ring pump

MBA Mercury baffle adapter

MFP Metal foil pump

NEMESIS Nozzle Experiment for Mercury Expansion Investigations

NTC No Time Counter

RTD Resistance temperature detector

TC Thermocouple

TPMC Test Particle Monte Carlo

VDP Vapor diffusion pump

VHS Variable Hard Sphere

VSS Variable Soft Sphere

VSS Variable Soft Sphere

1. Introduction

At the beginning of the last century, Albert Einstein's famous discovery of the equivalence of mass and energy [1] delivered the basis for our understanding of nuclear transmutation processes. These are defined by the conversion of elements: Light elements can fuse into heavier elements and heavy elements can undergo fission into lighter elements. Due to the mass defect between reactants and products these reactions involve conversion between mass and energy. The most stable element is ^{56}Fe, lighter elements release energy in fusion reactions and heavier elements in fission reactions. The energy that can be released per given mass is much higher in nuclear reactions than in chemical reactions. This fact enabled Arthur Eddington to finally propose nuclear fusion as the answer to the previously unaccountable longevity of the stars' energy source [2]. Stars, like our sun, fuse their hydrogen fuel to heavier elements over their lifetime [3].

The exploitation of nuclear energy on earth has ever since been a goal of mankind. Technical energy production by nuclear fission has proven to be much simpler and the first power plant was commissioned as early as 1954 [4]. Nuclear fusion is harder to realize due to the necessity to overcome the *Coulomb barrier*, i.e. the electrostatic repulsion of the positively charged nuclei. However, fusion power plants have some advantages over fission power plants: Firstly, the conditions required for nuclear fusion are very challenging to sustain, therefore uncontrollable chain reactions are impossible. Secondly, the reaction products of the fusion reaction are not radioactive. Only irradiated - mostly due to neutron bombardment - structural materials of the reactor have to be disposed of after their lifetime is reached. Additionally, a clever choice or design of these materials allows for a significant reduction of the half-life time. For example a lot of materials research was performed on developing a new steel composition with significantly reduced activation [5]. Fusion could therefore fulfill the role of a safe, reliable, continuous and carbon emission-free option in the energy mix of the future that does not produce long-lived nuclear waste.

1.1. Magnetic confinement fusion in Tokamaks

The present work has been carried out in the context of the European demonstration fusion power plant project (*EU-DEMO*). EU-DEMO will be a magnetic confinement fusion reactor currently conceptualized as a *Tokamak*. A simplified sketch of a Tokamak and its principal components is depicted in Fig. 1.1. In order to achieve nuclear fusion, temperatures in the order of 1×10^8 K are required to overcome the Coulomb barrier. In Tokamaks this is achieved by confining a hot plasma formed by the fusion fuel by means of a magnetic field with closed field lines. The magnetic field guides the positively charged fuel ions and thus prevents collisions with the reactor walls. Part of the magnetic configuration is generated by ramping up the electric potential difference of a central solenoid to induce an electric current in the plasma via the transformer principle. Tokamaks are therefore pulsed because the central solenoid has to be reset to its initial state in regular intervals (timescale of hours).

In principle all elements lighter than ^{56}Fe can theoretically be used in a fusion reaction with net energy gain. The most favorable reaction regarding the required conditions is the *D-T reaction*,

$$\mathrm{D} + \mathrm{T} \rightarrow {}^4\mathrm{He} + \mathrm{n} + 17.6\,\mathrm{MeV}, \tag{1.1}$$

or in abbreviated notation T(d,n)α between the two hydrogen isotopes *deuterium* D (^{2}H) and *tritium* T (^{3}H). These isotopes differ from the most abundant form of hydrogen (^{1}H) - also referred to as

protium - by the number of neutrons in the nucleus. Deuterium is a part of *heavy water*, which makes for a small part of natural water, and can therefore be purified at relatively low cost in abundant amounts. Tritium, on the other hand, is radioactive and has a relatively short half-life span of about 12.3 years. Thus, it is not naturally available in significant amounts and has to be created artificially. This can be achieved by breeding tritium from lithium via the nuclear reactions ^{7}Li(n,n'α)T and ^{6}Li(n,α)T in a *blanket* arranged around the plasma that is hit by the neutrons produced by the D-T reaction [6].

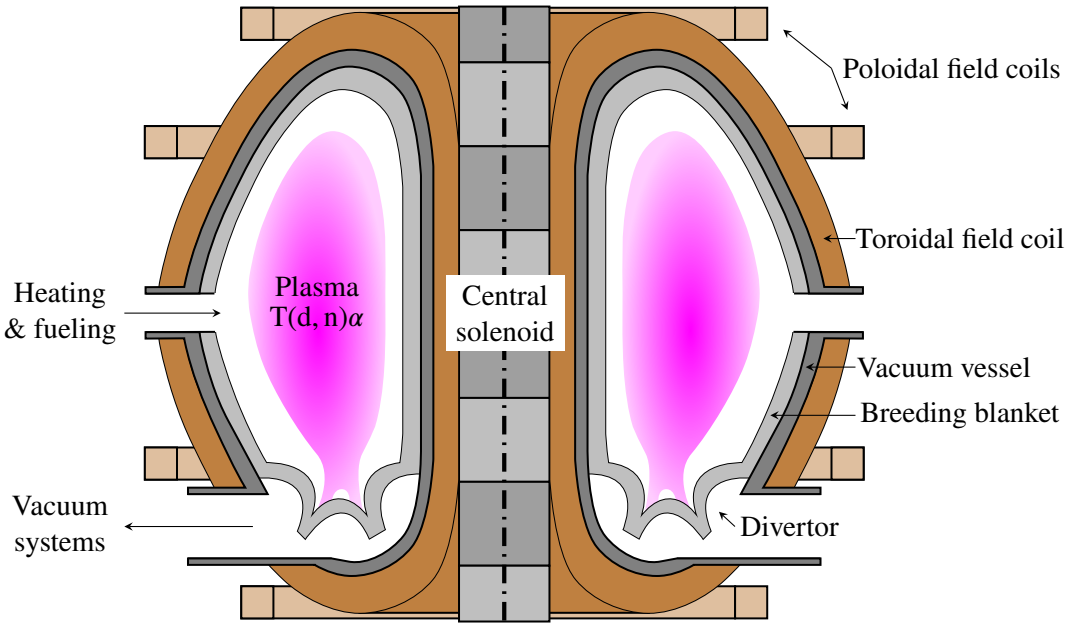

Figure 1.1.: Simplified sketch of a Tokamak including the principal components. The D-T reaction is performed in a plasma inside of a toroidal plasma chamber, which is surrounded by the breeding blanket. The plasma is confined by a strong magnetic field produced by toroidal and poloidal field coils and the plasma current induced by the central solenoid. Fueling and heating is performed by external systems. The heat released by the fusion reaction is extracted from the breeding blanket and divertor by flowing a coolant fluid through them. Particles are exhausted by the vacuum systems which are connected below the divertor.

1.2. Fusion fuel cycle and its impact on the exhaust gas pumping system

In Tokamaks, the D-T reaction, Eq. (1.1), is performed in a toroidal plasma chamber. The *fuel cycle*, which is depicted greatly simplified in Fig. 1.2, is responsible for providing fuel to the torus and for extracting the tritium that is generated in the blanket around the reaction chamber.

The fuel is provided by a fueling system. Deuterium is supplied externally and tritium is taken out of a storage system. In order to start up the reactor, tritium has to be imported externally. Fueling is primarily achieved by first producing frozen D-T pellets and then accelerating them to very high speeds before shooting them into the plasma. One of EU-DEMOs goals is to demonstrate a fusion power of approximately 2000 MW with a target of 500 MW net feed-in power to the electric grid [7]. The large power difference is a result of the inevitable losses during the conversion of thermal to electric energy in the power cycle (Carnot efficiency) and power demands of the aux-

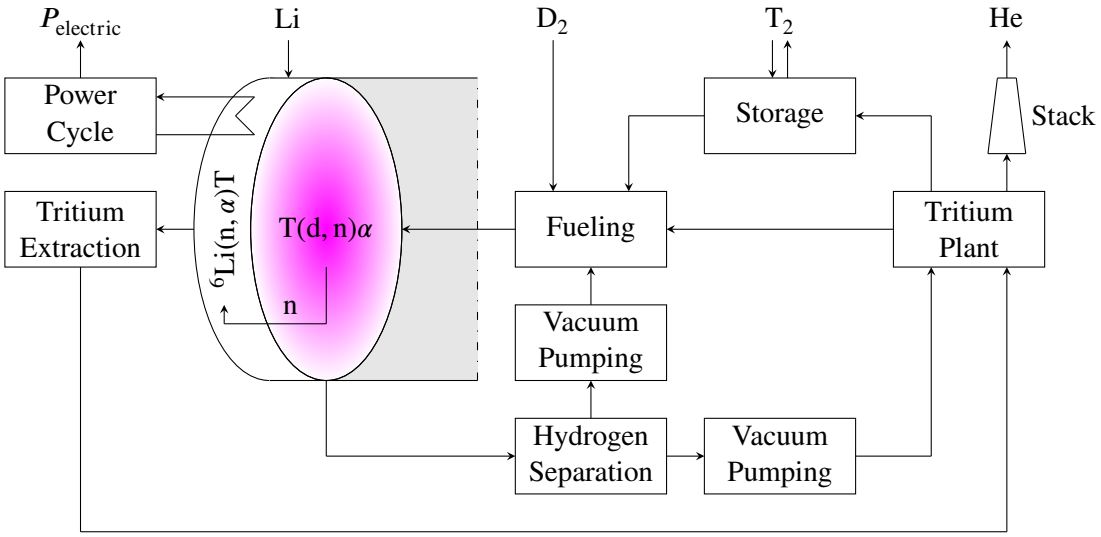

Figure 1.2.: Simplified sketch of the D-T fuel cycle in a fusion power plant including the essential material and energy streams in and out of the plant. The D-T fusion reaction is performed in the plasma chamber and produces energetic neutrons, which hit the blanket installed around the plasma chamber. Here, nuclear reactions between lithium and the neutrons produce ("breed") the necessary tritium. Furthermore, heat is extracted and used to drive a conventional power cycle. The plasma purity is ensured by the vacuum pumping system. In a first step unburnt fuel is separated from the other exhaust gases and recycled to the fueling system. The remaining exhaust gases and tritium from the blanket are processed in the tritium plant. Fuel is either send to storage or fueling systems. Helium can either be collected or discharged (as indicated here).

iliary plant systems (among other, the fuel cycle). Taking into account that every D-T reaction releases 17.6 MeV, a reaction rate of approximately $\dot{N}_r = 7.1 \times 10^{20}\,s^{-1}$ is required to reach the projected fusion power of 2000 MW. This means that tritium and deuterium ions are consumed at the rate $\dot{N}_r$, while α-particles (helium nuclei) are produced at the same rate. The corresponding burn-up rates of deuterium and tritium are approximately 2.37 mg $s^{-1}$and 3.55 mg s^{-1} respectively and the helium production rate is approximately 4.71 mg s^{-1}.

Despite this low fuel consumption by fusion, Tokamaks require large, powerful vacuum systems for two reasons:

- A low ultimate pressure is required to ignite the fusion reaction. As Tokamaks are pulsed devices, this is required frequently (timescale of hours). Power is only generated while the fusion reaction is burning, therefore it is of economic interest to reduce the downtime. Consequently, the pump-down time of the large plasma chamber has to be as short as possible.

- A high plasma purity is required to keep the fusion reaction going. Therefore, helium *ash* (a term commonly used because it is the product of the D-T reaction) has to be removed from the reactor core. Particle exhaust is realized by diverting the magnetic field lines at the plasma edge into a *divertor* area, where the plasma is directed onto actively cooled target plates [3]. As this cannot be implemented selectively for helium, it is necessary to continuously fuel and exhaust at a much higher rate than the fusion reaction rate $\dot{N}_r$. Therefore, the vacuum system connected to the divertor has to manage high throughputs.

The high fueling and exhaust flow rates mean that a large part of the exhaust gas mixture is composed of unburnt fuel (i.e. D_2, DT and T_2). That is why it is very beneficial to separate a fraction

of the unburnt hydrogenic species from the exhaust gas mixture before further treatment. This concept is called *direct internal recycling (DIR)* and has the central benefit that the systems for further exhaust treatment will have a potentially much smaller footprint, which reduces the tritium inventory in the plant [8]. The separated unburnt fuel is pumped directly back to the fueling system. The remaining fraction of the exhaust gas is pumped to the tritium plant, where helium ash and impurities are removed. The helium can either be released to the environment (as indicated in Fig. 1.2) or captured and sold.

The reduction of the tritium inventory in the fuel cycle is one of the key challenges on the way to a commercial fusion power plant for safety, nuclear regulation and economic reasons [8]. Therefore, it has been proposed to substitute cryopumps, which are used in the exhaust pumping systems of present day experimental fusion devices like *ITER* [9], with continuous technologies [8]. This is motivated by the fact that cryopumps work by trapping gas particles on cold surfaces and therefore inherently have a higher tritium inventory than gas transfer pumps. Thus, a mercury-based pumping train relying on vapor diffusion pumps as primary pumps and liquid ring pumps as backing pumps has been proposed as a potential alternative [10, 11].

1.3. Objective of work

The objective of the present work is to advance the development of mercury-driven vapor diffusion pumps for the application in the exhaust pumping train of a pulsed Tokamak. This involves the following steps:

- Identification of the main design driving aspects and limitations that will govern the application in a power plant based on the Tokamak concept.
- Physically consistent description of the pumping effect as a result of the gas-vapor interaction in the diffusion pump body.
- Development of a numerical vapor diffusion pump model allowing to predict the pump's main performance indicators.
- Verification of the model and subsequent validation by quantitative comparison within the frame of an experimental setup.
- Development of a numerical model for the description of a vapor trap that complements the vapor diffusion pump design and characterization of these traps in the operating conditions expected in the Tokamak.
- Determination of quantitative performance parameters of the vapor diffusion pump and vapor trap combination for the application in the EU-DEMO Tokamak.

1.4. Structure of work

The structure of the present thesis follows from the formulated objectives.

In Chap. 2 the vacuum pumping requirements and unconventional conditions arising from the Tokamak operation are discussed. Additionally, the KALPUREX process, which features mercury-driven diffusion pumps, is described. Afterwards, the operating principle and design of mercury vapor diffusion pumps are outlined.

Then, in Chap. 3 the physical modeling of rarefied gas and vapor flows is explained. Furthermore, the *Direct Simulation Monte Carlo (DSMC)* method is introduced in the context of numerical diffusion pump simulation. Since the DSMC method is particle-based this also includes modeling

of the intermolecular collisions between the mercury vapor and the pumped gas species. Additionally, the employed boundary conditions are introduced and justified.

Chapter 4 describes the modeling of the gas vapor interaction, which is responsible for the pumping effect. Here, first a one-dimensional model of the pumping process is introduced in dimensionless form based on existing models proposed in literature. The model is subsequently used to analyze the operational limits of diffusion pumps. The one-dimensional model is complemented by a sophisticated model using the DSMC method, which describes the interaction on the level of the kinetic gas theory and considers the interaction of vapor and gas with the pump structures.

The latter model is validated in Chap. 5, which introduces the experimental setup that has been designed, constructed and operated in the present work. In this setup mercury vapor jets expanded from a circular nozzle are investigated. Subsequently, the numerical model is validated by comparison with the experimental measurements.

Next, Chap. 6 focuses on the modeling of the vapor trap, which has to be installed upstream of the diffusion pumps in order to prevent mercury migration. A parametric sensitivity study of different geometric and operational parameters is performed in order to derive guidelines for designing such a trap.

In Chap. 7 diffusion pump and vapor trap designs meeting the requirements in the EU-DEMO torus exhaust pumping system are derived. Furthermore, an innovative semi-empirical analytical model of the integrated exhaust pumping system is introduced which combines the simulation results of the sophisticated models from Chaps. 4 and 6. Albeit its limited exactitude, this model has the benefit of identifying bottlenecks in the system mathematically.

Finally, the main results are summarized and recommendations for future work are derived in Chap. 8.

2. Vapor diffusion pumps for Tokamak exhaust pumping

The present chapter discusses the exhaust vacuum pumping requirements of Tokamaks and introduces the necessary vacuum fundamentals. Furthermore, the mercury-based exhaust pumping process *KALPUREX*, which features mercury-driven *vapor diffusion pumps (VDPs)*, is described. Subsequently, the operation principle, performance and design of VDPs are addressed in order to establish the requirements a diffusion pump model has to satisfy.

2.1. Tokamak operation modes and resulting load on fuel cycle

The exhaust pumping system of a Tokamak that uses the DIR concept to reduce the tritium inventory is separated in two loops called *direct internal recycling loop (DIRL)* and *inner tritium plant loop (INTL)*. The DIRL pumps the separated unburnt fuel, whereas the INTL pumps the remaining mixture composed primarily of unburnt fuel and helium ash.

The gas load on the fuel cycle of a pulsed Tokamak as currently foreseen for EU-DEMO is transient. A typical Tokamak cycle is divided into four parts [12]: Firstly, during so-called *dwell* phase, the device is prepared for the next ignition. Most importantly, the central solenoid, which is used to induce the plasma current by ramping up its voltage, has to be reset during the dwell period. Additionally, the pumping system is used to lower the neutral pressure in the torus to allow for the next plasma discharge. The plasma and fusion reaction are initiated during the so-called *ramp-up* phase. This phase is followed by the steady-state *burn* phase during which fusion occurs. The *ramp-down* phase is initiated when a reset of the central solenoid is necessary. After ramp-down the next cycle begins with its dwell phase. As energy is only produced during the burn phase, economic viability directly scales with the ratio of burn time to total pulse time.

The two main responsibilities of the vacuum pumping system are to ensure appropriate conditions for the next ignition during the dwell phase and to continuously pump during the burn phase. The specific requirements are discussed in the next two sections.

2.1.1. Dwell and ramp-up phases

During the dwell phase the torus vacuum pumping system has to reduce the pressure in the Tokamak torus to allow for the next plasma ignition, which is initiated during the subsequent ramp-up phase. The ramp-up phase in itself is subdivided into different stages, but a detailed explanation of these exceeds the scope of this work. A thorough review of these stages and the associated required conditions in the ITER Tokamak is presented in [13]. The prefill pressures required there for plasma breakdown and burn-through are in the range of 1 mPa [13], which implies that the pressure at the end of the dwell phase right before prefilling has to be even lower. To reduce the dwell time in EU-DEMO to approximately 10 min it is planned to relax this requirement by additional heating technologies [12, 14]. Thus, it is expected that the required terminal dwell pressure will lie in the range of some mPa in EU-DEMO.

2.1.2. Burn phase

During the burn phase of a Tokamak the plasma is actively burning and producing energy via the D-T fusion reaction. The main duty of the fuel cycle is to supply fuel to the reactor core and to remove helium ash from it. An overview of the fuel cycle during burn including all important streams is shown in Fig. 2.1. Fueling is performed with a rate $\dot{N}_\mathrm{f}$ and a 50/50 mixture of deuterium and tritium, when neglecting decay losses of tritium, which are small compared to the flow rates in the fuel cycle. Only a part of the injected fuel successfully reaches the plasma core, where the fusion reaction is occurring. This is expressed by the fueling efficiency η_f. In the plasma core deuterium and tritium ions fuse to produce α-particles at a rate of $\dot{N}_\mathrm{r}$ ($\approx 7.1 \times 10^{20}\,\mathrm{s}^{-1}$ for EU-DEMO). The fusion reaction is quite sensible to fuel dilution, which is why the helium concentration in the plasma core has to be kept low. On the other hand it has to be ensured that the α-particles are confined long enough to transfer their kinetic energy back to the fusion plasma (so-called *α-heating*) [15]. For EU-DEMO the maximum helium concentration in the core is currently estimated to be $x_\mathrm{c,He} \approx 0.07$ [16]. It is preferential to selectively remove helium from the plasma core, however, no technical solution exists up to now [17]. Extraction of particles happens at the divertor, which is an array of cooled plates outside the plasma on which incident ions (D, T, α) neutralize. Part of them are reflected into the plasma and ionized again while another part $\dot{N}_\mathrm{e}$ is pumped by the exhaust pumping system that is connected to the divertor. As this process is not selective a large part of the unburnt fuel is also exhausted together with the helium ash. As indicated before, the fueling rate $\dot{N}_\mathrm{f}$ and exhaust rate $\dot{N}_\mathrm{e}$ of the reactor must therefore be substantially larger than the actual fusion rate $\dot{N}_\mathrm{r}$. In plants that use the previously introduced DIR concept, the exhaust gas stream is subsequently separated into a stream containing only unburnt fuel $\dot{N}_\mathrm{DIRL}$, which can be directly used for fueling again, and a stream $\dot{N}_\mathrm{INTL}$, which contains unburnt fuel and the helium ash that is separated in the tritium plant. The efficiency of separation is referred to as the *DIR ratio* η_DIR, which is foreseen to be approximately 0.8 for EU-DEMO [18, 19].

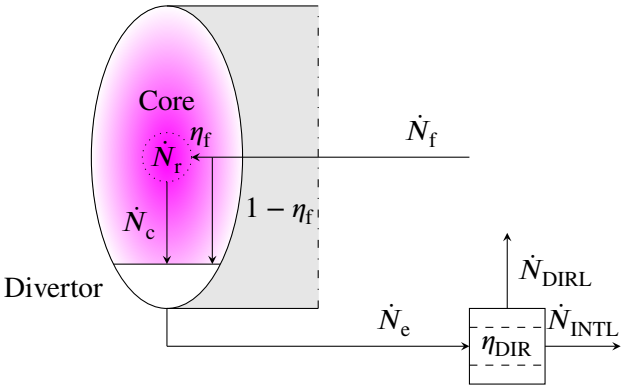

Figure 2.1.: Model for estimating the load of a D-T fuel cycle with DIR in a fusion power plant during burn. Displayed variables are defined as: $\dot{N}_\mathrm{f}$: fueling flow rate, $\dot{N}_\mathrm{r}$: fusion reaction rate, $\dot{N}_\mathrm{c}$: core exhaust flow rate, $\dot{N}_\mathrm{e}$: exhaust flow rate, $\dot{N}_\mathrm{DIRL}$: flow rate in direct internal recycling loop (DIRL), $\dot{N}_\mathrm{INTL}$: flow rate in inner tritium plant loop (INTL), η_f: fueling efficiency, η_DIR: direct internal recycling (DIR) ratio.

An estimate of the required fueling and exhaust rates and their respective species concentrations can be derived from particle balances around the different control volumes depicted in Fig. 2.1. The particle number is conserved, as the fusion reaction in the plasma core consumes one particle (molecule of D-T) and produces one other particle (helium atom). Therefore, fueling and exhaust rates are equal in steady-state. Since it does not matter if deuterium and tritium ions originate from a single DT molecule or from two D_2 and T_2 molecules, it is convenient to summarize them using

the common abbreviation Q = {H, D, T} to refer to hydrogen atoms (see e.g. [19]). It can be shown that the helium concentration $x_{\mathrm{e,He}}$ in the exhaust mixture is

$$x_{\mathrm{e,He}} = \frac{2\eta_{\mathrm{f}} x_{\mathrm{c,He}}}{1 + x_{\mathrm{c,He}}}, \tag{2.1}$$

which only depends on the purity requirement in the plasma core $x_{\mathrm{c,He}}$ and the fueling efficiency η_{f}. The helium concentration in the exhaust stream is closely related to the dimensionless *burn fraction* f_{b} [18], which compares the fusion reaction rate to the core fueling rate:

$$f_{\mathrm{b}} = \frac{\dot{N}_{\mathrm{r}}}{\eta_{\mathrm{f}} \dot{N}_{\mathrm{f}}} = \frac{2x_{\mathrm{c,He}}}{1 + x_{\mathrm{c,He}}} = \frac{x_{\mathrm{e,He}}}{\eta_{\mathrm{f}}}. \tag{2.2}$$

The flow rates and compositions in the two inner loops follow directly as

$$\dot{N}_{\mathrm{DIRL}} = \eta_{\mathrm{DIR}} x_{\mathrm{e,Q_2}} \dot{N}_{\mathrm{e}}, \tag{2.3}$$

which is a pure hydrogen stream, i.e. with $x_{\mathrm{DIRL,Q_2}} = 1$ and

$$\dot{N}_{\mathrm{INTL}} = \dot{N}_{\mathrm{e}} - \dot{N}_{\mathrm{DIRL}}, \tag{2.4}$$

where helium enriches to

$$x_{\mathrm{INTL,He}} = \frac{x_{\mathrm{e,He}}}{1 - \eta_{\mathrm{DIR}}(1 - x_{\mathrm{e,He}})}. \tag{2.5}$$

For EU-DEMO the product of fueling efficiency and burn fraction (cf. Eq. (2.2)) is estimated conservatively as $f_{\mathrm{b}}\eta_{\mathrm{f}} = x_{\mathrm{e,He}} \approx 0.006$ [19, 20]. Together with the core dilution limit ($x_{\mathrm{c,He}} \approx 0.07$) introduced above, this implies a minimum required fueling efficiency of approximately $\eta_{\mathrm{f}} \approx 0.048$. The load on the fuel cycle vacuum systems can then be estimated to be approximately $\dot{N}_{\mathrm{f}} = \dot{N}_{\mathrm{e}} \approx 11.3 \times 10^{22}\,\mathrm{s}^{-1}$, which is approximately 160 times higher than the fusion reaction rate. The exhaust stream is subsequently split into $\dot{N}_{\mathrm{DIRL}} \approx 9.0 \times 10^{22}\,\mathrm{s}^{-1}$ and $\dot{N}_{\mathrm{INTL}} \approx 2.3 \times 10^{22}\,\mathrm{s}^{-1}$ in the DIRL and INTL, respectively. Due to the direct recycling helium enriches in the INTL stream from $x_{\mathrm{e,He}} \approx 0.006$ to $x_{\mathrm{INTL,He}} \approx 0.031$. During burn the neutral pressure in the divertor is expected to lie in the range of $1 - 10\,\mathrm{Pa}$ (e.g. in the experimental Tokamak ASDEX Upgrade [21] and estimated for EU-DEMO [22]). This implies that the burn and dwell pressure differ by approximately 2–3 orders of magnitude. The combination of low dwell pressures and high burn throughput culminates in unique requirements on the torus exhaust pumping system.

2.2. Torus exhaust pumping

A high vacuum pumping system is necessary to handle the combination of high throughputs required during the burn phase at intermediate pressure (∼1 Pa) and the low pressures necessary during the dwell phase (∼1 mPa) in the Tokamak. A simplified sketch of the exhaust pumping train of a fusion reactor is depicted in Fig. 2.2. This figure is used to introduce the main technical terms regarding vacuum technology.

The *pumping speed* S of a vacuum pump (P1 and P2 in Fig. 2.2) corresponds to the volumetric exhaustion speed $\dot{V}$ of the *recipient* (the volume that is pumped) at given operating conditions, e.g. pressure p, temperature T or power supplied to the pump. Dimensionally, it is equivalent to a volumetric flow rate:

$$S(p, T, ...) = \dot{V} = \frac{\mathrm{d}V}{\mathrm{d}t} = A_{\mathrm{in}} \frac{\mathrm{d}x}{\mathrm{d}t}, \tag{2.6}$$

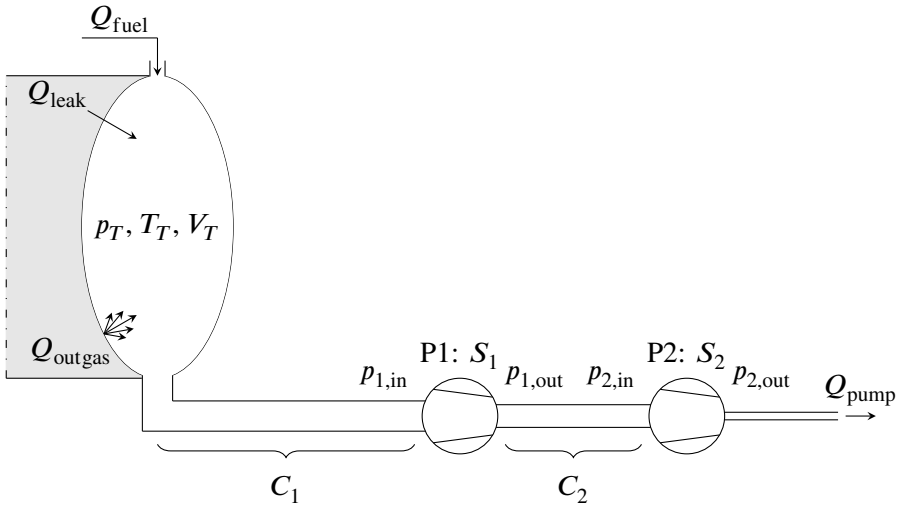

Figure 2.2.: Simplified sketch of a fusion reactor torus and its vacuum pump train. The conditions in the torus with volume V_T are given by pressure p_T and temperature T_T. The vacuum pump train consists of a high vacuum pump (P1; pumping speed S_1) and a backing pump (P2; pumping speed S_2). The connections between torus and pump P1 and between the pumps have conductances C_1 and C_2. All main gas load sources are shown ($Q_{\text{fuel}}, Q_{\text{leak}}, Q_{\text{outgas}}$). The pressure increase caused by the pumps ($p_{i,\text{out}} > p_{i,\text{in}}$) is visualized by the reduction in connection line diameter.

where A_{in} corresponds to the cross-sectional area by which vacuum pump and recipient are connected. This cross-section is also referred to as the *inlet* of the vacuum pump.

The *compression ratio* κ of vacuum pumps corresponds to the ratio of outlet to inlet pressure,

$$\kappa = \frac{p_{\text{out}}}{p_{\text{in}}}, \tag{2.7}$$

and is therefore by definition greater than unity for a successfully operating pump.

The *throughput* Q corresponds to the amount of pumped gas per unit time. It is defined as the product of pumping speed S and pressure in the recipient p_{in} and measured in $\text{Pa}\,\text{m}^3\,\text{s}^{-1}$:

$$Q = p\dot{V} = \dot{N} k_B T = S p_{\text{in}}. \tag{2.8}$$

Because vacuum systems are usually (assumed to be) operated under isothermal conditions, the throughput is often considered to be a conserved quantity because of its relation to the number flow rate through the ideal gas law. If the vacuum system displayed in Fig. 2.2 is considered to be isothermal, the steady-state mass balance around the system can be converted to a throughput balance yielding $Q_{\text{pump}} = Q_1 = Q_2 = Q_{\text{fuel}} + Q_{\text{leak}} + Q_{\text{outgas}}$. The throughput is also commonly specified at the reference temperature 273.15 K. In the following this is indicated by a lower case q. It then follows that $q = 1\,\text{Pa}\,\text{m}^3\,\text{s}^{-1} \equiv 2.65{\times}10^{20}\,\text{s}^{-1}$. Transformation of the normalized throughput q to the actual throughput Q at temperature T is possible by the relation $Q = q \cdot (T/273.15\,\text{K})$. As the throughput of a pump is linked with its pumping speed by the inlet pressure it follows that the required pumping speed per stage in a multistage serial connection of vacuum pumps successively reduces as the pressure increases, i.e. $S_2 < S_1$ for the example configuration in Fig. 2.2.

Many vacuum systems are operated without an explicit load like the fueling rate Q_{fuel}. The achievable ultimate pressure is then limited by parasitic loads, most commonly resulting from leakage or outgassing (primarily of hydrogen) as indicated in Fig. 2.2.

The *conductance* C corresponds to the reciprocal flow resistance of components (e.g. pipes, valves) in a vacuum system and has the same dimensions as the pumping speed. However, contrary to pumps, which increase the pressure in flow direction, the limited conductance results in a pressure drop.

$$C(\text{geometry}, p, T) = \frac{Q}{\Delta p}. \tag{2.9}$$

Apart from the component geometry, the conductance depends mostly on the gas species, the flow regime and the temperature. As a rule of thumb, the lower the pressure (i.e. the "higher" the vacuum) the more important the conductance of the system. With respect to the example presented in Fig. 2.2, the limited conductance of the piping between the torus and pump P1 results in the pressure drop $\Delta p_1 = p_T - p_{1,\text{in}} = Q_{\text{pump}}/C_1$ and reduces the *effective pumping speed* that is available at the torus to $S_T < S_1$.

The pressure evolution in a vacuum recipient over time is described by the pumping equation. In isothermal conditions it is equivalent to a mass balance. In case of the exemplary vacuum system depicted in Fig. 2.2, the pumping equation can be formulated as

$$\underbrace{V_T \frac{\mathrm{d}p_T}{\mathrm{d}t}}_{\text{temporal evolution}} = \underbrace{\sum Q_{\text{i}}}_{\text{loads}} - \underbrace{S_T p_T}_{\text{pumping}}, \tag{2.10}$$

where V_T corresponds to the volume of the recipient.

The pulsed operation of a Tokamak leads to a time varying load on the vacuum pumping system because the fueling throughput is only active during the burn phase. Assuming that the effective pumping speed in both phases remains constant, which is a realistic hypothesis, Eq. (2.10) can be integrated to find the pressure evolution over time. An example of the expected pressure evolution during Tokamak operation is depicted in Fig. 2.3.

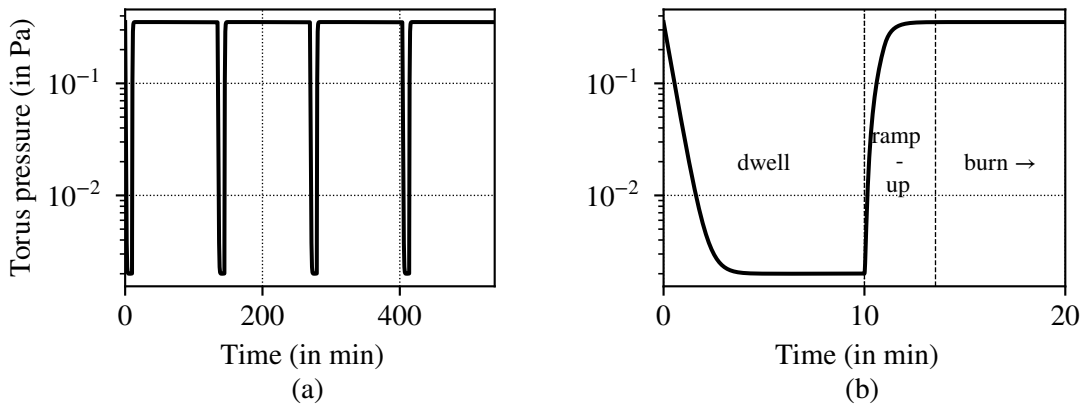

Figure 2.3.: (a) Torus pressure evolution over four cycles. (b) Torus pressure evolution during dwell, ramp-up and the initial part of the burn phase of a single cycle.

The torus exhaust pumping system and the required pressure levels and pump-down times require the exploitation of multiple pumping stages featuring different pump technologies. One option for the system design is proposed in form of the *KALPUREX* process for EU-DEMO with a closer description following in the next section.

2.3. The KALPUREX process

KALPUREX is the acronym for *Karlsruhe liquid metal based pumping-process for fusion reactor exhaust gases* [11, 23]. It is an implementation of the previously introduced DIR concept for reducing the tritium inventory in the fuel cycle by recycling part of the exhausted fuel and replacing discontinuous pumping solutions with continuous ones. The vacuum pumping system proposed in the KALPUREX process relies on a combination of three main pump types, that have been selected using a systematic screening process [23, 24]:

Metal foil pumps (MFPs) are proposed for separation and compression of a large part of the unburnt fuel from the exhaust gas mixture. These pumps rely on the principle of hydrogen *super-permeation* through a metal foil with a surface layer [25–27]: Conventional hydrogen permeation through a metal with surface layer of impurities involves the rate limiting step of hydrogen molecule dissociation to atoms on the surface layer. On the downstream side of the foil the atomic hydrogen will recombine to molecules. By providing a source of atomic hydrogen upstream of the foil the rate limiting dissociation step is skipped and the flux of permeating hydrogen greatly increased. Thus, if no atomization of hydrogen downstream the metal foil is provided compression can be achieved. As this effect only occurs for hydrogen the pump also fulfills the separation function required for the application of the DIR concept.

Vapor diffusion pumps (VDPs) are foreseen as continuously operating tritium compatible high vacuum (HV) pumps. For present day experimental fusion devices the high vacuum pumping function is typically performed by discontinuous cryopumps (e.g. in ITER [9]). However, a straightforward scale-up suggests problems regarding the tritium inventory hold-up and regeneration of these pumps [8]. These issues can be solved by using a continuous technology. Continuous cryopumps, turbomolecular pumps and diffusion pumps have been identified as the three technologies that can potentially fulfill this role [10]. A continuous cryopump design has been suggested in the form of the *snail pump*, which uses a scraper to continuously remove the adsorbed or deposited gases [28, 29]. Turbomolecular and diffusion pumps operate on the principle of momentum transfer - in case of turbomolecular pumps by a set of rotor-stator pairs and in case of vapor diffusion pumps by a high speed vapor jet. Diffusion pumps are identified as superior over the other pumping technologies mainly because they do not contain moving parts, which raises issues regarding the operation in magnetic fields and maintainability [10].

Liquid ring pumps (LRPs) are suggested as backing pumps for the vapor diffusion pumps. These pumps operate via the eccentric rotation of a bladed wheel. The gas is compressed by the varying volume formed between the wheel blades and a liquid ring formed by centrifugal forces. This type of pumps features high pumping speeds and is capable of operating continuously, which allows it to substitute discontinuous technologies like cryo viscous compressors [10].

Choice of mercury as the operating fluid Both VDPs and LRPs require an operating fluid, which has to be tritium compatible for the application in torus exhaust pumping. Tritium compatibility means that the fluid has to fulfill three main requirements:

- Absence of chemical or isotope exchange reactions with tritium, which can lead to an accumulation of tritium in the operating fluid and would result in an increase of the tritium inventory.
- Low solubility of tritium.

- No degradation under the tritium beta decay radiation.

These requirements limit the selection of potential operating fluids significantly, for example all of them raise potential issues with oils that are commonly used in vapor diffusion pumps [30]. The only practical fluid fulfilling all the requirements that could be identified is mercury [23, 24]. It does not perform chemical reactions with any of the exhaust gases under the expected operating conditions [31]. A tritium activity of $8.5\,\mu\mathrm{Ci\,kg^{-1}}$ is reported in filtered mercury used in tritium pumps collected over a span of 25 years [32]. Accounting for tritium decay, the initial activity can be conservatively estimated to be $\leq 34\,\mu\mathrm{Ci\,kg^{-1}}$. This corresponds to a negligible mass concentration of $3.5\,\mathrm{ng\,kg^{-1}}$. Additionally, the neutron activation of mercury itself in a fusion environment is acceptable as displayed in Fig. 2.4, which shows that the expected decay time until disposal is less than 100 years. Mercury has more favorable activation properties than tungsten [33], which is considered as first wall material and thus facing much higher neutron fluxes. For these reasons mercury has already been considered for the application in previous fusion device exhaust pumping systems [34].

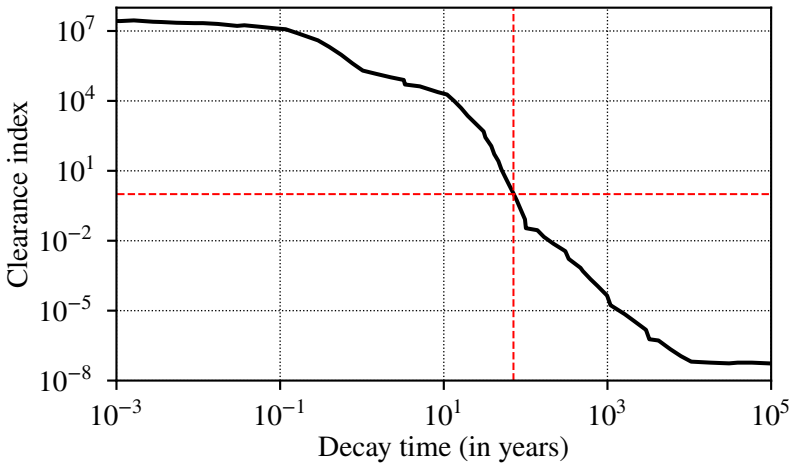

Figure 2.4.: Clearance index of mercury. The depicted data is extracted from [33] for the shield location of a conceptual fusion power plant corresponding to the projected position of the diffusion pumps [23]. Materials with a clearance index of ≤ 1.0 (indicated by dashed red lines) can be treated as non-radioactive (for mercury $\gtrapprox 71$ years).

2.4. Vapor diffusion pump operating principle

Vapor diffusion pumps (VDPs) belong to the class of high vacuum pumps. Their operating principle relies on the transfer of momentum from a vapor flow to the pumped gas by means of intermolecular collisions. Vapor diffusion pumps are known to be operable with mercury - in fact it was used as their original operating fluid [35]. An exemplary sketch of a basic VDP design featuring the essential components is depicted in Fig. 2.5.

Liquid mercury is evaporated in a *mercury boiler* by heating elements. Off the shelf VPDs typically feature electric resistance heaters, however in a power plant integration with available fluid streams is possible to improve the efficiency [23].

The mercury vapor produced in the boiler is guided towards a *nozzle* and expanded into the main pump body. The expansion produces a high-speed, nearly parallel vapor jet in pumping direction

thereby reducing the amount of mercury vapor backstreaming opposite to the pumping direction [36].

The mercury vapor jet is condensed upon impingement on the outer walls of the pump by actively cooling them for example by a *cooling jacket* [37, 38]. Efficient condensation can further reduce the amount of backstreaming vapor. The condensate collects at the bottom of the pump and recycles to the boiler, which is located below the pump, due to gravity. The pressure difference between the vapor in the boiler and the mixture in the fore-vacuum compartment of the pump is balanced by the hydrostatic pressure of the liquid mercury in the drain line.

Migration of residual backstreaming vapor is prevented by installing a cooled *vapor trap* between the VDP and the recipient. Vapor traps block the direct line of sight between the pump and the recipient by means of a cooled flow obstruction in order to condense or desublimate the incident mercury vapor. This is often achieved by an arrangement of baffle plates, which is why these traps are often simply referred to as *baffle*. While the vapor trap is not essential for the pumping effect, it is an integral part of any pumping concept that relies on mercury-driven diffusion pumps due to the high vapor pressure of mercury, which amounts to approximately 0.2 Pa at room temperature. Mercury migration towards the Tokamak torus has to be reduced to a minimum in order to prevent radiation losses, which can extinguish the fusion reaction [3, 39, 40]. Effective containment is therefore one of the main challenges for the application of mercury in fusion reactors [34, 41].

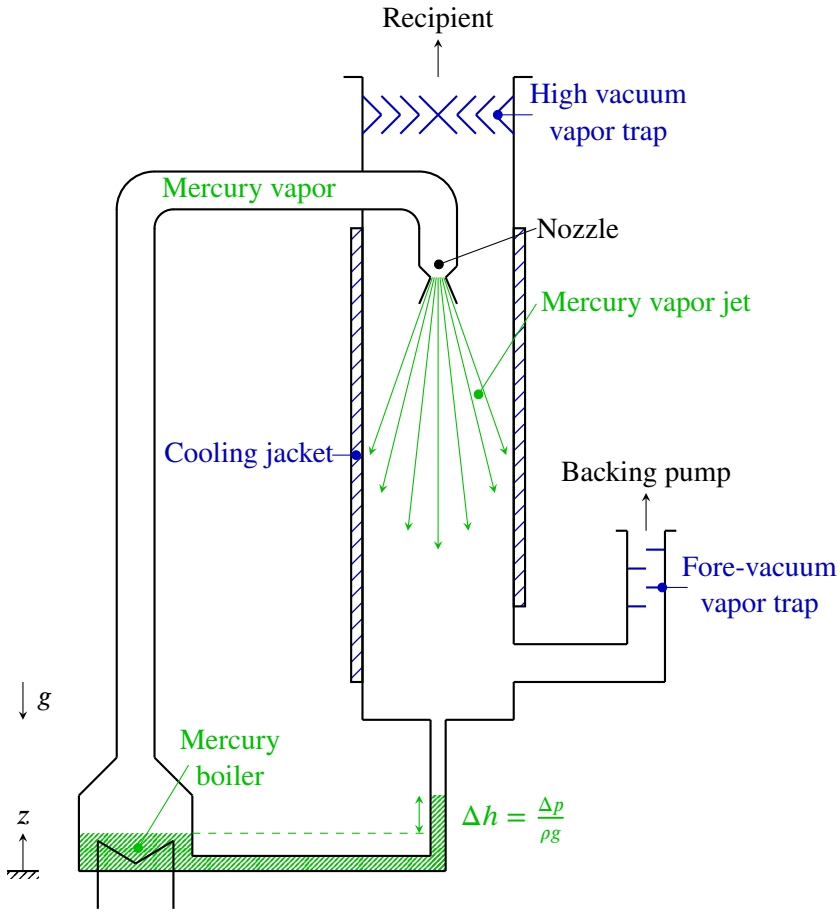

Figure 2.5.: Illustration of a single stage diffusion pump including the essential components. Mercury is depicted in green and cooled elements (cooling jacket, vapor traps) in blue.

2.5. Performance and design of mercury-driven vapor diffusion pumps

The applicability of a VDP design for a given pumping task is determined by its performance indicators. The relative importance of the performance indicators is governed by the specific application. In the following the performance indicators are described in combination with the respective influencing aspects of the pump design and operation. Additionally, the focus is laid on the specific application in the Tokamak exhaust pumping train. A more complete account of the development history of diffusion pumps, which amounts to some hundred publications, is available in literature [42–45]. Furthermore, most of the design optimizations after approximately 1930 have been performed for oil-driven VDPs[1] and are not directly transferable to mercury-driven VDPs [46].

Pumping speed The *pumping speed* is the most important quantity and has to satisfy both burn and dwell conditions. The pumping speed of diffusion pumps is known to depend on the molecular mass m of the pumped gas species [47–49]. The pumping speed of lighter gases is higher because of their higher thermal velocity, which scales with $1/\sqrt{m}$. This is especially relevant in the D-T fusion fuel cycle because the hydrogen isotopes feature the highest isotopic mass ratio of all isotopic substances.

As the pumping speed scales with the size of the pump, the area-related pumping speed has to be considered in order to compare pump designs. The pumping speed is determined by the vapor jet and its interaction with the pumped gas and is therefore affected by several factors in the pump design and operation. Regarding the basic pump design three different options are available (ordered by area-related pumping speed):

- Cylindrical diffusion pump with circular nozzle (as shown in Fig. 2.5), see for example [38]. This corresponds to the simplest design and is not used commonly nowadays due to the partial blockade of the pumping area by the vapor feed pipe. Due to its simplicity it is used in the present work as an illustrative example and validation case.

- Cylindrical diffusion pump with a central cylindrical vapor chimney with annular nozzle(s) (sometimes also referred to as *umbrella* design), see for example [38]. This design is used almost exclusively in off the shelf VDPs.

- Linear diffusion pump featuring a rectangular cross-section and nozzle pipe(s), see [50–52]. This design was established with the goal to build large diffusion pumps for applications where conventional pumps are not efficient. It was operated with mercury and reportedly features a 18 % higher pumping speed per pumping area when compared with conventional cylindrical pumps [52]. The linear design is currently favored in the KALPUREX process [11, 23].

Apart from the basic pump design the pumping speed is mostly affected by the nozzle geometry [53–58] and vapor conditions, for example superheating [59].

Fore-vacuum tolerance The type and number of required backing pumps depends strongly on the achievable *fore-vacuum tolerance* and resulting maximum *compression ratio* of the VDPs. The fore-vacuum tolerance indicates the maximum fore-vacuum pressure against which the diffusion

[1] Unexpected from the present view, the substitution was not driven by the toxicity of mercury, but because these oils have notably lower saturation pressures at ambient temperature. Nowadays, oil and silicone fluids with saturation pressures at room temperature in the 1×10^{-8} Pa range (as opposed to approximately 0.2 Pa for mercury) are available.

pump is able to maintain stable operation. The fore-vacuum tolerance is lower for lighter gases due to their higher diffusion coefficient in mercury vapor [48]. Consequently, this property is of particular importance in the D-T fusion context because the exhaust mixture predominantly contains light gas species.

The fore-vacuum tolerance of modern VDP designs is increased by including multiple (typically three) pumping stages which successively increase the pressure of the pumped gas [60]. In such a setup the first nozzle stage provides the pumping speed, whereas the subsequent stages provide the compression. Typically, the fore-vacuum tolerance of a given pump design has a linear relation with the boiler power [45].

Mercury backstreaming rate The mercury vapor *backstreaming rate* quantifies the amount of mercury vapor that flows toward the inlet of the VDP, i.e. opposite to the pumping direction. Backstreaming is therefore disadvantageous for two reasons: Firstly, backstreaming mercury vapor can reflect gas by intermolecular collisions and thereby reduce the pumping speed. Secondly, the migration of backstreaming mercury to upstream systems has to be prevented by means of the vapor trap. Thus, a higher backstreaming rate requires a more complex vapor trap design. In order to reduce backstreaming it is first necessary to identify the most important sources [61–63]:

- Scattering of vapor molecules due to intermolecular collisions (either with other vapor molecules or the pumped gas).
- Reflection of vapor at surfaces inside the pump.
- Evaporation of operating fluid condensate from surfaces inside the pump.
- Eruptive boiling, which can result in bursts of high pressure vapor being ejected from the nozzle.
- Design or assembly faults (e.g. leaks in the jet assembly, condensate boiling in the pump body).

Several design and operating changes have been suggested to mitigate these backstreaming sources. The first source of backstreaming in large parts depends on choosing the optimum boiler power [61]: If the boiler power is chosen too low the jet will not be able to compress the gas to the target outlet pressure, however if the boiler power is chosen too high the increase in intermolecular collisions inside the jet will lead to increased backstreaming without improving or even deteriorating the pumping speed. However, even if the boiler power is chosen perfectly, a part of the vapor will leave the nozzle with an upward direction because the vapor flow is in an underexpanded state (i.e. the pressure inside the jet is larger than the surrounding pressure at the nozzle exit), which leads to an over-divergent vapor stream directed opposite of the pumping direction [62].

Because a lot of backstreaming sources either originate or are most pronounced at the nozzle, different techniques have been proposed to reduce this backstreaming vector. The most successful approaches use cooled metal surfaces known as *cold / cone cap* [64–67] and *guard ring* [62] placed in the vicinity of the nozzle exit in order to condense the over-divergent part of the vapor jet. These installations can either be cooled actively by a coolant flow or passively by conductive joints with the outer pump walls. While they reduce the pumping speed slightly due to partly obstructing the pumping interface, the reduction is usually small and more than outweighed by the reduced backstreaming rate [65].

Vapor trap containment efficiency and conductance The vapor trap is characterized by two main parameters: Firstly, the *vapor containment efficiency*, which quantifies how much of the

backstreaming mercury vapor from the VDP is contained. Containment here either means that the mercury is recycled towards the pump in liquid form or accumulated in the vapor trap. The former is preferential but only possible above the mercury triple point at 234.32 K (corresponding to a vapor saturation pressure of 3×10^{-4} Pa) [68]. The second parameter characterizing the vapor trap performance is its *conductance*, which corresponds to the flow resistance imposed by the vapor trap. Baffles that obstruct the line of sight entirely are also referred to as being *opaque*. For an opaque trap three transport vectors for the vapor remain [69, 70]: Surface migration, intermolecular collisions (either vapor-vapor or vapor-gas) inside the trap that can allow vapor molecules to pass the trap without colliding with the cooled walls and finally reflection of vapor from the cooled surfaces.

For systems employing mercury a two-stage opaque baffle has been proposed [71, 72]. In such a configuration the first (closer to the pump) opaque stage is cooled slightly above the mercury triple point in order to condense mercury. The condensate can then fall back into the pump due to gravity. The second (closer to the recipient) opaque stage is cooled to lower temperatures (e.g. using liquid or gaseous nitrogen) to desublimate the residual mercury vapor. The two-stage concept is also considered for the application of mercury-driven VDPs for EU-DEMO [11, 23]. Optionally, a third stage similar to the second stage can be included to reduce the backstreaming further if necessary [72].

Effective pumping speed of the integrated system Closely related to the previous point, it is necessary to consider the integrated vacuum system because all components between the recipient, i.e. the torus, and the VDP reduce the *effective pumping speed* due to their limited conductance (cf. Fig. 2.2). The vapor trap is usually the largest influencing factor because of the inherent trade-off between vapor containment efficiency and conductance. A three to four times lower effective pumping speed has to be expected for a baffled pump compared with the nominal speed [71, 72]. For this reason these components have to be included in the optimization process as for example reported for a trap-valve combination [39, 73, 74]. Transferred to the KALPUREX process this implies that the vacuum duct and the metal foil pumps have to be considered as well because they are installed upstream of the diffusion pumps.

3. Description of rarefied gas and vapor flows

The purpose of the present chapter is to introduce the most important physical processes underlying the operating principle of diffusion pumps and their modeling. The description of vacuum gas flows is based on the *kinetic theory of gases*, which aims to describe the gas as a collective of individual particles[1] that move and collide. In vacuum flows long-range interactions between particles are usually negligible and only short-range interactions have to be considered, which leads to the simple model of an *ideal gas*.

The transport and interactions of particles are described in so-called *phase space* [75]. Phase-space refers to the six dimensional space spanned by three spatial and three velocity coordinates. While it is theoretically possible to achieve a deterministic description of a gas in phase space by considering all involved particles and their interactions, this is not feasible for real systems as the amount of gas particles involved is too high[2]. That is why a continuous, six dimensional particle velocity distribution function describing the statistical distribution of particles in phase space is introduced. Statistical mechanics therefore plays an important role in the mathematical framework of gas kinetics and leads to the *Boltzmann equation* describing the temporal evolution of the particle velocity distribution function. Macroscopic quantities of interest (e.g. density, pressure, temperature) follow as *moments* of the particle velocity distribution function. A more in-depth mathematical description of the aforementioned gas kinetics concepts is provided in Appendix A.2.

3.1. Description of equilibrium and molecular fluxes

A key empirical observation in nature is that a stationary macroscopic equilibrium will establish in a gas filled, isolated container in the absence of external forces. It can be shown that the particle velocity distribution function then takes the form

$$f_M(\vec{v}) = f_M(v_x) f_M(v_y) f_M(v_z) = n \left(\frac{m}{2\pi k_B T} \right)^{\frac{3}{2}} \exp\left\{ -\frac{m \left|\vec{v}\right|^2}{2 k_B T} \right\}, \tag{3.1}$$

which is called the *Maxwell-Boltzmann distribution function* or short *Maxwellian* [75]. The Maxwell-Boltzmann distribution $f_M(\vec{v})$ corresponds to a multivariate normal distribution, where each velocity component (v_x,v_y, and v_z) is independently normal distributed with expectation zero and variance $k_B T/m$. The number density n and temperature T in Eq. (3.1) correspond to the observable, uniform, macroscopic state of the gas in the aforementioned container. Imposing that the velocity distribution has to be isotropic, the distribution function for the velocity magnitude or speed $v = \left|\vec{v}\right| = \sqrt{v_x^2 + v_y^2 + v_z^2}$ can be found as [75]

$$f_M(v) = 4\pi n v^2 \left(\frac{m}{2\pi k_B T} \right)^{\frac{3}{2}} \exp\left\{ -\frac{m v^2}{2 k_B T} \right\}. \tag{3.2}$$

[1] The term *particle* will be used in the present work as a generic term for atomic (e.g. helium) and molecular (e.g. nitrogen) gases.

[2] For example a volume of 1cm^3 at 1 millionth of the atmospheric pressure still contains more than $2 \cdot 10^{13}$ particles.

Eqs. (3.1) and (3.2) show that the distribution of molecular velocities in equilibrium only depends on the temperature T and molecular mass m of the considered species. This dependency is illustrated in Fig. 3.1 for mercury vapor and helium at two different temperature levels to convey a sense of the different scales.

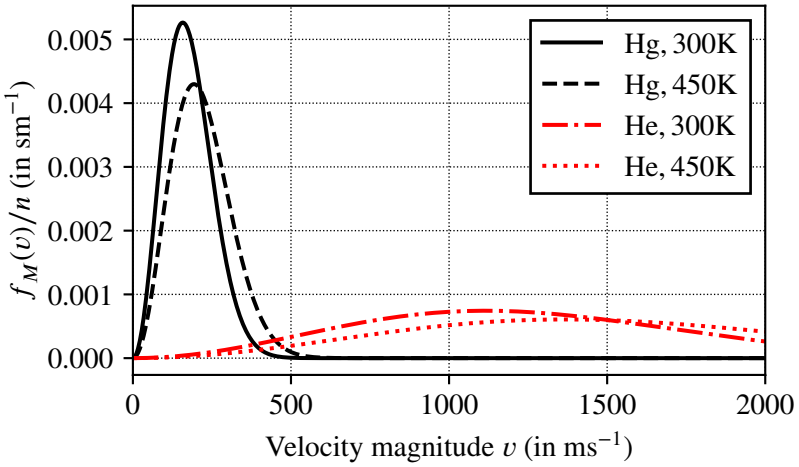

Figure 3.1.: Maxwell-Boltzmann distribution of velocity magnitude (normalized by the number density) for mercury vapor and helium at two different temperatures.

The most important properties following from the distribution defined by Eq. (3.2) are the *most probable thermal speed* of the particles, i.e. the maximum of the distribution function in Fig. 3.1, given by

$$v_{\mathrm{mp}} = \sqrt{\frac{2k_B T}{m}}, \tag{3.3}$$

and the *mean thermal speed* obtained either by Eq. (A.7) or equivalently by

$$\overline{v} = \frac{\int_0^\infty v f_M(v)\,\mathrm{d}v}{\int_0^\infty f_M(v)\,\mathrm{d}v} = \sqrt{\frac{8k_B T}{\pi m}}. \tag{3.4}$$

Where the latter is approximately 13 % larger than the most probable thermal speed.

3.1.1. Molecular fluxes in equilibrium

Under the assumption of thermal equilibrium it is possible to calculate molecular fluxes with the aid of the Maxwell-Boltzmann distribution function easily due to the isotropic distribution of the particle velocities. The equilibrium flux of particles impinging on a solid surface or crossing a virtual surface in one direction is of particular interest in the description of molecular phenomena, for example the effusion of gas through an orifice and the evaporation rate of molecules from a condensed phase [76]. To simplify the derivation of the equilibrium flux from the Maxwell-Boltzmann distribution function (Eq. (3.1)) the surface can be assumed to be aligned with the Cartesian coordinate system without loss of generality. If it is assumed that the surface normal points in $-x$-direction, the flux points in $+x$-direction. Therefore, the distribution function can be integrated in the relevant velocity ranges on any point lying on the surface to obtain the local flux

$$\dot{n}_+ = \int_0^{+\infty}\int_{-\infty}^{+\infty}\int_{-\infty}^{+\infty} v_x f_M(\vec{v})\,\mathrm{d}v_z\,\mathrm{d}v_y\,\mathrm{d}v_x = \frac{1}{4}n\bar{v}. \tag{3.5}$$

Naturally, for a gas in thermal equilibrium the molecular flux in opposite direction is $\dot{n}_- = -\dot{n}_+$, so that the net flux reduces to zero. This property is not shared among all moments of the distribution function. Most importantly, when considering the momentum flux it is found to be

$$p_- = p_+ = m \int_{-\infty/0}^{0/+\infty} \int_{-\infty}^{+\infty} \int_{-\infty}^{+\infty} v_x v_x f_M(\vec{v}) \, \mathrm{d}v_z \, \mathrm{d}v_y \, \mathrm{d}v_x = \frac{1}{2} n k_B T. \tag{3.6}$$

The net momentum flux is therefore not zero but

$$p = p_+ + p_- = n k_B T, \tag{3.7}$$

i.e. the pressure as given by the *ideal gas law*.

3.1.2. Local equilibrium in flows

The considerations for a stationary gas can be extended to gas flows. Gas flows are characterized by a non-zero bulk velocity[3] that follows as a moment of the distribution function (cf. Eq. (A.6)). It is thus common to write the particle velocities as a superposition of two contributions. For example the velocity $\vec{v}_p$ of a representative, individual particle at position $\vec{x}_i$ in the flow can be written as

$$\vec{v}_p = \vec{u}(\vec{x}_i) + \vec{c}_p, \tag{3.8}$$

where $\vec{u}(\vec{x}_i) = \vec{u}_i$ is the local bulk velocity at position $\vec{x}_i$ and $\vec{c}_p$ is the so-called *thermal* (also *peculiar* or *random*) velocity component [77]. It is noted that $\vec{v}_p$ and $\vec{c}_p$ are properties of an individual particle, whereas $\vec{u}_i$ corresponds to a macroscopic quantity obtained by averaging over all particles close to $\vec{x}_i$.

A special case arises if the thermal velocities of all particles close to position $\vec{x}_i$ are distributed according to the equilibrium distribution function (Eq. (3.1)), i.e.

$$f(\vec{v}, \vec{x}_i) = f_M(\vec{c}, \vec{x}_i) = n \left(\frac{m}{2\pi k_B T} \right)^{\frac{3}{2}} \exp \left\{ - \frac{m \left| \vec{v} - \vec{u}_i \right|^2}{2 k_B T} \right\}, \tag{3.9}$$

using the previously defined identity $\vec{c} = \vec{v} - \vec{u}_i$. As Eq. (3.9) corresponds to a multivariate normal distribution with non-zero expectation, it is often referred to as the *shifted Maxwell-Boltzmann distribution function* [76]. If Eq. (3.9) is valid at all positions, the flow is said to be in a so-called *local equilibrium* state. The molecular fluxes in flows, which are in local equilibrium, can be calculated similar to the ones for a stationary gas. Under the assumption that the bulk velocity is directed in $+x$-direction so that $\vec{u} = [u_x, 0, 0]^\mathrm{T}$, the molecular flux in the same direction results as

$$\begin{aligned} \dot{n}_+ &= \int_0^{+\infty} \int_{-\infty}^{+\infty} \int_{-\infty}^{+\infty} v_x f_M(\vec{v}, \vec{u}) \, \mathrm{d}v_z \, \mathrm{d}v_y \, \mathrm{d}v_x \\ &= \frac{1}{4} n \bar{v} \left[\exp \left\{ - \left(\frac{u_x}{v_\mathrm{mp}} \right)^2 \right\} + \sqrt{\pi} \frac{u_x}{v_\mathrm{mp}} \left(\mathrm{erf} \left\{ \frac{u_x}{v_\mathrm{mp}} \right\} + 1 \right) \right], \end{aligned} \tag{3.10}$$

where erf is the *error function* (cf. Appendix A.1.1). The superposition of the fluxes in both directions yields $\dot{n} = \dot{n}_+ + \dot{n}_- = n u_x$, i.e. the macroscopically measurable flux through the surface.

[3] Throughout this thesis $\vec{v}$ is used to denote the velocity of individual particles, whereas $\vec{u}$ is used to denote the bulk velocity of the collective.

3.2. Intermolecular collisions and flow regimes

When considering a closed container filled with gas at constant temperature, the average distance that particles will travel without colliding with each other and the time spent between these collisions will decrease the higher the gas density in the container. Because the particle velocities are distributed according to the Maxwell-Boltzmann distribution function in thermal equilibrium it is possible to define the *mean free path* λ and the *mean collision time* τ to characterize these properties on average. As the mean thermal speed of particles in thermal equilibrium is $\overline{v}$, as defined in Eq. (3.4), the relation between the mean free path and collision time is simply

$$\lambda = \overline{v}\tau. \tag{3.11}$$

The expressions for λ and τ depend on the assumed intermolecular potential. In the present work the *Variable Soft Sphere (VSS)* [78] model is employed due to its relative simplicity at acceptable accuracy. A detailed description of the VSS model and its binary collision cross-section is available in Appendix A.2.4. The binary collision cross-section of the VSS model depends on the relative velocity of the collision partners. In equilibrium the relative velocity is distributed according to a Maxwellian distribution so that

$$\tau_{\mathrm{VSS,eq}} = \left[4nd_{\mathrm{ref}}^2 \sqrt{\frac{\pi k_B T_{\mathrm{ref}}}{m}} \left(\frac{T}{T_{\mathrm{ref}}} \right)^{1-\omega} \right]^{-1}, \tag{3.12}$$

and

$$\lambda_{\mathrm{VSS,eq}} = \left[\sqrt{2}\pi nd_{\mathrm{ref}}^2 \left(\frac{T}{T_{\mathrm{ref}}} \right)^{0.5-\omega} \right]^{-1}, \tag{3.13}$$

follow [77]. Gas specific reference model parameters are indicated by "ref" and ω is the viscosity coefficient. As the mean free path of a hard sphere gas with $\omega = 0.5$ is temperature independent, it is very commonly used as a simplification in derived expressions in literature. In gas mixtures collisions between alike and different species have to be considered in the expressions of the mixture equilibrium mean free path and mean collision time. The expressions are given in Appendix A.2.5.

The mean free path λ is compared with a problem dependent characteristic length L_c to classify flow regimes according to their degree of rarefaction. The rarefaction degree is expressed by the dimensionless *Knudsen number* Kn, which is defined as

$$\mathrm{Kn} = \frac{\lambda}{L_c}. \tag{3.14}$$

Two principal limits are distinguished: At low Knudsen numbers the flow is said to be in the *continuum* regime. In this regime intermolecular collisions happen so frequently and on such small distances, that the flow can be described accurately by considering it as a continuous medium with locally averaged transport properties. On the other end of the spectrum flows featuring high Knudsen numbers are referred to as *free-molecular* because intermolecular collisions are of subordinate importance. Thus, these flows can be described mathematically by neglecting intermolecular collisions entirely. The flow is then only characterized by collisions of the particles with the boundaries. However, the transition between these regimes is continuous. The intermediate regime is referred to as the *transitional* regime. In this regime intermolecular and boundary collisions are both important. The flow regimes are illustrated in Fig. 3.2.

Because the flow inside a diffusion pump spans a large range of Knudsen numbers, their modeling is complex. The vapor flow upstream and in the initial part of the nozzle is usually in the continuum flow regime. The expanding vapor jet and the interaction zone with the gas are in the

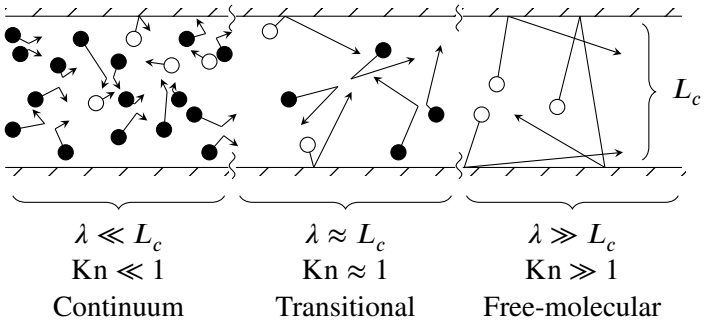

Figure 3.2.: Flow regimes and their respective Knudsen number range. From left to right: Continuum, transitional and free-molecular flow. Particles involved in intermolecular collisions are filled.

transitional flow regime. In fact, the operating principle *requires* the flow to be transitional in the interaction zone to facilitate the transfer of momentum between the jet and the gas. The flow regime of the gas upstream of the nozzle and especially in the baffle depends on the operating conditions but tends to be in the rarefied regime. For typical applications without large gas loads the flow will be free-molecular. In case of the EU-DEMO high vacuum pumping system the Knudsen numbers during burn and dwell phases can be estimated from the expected pressure levels and dimensions. The pressure levels in the sub-divertor volume during burn and dwell phases can be estimated to be approximately 1 Pa and 1 mPa, respectively. Assuming a realistic characteristic length of 10 cm in the baffle and the mean free path of helium of approximately 17.5×10^{-3} m (at 1 Pa) and 17.5 m (at 1 mPa) [79] the Knudsen number is 0.175 (transitional) during burn and 175 (free-molecular) during dwell. The Knudsen number of the mercury vapor inside the nozzle is even lower. These considerations imply that a diffusion pump model has to cover all flow regimes.

3.3. Mercury vapor expansion into vacuum

In vapor diffusion pumps a nozzle is used to produce a supersonic vapor jet in order to enable efficient momentum transfer to gas in pumping direction. Converging-diverging nozzles convert part of the fluid enthalpy into kinetic energy. Therefore, this process leads to an increase of the bulk velocity $\vec{u}$ at a concurrent decrease of pressure and temperature.

3.3.1. Isentropic expansion of mercury vapor

The properties of the expanding vapor jet can be estimated by considering an isentropic expansion of an ideal gas [43, 80]. The state after the expansion "1" is related to the stagnation state "0" by the *Mach* number Ma, which is the dimensionless ratio of the bulk speed to the local speed of sound

$$\mathrm{Ma} = \frac{u}{\sqrt{\frac{\gamma k_B T}{m}}}. \tag{3.15}$$

In Eq. (3.15) γ is the heat capacity ratio. The properties of a perfect gas (i.e. with constant heat capacity, e.g. a monatomic ideal gas) after the expansion then follow from energy conservation [80]:

$$T_{\mathrm{V},1} = T_{\mathrm{V},0}\left[1 + \frac{\gamma-1}{2}\mathrm{Ma}_{\mathrm{V},1}^2\right]^{-1}, \tag{3.16}$$

$$u_{\mathrm{V},1} = \sqrt{\frac{2}{m_{\mathrm{V}}}\frac{\gamma}{\gamma-1}k_B T_{\mathrm{V},0}\left(1 - \left[1 + \frac{\gamma-1}{2}\mathrm{Ma}_{\mathrm{V},1}^2\right]^{-1}\right)}. \tag{3.17}$$

Equation (3.17) implies that there exists a maximum jet velocity solely dependent on the stagnation temperature in the theoretical limit of an infinite expansion ($\mathrm{Ma} \to \infty$) [43],

$$u_{\mathrm{V},1,\max} = \underbrace{\sqrt{\frac{2}{m_{\mathrm{V}}}\frac{\gamma}{\gamma-1}k_B}}_{a)}\sqrt{T_{\mathrm{V},0}}, \tag{3.18}$$

where the term a) is constant for a given vapor species characterized by its mass m_{V}. Mercury vapor is monatomic [43, 81] and has an atomic mass of $m_{\mathrm{Hg}} = 3.331 \times 10^{-25}\,\mathrm{kg}$ [82] so that the constant term a) in Eq. (3.18) is approximately $14.4\,\mathrm{m\,s^{-1}\,K^{-0.5}}$ for mercury vapor.

During the expansion the vapor cools down (cf. Eq. (3.16)) and in the limit of infinite expansion the thermodynamic temperature approaches zero. It is important to highlight the difference between the thermodynamic temperature, which accounts for the local *relative* random motion of particles (cf. Eq. (A.9)), and the kinetic temperature, which is directly related to the average kinetic energy of the particles. The latter does of course not approach zero in the expansion process.

3.3.2. Condensation in the mercury vapor jet

The low temperatures after the vapor expansion imply that the vapor either has to be in a single-phase supersaturated state or that condensation leads to a two-phase flow. Condensation is unwanted in the normal diffusion pump operation as it weakens the vapor jet and thereby potentially deteriorates the performance (pumping speed and fore-vacuum tolerance).

Hagena developed a semi-empirical scaling law to predict the onset of condensation in jet expansions of noble gases and metals vapors depending only on the stagnation conditions and nozzle throat diameter [83, 84]:

$$\zeta^* = \zeta_{\mathrm{V}}^{-1} n_{\mathrm{V},0} d^{q_{\mathrm{V}}} T_{\mathrm{V},0}^{(q_{\mathrm{V}}-6)/4}, \tag{3.19}$$

where ζ^* is the dimensionless Hagena condensation parameter, ζ_{V} and q_{V} are a substance specific constants, $n_{\mathrm{V},0}$ and $T_{\mathrm{V},0}$ are the stagnation density and temperature of the vapor upstream of the nozzle and d is the nozzle throat diameter. The condensation parameter ζ^* is indicative of the tendency of cluster formation in an expansion process and three regimes are identified by Hagena [84]: $\zeta^* < 200$: supersaturated vapor without cluster formation, $200 \leq \zeta^* \leq 1000$: transitional region, $\zeta^* > 1000$: massive condensation. The approximate validity of this scaling law has been verified by numerical simulations of expanding copper vapor that considered cluster formation, however it was shown that the aforementioned critical value of $\zeta^* = 200$ only applies approximately [85, 86].

Figure 3.3 visualizes the dimensionless Hagena condensation parameter ζ^* for mercury (using the model constants ζ_{Hg} and q_{Hg} provided in [84]) as a function of the vapor saturation temperature and the nozzle throat diameter. Additionally, data on two experiments from literature is included. It is noted that both experiments have been performed at mercury stagnation pressures approximately one order of magnitude higher than prevalent in diffusion pumps.

In the first experiment (① in Fig. 3.3) mercury vapor flow fields visualized by a high frequency discharge have been compared with theoretical flow fields determined for both supersaturated vapor and two-phase flow [87]. Based on the comparison it is concluded that the vapor has been supersaturated in the experiments [87]. The corresponding Hagena condensation parameter lies in

the transitional regime. However, it is plausible that weak clustering could not be detected by the employed visual comparison method.

In the second experiment (② in Fig. 3.3) a nozzle has been used to isentropically expand metal vapors beyond the saturation point and the cluster distribution then measured by time-of-flight mass spectrometry of the ionized beam [88, 89]. Mercury is reported to not form clusters at low stagnation temperatures and only small amounts of Hg_2^+ are detected at intermediate temperatures [89]. Only above approximately 620 K larger clusters of mercury up to Hg_{25}^+ can suddenly be detected, however even then approximately 96% is Hg^+ [89]. This observation is correctly reflected by the Hagena condensation parameter which again lies in the transitional regime.

Furthermore, the design and operational range of the experimental setup NEMESIS, which has been operated within the scope of this work, is included (a detailed description follows in Chap. 5). Based on the Hagena condensation parameter $\zeta^* < 200$ no condensation is expected in the setup (see ③ in Fig. 3.3).

Lastly, the expected design and operational range of the EU-DEMO diffusion pumps is indicated in a range where no condensation is to be expected (see ④ in Fig. 3.3).

Therefore, based on this study single-phase flow can be assumed in the modeling of diffusion pumps.

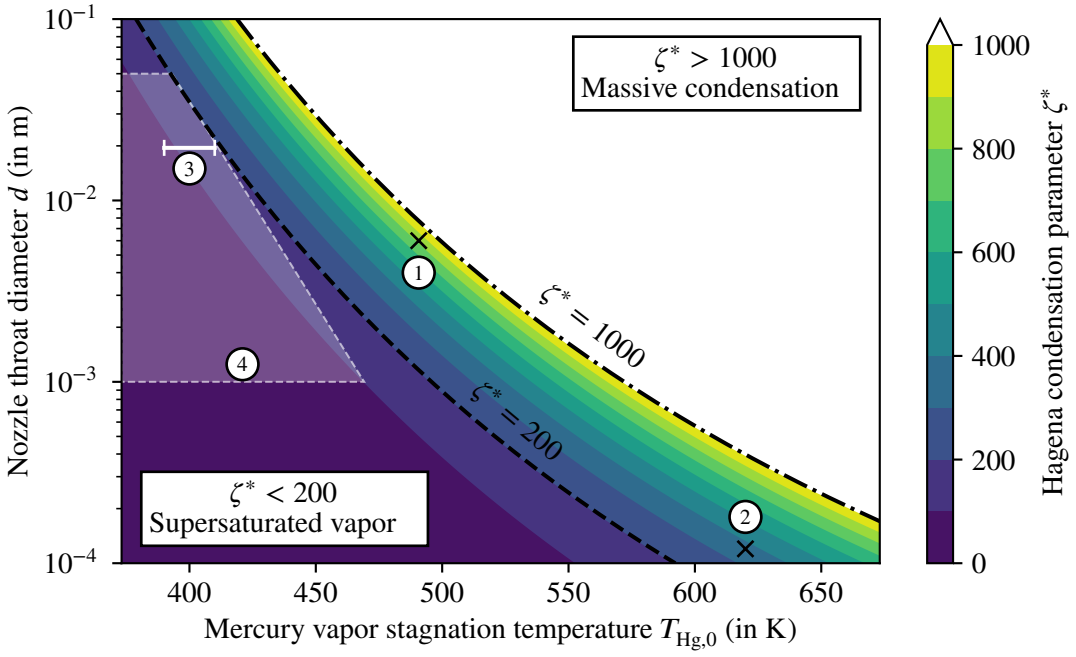

Figure 3.3.: Hagena condensation parameter ζ^* for mercury vapor as a function of reservoir (saturation) temperature $T_{Hg,0}$ and the critical nozzle throat diameter d. Correlation parameters for mercury vapor are taken from [84]. ①: Experiment (no condensation) reported in [87], ②: Experiment (weak clustering) reported in [88, 89], ③: NEMESIS operating range, ④: Expected operating and design range of the EU-DEMO diffusion pumps.

3.4. Numerical methods for solving the Boltzmann equation

The Boltzmann equation (cf. Eq. (A.3)) is capable of modeling the flow irrespective of the flow regime. However, due to its high dimensionality it is particularly hard to solve. This holds true for both analytical solutions (which only exist in special cases) and for numerical solutions. For this reason substantial simplifications are made if the flow regime permits this.

In the limiting case of a free-molecular flow ($\mathrm{Kn} \to \infty$) the collision operator ($C(f)$ in Eq. (A.3)) reduces to zero, which transforms the integro-differential Boltzmann equation into a partial differential equation that is significantly easier to solve. In this case the distribution function is Maxwellian everywhere. The only complexities are then introduced by collisions with solid boundaries and problems involving simple geometries can be solved analytically (for some examples see the works of Cai et al. [90–93]). More complex geometries are usually computed using the *Test Particle Monte Carlo (TPMC)* method. In the TPMC method the stochastic version of the free-molecular Boltzmann equation is discretized by computing the trajectories and boundary interactions of the eponymous test particles. Because there is no inter-particle interaction, the individual particles trajectories can be computed fully isolated from each other. A TPMC simulation can therefore be performed in a distributed parallel manner without synchronization.

In the second limit of continuum flow ($\mathrm{Kn} \to 0$), molecular collisions happen so frequently and the mean free path between collisions is so small, that the flow is in or close to local thermal equilibrium. This implies that macroscopic changes in the flow (e.g. a pressure gradient due to wall friction) happen on much larger time- and space-scales than the microscopic equilibration process caused by intermolecular collisions. In this case the gas can be treated as a continuum and the Boltzmann equation can be simplified to yield the Euler equations (local thermal equilibrium) or the Navier-Stokes-Fourier equations (close to local thermal equilibrium) [75]. In both cases the integro-differential equation is transformed into a set of partial differential equations with reduced dimensionality, which lowers the required computational resources. Continuum methods have been used previously to describe the vapor expansion in the diffusion pump as summarized in [94]. The continuum solutions of the vapor flow field have also been coupled with a modified TPMC method to approximate a one-way momentum transfer from vapor to gas [95]. While such a method can help in the design of an optimized pump as shown in [96], it has the inherent limitation that the influence of the pumped gas on the vapor is neglected. Therefore, this method is unsuited for the description of important phenomena like backstreaming and breakdown.

An appealing idea is to describe flows in the transitional regime as a superposition of free-molecular and continuum solutions. However, it turns out that this description is not successful because it fails to predict some phenomena that occur in the transitional regime, for example the Knudsen flow rate minimum [97]. It is thus necessary to solve the full or simplified Boltzmann equation in the transitional regime. The two main approaches are described in the following paragraphs.

Direct Simulation Monte Carlo (DSMC) The *Direct Simulation Monte Carlo (DSMC)* method [77, 98–100] is a stochastic approach to solve gas kinetic problems and provides results similar to the Boltzmann equation. Similar to the TPMC method, the DSMC method also uses computational particles to simulate the flow, however with the added complexity that intermolecular collisions are also considered. The DSMC method is therefore not as easy to parallelize as the TPMC method. Because it would be infeasible to simulate every physical particle in a system (typical order of magnitude of 10^{20}), each computational particle is representative of many real particles (typical order of magnitude of 10^{13}). The macroscopic flow properties are calculated as moments in the form of averaged microscopic particle properties. It is due to this averaging process that the DSMC method is better suited for high speed flows, as it suffers from statistical noise in

case of low speed flows. Successful use of the DSMC method has been reported for the modeling of oil-driven VDPs [101, 102]. Independent but in parallel to the present work, the DSMC method has also been used by Zhao et al. [103] and Liao et al. [104] to simulate mercury-driven VDPs in the context of fusion reactor exhaust pumping. Furthermore, the method has been used to simulate turbomolecular pumps, which also rely on momentum transfer as the pumping principle and operate in a similar pressure range [105–107].

The DSMC method has been implemented in open- and closed-source simulation tools. Nowadays, the two most commonly used software programs are the open source codes *dsmcFoam*(+) [108, 109], based on the widely used *OpenFOAM* [110], and *SPARTA* [111–113], which is a dedicated DSMC tool.

Discrete Velocity Method (DVM) The second commonly used method to solve the Boltzmann equation numerically is the deterministic *Discrete Velocity Method (DVM)* [114, 115]. In this method the Boltzmann equation is discretized in all six phase space dimensions (three in physical and velocity space respectively). The solution is then calculated on a six-dimensional grid. For complex problems (either in physical or velocity space) this can quickly result in very large number of variables, which is why the DVM was long not competitive with the DSMC method due to computational memory restrictions. The advantage of the DVM is that it is deterministic and thus not affected by noise. Therefore, it is superior to the DSMC method for low speed flows. However, the DVM is commonly used assuming simplified kinetic model equations that replace the collision operator of the Boltzmann equation with simpler terms. The most well-known of these kinetic models is the *Bhatnagar-Gross-Krook (BGK)* model [116] which describes the collision operator as a simple relaxation term that drives the distribution function to the Maxwellian distribution function. The kinetic models are responsible for recovering the correct transport properties. For example the Prandtl number, which describes the ratio of diffusive momentum to heat transport, is unity in the original BGK method, whereas the theoretical value for a perfect monatomic gas is $2/3$ [117]. As a consequence more complex kinetic models have been proposed (see e.g. [117]), which are capable of describing single species flows with acceptable precision. However, the correct description of gas mixtures remains an open issue. This is usually characterized by the fact that the models are not capable of reproducing all mixture transport coefficients (see for example [118]).

The DVM has been applied widely in literature, however up to now these works mainly focus on the development of new model equations and only benchmark problems are solved using dedicated tools. The first attempt to build a standardized tool for arbitrary geometries was proposed in the form of *dugksFoam* [119], which is also based on *OpenFOAM* [110]. However, it has to be noted that *dugksFoam* is limited to single species flows.

Choice of the simulation method for diffusion pump modeling The DSMC method has been chosen over the DVM in the present work for three main reasons: Firstly, at the present time the DSMC method has a clear advantage over the DVM regarding the simulation of gas mixtures. Secondly, the flow in the diffusion pump covers a wide velocity range. While the vapor flow will be supersonic in most parts of the domain, the gas has to stagnate at the outlet. This means that the DVM demands numerous discrete velocities, which can lead to performance and memory issues. Thirdly, there is a lack of a widely used, validated tool based on the DVM.

The *SPARTA* software [111–113] has been used for the DSMC simulations in the present work because it has a significantly higher performance than *dsmcFoam+*. Due to its open source nature *SPARTA* (version *26Feb2021*) has been extended in multiple ways to tailor to the special requirements imposed by the simulation of diffusion pumps.

Additionally, the TPMC method has been employed for the complex, three-dimensional simulation of the diffusion pump baffle due to its higher efficiency. The open source *MOLFLOW+* (version *2.9.0)* software [120, 121] was employed for these simulations. A detailed explanation of the TPMC method is not included in the present work, due to its conceptual similarity with the DSMC method (with the notable exception of the collision step).

3.5. Direct Simulation Monte Carlo for diffusion pump modeling

The Direct Simulation Monte Carlo method is a stochastic, particle-based procedure that can solve gas flow problems consistent with the Boltzmann equation. Here, the fundamental algorithm and its discretization parameters are described. Additionally, the implemented binary collision model to simulate the intermolecular collisions in the gas mixture is explained and the required parameters are derived for mercury vapor and all involved gas species. Furthermore, the application of particle weighting schemes for modeling of diffusion pumps is explained. Lastly, the boundary conditions that are required in the diffusion pump model are discussed.

3.5.1. Simulation algorithm and sensitivity of discretization parameters

The DSMC algorithm is visualized in Fig. 3.4. The algorithm features three main discretization parameters, which are the time step Δt, the computational cell size Δx and the weight F_N, i.e. the number of physical particles that each simulator particle represents.

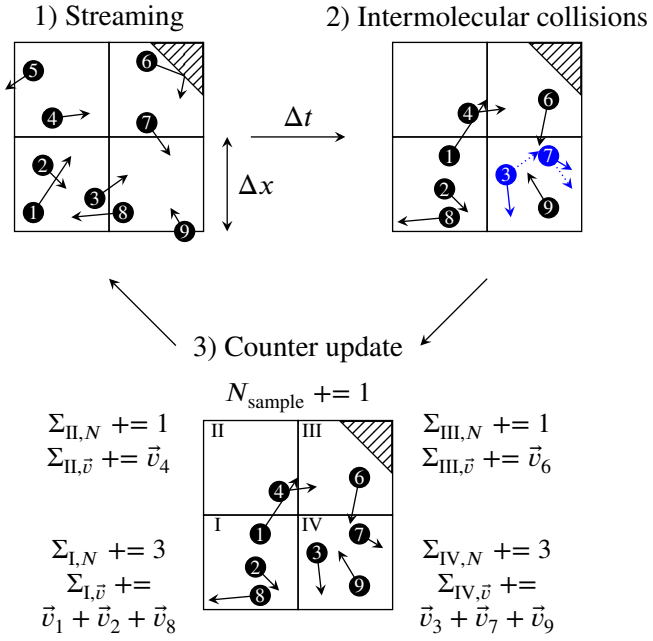

Figure 3.4.: Description of the DSMC algorithm: Streaming (step 1): Ballistic movement of particles and collisions with walls, here for particle ⑥. Intermolecular collisions (step 2): Stochastic collisions between particles in the same cell, here between particles ③ and ⑦. Counter update (step 3): Update of the cumulative moment counters in each cell (I-IV), shown here exemplarily for the zeroth (Σ_N) and first order ($\Sigma_{\vec{v}}$) moments.

The algorithm is structured into three main steps: In the first step, new simulator particles are created at inflow boundaries (particle ⑨ in Fig. 3.4) and all particles are moved for their respective distance $\vec{v}_i \Delta t$, where $\vec{v}_i$ is the particle velocity vector. Additionally, collisions with the solid walls

(particle ⑥ in Fig. 3.4) and cell transfers (particles ③, ⑦ and ⑧ in Fig. 3.4) as well as particles leaving the domain (particle ⑤ in Fig. 3.4) are computed. In the second step, binary collisions partners are randomly selected from particles that reside in the same cell and their collision is calculated for a random impact point (particles ③ and ⑦ in Fig. 3.4). Different methods exist to sample collisions, but the most common scheme is the *No Time Counter* scheme [122, 123], which is used in the present work (see Appendix A.3.1 for a detailed description). In steady-state simulations cumulative moment sums are updated during the averaging period in the third simulation step. After the simulation is finished the moments are calculated as averages from the cumulative sums in order to reduce the statistical noise. The calculation of the moments is demonstrated for the two examples depicted in Fig. 3.4 for an arbitrary cell i

$$n_i = \frac{\Sigma_{i,N} F_{N,i}}{N_{\text{sample}} V_i}, \tag{3.20}$$

$$\vec{v}_i = \frac{\Sigma_{i,\vec{v}}}{\Sigma_{i,N}}, \tag{3.21}$$

where Σ_i are the respective moment sums, V_i is the cell volume and $F_{N,i}$ the cell weight. The cell weight represents the scaling factor between simulator and physical particles. In case gas mixtures are simulated - as is the case for most simulations included in the present work - the mixture moments can be calculated using the expressions in Appendix A.2.3.

The requirements on the DSMC discretization parameters can be summarized as follows:

- The time step Δt has to resolve the mean collision time τ to enable the decoupling of particle movement and intermolecular collisions that is the basis of the DSMC algorithm.
- The cell size Δx has to resolve the mean free path λ to enable the statistical sampling of collision partners from particles within each cell.
- The weight F_N, which is inversely proportional to the average number of simulators N_p in each cell, has to be low enough to ensure representative sampling of collision partners. In the simplest configuration a constant weight is used for all cells.

Additionally, the combination of cell size and time step has to be chosen so that particles only travel a fraction of the cell size during their free flight step. If any of these discretization requirements are not met systematic errors are introduced in the moments that are calculated in the third simulation step. The sensitivity of the discretization parameters to the transport properties has been studied extensively in literature: Alexander et al. [124] apply the *Green-Kubo* theory [125, 126] to show that the error introduced by the finite cell size scales with $(\Delta x/\lambda)^2$. Later Hadjiconstantinou [127] performed a similar analysis for the time step and found that the error scales per $(\Delta t/\tau)^2$. In both cases the relative error introduced in the transport coefficients by choosing either $\Delta x/\lambda = 1$ or $\Delta t/\tau = 1$ is of the order of magnitude of 5 % [124, 127]. The error associated with the limited number of particles per cell was determined by Chen and Boyd [128] in two parts: The statistical error decreases with $1/\sqrt{N_{\text{sample}} N_p}$, whereas the systematic error scales with $1/N_p$. The most efficient combination of sample size and average number of particles per cell depends on the problem [128]. In [129] the relative error of the thermal conductivity in a Fourier flow, which is a typical DSMC benchmark problem, is found to be approximately $-8\%/N_p$.

Thus, to reduce the order of magnitude of all systematic errors introduced by the discretization parameters to below approximately 1 %, the parameters have to be chosen as $\Delta x \leq 1/3\lambda$, $\Delta t \leq 1/3\tau$ and $N_p \geq 10$. These are in line with empirical recommendations as for example given in [77, 130]. Generally, the cell size should be considered first because the choice of the other two parameters depends strongly on it: The number of simulators per cell is directly linked to the cell

size via the cell volume, which scales with Δx^3 (3d) or Δx^2 (2d). Furthermore, the time step scales linearly with the cell size to ensure that particles only travel a fraction of the cell size per step.

3.5.2. Elastic binary collision modeling

The collision interaction model determines how the particle trajectories of colliding particles are altered. All realistic collision interaction models have in common that they obey momentum and energy conservation in collisions. Consistent with the Boltzmann equation, the DSMC method only considers binary collisions, which is a reasonable assumption in low pressure gas flows. The collision step constitutes a significant part of the overall algorithm run time. For this reason it is necessary to compromise between physical accuracy and (computational) simplicity of the collision interaction model. The most common interactions models are extensions of the simple *Hard Sphere (HS)* model.

The scheme of an elastic binary collision between hard spheres in the center of mass frame of reference is illustrated in Fig. 3.5. The distance of the closest approach for spherical particles is

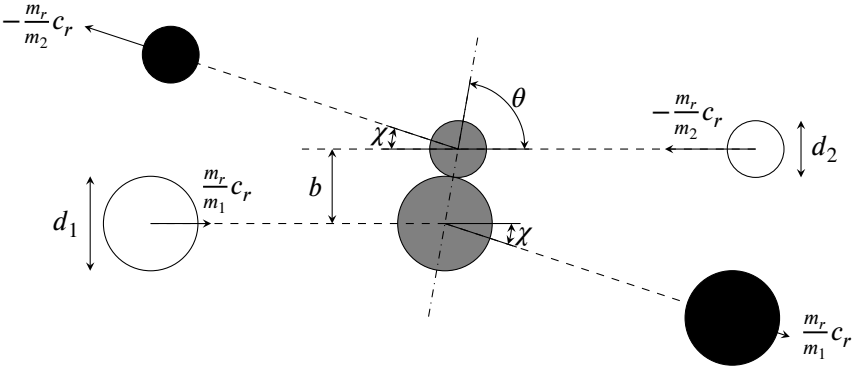

Figure 3.5.: Elastic binary collision in the center of mass frame of reference. White: Particles before collision, gray: during collision, black: after collision. $m_r = \frac{m_1 m_2}{m_1+m_2}$ is the reduced mass, c_r is the relative velocity magnitude, b refers to the distance of closest approach of the trajectories in the center of mass frame, and χ to the deflection angle. Based on [75, 77].

defined as [77]:

$$b = \frac{d_1 + d_2}{2} \sin(\theta) = d_{12} \sin(\theta). \tag{3.22}$$

However, in contrast to the normal HS model, the average diameter d_{12} depends on the relative velocity c_r of the collision partners and the viscosity index ω_{12} in the more advanced *Variable Hard Sphere (VHS)* [100] and *Variable Soft Sphere (VSS)* [78] models (for more details see Appendix A.2.4, specifically Eqs. (A.16) and (A.17)). This has the effect that the effective cross-section of identical particles reduces the higher their relative velocity, which is in line with experimental observations [100]. Additionally, the deflection angle χ is modeled as

$$\chi = 2 \arccos\left(\left(\frac{b}{d_{12}} \right)^{1/\alpha_{12}} \right). \tag{3.23}$$

The distinction between VHS and VSS model is that in the VHS model $\alpha = 1$, whereas it is a tune-able parameter in the VSS model. In summary, the models require the following parameters for a given gas species: The reference diameter d_{ref}, the reference temperature T_{ref}, the viscosity

index ω and the scattering coefficient α (only in VSS model). The advantage of the VSS model over the VHS model is that it is capable of reproducing viscosity as well as diffusion coefficient simultaneously [78]. For the diffusion pump operating principle both viscosity (momentum transfer from vapor jet to gas) and diffusion (gas transport into the jet, backstreaming of mercury vapor and counter-diffusion of light gases through the jet) are important. That is why the VSS model is used as the collision model in the present work. VSS parameters for common gas species are available in the literature, however this is not the case for mercury vapor and the uncommon hydrogen isotopologues. Their treatment is discussed in the following paragraphs.

Mercury vapor Different theoretical and (semi-)empirical models have been proposed over the years to describe the transport properties of mercury vapor. Independently performed works regarding DSMC simulations of mercury diffusion pumps (cf. [103, 104]) have either used the HS or VHS model for mercury (unfortunately it is not clear which model was used because the viscosity index is not provided). Furthermore, mercury has been approximated as a Maxwell molecule ($\omega = 1$, $\alpha = 1$) with a reference diameter derived from the viscosity in previous works by the author [131, 132]. However, no collision interaction parameters exist for the more accurate VSS model as of yet. The present work aims to rectify this by deriving a new set of VSS parameters for mercury vapor. As detailed temperature dependent data - especially of the diffusion coefficient - are scarce, a direct fit to experimental data is not feasible and a different approach is chosen here by fitting the transport properties of the VSS model to those of the more complex *Lennard-Jones (LJ)* model in the temperature range of interest. The LJ 12,6 potential[4] parameters, inversion distance $\sigma_{\mathrm{LJ}} = 2.898 \times 10^{-10}\,\mathrm{m}$ and depth of the potential well $\epsilon_{\mathrm{LJ}}/k_B = 851\,\mathrm{K}$, for mercury vapor are taken from [133, 134]. The fitting procedure outlined below is based on similar approaches in [135, 136]. The basic idea is to optimize the VSS model parameters to minimize the least squares error

$$E = \frac{1}{N}\sum_{i=1}^{N}\left(\frac{\mu_{\mathrm{VSS}}(T_i) - \mu_{\mathrm{LJ}}(T_i)}{\mu_{\mathrm{LJ}}(T_i)}\right)^2 + \left(\frac{D_{11,\mathrm{VSS}}(T_i) - D_{11,\mathrm{LJ}}(T_i)}{D_{11,\mathrm{LJ}}(T_i)}\right)^2, \tag{3.24}$$

between the viscosities μ_{VSS}, μ_{LJ} and self-diffusion coefficients $D_{11,\mathrm{VSS}}$, $D_{11,\mathrm{LJ}}$ over a defined, equally spaced temperature range $T_i \in \left[T_1, T_N\right]$. In the case at hand the temperature bounds are chosen as $T_1 = 0.1 \cdot \epsilon_{\mathrm{LJ}}/k_B = 85.1\,\mathrm{K}$ and $T_N = 523.15\,\mathrm{K}$. The lower bound corresponds to the minimum temperature for which reliable collision integrals for the LJ potential are available (see below). The upper bound is chosen based on the expected maximum temperatures in the mercury boiler. The optimization is performed using the *Nelder-Mead simplex* algorithm [137] as implemented in the Python library *scipy* [138]. As this algorithm converges to local minima the choice of initial guesses for the independent parameters is varied 100,000 times. For each of these iterations the following steps are performed:

1. Random values for the initial values of the free parameters $\omega \in [0.5, 1.5]$ and $T_{\mathrm{ref}} \in \left[T_1, T_N\right]$ are generated from a uniform distribution.

2. The LJ viscosity and self-diffusion coefficients are calculated according to the first-order Chapman-Enskog expansions (cf. e.g. [134]):

$$\mu_{\mathrm{LJ}}(T) = \frac{5\sqrt{\pi m k_B T}}{16\pi\sigma_{\mathrm{LJ}}^2\Omega^{(2,2)*}}, \tag{3.25}$$

[4] The short notation *12,6* refers to the powers with which the repulsive ($\propto r^{-12}$) and attractive ($\propto r^{-6}$) part of the potential scale with the distance r.

$$\rho D_{11,\mathrm{LJ}}(T) = \frac{3\sqrt{\pi m k_B T}}{8\pi\sigma_{\mathrm{LJ}}^2 \Omega^{(1,1)*}} \tag{3.26}$$

for $T = T_{\mathrm{ref}}$, where $\Omega^{(1,1)*}$ and $\Omega^{(2,2)*}$ are temperature dependent collision integrals. These can be found in tabulated form for the LJ 12,6 potential (e.g. in [134]), however for the optimization algorithm it is more convenient to use continuous fit functions. That is why, in the present work the fit functions by Neufeld et al. [139] are used. The validity range is specified as $0.3 \leq k_B T/\epsilon_{\mathrm{LJ}} \leq 100$, but by comparison with tabulated data in [140] it is verified that the error remains below 10 % down to $k_B T/\epsilon_{\mathrm{LJ}} = 0.1$, which is why this temperature is chosen as the lower bound of the temperature fit range.

3. The remaining VSS parameters are calculated from these reference values. Firstly, the *Schmidt number* Sc, which corresponds to the ratio of kinematic viscosity to mass diffusion, is calculated according to

$$\mathrm{Sc}_{\mathrm{LJ}} = \frac{\mu_{\mathrm{LJ,ref}}}{\rho D_{11,\mathrm{LJ,ref}}}. \tag{3.27}$$

By using the definition of the Schmidt number in case of the VSS model, the parameter α can be calculated as follows [77]:

$$\alpha = \frac{10}{3\,(7-2\omega)\,\mathrm{Sc}_{\mathrm{LJ}} - 5}. \tag{3.28}$$

Finally, the VSS reference diameter can be calculated according to [77]

$$d_{\mathrm{ref}} = \sqrt{\frac{5(\alpha+1)(\alpha+2)\sqrt{m k_B T_{\mathrm{ref}}}}{4\sqrt{\pi}\alpha(5-2\omega)(7-2\omega)\mu_{\mathrm{LJ,ref}}}}. \tag{3.29}$$

4. With all VSS parameters determined, the VSS viscosity and self-diffusion coefficients according to the first-order Chapman-Enskog expansion follow as [77]:

$$\mu_{\mathrm{VSS}}(T) = \frac{5(\alpha+1)(\alpha+2)\sqrt{m k_B} T^{\omega}}{16\alpha(3.5-\omega)(2.5-\omega)\sqrt{\pi} d_{\mathrm{ref}}^2 T_{\mathrm{ref}}^{\omega-0.5}}, \tag{3.30}$$

$$\rho D_{11,\mathrm{VSS}}(T) = \frac{3(\alpha+1)\sqrt{m k_B} T^{\omega}}{8(2.5-\omega)\sqrt{\pi} d_{\mathrm{ref}}^2 T_{\mathrm{ref}}^{\omega-0.5}}. \tag{3.31}$$

5. The Nelder-Mead simplex algorithm is used to minimize the error defined in Eq. (3.24) by optimizing the free parameters ω and T_{ref} that are provided as a guess in the first step. The algorithm is set to a tolerance of 10^{-9} and a maximum number of 10,000 optimization steps (each involving the computation of steps 2-4). As a result a local minimum close to the initial guess is found. Using the corresponding optimized VSS parameters the error according to Eq. (3.24) is calculated. If it is the first run or if this error is smaller than that of the previous best fit (that started with a different initial guess for ω and T_{ref}), the new parameters and error are stored. If the error is larger the parameters are discarded. Afterwards, the next run begins with the first step (for a total of 100,000 runs as specified above).

The final set of optimized VSS parameters for mercury vapor that feature the lowest error according to Eq. (3.24) is summarized in Tab. 3.1 together with the other species used in the present work. Additionally, the agreement between the LJ and the newly derived VSS model is compared in Fig. 3.6 over the fitting temperature range (85.1 - 523.15 K). The relative agreement is better than ±5 % over the entire temperature range. The largest deviations are observed close to the upper temperature bound.

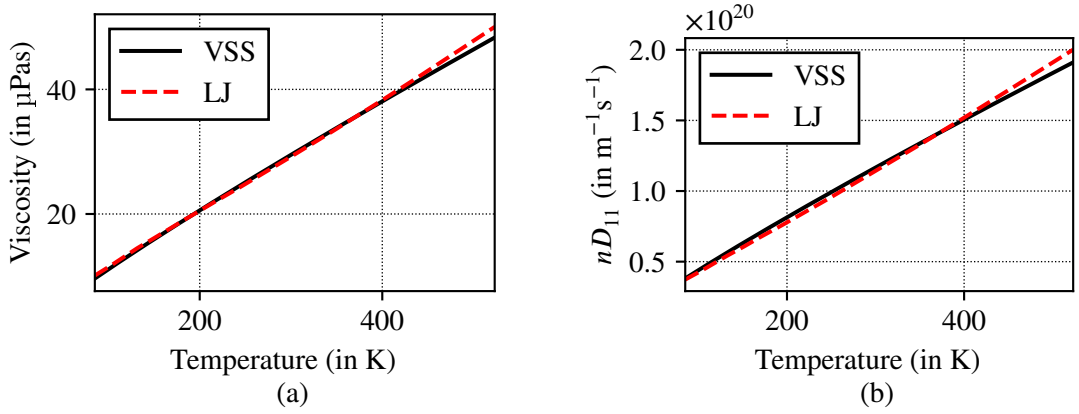

Figure 3.6.: (a) Viscosity as a function of temperature. (b) Product of number density and self-diffusion coefficient as a function of temperature. In both cases the VSS model with the newly derived parameters for mercury is compared against the LJ model (parameters from [133, 134]). In the temperature range 85.1 - 255.3 K the collision integrals used in the LJ model are linearly interpolated from the tabulated values from [140] to improve the accuracy. For all other temperatures the empirical fit functions from [139] are used. The relative agreement between both models is better than ±5 % over the entire temperature range for both coefficients.

Hydrogen isotopologues The VSS parameters for protium (H_2) are available in [77] but an apparent issue arises for the uncommon hydrogen isotopologues HD, D_2, HT, DT and T_2 for which no parameters are available. However, realizing that the intermolecular potential of atoms and molecules is determined by the electronic configuration it is expected that these are very similar for isotopologues. Based on the preceding hypothesis the transport properties of isotopes should only differ according to their different molecular masses. Inspection of the expressions for the transport properties for both the LJ potential (Eqs. (3.25) & (3.26)) as well as the VSS potential (Eqs. (3.30) & (3.31)) reveals that these are proportional to the square root of the molecular mass. Experimental investigations by Kestin et al. [141] and Assael et al. [142] have tested the validity of this scaling law for the viscosity of different hydrogen isotopologues. In both cases the validity is confirmed close to room temperature with less than 1 % deviation. Only at very low temperatures nuclear-spin effects start to become important, and the scaling law loses its validity, for example the error increases to about 2 % for deuterium D_2 and protium H_2 at a temperature of 100 K [142]. It is therefore expected that the scaling law is valid and accurate in case of diffusion pump modeling and the VSS potential parameters of protium H_2, which are available in [77], are used for all the hydrogen isotopologues in the present work (cf. Tab. 3.1). The comparison of the viscosity with experimental data and correlations from literature in Fig. 3.7 confirms the validity of this choice for HD and D_2 over a wide temperature span. Although no data is available for the isotopologues involving tritium, it is still expected that the extrapolation yields acceptable results.

Collisions involving unalike species Regarding collisions of particles of unalike species the present work follows the common approach to average the VSS collision parameters according to

$$\beta_{12} = \frac{\beta_1 + \beta_2}{2}, \tag{3.32}$$

with $\beta = \{d_{\mathrm{ref}}, T_{\mathrm{ref}}, \omega, \alpha\}$. The sensitivity of this assumption is assessed by comparison with some available experimental data on the binary diffusion coefficients of four mercury-gas mixtures in

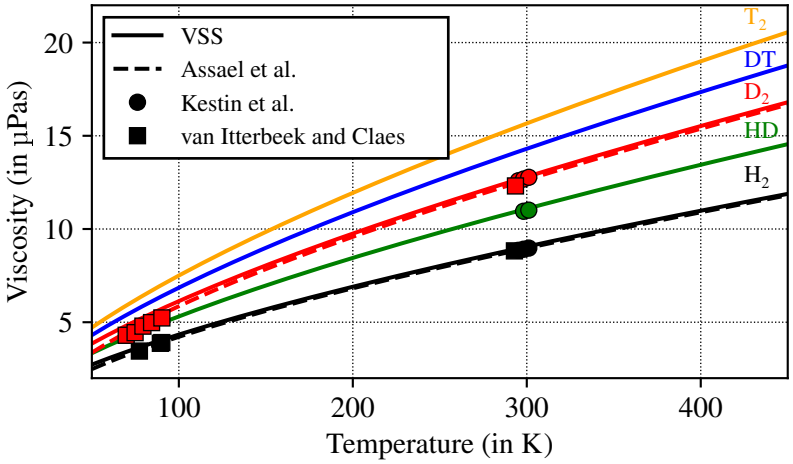

Figure 3.7.: Viscosity of the hydrogen isotopologues as a function of temperature. HT is not shown because it overlaps with D_2. The VSS model (using the hydrogen parameters from [77]) is compared with the following correlations and experimental measurements from literature: Assael et al. [143] (H_2) and [142] (D_2), Kestin et al. [141], van Itterbeek and Claes [144].

Table 3.1.: Summary of VSS parameters for all species used in the present work.

Species	d_{ref} **(in m)**	T_{ref} **(in K)**	ω	α	**Ref.**
Mercury vapor	$5.3160 \cdot 10^{-10}$	372.20	0.88762	1.4494	see above
Helium	$2.30 \cdot 10^{-10}$	273	0.66	1.26	[77]
Neon	$2.72 \cdot 10^{-10}$	273	0.66	1.31	[77]
Argon	$4.11 \cdot 10^{-10}$	273	0.81	1.40	[77]
Hydrogens Q_2	$2.88 \cdot 10^{-10}$	273	0.67	1.35	see above and [77]
Nitrogen	$4.11 \cdot 10^{-10}$	273	0.74	1.36	[77]

Fig. 3.8. However, most of the experimental data are only available for temperatures above 450 K, whereas the typical operational temperature range of mercury diffusion pumps is 250-450 K. Evidently, the VSS model generally underestimates the binary diffusion coefficient. Average errors in the order of magnitude of 10 % are observed for the binary systems Hg-H_2, Hg-N_2 and Hg-Ar. The largest deviations of approximately 20 % are observed for the mixture Hg-He at high temperatures. At room temperature slightly lower deviations are observed, however still exceeding 15 %. It should be noted, that the diffusion coefficient is also inversely proportional to the density (not observable in Fig. 3.8 because the product $n_{\mathrm{mix}} \cdot D_{12}$ is plotted). The vapor expansion inside the diffusion pump body effectuates density gradients spanning several orders of magnitude. Thus, it is expected that the deviations with respect to the temperature discussed above will not deteriorate the simulation results significantly.

The modeling of interspecies collisions can be improved in the future by introducing collision specific VSS parameters (e.g. for a collision between mercury and helium). There are two approaches for obtaining these parameters: Firstly, they can be determined from detailed experimental data of mixture transport properties. However, these are not available in the operational temperature range of diffusion pumps and thus require a dedicated experimental study. Secondly,

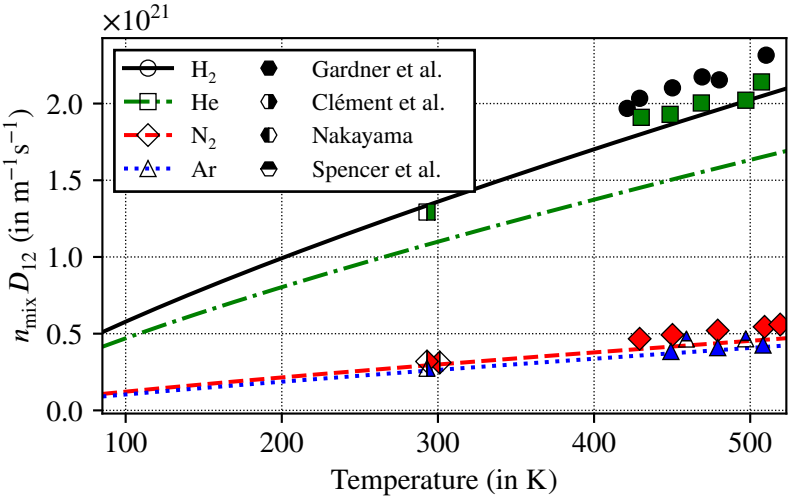

Figure 3.8.: Product of number density and binary diffusion coefficients as a function of temperature for the mixtures Hg-H_2 (solid black line), Hg-He (dashdotted green line), Hg-N_2 (dashed red line) and Hg-Ar (dotted blue line). The lines correspond to the prediction by the VSS model with averaged species parameters as listed in Tab. 3.1. The symbols correspond to experimental data from Gardener, Pang and Preston [145], Clément et al. [146], Nakayama [147] and Spencer, Toguri, and Kurtis [148].

they can be calculated from the Lennard-Jones potential by the same procedure that has been used to derive the mercury VSS parameters above. The Lennard-Jones potential parameters of interspecies collisions can be estimated by means of empirical combining rules like the well-known Lorentz-Berthelot rule, which is a common approach in molecular dynamics simulations [149]. However, it is noted that this empirical combination rule is also known to be only approximately valid as for example discussed in [150]. For this reason, the former approach should be preferred.

3.5.3. Inelastic binary collision modeling

Gas molecules composed of more than a single atom - so-called *polyatomic gases* - can have internal degrees of freedom in addition to the translational degrees of freedom. Diatomic molecules, like the hydrogen isotopologues or nitrogen, have up to two rotational and vibrational degrees of freedom respectively. However, not all of the theoretically available degrees of freedom are active unconditionally. This is because they require a minimum amount of energy to be excited, which implies that the number of available degrees of freedom grows with respect to the average collision energy (i.e. temperature). Vibrational degrees of freedom require substantially higher excitation energies than rotational degrees of freedom [151]. Inactive degrees of freedom are said to be *frozen out* [151]. The number of active degrees of freedom is a continuous function of the temperature because the energy distribution function is smooth, which leads to an increasing fraction of collision with sufficient energy to excite a given degree of freedom with increasing temperature. A plateau value is reached when practically every collision has at least the required excitation energy. The number of active internal degrees of freedom z is depicted as a function of the temperature in Fig. 3.9 for nitrogen and the hydrogen isotopologues, which are the only polyatomic gas species considered in the present work. It can be seen that for all of these gases only the two easier to excite rotational degrees of freedom are active within the temperature range relevant in diffusion pumps.

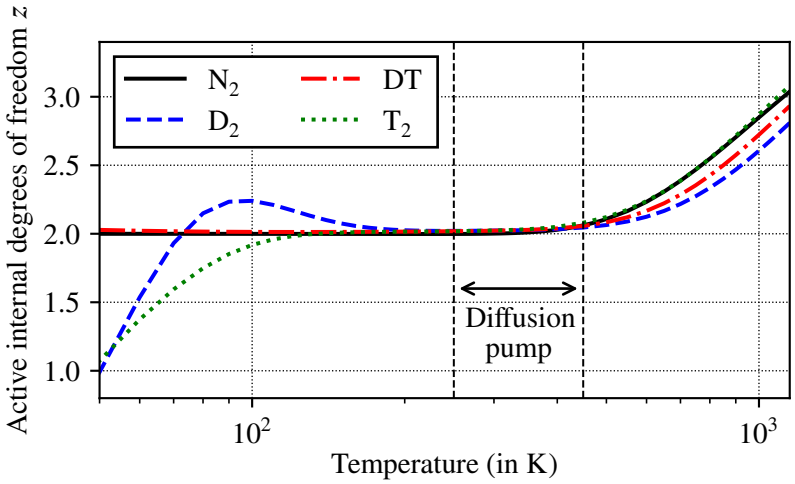

Figure 3.9.: Active internal degrees of freedom z of N_2 (data from [152]) and the hydrogen isotopologues D_2, DT, T_2 (data from [153]) as a function of the temperature. Additionally, the expected temperature range in mercury-driven diffusion pumps is indicated.

Binary collisions involving these gas species can be inelastic - in contrast to the elastic collisions discussed in the previous sections. In inelastic collisions the translational energy is not conserved. Instead, part of the exchanged translational energy can be transferred into the rotational degrees of freedom of one or both collision partners and vice versa. In SPARTA inelastic collisions are treated using the *Larsen-Borgnakke* scheme [154]. If a collision pair has been selected using the NTC algorithm described in Appendix A.3.1 it is checked if one or both collision partners have active rotational degrees of freedom. If this is the case a potential transfer of energy to the rotational degrees of freedom is checked for both collision partners individually by comparing a uniformly distributed random number between zero and unity to the relaxation probability. This relaxation probability corresponds approximately to the inverse of the rotational relaxation number Z_{rot} [77]. For example a rotational relaxation number of $Z_{\mathrm{rot}} = 5$, implies that approximately every fifth collision is inelastic and involves energy transfer from or to the internal degrees of freedom. If one or both collision partners (1, 2) exchange energy with their rotational degrees of freedom the total collision energy is conserved according to

$$\frac{1}{2}m_r(c_r)^2 + E_{\mathrm{rot},1} + E_{\mathrm{rot},2} = \frac{1}{2}m_r(c_r')^2 + E_{\mathrm{rot},1}' + E_{\mathrm{rot},2}', \tag{3.33}$$

where the left side corresponds to the pre-collisional state and the right side (dashed) to the post-collisional state. The average amount of energy that is exchanged between translational and rotational degrees of freedom can be calculated from the equipartition of energy in equilibrium and the molecular interaction model [77, 154].

The following rotational relaxation numbers for the diatomic molecules considered in the present work are assumed: $Z_{\mathrm{rot},N_2} = 5$ [155] and $Z_{\mathrm{rot},H_2} = 174$ [156]. It is noted that these are only approximately correct, especially in case of hydrogen as evident from the strong scattering of reported values that is compared in [156]. Furthermore, the relaxation rates are temperature dependent in reality which is neglected here for reasons of simplicity and efficiency. Quantum calculations in [157] show that the relaxation number of normal deuterium is about 30 % smaller than that of normal hydrogen. Experimental measurements in [158] have resulted in a value of $Z_{\mathrm{rot},D_2} = 150$ at room temperature. Furthermore, it is stated that mixed isotopologues feature smaller rotational relaxation numbers because their center of mass does not correspond to the geometrical molecule

center [158]. Nonetheless, the rotational relaxation number of hydrogen ($Z_{\mathrm{rot,H_2}} = 174$ [156]) has been used for all isotopologues due to the large uncertainties in the available data. These simplifications are justified in the context of diffusion pump modeling because it has been found that they have only minor influence on the results of interest.

3.5.4. Particle weighting schemes

The particle weight F_N determines how many physical particles one simulator particle represents. In the classic DSMC algorithm this value is a constant for all cells and species. While this simplifies the algorithms for particle movement and collisions it is not efficient in case of diffusion pump simulations. Hence, two different particle weighting schemes are applied in the present work and described below: Firstly, *spatial weighting* is used to improve the homogeneity of the simulator particle distribution (e.g. in axisymmetric simulations of cylindrical diffusion pumps). Secondly, *species weighting* is employed to account for the density differences between mercury vapor and the pumped gas.

Spatial weighting is a technique that is used to achieve a more equally distributed number of simulator particles per cell (see e.g. [159, 160]). The scheme aims to achieve a homogeneous number of particles per cell N_p by assigning a cell specific weight $F_{N,i}$ so that

$$F_{N,i} = \frac{n_i V_i}{N_p}, \tag{3.34}$$

where n_i and V_i are the number density and volume of the cell i. The spatially varying cell weights have to be accounted for during the movement step for particles crossing cell boundaries by cloning or deletion of particles. Consider a particle crossing the cell boundary from a cell with weight $F_{N,o}$ (origin) to a cell with weight $F_{N,d}$ (destination). The particle is eligible for cloning or deletion if one of the following criteria is met:

- $F_{N,d} < F_{N,o}$: Create $\lfloor F_{N,o}/F_{N,d} + \mathfrak{R} \rfloor$ clones[5] of the particle which inherit its position and velocity.
- $F_{N,d} > F_{N,o}$: Delete the particle if $\mathfrak{R} > F_{N,o}/F_{N,d}$.

In both cases $\mathfrak{R}$ are random numbers uniformly distributed between zero and unity. It is important to note that a cloned particle will only improve statistics after it has undergone at least one random interaction, i.e. an intermolecular or wall collision. Because all particles within each cell have the same weight no change is necessary to the collision sampling via the NTC method.

The two main use cases of this technique are to account for spatially inhomogeneous density and volume distributions. Both cases are relevant for the diffusion pump model: Highly inhomogeneous density distributions occur due to the expanding vapor flow through the nozzles. Inhomogeneous cell volume distributions are mainly an issue in axisymmetric simulations of cylindrical diffusion pumps. In axisymmetric simulations symmetry is used to convert a three-dimensional cylindrical problem into a two-dimensional projection. However, when considering two cells having identical radial and axial dimensions the cell closer to the axis will have a much lower volume than the one further apart. Thus, a constant weight, as employed in the classic DSMC scheme, will lead to an inhomogeneous distribution of simulator particles per cell even if the number density is homogeneous. To rectify this spatial weighting is employed to increase the particle weight as a linear function of the radial position of the cell center (for this reason also referred to as *radial weighting* [77]).

[5] $\lfloor ... \rfloor$ is the *floor function*, e.g. $\lfloor 4.8 \rfloor = 4$.

Species weighting can be regarded as an extension of spatial weighting. Instead of the single weighting factor per cell introduced by the spatial weighting, species weighting introduces separate weighting factors for each species. This allows to account for significant global or local concentration differences between the simulated species. The particle movement step is handled analogous to the spatial weighting scheme, i.e. particles are cloned or deleted as they move between cell with different weights. The sampling of collisions via the NTC algorithm (cf. Appendix A.3.1) and the collision process (cf. Sec. 3.5.2), however, now require a different treatment because particles of different species within the same cell can have different weights. As species grouping is used in the NTC algorithm the necessary changes can be described for two species A and B without loss of generality. The implementation in the present work follows the scheme suggested in [77, 160, 161]. Because all particles of alike species have the same weight, nothing changes for the collision groupings $A - A$ and $B - B$. In case of interspecies collisions the number of potential collision pairs is calculated using the greater weight of the abundant species (in the following $F_{N,B} > F_{N,A}$ is assumed without loss of generality). If the collision of a pair of particles is accepted as per Eq. (A.23), the binary collision is computed as described in Sec. 3.5.2. However, to account for the different weights only the post-collision velocity of the particle of rare species A is updated unconditionally. The post-collision velocity of the particle of abundant species B is updated with the probability $F_{N,A}/F_{N,B} < 1$. This is necessary because simulator particles of the abundant species represent a greater number of real particles than the simulator particles of the rare species. A visual explanation of the process is provided in Fig. 3.10. It is emphasized that this scheme does not conserve momentum and energy for individual collisions but only on average for many collisions.

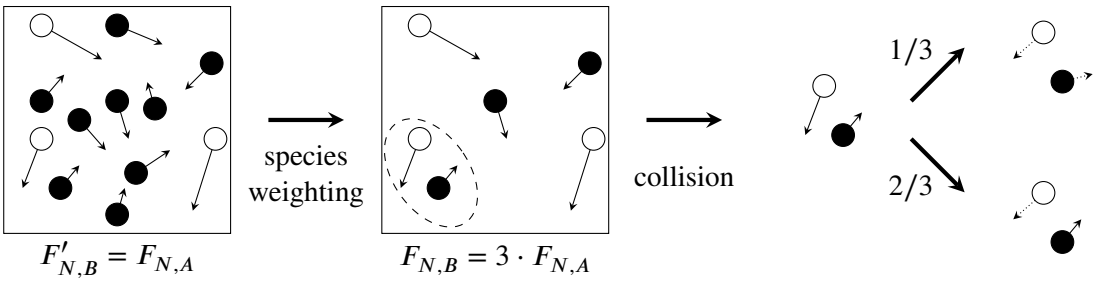

Figure 3.10.: Graphical illustration of the implemented species weighting algorithm. Non-filled simulator particles belong to rare species A, whereas filled simulator particles belong to abundant species B. Species weighting is used to reduce the number of abundant simulator particles ($F_{N,B} = 3 \cdot F'_{N,B}$). The ratio of the species weights determines whether the post-collision properties of the particle belonging to the abundant species B are updated in a collision.

Although species weighting is a well-known technique, it is not commonly implemented (neither SPARTA nor dsmcFoam+ support species weighting). The reason for this are *random walks*, which are introduced by only conserving momentum and energy in collisions on average. A random walk originates from an unlikely event and can then amplify with time due to subsequent collisions. Thus, the reduction in statistical scatter for the rare species that is achieved by introducing species weights can be outweighed by the error resulting from random walks [77]. Careless application of species weights is therefore discouraged [77, 100]. More advanced species weighting schemes have been proposed, which allow conserving momentum and / or energy in collisions see e.g. [162–165]. However, these come at the expense of additional assumptions and computational complexity.

Despite the aforementioned disadvantages the application of species weights is necessary in some diffusion pump simulations to overcome prohibitive numbers of simulator particles that would be required for the conventional DSMC scheme. Fortunately, some of the disadvantages are

mitigated by the specific setup in diffusion pumps: Firstly, the vapor particles have a significantly higher molecular weight (up to factor 50 higher in case of mercury vapor and helium or deuterium). Thus, their velocity vector and magnitude is not altered that much in collisions with gas particles. Consequently, the impact of random walks originating from the random decision whether to keep the pre-collision vapor properties or update them is less pronounced. Secondly, the vapor flow is supersonic in large parts of the computational domain, which reduces the statistical noise so that the algorithm operates well even with the reduced sample size.

The species weighting scheme has been implemented in SPARTA. This required significant changes in core parts of the code, the most important ones being the particle cloning / deletion at the end of the movement step, the sampling and execution of intermolecular collisions and the correct consideration of the species weights during the calculation of the macroscopic moments. The implemented changes have been verified using a test case that involves the counter diffusion of nitrogen and argon. The results of the test case are depicted in Fig. 3.11. The test case features a one-dimensional domain $0 \leq x \leq L$ with periodic boundary conditions in the other two directions. Nitrogen enters the domain on the left-hand side at a fixed temperature under the assumption that no energy is stored in its rotational degrees of freedom. Similarly, argon enters from the right-hand side. Due to inelastic intermolecular collisions between either N_2-N_2 or N_2-Ar energy can be transferred to the rotational degrees of freedom of nitrogen, which causes energy equilibration between translational and rotational degrees of freedom. To verify the correct implementation of the species weighting algorithm three different cases are compared: Firstly, the case is computed without species weights (solid lines). Secondly, the nitrogen weight $F_{N,\mathrm{N_2}}$ is halved, thus doubling the number of nitrogen simulator particles. Lastly, the former is repeated for the argon weight $F_{N,\mathrm{Ar}}$. The results for the number of particles per species and the ratio of rotational to translational temperature of nitrogen are compared in Fig. 3.11. The number of simulator particles increases as expected in the cases that use species weights, whereas the ratio of rotational to translational temperatures of nitrogen is identical for all three case setups, thereby verifying the correct implementation of the species weighting algorithm.

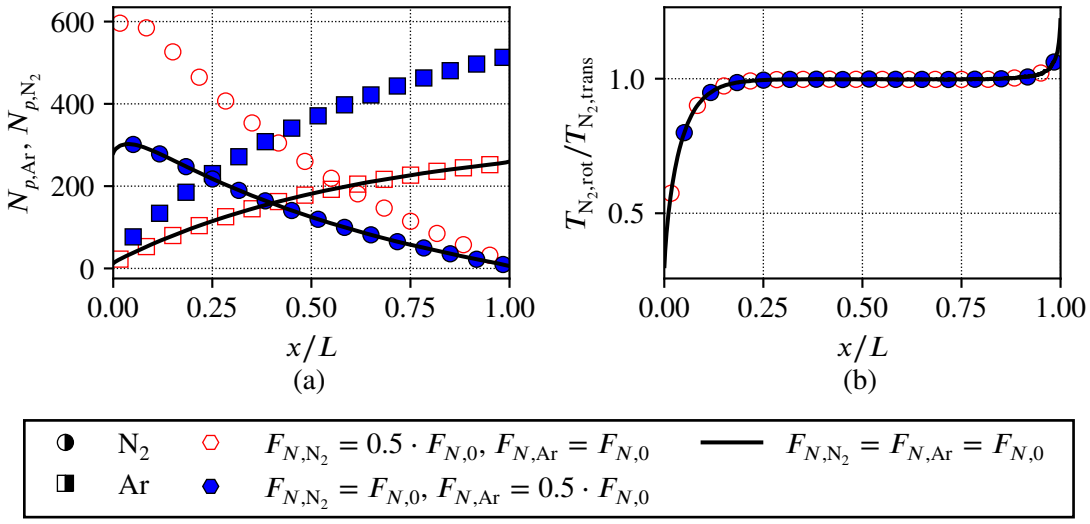

Figure 3.11.: (a) Number of simulator particles per species as a function of the dimensionless domain size. (b) Ratio of nitrogen rotational to translational temperature as a function of the dimensionless domain size. The solid lines correspond to the case without species weighting. Empty and filled symbols represent the simulations with enabled species weighting.

3.5.5. Boundary conditions

The second cornerstone of the DSMC diffusion pump model are its boundary conditions. Physical boundary conditions can be grouped into two main categories: Firstly, open boundaries are responsible for inserting particles into the computational domain and removing particles that leave the domain. Secondly, solid boundaries cause particles to interact with the respective boundary when they collide with it. Moreover, combinations between these are also possible, here most prominently represented by the mercury condensation boundary condition. Notably, boundary conditions can also be species-specific, which is particularly important in case of the present work due to the phase change of mercury. Besides physical boundary conditions there are also virtual, transparent boundaries that are used to sample properties of traversing particles.

Open boundaries

Open boundary conditions represent the interfaces of the computational domain with up- and downstream systems. Thus, they are responsible for introducing new simulator particles into the computational domain and for removing leaving particles. The latter is trivial, but the former requires either knowledge or assumption concerning the particle phase space distribution function at the respective interface. As the distribution function is in general not known a priori it has to be assumed. In the present work the velocities of entering particles at the open boundaries are assumed to be distributed according to (shifted) Maxwell-Boltzmann distributions (cf. Secs. 3.1.1-3.1.2). The same assumption is also taken in previous diffusion pump DSMC models [101, 102], in DSMC models of turbomolecular pumps, which operate under comparable conditions [105–107] and for modeling the gas flow in the divertor [166, 167].

In the DSMC algorithm the instantiation of particles is performed at the beginning of the advection step. The number of particles that are created in each cell containing part of an inflow boundary is computed from the specified inflow conditions (temperature, number density and bulk velocity) and the DSMC properties (time step and weights). The position is chosen randomly on the part of the inflow boundary that lies within the cell. To account for the fact that particles can enter the domain at any time during the time step they are assigned a random number between zero and unity that determines the fraction of the advection time step that they experience inside the simulation domain.

In the present work open boundaries are implemented in two different ways, depending on whether the pressure or the flow rate (i.e. throughput) is to be fixed. Both approaches are discussed in detail in the following paragraphs and for visual clarification a comparison is shown in Fig. 3.12.

Prescribed pressure is modeled by ensuring that all particles crossing the open boundary from within the simulation domain are removed. The phase space distribution function of particles at the open boundary then results as a superposition of the imposed distribution function of inflowing particles and the calculated distribution function of outflowing particles. When assuming a Maxwell-Boltzmann distribution function for the inflowing particles and conditions p_B and T_B at the boundary, the flux of injected particles follows as

$$\dot{n}_{\mathrm{fixed}\,p} = \frac{1}{4}\frac{p_\mathrm{B}}{k_B T_\mathrm{B}}\bar{v}, \tag{3.35}$$

where $\bar{v}$ is the mean thermal speed of the respective gas species at temperature T_B as given by Eq. (3.5). It is noted that this is a simplification because it assumes that the flow is at rest (i.e. $\vec{u} = \vec{0}$).

Prescribed throughput is achieved by reflecting all particles crossing the open boundary from within the simulation domain. By ensuring the former the net flux is equivalent to the flux of injected particles and can readily be computed from the targeted throughput Q_B, the boundary temperature T_B and flow cross-section A_B

$$\dot{n}_{\mathrm{fixed}\,Q} = \frac{Q_\mathrm{B}}{A_\mathrm{B} k_B T_\mathrm{B}} = \frac{q_\mathrm{B}}{A_\mathrm{B} k_B \cdot 273.15\,\mathrm{K}}, \tag{3.36}$$

where the latter corresponds to the normalized throughput at the reference temperature of 273.15 K. This boundary condition can only be used at inflow surfaces (i.e. only for $\dot{n}_{\mathrm{fixed}\,Q} > 0$).

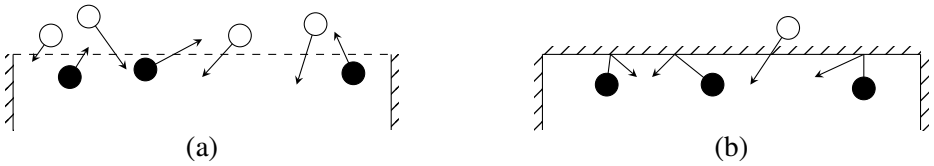

Figure 3.12.: Comparison of the two types of inflow boundary conditions employed in the present work: (a) Prescribed pressure and (b) prescribed flow rate / throughput. Non-filled particles correspond to newly generated ones. Filled particles correspond to existing particles inside the domain that collide with the boundary. Newly generated particles are drawn outside the domain to illustrate that they only travel part of the time step inside the domain.

Solid boundaries

As gas particles collide with the solid walls they are reflected in most cases. The three types of solid interactions used in the present work are described in the following paragraphs. Additionally, they are compared visually in Fig. 3.13.

Specular reflections conserve the particle's velocity magnitude and tangential velocity component. Merely the normal velocity component is inverted. Thus, the wall behaves like a mirror. As the velocity magnitude of the particle is conserved the same is true for its kinetic energy. Therefore, no energy is transferred between the particle and the wall. While the interaction between gas particles and technical surfaces is better described using diffuse reflections (cf. next paragraph), specularly reflective surfaces are used to implement virtual symmetry planes into the DSMC simulation.

Diffuse reflections are more relevant for technical surfaces. In diffuse collisions particles are scattered isotropically from the surface. The applicability of the cosine law for gas reflections was demonstrated experimentally by Knudsen (incidentally using mercury vapor) [168], therefore it is sometimes also referred to as *Knudsen's cosine law*[6]. The physical reasoning is twofold [77]: On the one hand, particles might not be reflected immediately but momentarily be adsorbed on the surface before being randomly re-emitted to the gas phase. On the other hand, plane technical surfaces are still rough on the microscopic level. The latter has been investigated by simulations for different periodic microstructures in [169]. They find that the cosine law is approached even if individual scattering events are considered as specular because particles will perform repeated collisions with the microstructures before eventually leaving the surface. Furthermore, a superposition of both effects is also possible. Apart from the scattering according to the cosine law, it is

[6]The same law is known also as *Lambert's cosine law* when considering the diffuse reflection of light.

also generally assumed that particles will accommodate to the wall temperature. Thus, energy can be transferred between wall and gas flow.

Adiabatic reflections are a special case of diffuse reflections without energy transfer between gas flow and wall. In the diffusion pump simulation they are used for the nozzle walls. Two possibilities exist to implement the adiabatic boundary condition in the DSMC method. An overview, discussion and implementation guidelines are given in [170]: The first option is to adjust the local wall temperature iteratively until the heat flux from flow to wall reduces to zero. As DSMC is a statistical method this process is prone to noise. The second option is to conserve the energy of each individual scattering particle. This is achieved by scattering the particle isotropically whilst conserving the velocity magnitude (and thus kinetic energy). The benefit of this implementation is that it does not require iterations. For this reason the second option has been implemented into SPARTA (cf. [132]) and used in the present work.

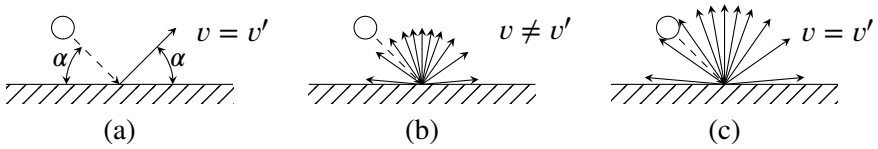

Figure 3.13.: Comparison of the three solid boundary conditions used in the present work: (a) Specular reflection, (b) diffuse reflection and (c) adiabatic reflection. In all cases the velocity magnitude before (v) and after (v') the collisions are compared. For the isotropic reflections the density of the arrows is indicative of the reflected flux density.

Condensation of the operating fluid vapor

The cooled walls of the pump are an example of a boundary condition that is species-specific. While the wall resembles a solid boundary condition for gas particles, mercury vapor can condense and thus leave the gas phase simulation domain. The condensation of mercury vapor on the cooled walls of the pump constitutes a vital part of the diffusion pump operating principle, because it (partially) prevents the reflection of mercury atoms striking the wall. Thereby, the directed momentum of the mercury vapor in pumping direction is preserved. Mathematically, the condensation is described using the *condensation coefficient* α_c. The condensation coefficient determines the fraction of impinging vapor particles that undergo a phase change when they hit the surface whereas the remainder will be reflected into the gas phase. Additional complexity is introduced if the saturation vapor pressure at the wall temperature is not negligible. In this case particles will also evaporate from the liquid surface. The situation is illustrated in Fig. 3.14. In the most general case the net

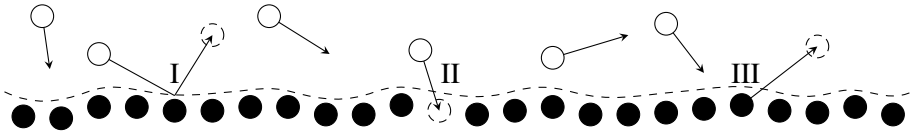

Figure 3.14.: Simplified illustration of the molecular fluxes at a vapor-liquid phase interface. Gas phase particles are represented by the empty circles whereas liquid phase particles are represented by the filled circles. The molecular processes at the phase boundary are: I: reflection, II: condensation, and III: evaporation.

condensation flux can then be expressed as

$$\dot{n}_{\text{net}} = \dot{n}_{\text{incident}} - \dot{n}_{\text{emit}} = \dot{n}_{\text{incident}} - \dot{n}_{\text{reflect}} - \dot{n}_{\text{evaporate}}. \tag{3.37}$$

The flux of evaporating particles can be expressed by

$$\dot{n}_{\text{evaporate}} = \alpha_c \frac{p_{\text{sat}}(T_w)}{\sqrt{2\pi m_{\text{V}} k_B T_w}}, \tag{3.38}$$

where the prefactor α_c has to be introduced to ensure that the net flux according to Eq. (3.37) reduces to zero for vapor-liquid-equilibrium [76, 171–173]. It should be noted that Eq. (3.38) is identical to the molecular flux in equilibrium as calculated in Eq. (3.5) if $\alpha_c = 1$. According to the definition of the condensation coefficient, the reflected flux is simply

$$\dot{n}_{\text{reflect}} = (1 - \alpha_c)\dot{n}_{\text{incident}}. \tag{3.39}$$

Usually, diffuse reflections similar to the solid walls (cf. Sec. 3.5.5) are assumed. In this case the velocities of the reflected and evaporating particles are both distributed according to the same Maxwell-Boltzmann distribution function at the temperature of the wall. If it is further assumed that the impingement positions of incident particles are uniformly distributed, the reflected and evaporated fluxes follow the same velocity distribution function and can be summarized. Therefore, an *effective condensation coefficient* $\alpha_{c,\text{eff}}$ can be introduced to rewrite Eq. (3.37) to

$$\dot{n}_{\text{net}} = \dot{n}_{\text{incident}} - \dot{n}_{\text{emit}} = \alpha_{c,\text{eff}} \dot{n}_{\text{incident}}, \tag{3.40}$$

where

$$\alpha_{c,\text{eff}} = \alpha_c - \frac{\dot{n}_{\text{evaporate}}}{\dot{n}_{\text{incident}}} \leq \alpha_c. \tag{3.41}$$

It is noted that the term *condensation coefficient* is often ambiguously used for both α_c and $\alpha_{c,\text{eff}}$ in literature, although they express fundamentally different physical quantities. The same is true for the terms *condensation / evaporation rate*, which are sometimes used to describe the individual contributions to Eq. (3.37) as done in the present work and sometimes refer to the net flux. Thus, special care has to be taken to identify which quantities are considered in the respective context.

Regarding diffusion pumps the effective condensation coefficient should be as high (i.e. close to unity) as possible while still economically viable. The most sensitive performance indicator on the effective condensation coefficient is the vapor backstreaming rate. In the theoretical limit of $\alpha_{c,\text{eff}} = 1$, the only pathway for backstreaming vapor are intermolecular collisions (either vapor-vapor or vapor-gas) because there is no direct line of sight between the nozzle and the inlet. Thus, lower effective condensation coefficients can have a significant impact on the backstreaming rate. It is therefore important to determine the effective condensation coefficient of mercury vapor at the expected temperatures of the cooled outer walls of the diffusion pump to accurately consider these effects.

Several previous studies were dedicated towards the determination of the mercury vapor condensation coefficient of which a few are summarized in the following. It is reported that the condensation / evaporation coefficient (α_c) is close to unity for liquid mercury evaporating into a vacuum maintained by a liquid air cooled surface [174–176]. However, even slight impurities can inhibit condensation and evaporation significantly. For example, Knudsen found that the evaporation coefficient was reduced to $\alpha_c = 5 \cdot 10^{-4}$ for mercury contaminated with small amounts of a sealing agent [174]. Evaporation coefficients close to unity were obtained in [177] for the condensation of pure mercury vapor during film and drop wise condensation of mercury vapor at temperatures around 100 °C. Additionally, it is noted that the best condensation properties are achieved once the walls are fully wetted [177]. Narusawa and Springer [178] determined the effective condensation coefficient by measuring the reflected mercury distribution resulting from a molecular mercury vapor beam directed at a liquid mercury surface. They find $\alpha_{c,\text{eff}} = 1$ for specular reflections

and $\alpha_{c,\mathrm{eff}} > 0.65$ for diffuse reflections. As these values did not change significantly when varying the temperature of the liquid mercury surface between 20 and 40 °C, it can be concluded that evaporated mercury vapor does not have a significant contribution and hence that $\alpha_{c,\mathrm{eff}} \approx \alpha_c$ in their measurements. Heat transfer investigations during mercury film condensation yielded values around $\alpha_c = 0.45$, but it is noted again that this is sensitive to contamination [179]. Similar measurements on film condensation of mercury are reported with values close to unity in [180, 181]. An extensive review of previous experiments for potassium, sodium and mercury is included in [181] (Fig. 1 in particular), which shows that the condensation coefficient is close to unity for all three metals especially at low pressures < 1000 Pa. Based on these experimental findings the condensation coefficient of mercury is assumed to be unity, i.e. $\alpha_c = 1$, in the present work. This choice simplifies the numerical modeling, as no reflections of the incident vapor have to be considered. However, it is noted that a more detailed study might be justified in the future.

All previous DSMC models of oil- and mercury-driven diffusion pumps in literature have only assumed perfect condensation with $\alpha_{c,\mathrm{eff}} = 1$ and thus $\dot{n}_{\mathrm{net}} = \dot{n}_{\mathrm{incident}}$ [101–104, 132] or have studied a variation of the global effective condensation coefficient, i.e. $\dot{n}_{\mathrm{net}} = \alpha_{c,\mathrm{eff}} \dot{n}_{\mathrm{incident}}$ [131]. In oil diffusion pumps (DSMC simulations in [101, 102]) this assumption is somewhat more justified due to the much lower vapor pressure of the oil at common cooling temperature levels (see e.g. [66]). However, in mercury diffusion pumps the saturation pressure at the cooled walls can reach or even exceed the inlet gas pressure. Therefore, a closer investigation is justified.

While flows subject to condensation and evaporation have been investigated using DSMC or kinetic model equations in different levels of detail in the past, these have mostly considered one-dimensional problems [171–173, 182–185]. With respect to diffusion pump simulations the main implementation difficulty in DSMC arises from the fact that it is not known a priori which part of the cooled wall is wetted by the incident mercury vapor. The naive assumption of a uniform, steady evaporation from the entire cooled wall thus grossly overestimates the actual mercury evaporation rate especially in the upper parts of the pump that contribute most to the backstreaming rate.

For the reasons outlined above, a boundary condition that is capable of keeping track of the local condensation rate during the simulation run time has been developed in the present work. This allows to determine the presently wetted parts of the wall and thus enables a much more precise prediction of the evaporation rate. The boundary condition is implemented in the following two-step process:

1. All incident mercury particles are assumed to condense (i.e. $\alpha_c = 1$, as discussed above) and the local condensation fluxes $\dot{n}_{\mathrm{condense}}(x)$ are determined as

$$\dot{n}_{\mathrm{condense}}(x) = \alpha_c \dot{n}_{\mathrm{incident}}(x). \tag{3.42}$$

2. The local evaporation flux is given by

$$\dot{n}_{\mathrm{evaporate}}(x) = \min \left\{ \dot{n}_{\mathrm{condense}}(x), \alpha_c \frac{p_{\mathrm{sat}}(T_w)}{\sqrt{2\pi m_{\mathrm{V}} k_B T_w}} \right\}, \tag{3.43}$$

   i.e. bounded either by the local condensation flux or by the maximum evaporation rate (again taking $\alpha_c = 1$) at the wall saturation conditions. The former ensures that the evaporation rate at the unwetted parts of the cooled wall is correctly represented.

The combination of these two local opposing fluxes yields the local net flux

$$\dot{n}_{\mathrm{net}}(x) = \dot{n}_{\mathrm{condense}}(x) - \dot{n}_{\mathrm{evaporate}}(x) = \max \left\{ 0, \alpha_c \dot{n}_{\mathrm{incident}}(x) - \alpha_c \frac{p_{\mathrm{sat}}(T_w)}{\sqrt{2\pi m_{\mathrm{V}} k_B T_w}} \right\}, \tag{3.44}$$

where the second term in the maximum function resembles the Hertz-Knudsen equation if the velocity distribution function of the incident particles is Maxwellian [186]. Additionally, a visual comparison of the fluxes is available in Fig. 3.15, which depicts the local evaporation and net fluxes as functions of the local condensation flux in dimensionless form. Two principal regions are distinguishable: At incident fluxes smaller than the theoretical saturated evaporation flux at the wall temperature the net flux reduces to zero because all condensing particles are re-emitted. In this region the wall behaves similar to a dry diffuse surface. If the incident flux exceeds the saturated evaporation flux, the net flux becomes positive and indicates a net condensation, i.e. an effective condensation coefficient $\alpha_{c,\mathrm{eff}} = \dot{n}_{\mathrm{net}}/\dot{n}_{\mathrm{incident}} > 0$. As gravitational transport of mercury condensate is neglected in Eqs. (3.43)-(3.44) the wall is considered wetted in this region. The motivation for this assumption, which is conservative with respect to the backstreaming rate, is that mercury vapor tends to form small droplets while condensing [187]. These grow until the gravitational force outweighs the adhesion force. It is therefore likely that condensate transport is only relevant in those regions of the cooled walls that are sufficiently wetted by the vapor so that the evaporation rate will be limited by the second term in Eq. (3.43) anyways.

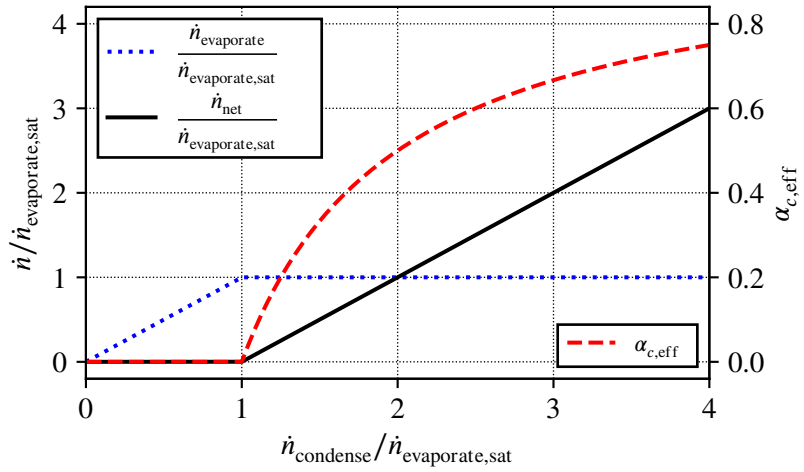

Figure 3.15.: Local evaporation flux $\dot{n}_{\mathrm{evaporate}}$ (Eq. (3.43)) and local net flux $\dot{n}_{\mathrm{net}}$ (Eq. (3.44)) as a function of the local condensation flux $\dot{n}_{\mathrm{condense}}$ (Eq. (3.42)). All fluxes are scaled with the theoretical evaporation flux at saturation conditions $\dot{n}_{\mathrm{evaporate,sat}}$. Furthermore, the local effective condensation coefficient $\alpha_{c,\mathrm{eff}}$ is shown on the right axis.

The developed boundary condition has been implemented into SPARTA by adding the capability to track the local rates of incident mercury particles (Eq. (3.42)). The implementation pursued is based on per-cell and per-surface counters that are updated if a mercury particle hits the cooled wall. These counters are then used during the next particle insertion step to determine how many mercury particles are evaporated from each surface element in every cell. If a particle is evaporated the counter is decremented accordingly. In this way mass conservation is ensured in cells in which the evaporation rate is bounded by the local rate of incident particles (i.e. first term in Eq. (3.43)). The positions of evaporated particles are determined randomly under the assumption of a uniform distribution on the evaporating surface. Because the fluxes are determined on the cell level the spatial discretization error involved with this process is reasonably small.

The correct implementation of the implemented DSMC condensation boundary condition is verified by comparing with the analytical solution in the free-molecular regime. A verification in the free-molecular regime is possible because the code adaptations do not influence the routines for in-

termolecular collisions. The analytical solution is based on the methodology derived and presented in [188] for a jet impinging on a flat plate with fully diffuse reflections. The analytical expressions are modified so as to change the fully diffuse reflection to partial condensation according to the condition given in Eqs. (3.42)-(3.43). The DSMC solution agrees perfectly with the analytical solution as apparent from Fig. 3.16 which verifies the correct implementation of the scheme in the DSMC.

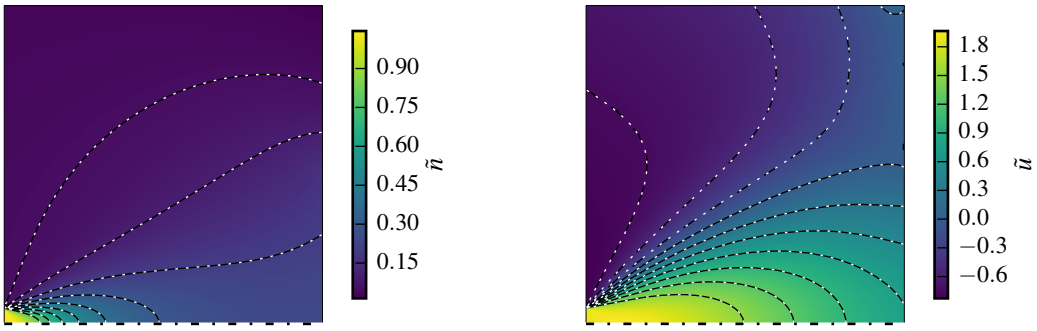

(a) (b)

Figure 3.16.: Jet impinging on a flat plate (right boundary) with condensation and partial re-evaporation in the free-molecular regime (Kn $\rightarrow \infty$). Flood and black contour lines: DSMC, white dotted contour lines: analytical solution. (a) Normalized number density $\tilde{n} = n/n_0$. (b) Normalized x-velocity $\tilde{u} = u/\sqrt{2k_B T_0/m}$ (left to right). The jet enters at the lower left side with a shifted Maxwell-Boltzmann distribution according to n_0, $[\tilde{u}, \tilde{v}]^{\mathrm{T}} = [2, 0]^{\mathrm{T}}$ and T_0. Outflow to vacuum is assumed on left and top boundaries and symmetry on the bottom boundary. Condensation and re-evaporation is assumed at the right boundary with conditions $\alpha_c = 1, T_w = T_0$ and $n_{\mathrm{sat}}(T_w) = 0.25 \cdot n_0$.

Transparent boundaries

Typically, macroscopic properties are sampled within the computational cells as previously outlined at the beginning of Sec. 3.5. However, for some cases it can be beneficial to sample these properties at virtual, so-called *transparent*, boundary surfaces that can be placed arbitrarily in the flow. For example, it is convenient to compute the compression ratio of a vacuum pump by obtaining the average pressures at inlet and outlet cross-sections by means of transparent surfaces. These surfaces do not interact with the simulation particles but count some properties of traversing particles. During every particle movement step it is checked whether any of the particles crosses a transparent surface. If this is the case the particle's properties are recorded.

The SPARTA implementation of transparent surfaces has been extended with the capability to calculate thermodynamic properties (e.g. density, pressure, temperature) at the surface in the present work. This requires the definition of a control volume. Therefore, it is necessary to scale the properties of individual particles with their residence time in a virtual extrusion volume around the transparent surface. This approach is better known in the context of the TPMC method, which is commonly implemented without a grid and thus has to rely on surfaces to compute thermodynamic

properties [121]. For example the average density is computed as

$$\overline{n}_{\text{trans}} = \frac{1}{N_s} \sum_{s=1}^{N_s} \sum_{i=1}^{N_p(s)} \frac{F_{N,i}}{v_{i,\perp} \Delta t A_{\text{trans}}}, \tag{3.45}$$

where N_s is the number of sampling time steps, each of duration Δt. $N_p(s)$ is the number of particles traversing the transparent surface within each sampling time step s. The volume swept out by each particle is given by the product of the perpendicular component of the particle speed $v_{i,\perp}$, the time step Δt and the area of the transparent surface A_{trans}.

4. Modeling and analysis of mercury-driven diffusion pumps

Diffusion pumps can be modeled on different levels of detail.

For a basic model, it is possible to focus exclusively on the pumping process resulting from the momentum transfer from the vapor jet to the pumped gas. In a first approximation it is possible to describe this effect in one dimension by means of a simplified analytical model. Due to the sole focus on the pumping process (i.e. the vapor gas interaction), the application of such a model is limited to providing fundamental constraints of the design space, however with the principal advantage that it is very easy and fast to compute.

A more detailed description of diffusion pumps is possible by means of numerical simulation using the Direct Simulation Monte Carlo (DSMC) method. In a first step, the analytical and DSMC model are compared with respect to the description of the pumping process in order to verify the analytical model. Next, a detailed DSMC model of a simple cylindrical diffusion pump is developed. This model includes all physical effects resulting from the interaction of vapor and gas with the geometric boundaries of the pump. Therefore, comparison with the models focusing exclusively on the pumping process allows to determine the impact of the pump geometry on the performance.

4.1. Dimensionless model of the pumping process and performance assessment

Several analytical models have been proposed to describe the pumping process in vapor diffusion pumps and a good overview is given in [189]. In the following a dimensionless model is derived based on the successive works of Wertenstein, Matricon and Jaeckel [190–192]. The derivation in the present work closely follows these previous works, mainly [192], as well as improvement suggestions by Wutz [44]. Furthermore, the model is converted to a fully dimensionless representation including the identification and interpretation of the determining dimensionless numbers. Fundamentally, this model describes the gas transport in the vapor jet as a superposition of advection and counteracting diffusion. Similar models have been proposed for turbomolecular pumps because these also rely on momentum transfer, albeit replacing the vapor jet by a rotor-stator combination [193–196]. The focus here lies on the main physical aspects involved in the interaction between mercury vapor and pumped gas. The model is restricted to one dimension and thereby by definition neglects any impact of the pump geometry. This choice allows identifying fundamental limitations of the design space, which is not possible for more detailed models which to a varying degree include geometrical features of the pump.

Figure 4.1 shows the simplified diffusion pump domain considered in the one-dimensional model and is used to illustrate the following derivation, which closely follows Jaeckel [192]. For the purpose of simplifying the model the driving operating fluid vapor jet is assumed to start at $x = 0$ and to have uniform properties (density n_V and bulk velocity u_V) in the entire domain, i.e. $n_\mathrm{V}(x) = n_\mathrm{V}$, $u_\mathrm{V}(x) = u_\mathrm{V}$. To ensure momentum conservation the former assumption implicitly requires that the mass density of vapor is much higher than the mass density of gas in the entire domain. Additionally, the backstreaming of mercury vapor (to the region $x < 0$) is neglected, which corresponds to

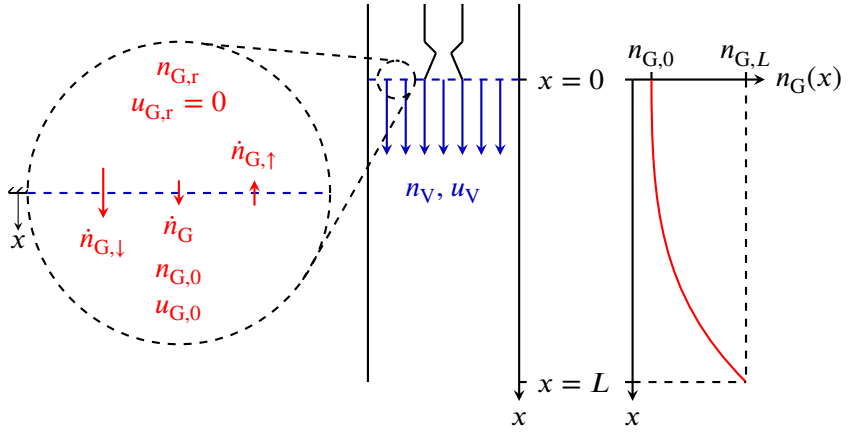

Figure 4.1.: Simplified diffusion pump domain considered in the one-dimensional model (partly based on [192]). Indices "G" and "V" refer to the gas and vapor respectively. A sketch of a converging-diverging nozzle is included to give a visual indication of the position of the interface between the gas reservoir (index "r") and the vapor jet, which is located at $x = 0$. A zoom of this interface is shown on the left-hand side. The evolution of the gas number density $n_G$with respect to the one-dimensional domain size x is shown on the right-hand side.

ideal operation of the diffusion pump. The aim of the one-dimensional model is to find an expression for the *capture coefficient* ς of the diffusion pump, which is defined as the ratio of pumped flux $\dot{n}_G$ to the theoretical incoming flux through the pump inlet $\dot{n}_{G,\downarrow}$, i.e.

$$\varsigma = \frac{\dot{n}_G}{\dot{n}_{G,\downarrow}}. \tag{4.1}$$

The gas flow between the vacuum recipient and the vapor jet (cf. Fig. 4.1, left) is considered to be free-molecular, which is a reasonable assumption for most applications. This assumption implies that there are no intermolecular collisions upstream of the jet interface. As a consequence the net pumped flux of gas $\dot{n}_G$ can be described as the superposition of the molecular gas fluxes entering ($\dot{n}_{G,\downarrow}$) and leaving ($\dot{n}_{G,\uparrow}$) the jet

$$\dot{n}_G = \dot{n}_{G,\downarrow} - \dot{n}_{G,\uparrow}. \tag{4.2}$$

The upstream vacuum recipient is modeled as a gas reservoir at rest, i.e. $u_{G,r} = 0$. This is a reasonable approximation of real systems because the physical dimensions of the recipient (e.g. the Tokamak torus) are usually much larger than the connection to the pump. Therefore, according to the kinetic theory of gases the downward molecular flux through the jet interface at $x = 0$ is

$$\dot{n}_{G,\downarrow} = \frac{n_{G,r}}{4}\sqrt{\frac{8k_B T_{G,r}}{\pi m_G}}. \tag{4.3}$$

Inside the jet, momentum is transferred from the vapor molecules to the gas by intermolecular collisions. Consequently, the gas is accelerated whilst its density at the interface decreases below the reservoir density (i.e. $u_{G,0} > 0$ and $n_{G,0} < n_{G,r}$). In the model of Jaeckel [192], the gas flux is modeled using the same expression as in Eq. (4.3), albeit with different gas density. However, as also pointed out by Wutz [44], this is inaccurate because it neglects the non-zero bulk motion of the gas in the jet. Instead, the more general expression for the molecular flux has to be used (cf. Eq. (3.10)) [44], i.e.

$$\dot{n}_{\mathrm{G},\uparrow} = \frac{n_{\mathrm{G},0}}{4}\sqrt{\frac{8k_B T_{\mathrm{G},0}}{\pi m_{\mathrm{G}}}}\left[\exp\left\{-\varphi^2\right\} - \sqrt{\pi}\varphi\left(1-\mathrm{erf}\left\{\varphi\right\}\right)\right], \tag{4.4}$$

where the speed ratio $\varphi = u_{\mathrm{G},0}/\sqrt{2k_B T_{\mathrm{G},0}/m_{\mathrm{G}}}$ is introduced. In Eq. (4.4) $n_{\mathrm{G},0}$, $T_{\mathrm{G},0}$ and $u_{\mathrm{G},0}$ correspond to the up to now unknown conditions of the gas in the jet. Due to mass conservation the gas flux $\dot{n}_{\mathrm{G}}$ can also be expressed as

$$\dot{n}_{\mathrm{G}} = n_{\mathrm{G}}(x)\cdot u_{\mathrm{G}}(x) = n_{\mathrm{G}}(x)\cdot u_{\mathrm{V}} - D\frac{\mathrm{d}n_{\mathrm{G}}(x)}{\mathrm{d}x}, \tag{4.5}$$

where D is the diffusion coefficient of gas in the vapor jet. The net gas flux $\dot{n}_{\mathrm{G}}$ results from advection (first term on the r.h.s. of Eq. (4.5)) with the vapor jet and counteracting diffusion of gas through the jet (second term on the r.h.s. of Eq. (4.5)). The ordinary differential Eq. (4.5) can be integrated subject to the boundary condition $n_{\mathrm{G}}(x = L) = n_{\mathrm{G},L}$ to find an expression for the evolution of the gas number density along the domain. Solving this at the interface ($x = 0$), yields

$$n_{\mathrm{G},0} = \frac{\dot{n}_{\mathrm{G}}}{u_{\mathrm{V}}}\left(1-\exp\left\{-\mathrm{Pe}\right\}\right) + n_{\mathrm{G},L}\exp\left\{-\mathrm{Pe}\right\}, \tag{4.6}$$

where the dimensionless mass transfer Péclet number $\mathrm{Pe} = u_{\mathrm{V}}L/D$, describing the ratio of advective to diffusive transport of gas in the jet, is introduced. The last unknown is now the temperature of the gas at the interface, $T_{\mathrm{G},0}$. A conservative overestimation, consistent with [192], is to assume the same temperature as in the upstream reservoir, i.e. $T_{\mathrm{G},0} = T_{\mathrm{G,r}} = T_{\mathrm{G}}$, which leads to an overestimation of the molecular gas flux $\dot{n}_{\mathrm{G},\uparrow}$ that leaves the jet toward the upstream reservoir and therefore to a conservative underestimation of the capture coefficient. After some algebraic transformations Eqs. (4.1)-(4.6) can be combined to identify the final dimensionless model of the capture coefficient in form of the non-linear system of equations

$$\varsigma = \left[1 + \frac{1}{2\sqrt{\pi}\varphi}\left[\exp\{-\varphi^2\} - \sqrt{\pi}\varphi\left(1-\mathrm{erf}\{\varphi\}\right)\right]\right]^{-1}, \tag{4.7}$$

$$\varphi = \Phi\varsigma\left[\varsigma\left(1-\exp\{-\mathrm{Pe}\}\right) + 2\sqrt{\pi}\kappa\Phi\exp\{-\mathrm{Pe}\}\right]^{-1}, \tag{4.8}$$

where a second speed ratio $\Phi = u_{\mathrm{V}}/\sqrt{2k_B T_{\mathrm{G}}/m_{\mathrm{G}}}$ and the compression ratio $\kappa = n_{\mathrm{G},L}/n_{\mathrm{G},0}$ are introduced as the final two dimensionless numbers. An overview of all the involved dimensionless numbers including their physical interpretation is presented in the following:

- Capture coefficient $\varsigma \in [0, 1]$: Corresponds to the normalized pumping speed (cf. Eq. (2.6)). In literature this is sometimes also referred to as the *Ho*-coefficient in the context of diffusion pumps [56].
- Mass transfer Péclet number $\mathrm{Pe} \in [0, \infty)$: Ratio of advective to diffusive gas transport in the jet.
- Speed ratio $\Phi \in [0, \infty)$: Compares the speed of the vapor jet to the thermal speed of the gas in the jet. For practical application $\Phi \in [0, 1]$ holds true, because the vapor molecules typically have a significantly higher molecular mass than the pumped gas.
- Speed ratio $\varphi \in [0, \infty)$: Compares the effective gas bulk speed (resulting as the superposition of advection and counter-diffusion) to the thermal speed of the gas in the jet. By definition $\varphi \leq \Phi$, where equality holds true if advection is dominating diffusion, i.e. in the limit $\mathrm{Pe} \to \infty$.

- Compression ratio $\kappa \in [0, \infty)$: Ratio of the gas number density at the outlet to the one in the recipient. Because of the assumption of an isothermal process this is equivalent to the typical definition using the respective pressures (cf. Eq. (2.7)). For an operational pump $\kappa \in [1, \infty)$ holds true. The range $\kappa \in [0, 1)$ corresponds to the case where the backing pump is pumping through the diffusion pump.

Due to the complex interdependence of Eqs. (4.7) and (4.8) it is not possible to derive a purely analytical solution for the capture coefficient ς by elimination of φ. This is a possible explanation for the fact that the more appropriate but also more complex expression for the backdiffusing gas flux in Eq. 4.4 has been recognized (e.g. by Wutz [44]) but - to the best of the author's knowledge - not been implemented in the model so far. However, the system of equations can easily be solved numerically, e.g. using a least-squares algorithm. In the present work the *Trust Region Reflective* algorithm [197] as implemented in the Python library *scipy* [138] is used for this purpose. Figure 4.2 illustrates the dependency of the capture coefficient ς on the two main variables $\boldsymbol{\Phi}$ and κ for two Péclet numbers. The main interdependencies can be summarized and explained as follows: Firstly, increasing the speed ratio $\boldsymbol{\Phi}$ leads to an increase of the capture coefficient. This is expected because the speed ratio compares the velocity of the jet to the velocity of the thermal motion of the gas. Thus, the higher this ratio the fewer gas particles are capable of escaping the jet once they have entered it. Secondly, the sensitivity of the capture coefficient to the compression ratio is strongly dependent on the Péclet number as apparent by comparing 4.2 (a) with (b). At higher Péclet numbers increasing the compression ratio has a negligible effect on the capture coefficient for a wide range of compression ratios. However, once a threshold, which depends on the Péclet number at a given speed ratio, is exceeded, the capture coefficient quickly reduces if the compression ratio is increased further. This threshold corresponds to the point where backdiffusion of gas through the jet becomes comparable to the advective transport, which also explains its dependency on the Péclet number.

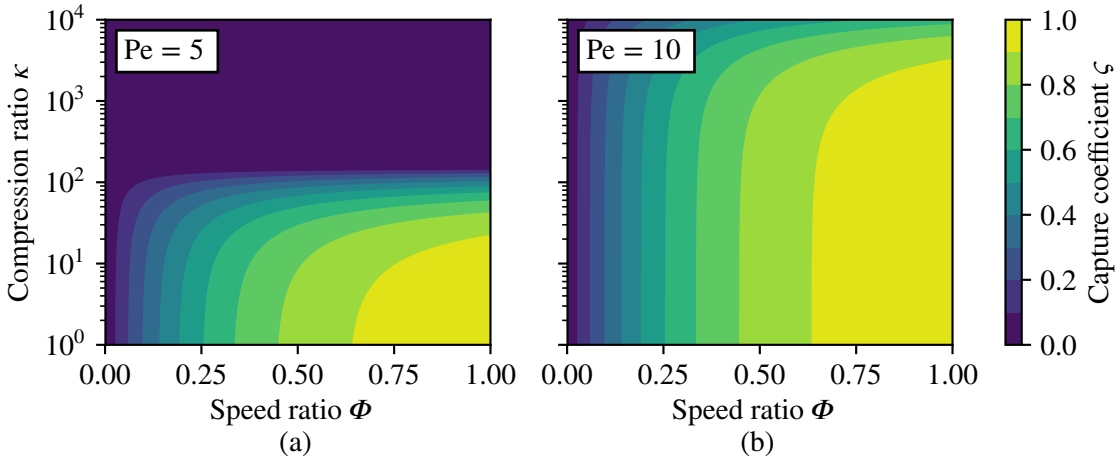

Figure 4.2.: Capture coefficient ς as a function of the speed ratio $\boldsymbol{\Phi}$ and compression ratio κ for Péclet numbers 5 (a) and 10 (b).

4.1.1. Operational range and maximum performance

One of the typical characteristics of diffusion pumps is their plateauing pumping speed over several orders of magnitude of inlet pressures and compression ratios. This occurs if advective transport dominates the opposing diffusive gas transport. Mathematically this is equivalent to re-

quiring Pe $\to \infty$, which implies $\varphi \to \Phi$. In this case Eqs. (4.7) & (4.8) collapse to the simplified, fully analytical expression

$$\varsigma_0 = \left[1 + \frac{1}{2\sqrt{\pi}\Phi}\left[\exp\{-\Phi^2\} - \sqrt{\pi}\Phi\,(1 - \mathrm{erf}\{\Phi\})\right]\right]^{-1}, \tag{4.9}$$

which only depends on the speed ratio Φ between the vapor jet velocity and the thermal speed of the gas. A study of this simplified model has previously been published by the author in [198]. The dependency of the maximum capture coefficient ς_0 on the speed ratio Φ is depicted in Fig. 4.3. The speed ratio is limited to the interval $\Phi \in [0, 1]$ as this is the relevant range for practical applications due to the aforementioned mass ratio between typical pumped gases and the vapor. The capture coefficient approaches zero at small speed ratios. This is physically reasonable as a low speed ratio implies that the jet velocity is negligible compared to the thermal velocity of the gas. At high speed ratios (> 1) the capture coefficient asymptotically approaches its theoretical limit of unity because a large speed ratio indicates that few gas particles have a high enough thermal velocity to escape the jet once they entered it. Equation (4.9) is practically relevant in two ways: Firstly, it provides

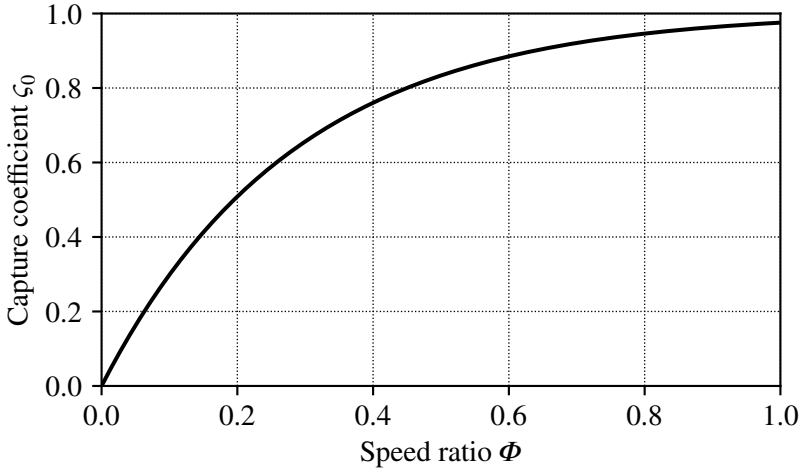

Figure 4.3.: Maximum capture coefficient ς_0 as a function of the speed ratio Φ between the vapor jet velocity and the most probable thermal velocity of the gas.

a theoretical upper limit on the achievable capture coefficient in any given diffusion pump setup. This can, for example, be useful to estimate the required pumping surface. Secondly, it can be used to estimate the capture coefficient of different gases from measurements limited to a single gas species. In that case one can use the experimentally determined capture coefficient $\varsigma_{0,\mathrm{exp}}$ for a given gas species (e.g. air) and Fig. 4.3 to find its speed ratio Φ_{exp}. Subsequently, the speed ratio can be scaled with the square root of the mass ratio, $\sqrt{m/m_{\mathrm{exp}}}$, to read the predicted capture coefficient for a different gas species from Fig. 4.3.

As the model depends on the speed ratio Φ, it is important to understand the underlying physical contributions to it, which are:

- $\propto u_{\mathrm{V}}$,
- $\propto \sqrt{m_{\mathrm{G}}}$ and
- $\propto 1/\sqrt{T_{\mathrm{G}}}$.

The type of gas (determining its molecular mass m_G) as well as the temperature of the vacuum recipient T_G are usually specified parameters in a practical application. Therefore, the jet velocity u_V is the only free parameter that can be adjusted to influence the speed ratio. An upper limit of the jet velocity can be established under the assumption of infinite isentropic expansion leading to Eq. (3.18). For mercury vapor this results in $u_{Hg,max} = 14.4\sqrt{T_{Hg,0}}\,\mathrm{K}^{-0.5}\,\mathrm{m\,s}^{-1}$ as a function of the stagnation temperature $T_{Hg,0}$. Tab. 4.1 lists the upper limits of the capture coefficient for the gases in the Tokamak exhaust mixture for some feasible mercury vapor stagnation temperatures. Due to the non-linear mercury saturation pressure curve [68], the pressures for the three temperature levels vary between 37 Pa and 33 kPa. It can therefore be concluded that the vapor temperature does not have a high influence on the maximum achievable capture coefficient as it varies by less than 16 % even for the lightest species (protium) for which the largest deviation is found. For this reason the tabulated values can be used to approximate a theoretical upper bound for the achievable capture coefficient and the associated efficiency of a given pumping setup.

Table 4.1.: Estimations of the expected upper limit of the diffusion pump capture coefficient for the different species in the exhaust gas mixture for different mercury vapor stagnation temperatures $T_{Hg,0}$ under the assumption of infinite expansion. For reference the corresponding saturated vapor pressures calculated from the correlation in [68] are also given. The temperature of the gas is assumed to be 273.15 K.

	Mercury vapor stagnation temperature $T_{Hg,0}$ (in K)		
	373.15	473.15	573.15
	Mercury vapor saturation pressure $p_{Hg,0}$ (in Pa)		
	37.2	2307	32965
Exhaust gas species	**Maximum capture coefficient ς_0 (Eq. (4.9))**		
Protium H_2	0.482	0.523	0.558
Deuterium D_2	0.606	0.65	0.685
DT	0.647	0.691	0.726
Tritium T_2	0.681	0.724	0.758
Helium	0.605	0.649	0.684
Neon	0.879	0.908	0.929
Argon	0.951	0.967	0.978
Xenon	0.997	0.999	0.999

4.1.2. Maximum compression, ultimate pressure and breakdown

The maximum compression ratio κ_{max} of the diffusion pump is reached when the counteracting advective and diffusive gas transport through the vapor jet are exactly the same, so that the net flow rate reduces to zero. Thus, Eq. (4.6) can be simplified to yield

$$\kappa_{max} = \exp\{\mathrm{Pe}\}\,, \tag{4.10}$$

which agrees with previous models [191, 192]. The technical interpretation of the maximum compression ratio depends on the application: If the pump is operated under negligible load, e.g. during the dwell phase of a Tokamak, the corresponding pressure in the recipient corresponds to the theoretical ultimate pressure that can be achieved. However, if the diffusion pump is operated under

load, e.g. during the burn phase of a Tokamak, it has to be ensured that the actual compression ratio is significantly below the maximum compression ratio so that the pump operates in or close to the plateau. Therefore, in the latter case it is of more use to define a limiting breakdown compression ratio as a function of the ratio ς/ς_0 (e.g. by limiting this ratio to 0.9) and to ensure that the pump is operated below that limit. The practical applicability of Eq. (4.10) is limited because it does not consider the effect of the gas on the vapor jet as well as the interaction with the pump geometry, which are both important during breakdown.

4.2. DSMC model of the pumping process and comparison with the analytical model

A more detailed description of the pumping process including the full vapor gas interaction is possible by means of the DSMC method. Furthermore, a comparison with DSMC results allows verification that the analytical model is able to capture all relevant physical dependencies.

The DSMC model is setup to resemble the one-dimensional model (cf. Fig. 4.1) by using periodic boundary conditions in the other two dimensions. At the inlet ($x = 0$ in Fig. 4.1) gas and mercury particles are injected based on Maxwellian velocity distribution functions. Gas is assumed to enter at zero bulk velocity from an infinite reservoir at number density $n_{\mathrm{G,r}}$ and temperature $T_{\mathrm{G,r}}$. The mercury vapor jet enters with bulk velocity u_{V}, number density n_{V} and temperature T_{V}, which are calculated from the isentropic relationships as described in Sec. 3.3.1. Mercury vapor is assumed to leave at the downstream boundary ($x = L$ in Fig. 4.1) and a sticking coefficient modeling the limited uptake capacity of the backing pump is assumed for the gas. The sticking coefficient corresponds to the chance that a gas particle hitting the downstream boundary is considered to be pumped, whereas gas particles that are not pumped are reflected diffusely. In the operational regime the resulting capture coefficient is independent of both the upstream gas number density $n_{\mathrm{G,r}}$ and the choice of the outlet sticking coefficient over a wide range, which is verified by altering these independently. A more thorough description of the test case setup is available in Appendix A.4.

To scan a sufficient range of the speed ratio Φ in the DSMC model, three different gases (helium, neon and argon), three different gas reservoir temperatures ($T_{\mathrm{G,r}} = 200$, 300 and 400 K) and three different jet speeds ($u_{\mathrm{V}} = 201.6$, 255.2 and 286.0 m s^{-1}) are simulated (see Appendix A.4 for an overview of all cases). The DSMC simulation results are compared to the analytical results of Eq. (4.9) in Fig. 4.4, which depicts the capture coefficient as a function of the speed ratio similar to Fig. 4.3. The curve characteristics of the analytical model have been explained in Sec. 4.1.1. The DSMC results demonstrate the strong species dependency of the mercury vapor jet capture coefficient, especially in the case of light species like helium due to the high thermal velocity. The DSMC and analytical model agree within less than 15 % for all simulated cases. Additionally, both methods agree regarding the qualitative behavior for changes of all three varied parameters (u_{V}, m_{G} and $T_{\mathrm{G,r}}$). The remaining deviation is a result of the conservative estimation of the gas temperature at the jet interface that has been taken during the derivation of the analytical model in Sec. 4.1. The comparison verifies that the analytical model is capturing all relevant aspects of the pumping process. A similar comparison was performed between the analytical, DSMC and two DVM models by the author in [198] but for different input parameters and under the assumption of hard-sphere particle collisions because the employed DVM code is limited to this intermolecular potential. The found qualitative and quantitative agreement is similar to the present work.

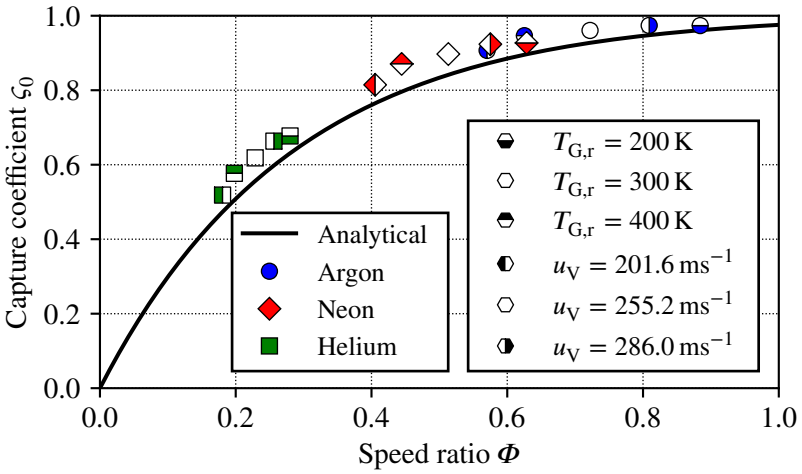

Figure 4.4.: Comparison of the maximum capture coefficient ς_0 as predicted by the analytical model (Eq. (4.9)) with the capture coefficients obtained from the DSMC simulations for different speed ratios Φ.

4.3. DSMC model of the cylindrical NEMESIS diffusion pump

A full description of a diffusion pump requires that the geometry of the pump and boundary interactions are included in the model. Here, a model of simple cylindrical diffusion pump is established and realistic boundary conditions are applied. The axisymmetric geometry of the considered cylindrical pump and the DSMC boundary conditions are shown in Fig. 4.5. The dimensions are chosen similar to the experimental setup *NEMESIS (Nozzle Experiment for Mercury Expansion Investigations)*, which is used to validate the numerical model in the next chapter. The following boundary conditions are chosen at the surfaces indicated in Fig. 4.5:

- ① nozzle throat: Injection of mercury vapor particles according to a shifted Maxwell-Boltzmann distribution function. The nozzle throat corresponds to the critical nozzle cross-section where the flow chokes. Thus, the number density, temperature and speed at the boundary can be estimated from the one-dimensional isentropic relationships by assuming a uniform sonic surface, i.e. with Mach number of unity, at the throat. As the mercury vapor is supplied from a boiler, the stagnation conditions are assumed to be saturated vapor. The saturation curve by Huber et al. [68] is used to determine the saturation conditions. Mercury vapor as well as gas particles colliding with the throat from inside the computational domain are leaving the simulation domain.

- ② nozzle walls: Adiabatic boundary conditions are assumed for all particle collisions with the nozzle walls.

- ③ the boundary condition depends on the operating mode of the pump:

  a) open inlet: This boundary condition represents the case when a vacuum recipient is connected at the top of the diffusion pump. The pressure of the gas is prescribed at this interface. Gas particles are emitted based on a Maxwell-Boltzmann distribution function assuming zero bulk velocity and a temperature of 288.15 K. Gas and mercury particles hitting the interface are removed from the simulation.

  b) closed top flange: This boundary conditions represents the case when no recipient is connected and the top of the diffusion pump is closed by a flange, which resembles the

experimental setup that is discussed in Chap. 5. In this case the boundary conditions is identical to the cooled outer wall ④.

- ④ cooled outer wall: Isothermal boundary conditions for gas and mercury vapor are assumed at a wall temperature of 288.15 K. Gas particles are reflected diffusely with full thermal accommodation. Simultaneous condensation and re-evaporation of mercury at saturation conditions is assumed, i.e. the effective condensation coefficient $\alpha_{c,\mathrm{eff}}$ varies locally as shown in Fig. 3.14.

- ⑤ outlet: Similar to the open inlet ③ a), the pressure of the gas is prescribed and particles are injected according to a Maxwell-Boltzmann distribution function assuming zero bulk velocity and a temperature of 288.15 K. Additionally, colliding gas particles are removed from the simulation domain. Collisions of mercury vapor are treated similarly to the cooled outer wall ④.

- ⑥ symmetry axis: An axisymmetric boundary conditions is assumed here to improve the simulation efficiency by dimensionality reduction.

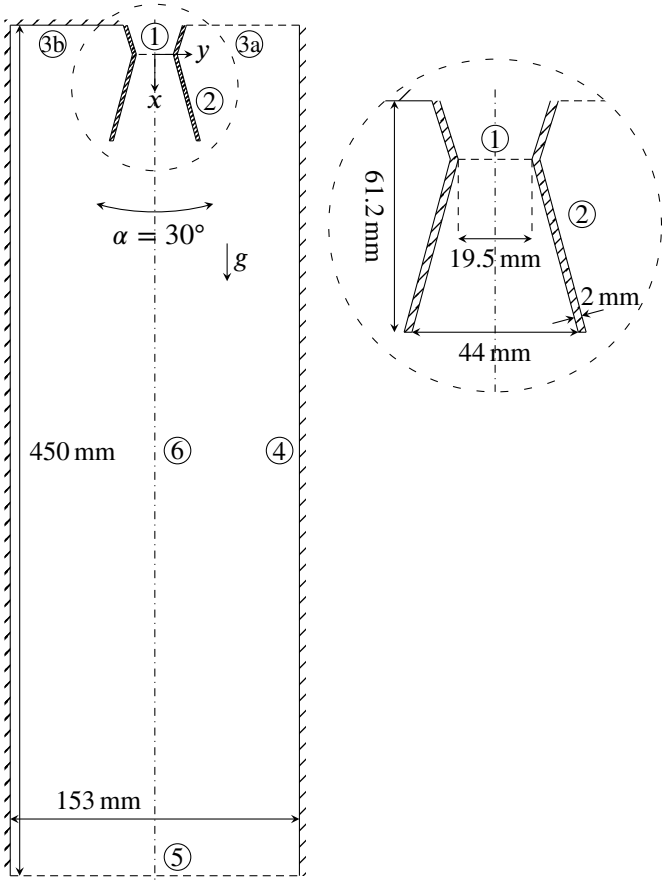

Figure 4.5.: Axisymmetric DSMC model of the cylindrical NEMESIS diffusion pump. The boundaries are labeled: ① nozzle throat (critical cross-section), ② nozzle walls, ③ a) open inlet and b) closed top flange, ④ outer vessel wall (cooled), ⑤ outlet (connection to backing pump), ⑥ symmetry axis. The respective boundary conditions are described in the text.

The axisymmetric DSMC simulations are initially set up with a structured, rectangular grid of

34,650 cells (each 1×1 mm^2). This grid is dynamically refined during the simulation run time based on two criteria: Firstly, the ratio of local mixture mean free path (cf. Eq. (A.20)) to cell size should be within the range 2.9 to 6.1. The correct implementation of this procedure in SPARTA has been verified in a previous publication ([132]) by the author. Secondly, each cell should contain between 14 - 60 simulators concurrently on average to ensure that enough collision partners are present. If a cell is selected for refinement, it is split into four equally sized child cells. Alternatively, if a cell is selected for coarsening (e.g. if it contains too few particles), four child cells are merged to form the new cell. This procedure ensures a good trade-off between grid refinement in regions where the mean free path is small (primarily in and close to the nozzle) and maintaining an acceptable number of simulator particles in cells with low pressure and large mean free paths (e.g. in the space between the top flange and the nozzle that is actively pumped by the mercury vapor jet). The time step is chosen as $\Delta t = 2.5 \times 10^{-8}$ s, which ensures that the mean collisions time is resolved and that particles travel less than one cell per time step on average. Spatial weighting factors proportional to the radius (cf. Sec. 3.5.4) are used to compensate for the change in cell volume due to the axisymmetry of the problem.

The DSMC simulations are started with an empty domain. Hence, a certain number of time steps are required to establish the stationary particle distribution in the system, which is characterized by a stabilized number of simulator particles per species. The attainment of steady-state is sped up by starting with a time step and numerical weight four times higher than the final value and reducing it two times after steady-state is reached for the previous setting. Afterwards, the collection of moment averaging samples is started to facilitate the calculation of the macroscopic quantities of interest. Samples are collected in every time step for 200,000 total time steps.

The DSMC case setup outlined above reflects a balanced compromise between accuracy and efficiency (i.e. computational cost). It has been verified that the solution is independent of the choice of the aforementioned DSMC parameters by comparing with a simulation with smaller time step ($\Delta t = 1 \times 10^{-8}$ s), more particles and a higher grid refinement for representative cases for both boundary condition setups at ③. The comparison reveals, that the standard case setup provides independent results; for more details see Appendix A.5.1. The total error, which consists of a statistical part associated with the limited sample size and systematic part associated with the discretization, can be estimated to be within 2-3 % for the quantities of relevance for both boundary condition setups ③ a) and b).

4.4. Numerical simulation of the NEMESIS diffusion pump performance

The established DSMC model of the cylindrical NEMESIS diffusion pump is used to analyze the numerical pump performance by choosing the open inlet boundary condition (③ a) in Fig. 4.5). Similar to the preceding one-dimensional analyses helium, neon and argon are considered as pumped gas, respectively. The pressures at in- and outlet are prescribed at 0.1 Pa and 0.5 Pa. The similar choice of the boundary conditions facilitates the comparison of the predicted performance with the simple models of the pumping process to quantify the impact of the pump geometry and operating conditions.

4.4.1. Vapor expansion and speed ratio

As the DSMC simulations include the interactions of the vapor and gas with the pump structures a detailed flow field can be extracted. The distribution of the speed ratio Φ, which is calculated as the local ratio of the vapor jet speed in x-direction (downward) and the thermal velocity of the respective gas at inlet temperature (288.15 K), is depicted in Fig. 4.6. The vapor flow is in

an underexpanded state when leaving the nozzle, which results in the observed over-divergent expansion at the nozzle outlet. As the vapor stagnation conditions are the same in all three cases, the speed ratio deviations are determined solely by the thermal velocity of the gas species (i.e. its molecular mass). Furthermore, it is clear that the assumption of a uniform vapor gas interface (as done in the aforementioned one-dimensional models) does not correspond to the real situation in a diffusion pump. Firstly, the jet direction is not uniform in radial direction as an effect of the expansion and condensation at the outer walls. Secondly, the vapor jet requires a certain axial distance to expand to the entire cross-section of the pump body. A first approximation of this axial distance is given by the intersection of the prolongation of the nozzle skirt with the outer pump wall, which is at $x = 249\,\mathrm{mm}$.

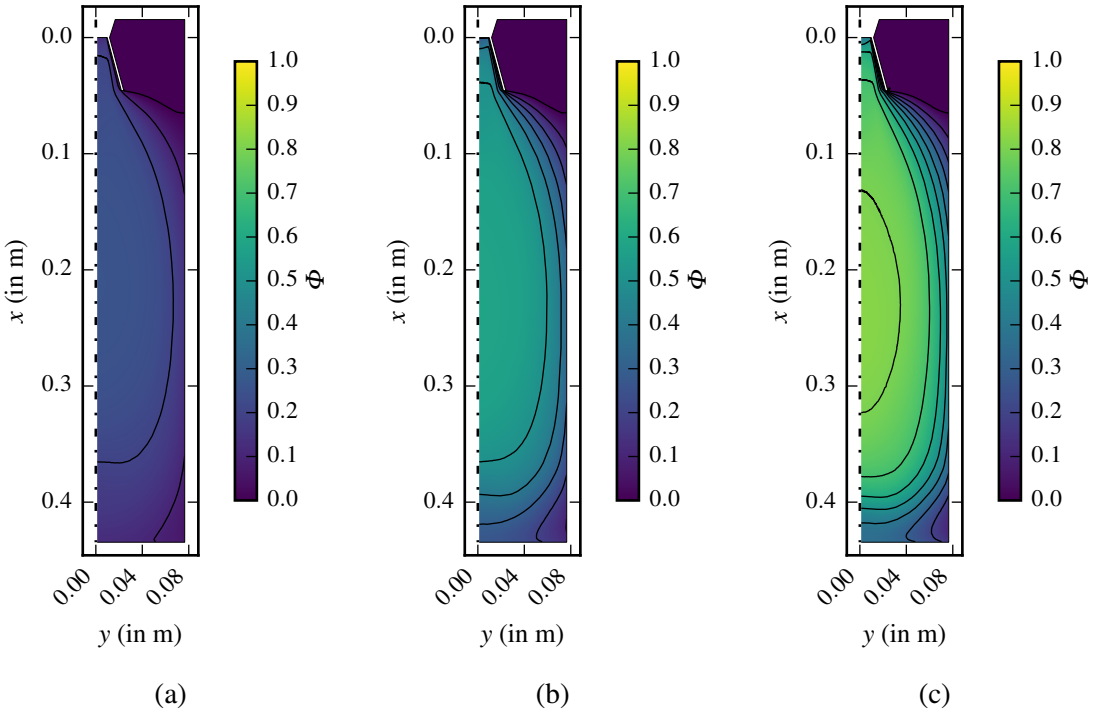

Figure 4.6.: Axisymmetric DSMC simulations of the speed ratio Φ in the NEMESIS diffusion pump. The mercury stagnation temperature for the displayed cases is $T_0 = 403.15\,\mathrm{K}$. Helium (a), neon (b) and argon (c) are considered as the pumped gas.

The area-averaged speed ratios $\bar{\Phi}$ at this position are summarized in Tab. 4.2 for the considered gas species and for four different vapor stagnation conditions. A positive monotonic relationship is observed between the average speed ratio and the vapor stagnation temperature and its related saturation pressure. As the temperature of the gas at the pump inlet is constant, this implies that the average jet speed in x-direction increases as expected from the theoretical estimation via the isentropic relationship (Eq. (3.17)).

4.4.2. Pumping speed and capture coefficient

The capture coefficient ς is calculated according to Eq. (4.1) by calculating the pumped flux of gas particles in the DSMC simulation and scaling it with the equilibrium molecular flux at the inlet boundary conditions (0.1 Pa and 288.15 K). The associated pumping speed is given by

$$S = \frac{1}{4} A_{\mathrm{inlet}} \bar{v}_{\mathrm{gas,inlet}} \varsigma, \tag{4.11}$$

Table 4.2.: Area-averaged speed ratio $\bar{\Phi}$ calculated at $x = 249$ mm for different pumped gas species and mercury vapor stagnation conditions ($T_{\mathrm{Hg},0}$, $p_{\mathrm{Hg},0}$).

	Mercury vapor stagnation temperature $T_{\mathrm{Hg},0}$ (in K)			
	393.15	398.15	403.15	408.15
	Mercury vapor saturation pressure $p_{\mathrm{Hg},0}$ (in Pa)			
	100.9	127.4	159.9	199.6
Gas species	**Average speed ratio $\bar{\Phi}$ at $x = 249$ mm**			
Helium	0.186	0.206	0.222	0.233
Neon	0.437	0.475	0.503	0.524
Argon	0.622	0.671	0.708	0.737

where the mean thermal speed of the gas $\bar{v}_{\mathrm{gas,inlet}}$ is calculated at the inlet temperature 288.15 K.

Figure 4.7 depicts the pumping speed and capture coefficient as functions of the area-averaged speed ratio as determined in the previous section. The pumping speed and capture coefficient are found to be nearly independent of the speed ratio for neon and argon. Only for the substantially lighter helium a significant sensitivity towards the speed ratio is observed. The capture coefficient is generally found to be much lower than that predicted by the one-dimensional model (Eq. (4.9)) of the pumping process at the same speed ratio. This has two physical reasons: Firstly, the capture coefficient of the pump is reduced due to the limited conductance between the inlet of the pump and the actual pumping interface formed by the expanding vapor jet. Gas particles in this region can collide with the nozzle or outer walls of the pump and thus have a chance to be reflected. This effect is fully independent of the vapor jet, which explains why the capture coefficient does not approach unity for high speed ratios but plateaus at a value below 0.4. Secondly, the area-averaged speed ratio does not account for the non-uniform distribution of the gas in the jet. As the gas enters at the edges of the jet, the gas concentration is small in the core of the jet (close to the x-axis) where the speed ratio is highest. Therefore, the area-average speed ratio overestimates the actual speed ratio.

4.4.3. Efficient model-based design of diffusion pumps

The models that have been developed and analyzed in the present chapter open the way toward a model-based design of diffusion pumps for specific applications. The analytical model of the pumping process has been verified to be accurate within 15 % over a wide range of speed ratios by a model to model comparison with the DSMC model that reflects the physical behavior of the vapor gas interaction driving the pumping process. Subsequently, a DSMC model describing the entire pump is established for the example of the NEMESIS diffusion pump. The comparison with the simpler models, which focus on the pumping process, emphasizes that these can only provide upper limits but overestimate the obtainable performance.

Therefore, the models have different application scopes. On the one hand, the analytical model provides a fast estimation of the theoretical limit of the achievable capture coefficient, which can be used as a reference to determine and compare the efficiencies of diffusion pump designs. Additionally, it provides insight into the expected performance impact of operating conditions changes like vapor superheating. On the other hand, the detailed DSMC pump model allows for a more accurate prediction of the capture coefficient and the other performance indicators as they are affected by the pump geometry. The validation of this model is performed in the next chapter with experimental measurements in the NEMESIS setup.

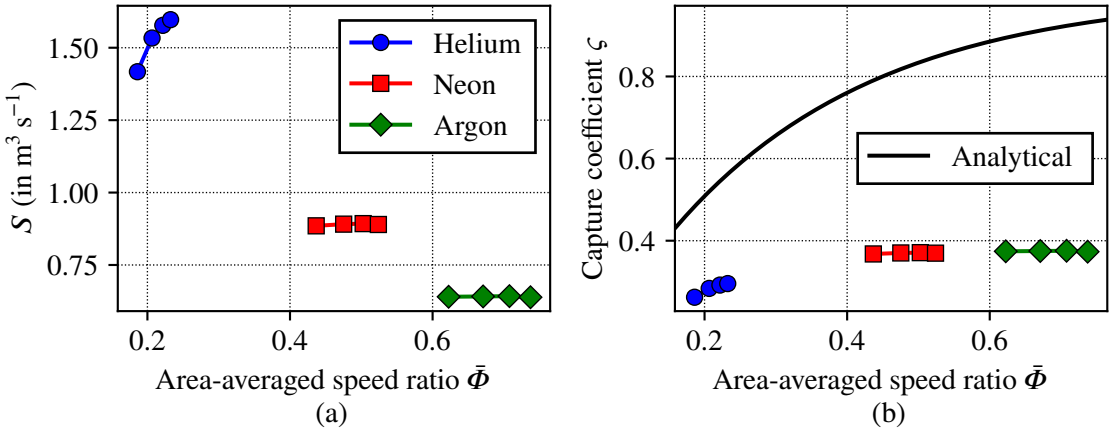

Figure 4.7.: (a) Pumping speed S and (b) capture coefficient ς as functions of the area-averaged speed ratio $\bar{\Phi}$ for helium, neon and argon and for different mercury vapor stagnation conditions. Simulation results are indicated by the symbols and connected with straight lines to guide the eye. For comparison, the capture coefficient as predicted by the analytical model (Eq. (4.9)) is included.

As the simulations with the detailed DSMC pump model are computationally expensive an efficient workflow combines both methods by using the analytical model to inter- and extrapolate the simulation results of the DSMC pump model. It is demonstrated later in Chap. 7 that detailed simulations of a single pumped species are sufficient to extrapolate to all species in the exhaust gas mixture with acceptable precision using the analytical model.

5. NEMESIS mercury vapor experiment and validation of numerical model

There is a lack of modern experimental results in the literature that can be used to validate numerical tools describing mercury-driven diffusion pumps. Thus, an extensive experimental program is necessary to further develop diffusion pumps for torus exhaust pumping. The first step in this program is the *Nozzle Experiment for Mercury Expansion Investigations (NEMESIS)*, whose conceptualization, assembly and operation is part of the present work and is discussed in this chapter. Furthermore, a validation of the numerical DSMC pump model, which has been introduced in the last chapter, is performed.[1]

5.1. Description of the experimental setup, sensors and measurement uncertainty

The design of the experimental setup is inspired by previous experiments focused on studying diffusion or ejector pump jets, especially the ones performed by Dayton [48] (mercury and oil), Nöller [87] (mercury) and Kutscher [200] (oil ejector). The measurement region of NEMESIS resembles a mercury-driven cylindrical diffusion pump of the Langmuir type, however no recipient is connected to this pump. Three diffusion pump aspects are analyzed:

- The mercury vapor pressure distribution in the expanding vapor jet,
- its mass flow rate and
- its fore-vacuum tolerance.

Figure 5.1 shows a photograph of the NEMESIS experiment as assembled and operated in one of the fume hoods of the HgLab Karlsruhe at KIT (for an introduction to the HgLab infrastructure see [201]). As several of the key components are insulated a CAD drawing is also included showing the components without the insulation. A process flow diagram of NEMESIS depicting all main components and important sensors is displayed in Fig. 5.2.

Firstly, the auxiliary systems are described: Vacuum is generated in the experiment by a two-stage pumping system. The primary stage is an off-the-shelve cylindrical oil diffusion pump (⑥ / purple) with a nominal pumping speed of $0.8\,\mathrm{m^3\,s^{-1}}$ (for air) by *HSR AG*. The diffusion pump is operated with ca. 200 mL of *Santovac 5* (pentaphenylether) as operating fluid. The cooling water is supplied from the HgLab circuit at approximately 10 °C. This pump is backed by a rotary vane pump (⑦ / orange) with a nominal pumping speed of ca. $6\,\mathrm{m^3\,h^{-1}}$ by *vacuubrand GmbH & Co. KG*. The pumping train is connected to the experiment via a high vacuum angle valve (V01, ⑤ / blue) with a nominal free-molecular conductance of $1\,\mathrm{m^3\,s^{-1}}$ by *VAT AG*. Additionally, a bypass with a smaller valve (V03) is installed that allows to pump only with the backing pump. Another similar small valve (V02) can be used to disconnect the diffusion pump from the backing pump.

[1] Parts of the present chapter are included in an accepted manuscript [199] by the author. The description and discussion in this chapter include more details. Additionally, the numerical model uses the more sophisticated condensation boundary condition introduced in Sec. 3.5.5, whereas perfect condensation is assumed in [199].

This is for example necessary when pumping down the experiment from ambient pressure. The pumping system and the main experimental vessel are separated by an opaque angle baffle (④ / green) with a nominal free-molecular conductance of 0.8 $m^3\ s^{-1}$ (for air) by *HSR AG*. The internal baffle structures are cooled by a thermostat by *Huber Kältemaschinenbau AG* using a silicone-based heat transfer fluid *Thermal HL60* by *JULABO GmbH* in a closed circuit.

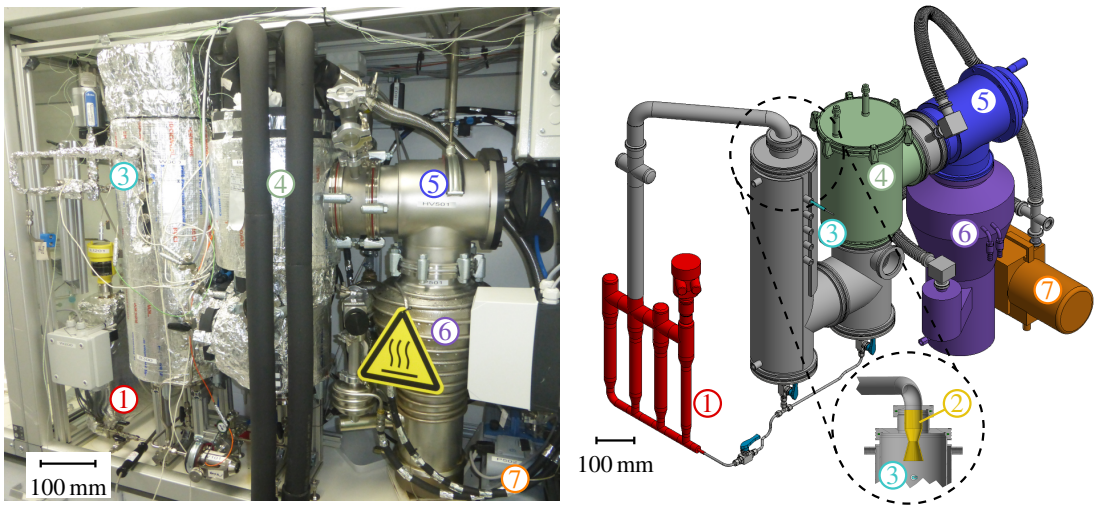

(a) (b)

Figure 5.1.: (a) Photograph of the NEMESIS setup in the HgLab fume hood. (b) CAD drawing of NEMESIS providing a better view of the insulated parts. Additionally, a cut through the upper part of the test vessel showing the nozzle is displayed at the bottom. The major components are numbered and colored in the drawing: ① / red: mercury boiler, ② / yellow: nozzle, ③ / teal: axial pressure probe and five installation ports (probe is installed in top port here), ④ / green: angle baffle, ⑤ / blue: high vacuum valve, ⑥ / purple: oil diffusion pump, ⑦ / orange: rotary vane backing pump.

The main experiment is comprised of three functional components: Liquid mercury is evaporated in a custom designed boiler (① / red) manufactured in the KIT workshop. This boiler features four vertical pipes. Three of these feature identical dimensions and are fitted with two heating sleeves each (nominal power of 205 W, total 1230 W) by *TC Mess- und Regeltechnik GmbH*. The mercury vapor is then guided through a riser pipe towards the circular nozzle (② / yellow, custom design manufactured in the KIT workshop), where it is expanded into the NEMESIS main vessel, which is cylindrical with an inner diameter of 153 mm. The converging-diverging nozzle features a critical cross-section of 19.5 mm diameter and an outlet cross-section of 44 mm diameter (area ratio of 5.1). The converging and diverging nozzle parts have angles of 35° and 30°, respectively. The axial pressure distribution is measured using a pressure probe (③ / teal) that can be installed at five different axial positions (in Fig. 5.1 the probe is shown in the top position). To facilitate the condensation of mercury vapor striking the walls of the main vessel, it features two welded on cooling jackets, which are supplied with cooling water from the HgLab circuit similar to the oil diffusion pump. Furthermore, two cooling coils are wound around the connection between the NEMESIS main vessel and the side vessel below the baffle. The side vessel features two large sight glasses on the front and back that allow a view inside the lower part of the baffle. Both, the main and the side vessel, have drain lines for the mercury condensate at the bottom. To simplify the mercury draining the two bottom flanges were tapered in the KIT workshop. The mercury return line between the two vessels and the boiler features three valves (V04, V05 and V06) that allow to

control the condensate return flow. Gas can be dosed in at the top of the main vessel from a gas bottle with pressure reducer through a fine valve (V07) and subsequent 0.1 mm orifice.

The experiment is equipped with several sensors, the measurement position of which is indicated in Fig. 5.2. A detailed explanation of the underlying technologies of the sensors and data acquisition system are omitted here for brevity and are available in Appendix A.6.1. In the mercury boiler the temperature of the liquid mercury is measured by the *Pt100 resistance temperature detector (RTD)* TI01. In addition, the liquid level of mercury is measured using a *guided wave radar sensor* LI01. The measured liquid level is converted to a volume by a calibration curve that has been recorded using water (cf. Appendix A.6.2). This allows to calculate the liquid mercury mass by means of the temperature-dependent density correlation (valid between -20-300 °C) from [202]. The temperature of the produced mercury vapor is measured in the riser pipe between boiler and nozzle by RTD TI02. Additionally, the temperature of the outer wall of this pipe is measured close to the nozzle by a contact *thermocouple (TC)* TI03. Inside the test vessel the pressure is recorded by capacitance pressure transducers above (PI01) and below (PI02) the mercury vapor jet. Furthermore, a pressure probe can be inserted into the mercury vapor jet at five different axial positions. The pressure probe is connected in parallel to two capacitance pressure transducers PI03 and PI04 with different measurement ranges. The temperature of the pressure probe inside the vacuum vessel as well as the connection line to the transducers outside the vacuum vessel are temperature controlled by two thermocouples TI04 and TI05 that control heating wires. All capacitance pressure transducers (PI01-PI04) feature an internal automatic temperature control to 100 °C.

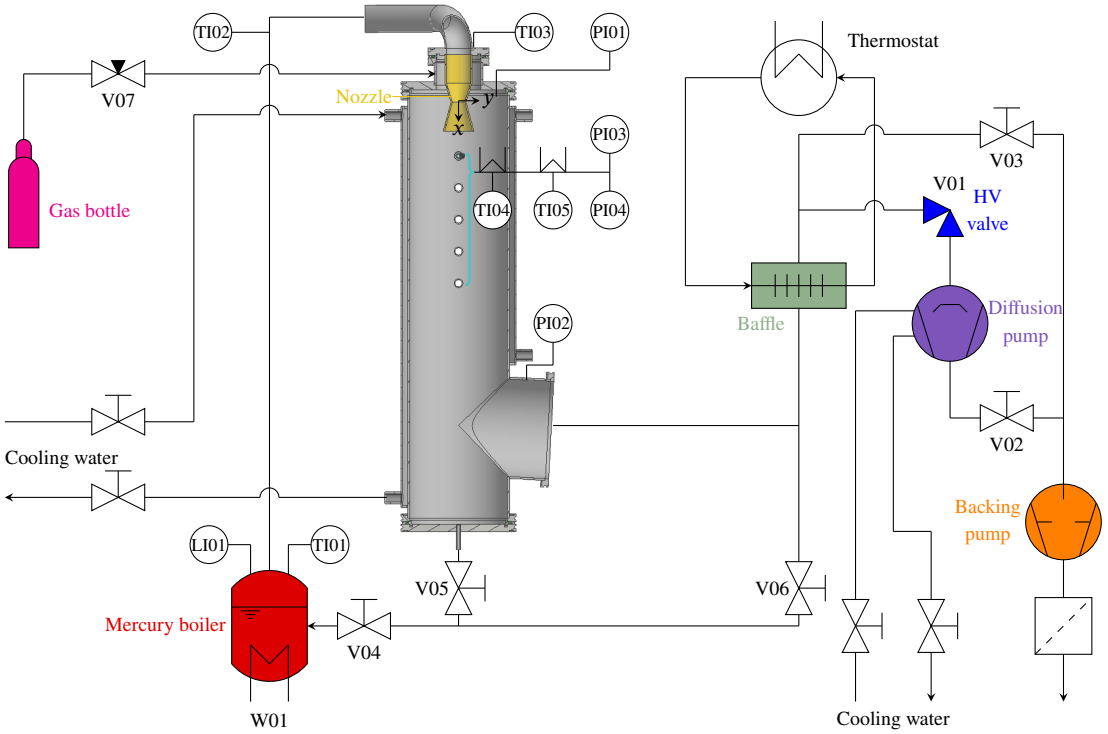

Figure 5.2.: Schematic process flow diagram of the NEMESIS experiment featuring the main components (colored similar to Fig. 5.1) and sensors. The test vessel with the mercury nozzle is shown as a detailed CAD sectional view to better convey the sensor measurement positions.

The uncertainties of the measured quantities are estimated as *Type B* uncertainties as detailed in section 4.3 in the *Guide to the expression of uncertainty in measurement* [203]. This includes

all uncertainties in the measurement chain from sensor to data acquisition system. The tabulated uncertainties of all components and more details on the estimation of the combined uncertainty of the respective measurement chains are given in Appendix A.6.3. Here, an overview of the combined measurement uncertainties for all sensors is provided in Tab. 5.1 for representative lower and upper values. The pressure transducers exhibit the highest relative uncertainties close to their respective lower measurement range. Furthermore, the boiler volume and mass are found to have relatively high uncertainties, the reason for this mainly being the limited accuracy of the highly non-linear calibration curve (cf. Appendix A.6.2).

Table 5.1.: Overview of the estimated combined measurement uncertainties for representative upper and lower values.

ID	**Value ± uncertainty (relative in %)**	
	Lower range	Upper range
Pressures		
PI01	0.01 ± 0.0014 Pa (14)	10 ± 0.04 Pa (0.4)
PI02	0.01 ± 0.0014 Pa (14)	10 ± 0.04 Pa (0.4)
PI03	0.01 ± 0.0014 Pa (14)	10 ± 0.04 Pa (0.4)
PI04	0.5 ± 0.14 Pa (27)	1000 ± 2 Pa (0.2)
Temperatures[1]		
TI01	0 ± 0.3 °C (0.11)	250 ± 1.6 °C (0.3)
TI02	0 ± 0.3 °C (0.11)	150 ± 1.1 °C (0.25)
TI03	0 ± 3 °C (1.1)	150 ± 3 °C (0.71)
TI04	0 ± 3.1 °C (1.1)	150 ± 3.1 °C (0.74)
TI05	0 ± 3.1 °C (1.1)	150 ± 3.1 °C (0.74)
Boiler liquid level, volume and mass		
LI01	30 ± 0.13 % (0.44)	60 ± 0.15 % (0.24)
Volume	187.2 ± 2.2 mL (1.2)	421 ± 4 mL (1)
Mass @ 0 °C	2545 ± 30 g (1.2)	5730 ± 60 g (1)
Mass @ 250 °C	2433 ± 28 g (1.2)	5470 ± 60 g (1)

[1]Relative uncertainty of temperatures is calculated in K.

5.2. Description of the measurements

A representative experiment in NEMESIS is depicted in Fig. 5.3. In stand-by state the two cooling water loops of NEMESIS (for both test vessel and oil diffusion pump) as well as the cooling loop of the baffle are active. Additionally, the oil diffusion pump is used to maintain a low base pressure in the region of 0.1 Pa in the experimental vessel. An experiment is initiated by activating the mercury boiler at the chosen power level. It then takes approximately 120 to 180 min to obtain steady-state in the experiment, as the connection pipe between the boiler and the nozzle and the nozzle itself have to heat up to operating temperature. Steady-state is assumed to be achieved once the temperature indicated by the thermocouple TI03, that is located closest to the nozzle shows a plateau. After the start-up phase, the experimental phase is started. Usually, three experiments are

performed in this phase:

- First the steady-state static pressure in the jet is recorded via the pressure probe that is connected to transducers PI03 and PI04 (cf. Sec. 5.2.1).
- Afterwards, the fore-vacuum tolerance is analyzed by closing the high vacuum valve V01 and comparing the pressure rise above (PI01) and below (PI02) the mercury vapor jet (cf. Secs. 5.2.2 and 5.2.3).
- Finally, the mercury mass flow rate is determined by closing the condensate return valve V04 between the vessels and the boiler and recording the decrease of the liquid mercury volume in the boiler (cf. Sec. 5.2.4).

Subsequently, the next experiment is initiated by adjusting the boiler power. Since all structures are already hot the next steady-state is reached faster (approximately 90 to 120 min). Afterwards, the three experiments are repeated for the new boiler power. Due to the waiting periods necessary to achieve steady-state at most three boiler powers have been investigated consecutively without switching off the boiler and cooling down the setup. For the example shown in Fig. 5.3 the boiler power has been set to the highest value at the beginning and then reduced in two steps. This is reflected in the change of the plateaus of the static pressure measured in the jet (PI03 & PI04) and the vapor temperature (TI02 & TI03). Finally, the mercury boiler is deactivated, and the setup cools down. As cool-down takes several hours, only the beginning of the process is shown in Fig. 5.3.

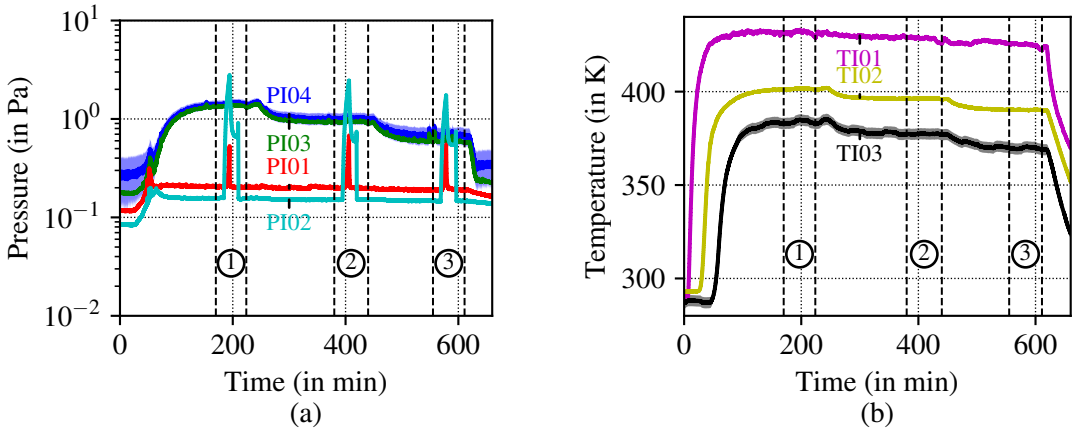

Figure 5.3.: Readings of pressure (a) and temperature (b) sensors during a representative series of three experiments in NEMESIS. The time spans in which the experiments are performed at the three boiler powers are indicated by the dashed lines and circled numbers. The experimental procedures are explained in the text.

In total four boiler powers (184.5, 215.25, 246.0 and 307.5 W) have been investigated in the present work. This choice represents a compromise between covering a wide power range and performing multiple measurements at the same boiler power to determine the repeatability.

5.2.1. Axial pressure distribution in the mercury vapor jet

The NEMESIS test vessel contains five axial measurement ports for inserting a pressure probe into the mercury vapor jet. These ports are visible in Fig. 5.1. In the photograph and CAD the

pressure probe ③ is installed in the top position (closest to the nozzle). The pressure probe is custom-designed and has been manufactured by the KIT workshop. A photograph of the probe is depicted in Fig. 5.4 (a) and the important components are indicated. Furthermore, the mounting position of the probe in the top port is shown in the CAD sketch in Fig. 5.4 (b). The probe consists of an inner 3×0.7mm pipe that is surrounded by an 8×1mm cladding tube. A heating wire is installed in the annular gap formed between the pipe and the cladding tube. Furthermore, the thermocouple TI04 is also installed in the annular gap close to the tip of the probe as indicated in Fig. 5.4 (a) and has been used to control the temperature of the inner pipe. The screw connector is used to install the probe in one of the five axial measurement ports of the test vessel. The fitting is installed so that the probe tip lies on the vertical axis of the main chamber (the associated uncertainty is estimated to ±2 mm, cf. Tab. A.7). The fitting can be untightened to control the rotation of the probe tip using the welded flag on the left side, which is outside the test vessel, as an indicator. On the outside (left in Fig. 5.4) the inner 3 × 0.7mm coaxial pipe is connected to two pressure transducers (PI03 and PI04). This connection line (visible in Fig. 5.1) is also temperature controlled using a heating wire wound around the pipe and a thermocouple (TI05). Heating the pressure probe is necessary to prevent mercury condensation inside the pipe. The temperature control for the heaters has been set to 120 °C at TI04 for the part inside the test vessel and 100 °C at TI05 for the connection pipe outside the test vessel (similar to the internal heating of the pressure transducers PI03 and PI04).

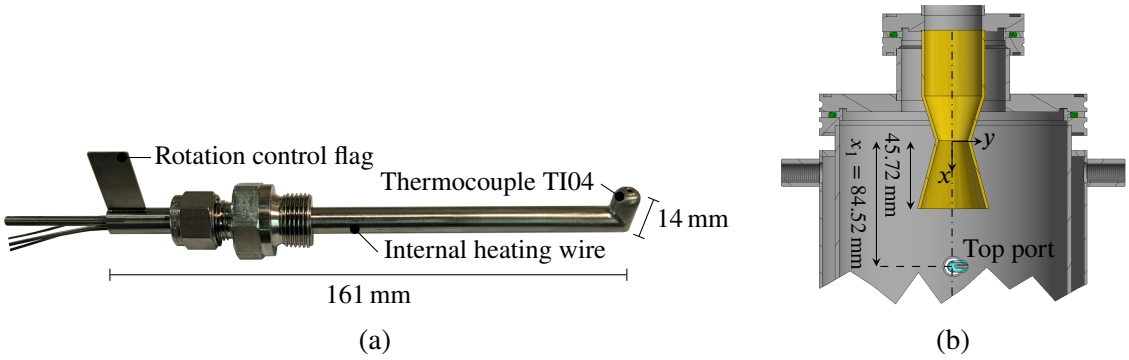

Figure 5.4.: (a) Photograph of the pressure probe used during the axial pressure measurements. (b) CAD sketch of the upper part of the test vessel showing the installation position of the pressure probe in the top port and its distance $x_1 = 84.52\,\text{mm}$ to the nozzle throat. The ports are spaced 50 mm apart from each other in x-direction, i.e. $x_n = x_1 + (n-1) \cdot 50\,\text{mm}$.

Originally, it was planned to perform measurements of the Rayleigh-Pitot pressure, similar to the measurements of Kutscher [200] for oil-driven vapor ejectors. This pressure can be measured in supersonic flows if the probe is installed so that the aperture faces the jet directly. However, even with several iterations it has been impossible to perform reliable measurements, as the sensors (PI03 and PI04) have only shown a constant pressure approximately corresponding to the mercury saturation pressure at the heating temperature of the connection line (100 °C). This indicates that liquid mercury entered the pressure probe. Further evidence to confirm this assessment is the change of the constant pressure indicated by the sensors when the temperature has been increased and decreased. The hypothesis is therefore that liquid mercury entering the probe evaporates due to it being actively heated, thus explaining the saturation pressure indicated by the pressure transducers. Two plausible explanations have been identified: Either the flow is two-phase during operation or condensate collects in the sensor during the warm-up and cool-down phases of the experiment. Later comparison with the simulation results lead to the conclusion that the flow is most likely slightly two-phase due to condensation in the connection pipe between boiler and nozzle. Due to

the high density of liquid mercury even a small volumetric liquid fraction not impairing the vapor flow is enough to impair the pressure probe measurement principle. For this reason only static pressure measurements have been performed.

The same pressure probe is used in the static pressure measurements. However, the probe is rotated by 90° so that there is no direct line of sight between the aperture and the vapor jet as shown in Fig. 5.4 (b). In this configuration no issues with condensed mercury have been detected. Moreover, it has also been confirmed that changing the temperature control of the probe heaters does not influence the indicated pressure significantly. Experiments have been performed at four different boiler powers (184.5, 215.25, 246.0 and 307.5 W) and for the upper three axial positions (cf. Fig. 5.4 (b): $x_1 = 84.52\,\text{mm}$, $x_2 = 134.52\,\text{mm}$ and $x_3 = 184.52\,\text{mm}$). The static pressure is recorded once steady-state is achieved. A full account of all performed static pressure measurements at the different boiler powers and probe positions is available in Tab. A.8 in Appendix A.6.4. Comparison of the sensor readings of PI03 and PI04 confirms that they agree within uncertainty for all measured static pressures. For this reason, only the readings of PI03 are shown in Fig. 5.5 as a function of the axial coordinate to improve the readability. First, focusing on the influence of the boiler power at fixed probe position, it can be seen that the static pressure increases with increasing boiler power. This is also expected from the theoretical consideration of the isentropic vapor expansion at higher stagnation conditions. Secondly, by comparing measurements at the same boiler power but different axial positions, it is evident that the static pressure decreases non-linear if the distance to the nozzle is increased as expected from an expanding flow. Furthermore, it is noticeable that the static pressures at different boiler powers start to converge for axial positions located further from the nozzle. The converged pressures of about 0.3 Pa correspond to the saturation pressure of mercury at around 28 °C. In case of the lowest boiler power (184.5 W), a small increase is observed between 134.52 and 184.52 mm. This could either be a result of a deceleration of the vapor jet which increases pressure and temperature or a measurement outlier because both values are single determinations. With regard to the latter, a comparison of experiments performed under

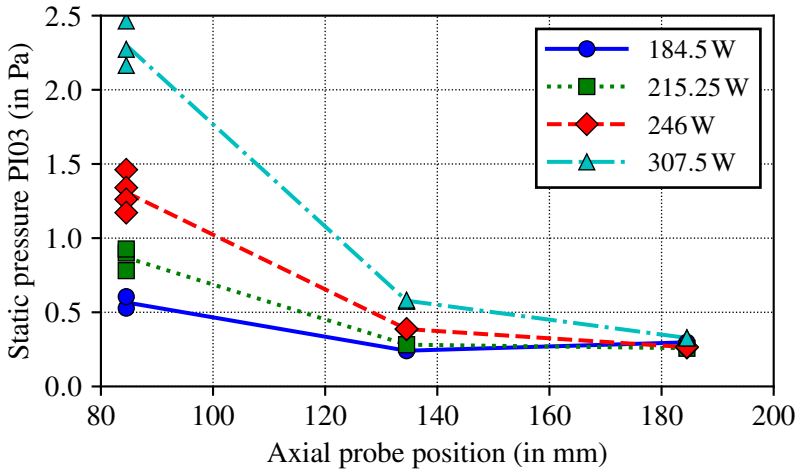

Figure 5.5.: Measured static pressure as indicated by PI03 (symbols) as a function of the axial coordinate x at four different boiler powers. Straight lines connect the averages of the measurements at the respective axial coordinate and power as a visual aid. Error bars are omitted because they are smaller than the symbols.

similar conditions reveals that the repeatability typically lies in the order of approximately 10-20 %. This extends the uncertainties of the pressure transducers significantly (especially PI03, which has a higher resolution in the relevant pressure range). One plausible reason for these deviations is a

strong sensitivity toward the level of liquid mercury in the boiler, which changes slightly between the experiments as mercury collects in undercuts and the baffle and is therefore not recycled completely which made refills necessary. Other reasons are changes in ambient conditions during the experiments, which causes a change of the heat losses in the boiler, riser pipe and connection to the vessel. Additionally, it has been tested how sensitive the readings of the probe are with regard to rotation around its longitudinal axis, which is determined during installation of the probe by eye using the control flag shown in Fig. 5.4 (a), by rotating the probe by 180°. The observed pressure changes in reading in Tab. A.8 confirm that the probe is sensitive to the rotation but that the indicated pressure remained in the same order of magnitude as the standard repeatability.

5.2.2. Fore-vacuum tolerance

In NEMESIS the fore-vacuum tolerance is determined by closing the high vacuum valve V01 while the mercury vapor jet is active in steady-state. Due to constant leakage of environmental air into the experiment (order of magnitude of 1×10^{-4} Pa m^3 s^{-1}) the pressure in the experiment starts to increase. The main source of leakage is located at the screw connection of the immersion sleeve housing the RTD TI02 to the connection pipe between boiler and nozzle. Due to the pumping action of the mercury vapor jet the pressure first only rises downstream of the jet (PI02), while the pressure measured upstream of the jet (PI01) remains constant. However, if a certain fore-vacuum pressure - the *fore-vacuum tolerance* - is exceeded the pressure upstream also starts to increase. For the measurements in NEMESIS a procedure similar to the standardized procedure laid out in the diffusion pump norm [204] is followed, which defines the fore-vacuum tolerance as the point where the rate of pressure increase on the high vacuum side reaches 10 % of that on the fore-vacuum side, i.e. the condition

$$p_{\mathrm{FT}} \equiv p_{\mathrm{FV}} \left(\frac{\mathrm{d}p_{\mathrm{HV}}}{\mathrm{d}p_{\mathrm{FV}}} = 0.1 \right). \tag{5.1}$$

An exemplary experiment is depicted in Fig. 5.6. Figure 5.6 (a) shows the pressure evolution during the experiment. The pressure on the fore-vacuum side starts to rise immediately after the valve V01 is closed. It can be seen that the pressure rise is approximately linear which corresponds to a constant leakage rate. A period of approximately 10 min follows where the high vacuum pressure remains at a constant level. Afterwards, the high vacuum pressure starts to increase, indicating the beginning of breakdown. After waiting approximately 3 min until the high vacuum pressure increases to approximately 0.4 Pa the valve V03 to the backing pump is opened to reduce the pressure in the experiment without overloading the oil-diffusion pump. When the pressure is low enough, V03 is closed and V01 opened. It can be seen that the same constant base pressure levels for both high and fore-vacuum are recovered as before the experiment. The observed base pressures around 0.15 to 0.2 Pa are likely a result of the steady evaporation of small mercury droplets that collect in undercuts during and between experiments and for a smaller part due to outgassing. The former effect has been confirmed to be dominant by dry ice cooling parts of the connection line of PI01 during some experiments which decreased the base pressure substantially. The indicated base pressure of PI01 (high vacuum) is consistently slightly higher than that of PI02 (fore-vacuum) which correlates well with the expected temperatures of the vessel and connections close to the respective transducers (hotter close to PI01, cooler close to PI02). Figure 5.6 (b) visualizes the determination of the fore-vacuum tolerance. Due to the noise in the experimental data it is necessary to first smooth the data before the derivative according to Eq. (5.1) can be computed reliably. In the present work this has been achieved by applying a Savitzky-Golay filter [205] to the data. This filter works by locally fitting polynomials (here of 5$^{\mathrm{th}}$ order) over a moving symmetric time window (here 120 s). The resulting smooth approximation, which essentially resembles a low-pass filter, of the experimental data is also depicted in Fig. 5.6 (b).

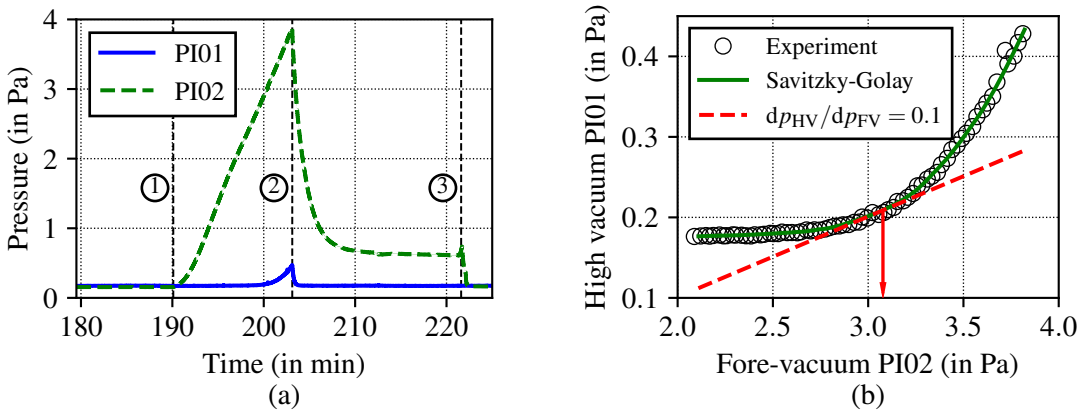

Figure 5.6.: (a) Temporal evolution of the high vacuum (PI01) and fore-vacuum pressures (PI02). The respective timings of manual valve actuations are indicated by the labeled dashed lines: ① close V01, ② open V03, ③ close V03 and open V01. (b) Variation of the high vacuum pressure (PI01) as a function the fore-vacuum pressure (PI02). Error bars are omitted because they are smaller than the symbols. Additionally, only every 10^{th} experimental point (acquisition rate 2 Hz) is drawn to improve the readability. The green line corresponds to the smoothed curve generated by applying the Savitzky-Golay filter. The dashed red line and arrow demonstrate the graphical determination of the fore-vacuum tolerance.

The fore-vacuum tolerance has been determined in NEMESIS for different boiler powers and with and without the pressure probe, which has been used to measure the static pressure. The results are depicted in Fig. 5.7 as a function of the boiler power. Similar to previous reports, see e.g. [45, 206], the fore-vacuum tolerance is found to be approximately linearly dependent on the boiler power. Moreover, it is evident, that the pressure probe affects the fore-vacuum tolerance. The closer the probe is installed to the nozzle, the lower the achievable fore-vacuum tolerance. This is expected because the probe disturbs the expansion of the supersonic vapor jet, which in turn leads to a reduced fore-vacuum tolerance. Only the data without installed pressure probe is relevant for comparison with the simulation and for designing an actual diffusion pump. That is why, for brevity only the fore-vacuum tolerances without pressure probe are documented in Tab. 5.2. As supplementary information the base pressure levels for both the high vacuum region (PI01) and the fore-vacuum region (PI02) are also provided. In terms of the order of magnitude these results are in good agreement with the operating characteristics reported by Langmuir, who claims that his pump that uses a straight nozzle with 22.2 mm diameter (close to the 19.5 mm diameter of the critical cross-section of the converging-diverging nozzle used in NEMESIS) started to operate at about 220 W and that an increase of the power input to 550 W changed the acceptable fore-vacuum from 5 Pa to 80 Pa [38].

5.2.3. Fore-vacuum tolerance for different gas species

Besides the determination of the fore-vacuum tolerance for air that have been discussed in the previous section, similar experiments have also been performed for different gas species. The relevant experiments have been performed after an incident with the oil-driven diffusion pump led to the deposition of a persistent oil film on the walls of the test vessel. Afterwards, the measured fore-vacuum tolerance for air reduced by approximately 15 % compared to the results prior to the incident discussed in the previous section. This is presumably due to a change in the mercury

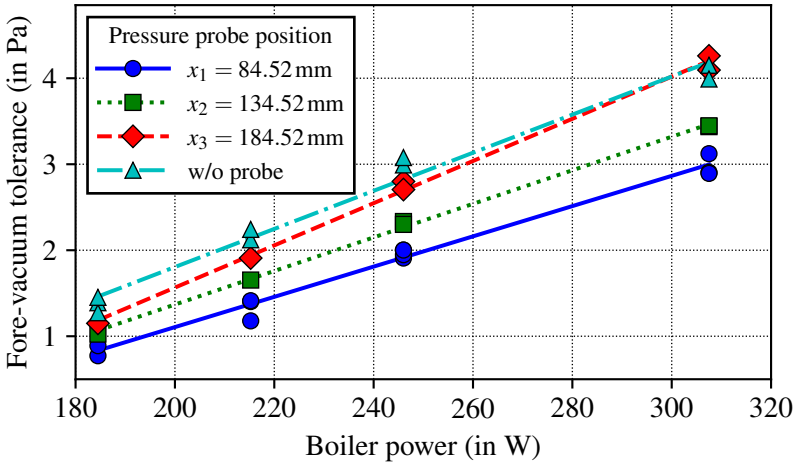

Figure 5.7.: Fore-vacuum tolerance as a function of the boiler power and with and without installed pressure probe. The lines correspond to linear regressions of the measurements.

Table 5.2.: Fore-vacuum tolerance and base pressures for different boiler powers. The pressure probe has not been installed for these measurements. Additionally, the temperature of the mercury vapor in the riser pipe (TI02) and the pipe temperature close to the nozzle (TI03) are reported.

Boiler power	**TI02**	**TI03**	**HV base press.**	**FV base press.**	**FV tol.**
(in W)	**(in K)**	**(in K)**	**(in Pa)**	**(in Pa)**	**(in Pa)**
184.5	391 ± 0.9	370 ± 3	0.179 ± 0.00166	0.151 ± 0.00159	1.39
	389 ± 0.9	368 ± 3	0.175 ± 0.00165	0.152 ± 0.00159	1.27
	391 ± 0.9	371 ± 3	0.213 ± 0.00174	0.147 ± 0.00158	1.45
215.25	396 ± 0.9	376 ± 3	0.183 ± 0.00167	0.157 ± 0.00161	2.12
	397 ± 0.9	378 ± 3	0.170 ± 0.00163	0.151 ± 0.00159	2.24
246.0	401 ± 1	383 ± 3	0.181 ± 0.00166	0.153 ± 0.00160	2.99
	402 ± 1	385 ± 3	0.174 ± 0.00164	0.155 ± 0.00160	3.08
307.5	410 ± 1	393 ± 3	0.189 ± 0.00168	0.161 ± 0.00161	4.15
	410 ± 1	393 ± 3	0.186 ± 0.00167	0.164 ± 0.00162	3.99

condensation rate on the cooled walls of the pump due to the oil film, which is in agreement with previous reports [174, 207]. Furthermore, only the backing pump could be operated during these experiments. For this reason only a qualitative comparison of the results is presented here.

During the experiments gas has actively been dosed into the test vessel by opening the precision valve V07. This gas line is connected to the top of the test vessel by a 0.1 mm orifice. The gas dosage rate is adjusted to ensure that it is at least as high as the air leakage rate. The fore-vacuum tolerance has been determined using two different approaches: The first approach is similar to the one discussed in the previous section, i.e. the test vessel has not been pumped during the experiment. In case of the second approach the setup has been actively pumped through valve V03 using the backing pump for the entire duration of the experiment. The fore-vacuum tolerance is then determined by increasing the dosage rate of gas to much higher values than the air leakage rate.

Figure 5.8 shows the determined fore-vacuum tolerances for helium and argon. In addition, the "normal" experiments using air leakage are performed to serve as a reference. When comparing the helium and argon experiments performed without and with connected backing pump it is evident, that the determined fore-vacuum tolerance is independent of the configuration. An interesting detail is that the curves with backing pump for helium are slightly higher and the ones for argon slightly lower than the corresponding curves without backing pump. A physical explanation is that these curves correspond to the experiments with the purest composition, because the dosage rates are the highest and the superposed air leakage can be considered constant. Thus, the good agreement of the curves and associated fore-vacuum tolerances also indirectly confirm that the influence of air leakage can be considered negligible for the shown measurements. When comparing the different gas species, argon and air show nearly the same evolution and fore-vacuum tolerance, whereas the evolution for helium is flatter and features a lower fore-vacuum tolerance. This is expected due to the significantly higher diffusivity of helium when compared with heavier species like air and argon. Similar observations are reported by Dayton, who compares hydrogen, helium and air in mercury- and oil-driven diffusion pumps [48].

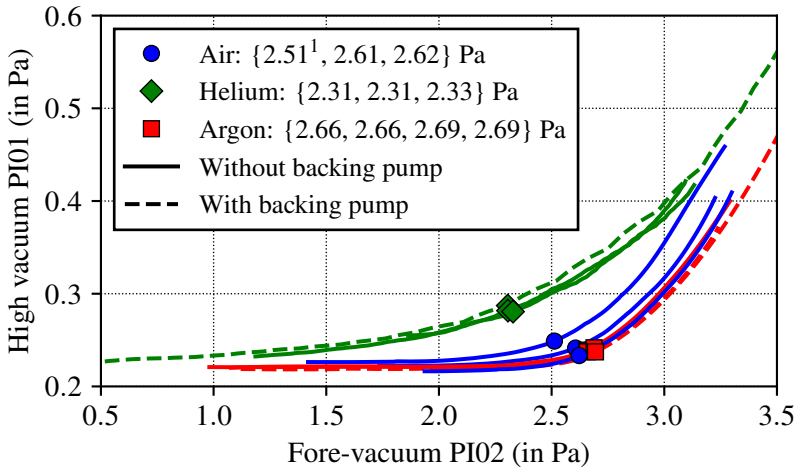

Figure 5.8.: High vacuum pressure (PI01) as a function of the fore-vacuum pressure (PI02) during the fore-vacuum tolerance experiments for different gas species. The lines correspond to the smoothed experimental curves generated by applying the Savitzky-Golay filter. The symbols show the fore-vacuum tolerance determined according to the procedure described in Sec. 5.2.2. Additionally, the determined fore-vacuum tolerances are listed in the legend. Solid lines refer to experiments performed without pump (V03 closed, similar to Sec. 5.2.2). Dashed lines refer to experiments performed with connected backing pump (V03 open). [1](see legend): Air experiment performed before steady-state was fully reached and only included as supplementary information.

5.2.4. Mercury mass flow rate

The mercury mass flow rate is measured by closing valve V04 in the mercury condensate return line to the boiler. The average mass flow rate is calculated from the change of the liquid mercury volume in the boiler over time and the temperature-dependent density. The temporal evolution of the mercury mass in the boiler during a mass flow rate measurement is depicted in Fig. 5.9 (a). The mass is calculated from the liquid level as indicated by level sensor LI01, the boiler volume calibration curve (cf. Appendix A.6.2) and the temperature-dependent density correlation from

[202]. The spike at approximately 215 min results from mercury condensate dropping back into the boiler from the riser pipe. Based on the substantial amount of about 45 g (corresponding to 3.5 mL) it is most likely that the condensate originates from either the slightly inclined horizontal connection between the riser pipe and the nozzle or from the crosspiece in the riser pipe where RTD TI02 is located. Another hypothesis is that droplets running down the walls can trigger a cascade by entraining further droplets. Based on the experience gathered during the measurements these events occur approximately every 10-20 min. They are accounted for in the determination of the mass flow rate because the effective vapor mass flow rate that is expanded through the nozzle and not the evaporation rate (which corresponds to the steady slope of the curve) is of interest here. In order to reduce the associated uncertainty multiple measurements have been performed. The averages of the determined mass flow rates are depicted as a function of the boiler power in Fig. 5.9 (b). The mass flow rate increases approximately linear with the boiler power. Physically, this is explained by the fact that sensible heating is negligible compared to the latent heat of vaporization of mercury, which changes by less than 1.5 % in the experimental temperature range [208]. It is emphasized here, that the employed measurement principle can only measure the total mercury mass flow rate that is ejected through the nozzle and it is not possible to draw a definitive statement if the flow is single- or two-phase.

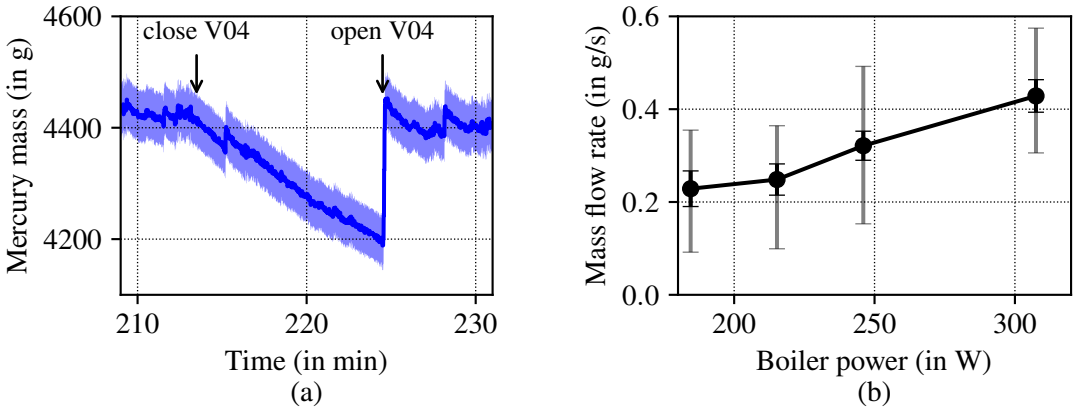

Figure 5.9.: (a) Liquid mercury mass in the boiler as a function of time during a representative mass flow rate measurement at a boiler power of 246 W. (b) Mass flow rate as a function of the boiler power. Symbols represent the average of multiple determinations at the same boiler power and are connected with straight lines to guide the eye. The outer error bars correspond to minimum and maximum individual measurements (including uncertainty), whereas the inner error bars correspond to the uncertainty of the average calculated assuming independent measurements.

5.3. Validation of the DSMC diffusion pump model

Comparison with the experimental data allows to validate the numerical diffusion pump model that has been introduced in Sec. 4.3. The computational domain of the model resembles a simplified version of the NEMESIS test vessel. The main simplification is the assumption of a circular outlet surface in the model to make the computational domain axisymmetric, whereas the experiment features a transversal connection to the vessel below the baffle. This choice reduces the computational effort by more than two orders of magnitude. As no vacuum recipient is installed in the experimental setup, boundary condition ③ b), as described in Sec. 4.3, is used in the validation

DSMC simulations. The validation strategy comprises three steps:

- The fore-vacuum tolerance is compared between DSMC simulations and experiments (cf. Secs. 5.3.1 and 5.3.2). The comparison allows to establish a mapping between the mercury vapor state that is assumed in the DSMC simulations and the experimental boiler power.
- The axial pressure distribution is compared between experiments and DSMC simulations (cf. Sec. 5.3.3).
- The mercury mass flow rates are compared (cf. Sec. 5.3.4).

A similar comparison between simulations and experiments is discussed in an accepted manuscript [199] by the author. However, the numerical model discussed in [199] assumes an effective condensation coefficient of $\alpha_{c,\mathrm{eff}} = 1$, whereas the more physical condensation boundary condition introduced in Sec. 3.5.5 is used here. A direct comparison of the simulation results is discussed in Appendix A.5.2.

5.3.1. Fore-vacuum tolerance

In the experiments the fore-vacuum tolerance has been determined for different boiler powers (cf. Sec. 5.2.2). Increasing the boiler power increases the temperature and pressure of the mercury vapor leaving the boiler. In order to replicate the experimental setup in the DSMC pump model it is necessary to identify the vapor state upstream of the nozzle in order to determine the properties of the boundary condition at the nozzle throat. A direct measurement of the vapor pressure upstream of the nozzle has not been possible due to the limited operating temperature of available pressure transducers. Thus, the pressure is estimated from temperature measurements and the saturation pressure curve of mercury vapor [68]. Two temperature measurements are available from the experiments: Firstly, the vapor temperature in the riser pipe between nozzle and boiler has been measured using RTD TI02 in an immersion sleeve. Secondly, the outer temperature of the vapor pipe underneath the insulation layer has been measured using TC TI03 close to the nozzle. The temperature indicated by TI03 is consistently approximately 10-15 K lower than that of TI02, which is partly due to the location of TI03 on the outer pipe wall and partly due to heat losses in the pipe between the two measurement locations. Therefore, the actual vapor temperature directly upstream the nozzle lies between the temperatures indicated by TI02 and TI03. Due to the uncertainty of the exact vapor temperature several different temperatures between TI02 and TI03 have been assumed and simulated using the DSMC pump model. The experiments have been performed by exploiting the leakage rate of environmental air into the setup. As a simplification pure nitrogen is assumed in the simulations.

By presuming a quasi-static process the continuous experimental determination of the fore-vacuum tolerance can be replicated as a set of stationary DSMC simulations at different fore-vacuum pressure levels. Afterwards, the fore-vacuum tolerance is determined similarly to the experiments by determining the rate of high vacuum pressure rise to fore-vacuum pressure rise. As discussed in Sec. 5.2.2 and reported in Tab. 5.2 both the high vacuum (PI01) and the fore-vacuum (PI02) transducers show very similar base pressures of approximately 0.15 to 0.2 Pa, which is likely for the major part a result of the steady evaporation of small mercury droplets collecting during and between experiments (e.g. during start-up and shutdown phases) and for a smaller part due to outgassing. Both effects are difficult to reproduce in the simulations, which is why it is expedient to assume that the base pressure stays constant during the experiment so that it can be subtracted from the experimental readings and compared with the gas partial pressure obtained from the simulations. The evolution of the high vacuum pressure as a function of the fore-vacuum pressure for simulations and experiments is shown in Fig. 5.10. As outlined above, several DSMC simulations

with different vapor stagnation temperatures have been performed. In order to preserve readability only the simulations featuring the best agreement with the experiments are plotted in Fig. 5.10. A similar non-linear dependency of the high vacuum to fore-vacuum pressure is observed. At higher boiler powers and corresponding vapor stagnation states the onset of the high vacuum pressure increase shifts to higher fore-vacuum pressures. A direct comparison between the experiments and the respective identified simulation with respect to the fore-vacuum tolerance and vapor temperature is available in Tab. 5.3. As expected based on physical reasoning the simulation stagnation temperatures fall between the two respective experimentally measured values with a tendency to RTD TI02, which measures the vapor temperature directly. The assumed simulation stagnation temperatures are lower by 1.6 to 1.9 % than the respective measured temperatures at TI02. This can be partly attributed to heat losses in the experiments as well as the ideal assumption of a nozzle discharge coefficient of unity in the simulations.

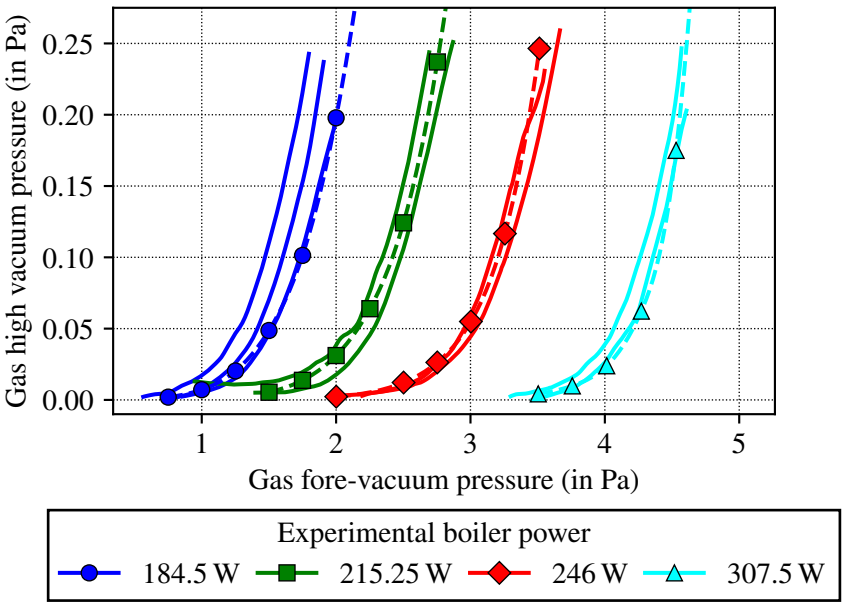

Figure 5.10.: High vacuum pressure as a function of the fore-vacuum pressure comparing experiments (solid lines) with DSMC simulations (individual: symbols, cubic spline fit: dashed lines). As described in the text the experimental pressures are corrected by their respective base pressures (cf. Tab. 5.2) and the shown curves are smoothed as described in Sec. 5.2.2. In case of the simulations the nitrogen partial pressure is plotted.

Furthermore, it has been shown that the fore-vacuum tolerance predicted by the DSMC pump model is not sensitive to the main modeling assumptions including the condensation boundary condition and the rotational degrees of freedom of the nitrogen molecule (for details cf. Appendix A.5.2). Thus, it can be concluded that the DSMC pump model is capable of predicting the fore-vacuum tolerance with acceptable accuracy. The identified mapping between experimental boiler powers and stagnation conditions employed in the simulations as listed in Tab. 5.3 are used in the subsequent sections for the follow-up comparisons.

5.3.2. Fore-vacuum tolerance for different gas species

Next, the fore-vacuum tolerance has been determined for different gas species. Similar to the experiments, argon and helium have been simulated. As previously discussed, the relevant ex-

Table 5.3.: Comparison of the vapor temperatures and fore-vacuum tolerance between experiments and the identified DSMC simulations (cf. Fig. 5.10). The experimental values are averaged from two (215.25, 246.0 and 307.5 W) or three (184.5 W) independent measurements.

Experiments				**DSMC simulations**	
Boiler power	**TI02**	**TI03**	p_{FT} **(min, max)**	T_0	p_{FT}
(in W)	**(in K)**	**(in K)**	**(in Pa)**	**(in K)**	**(in Pa)**
184.5	390.4 ± 0.9	369.9 ± 3.0	1.22 (1.12, 1.31)	383.15	1.33
215.25	396.4 ± 0.9	377.4 ± 3.0	2.03 (1.96, 2.09)	389.15	2.02
246.0	401.7 ± 1.0	383.9 ± 3.0	2.88 (2.84, 2.92)	395.15	2.84
307.5	409.7 ± 1.0	393.0 ± 3.0	3.91 (3.83, 3.99)	403.15	4.04

periments have been performed after an incident with the oil-driven diffusion pump led to the deposition of an oil film on the test vessel walls. For this reason the oil-driven diffusion pump could not be operated during these experiments and pumping has been provided only by the rotary vane backing pump. Since this pump has a much lower pumping speed it has not been possible to determine the fore-vacuum background pressure during these experiments. Instead, the average of the previously measured background pressures (cf. Tab. 5.2), which is 0.154 ± 0.004 Pa (95 % confidence interval), was used to correct the fore-vacuum pressure. The background pressure on the high vacuum side could be determined reliably because its pumping is provided by the mercury vapor jet. In addition to the aforementioned issues regarding the fore-vacuum background pressure the oil film deteriorated the fore-vacuum stability of the mercury vapor jet slightly (approximately 15 % lower fore-vacuum tolerance).

The evolution of the gas high vacuum pressure as function of the fore-vacuum pressure for experiments and DSMC simulations is depicted in Fig. 5.11. The experimental results are corrected by the aforementioned background pressures. A quasi-static process is again assumed in the DSMC simulations and the breakdown curve then extracted as a fit of individual simulation results at discrete values of the fore-vacuum pressure. Very similar sensitivity of the high vacuum pressure to the fore-vacuum pressure is observed for air / nitrogen and argon in both simulation and experiment. Furthermore, a higher sensitivity is displayed by helium than for the former two gases. Physically, this is explained by the binary diffusion coefficients of the mixtures of mercury vapor with the respective gas species (cf. Fig. 3.8). At the same temperature the diffusion coefficients of air / nitrogen and argon differ by only approx. 15 %, whereas helium features an approximately four times higher diffusion coefficient. The qualitative agreement between DSMC simulation and experiment with regard to this effect indicates that the main physical processes responsible for the fore-vacuum stability are described accurately by the DSMC pump model.

Quantitatively speaking, the predicted increase of the helium high vacuum pressure is stronger and begins at lower fore-vacuum pressures in the simulations than observed in experiments. The first assumption that this deviation is caused by the inaccurate binary diffusion coefficient of the Hg-He mixture produced by the averaged VSS parameters has been disproved by a sensitivity study of the interspecies scattering coefficient α_{12} (cf. Appendix A.5.2). In fact, this study shows that the deviation of the simulation results to the experimental results increases if α_{12} is adjusted to achieve a better agreement with the experimentally measured diffusion coefficient. Based on this, the choice of the lower boundary condition in the DSMC pump model, where a resting gas reservoir is assumed at a similar pressure as measured experimentally with PI02, is identified as the most plausible reason for the observed deviation. This effect is more pronounced for helium due to its

significantly higher thermal velocity (factor 2.6 compared to air / nitrogen and 3.2 compared to argon) and diffusion coefficient.

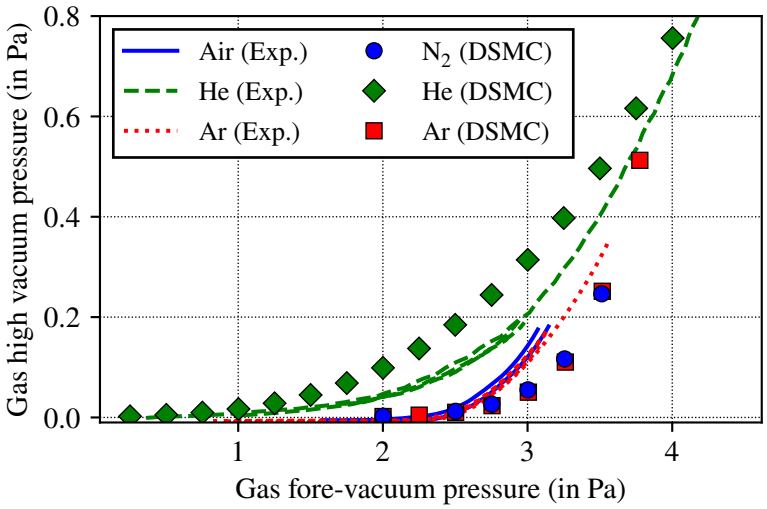

Figure 5.11.: High vacuum pressure as a function of the fore-vacuum pressure comparing experiments (lines) with DSMC simulations (symbols) for different gas species (solid / blue: air leakage, dashed / green: helium, dotted / red: argon). The experimental pressures are corrected by their respective background pressures and the shown curves are smoothed as described in Sec. 5.2.2. In case of the simulations the partial pressure of the respective gas is plotted. The experiments have been performed at a boiler power of 246 W corresponding to a simulated vapor stagnation temperature of 395.15 K. The experiment for air performed before steady-state had been reached is omitted here but included in Fig. 5.8.

5.3.3. Axial pressure distribution in the mercury vapor jet

Next, the axial pressure distribution is compared. The static pressure has been measured in the experiments by inserting a pressure probe into the flow. The pressure probe has originally been designed to perform measurements of the Rayleigh-Pitot pressure, which is approximately one order of magnitude higher than the static pressure. Thus, it can be hypothesized that the probe influences the measurements due to the shock wave establishing as the supersonic mercury vapor jet impinges on it. To test this hypothesis the DSMC simulation domain is extended with a flow obstacle in the form of an axisymmetric disk with adiabatic boundary conditions and similar dimensions as the pressure probe and at the respective axial position. All simulations presume the mapping identified in Fig. 5.10 and Tab. 5.3 between experimental boiler power and assumed mercury stagnation temperature at the DSMC inflow boundary. Additionally, only mercury vapor is simulated because the experiments have been performed with active pumping.

Figure 5.12 compares the experimentally measured static pressures as a function of the axial distance to the nozzle with the results obtained from the DSMC simulations. Firstly, the comparison clearly shows that the simulations are predicting the same qualitative and quantitative axial pressure distribution as measured with the pressure probe in the experiments. Secondly, the hypothesis that the probe influences the measurement is confirmed by comparing the simulations without flow obstacle (lines in Fig. 5.12) with those including the flow obstacle supposed to model the experimental pressure probe (symbols in Fig. 5.12). This effect is more pronounced in simulations as

well as experiments at higher boiler powers, e.g. when comparing the results for the lowest and highest boiler power at $x = 84.52\,\text{mm}$.

Additionally, the pressure distribution is compared for a single vapor stagnation temperature at the three axial probe positions in Fig. 5.13. This comparison confirms the hypothesis, that the probe influences the measurement due to a shock wave forming upstream of the probe. Furthermore, it is clearly visible that this effect is more pronounced the closer the probe is located to the nozzle, which is in agreement with the observations discussed above. The remaining disagreement can be attributed to the probe sensitivity to rotation along its longitudinal axis, the uncertainty regarding the position of the probe in the experiments, which is estimated to $\pm 2\,\text{mm}$ (cf. Tab. A.7), and the simplifications assumed in the DSMC model.

Finally, the agreement between the simulation results and experimental measurements is considered good and the validity of the mapping of Tab. 5.3 between experimental boiler powers and stagnation conditions assumed in the simulations is noted.

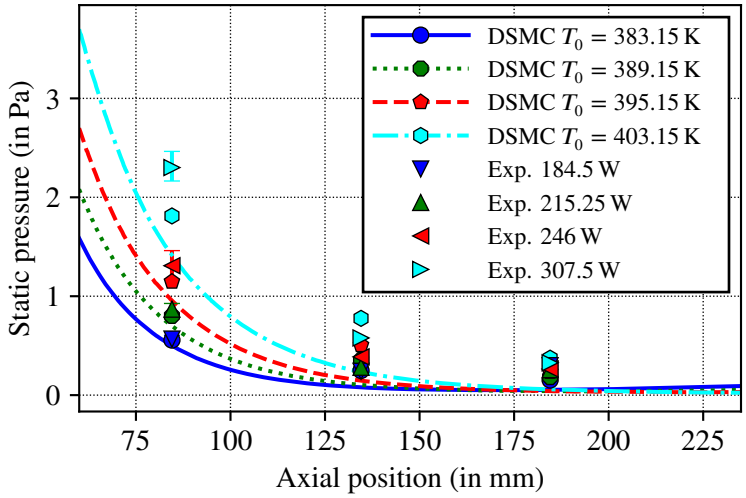

Figure 5.12.: Static pressure as a function of the axial distance to the nozzle throat. The radial distance to the symmetry axis is fixed at 10 mm. Experimental measurements (triangles) are averaged where multiple determinations are available with the error bars indicating the respective minimum and maximum values (a complete list of the results is available in Tab. A.8). The DSMC simulations are performed at the vapor stagnation conditions matching the experimental boiler power (cf. Tab. 5.3). Symbols indicate DSMC simulation results including a flow obstacle to model the experimental pressure probe at the respective axial position, whereas lines indicate DSMC simulation results without the flow obstacle.

5.3.4. Mercury mass flow rate

The established mapping between experimental boiler power and stagnation conditions in the simulations is used to compare the simulated and experimental mass flow rates. In the DSMC simulations the choked mercury vapor flow in the nozzle throat is modeled by assuming uniform conditions in the entire cross-section. The properties at the throat are calculated by the one-dimensional isentropic relationships. Therefore, the mass flow rate is effectively an input parameter and can be

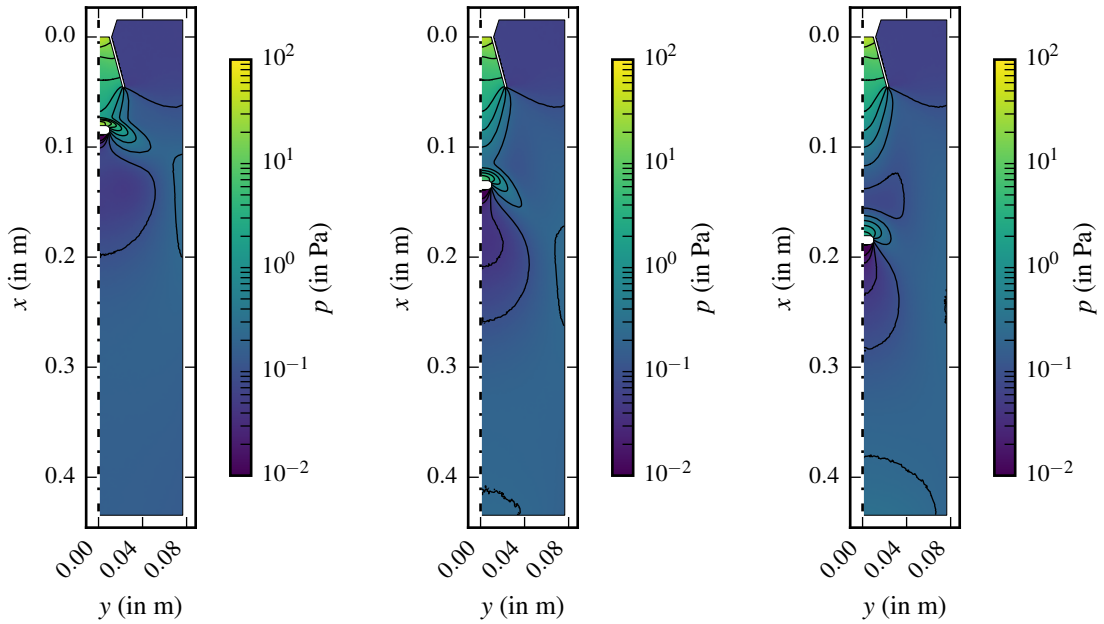

Figure 5.13.: Axisymmetric DSMC simulations of the static mercury vapor pressure distribution in NEMESIS including an axisymmetric disk with similar dimensions to the experimental pressure probe at the three axial measurement positions: (a): $x = 84.5\,\mathrm{mm}$, (b) $x = 134.5\,\mathrm{mm}$ and (c) $x = 184.5\,\mathrm{mm}$. The mercury stagnation temperature for the displayed cases is $T_0 = 389.15\,\mathrm{K}$ approximately matching an experimental boiler power of 215.25 W.

estimated as

$$\dot{m} = A_{\mathrm{throat}} p_{\mathrm{V},0} \sqrt{\frac{\gamma m_{\mathrm{V}}}{k_B T_{\mathrm{V},0}} \cdot \left(\frac{2}{\gamma+1}\right)^{\frac{\gamma+1}{\gamma-1}}}, \tag{5.2}$$

which depends only on the throat cross-section A_{throat} and the stagnation conditions $p_{\mathrm{V},0}$ and $T_{\mathrm{V},0}$ [209]. The mercury vapor stagnation conditions in turn are related by the saturation condition [68]. A comparison of the resulting vapor mass flow rate in the DSMC simulations (superposition of injected and reflected simulator particles at the throat) confirmed that Eq. (5.2) is met with less than 1 % deviation.

Table 5.4 compares the mass flow rates as measured in the experiments for different boiler powers with the choked vapor mass flow rates according to Eq. (5.2) for the respective experimentally measured vapor temperatures by TI02 and the simulated stagnation temperatures. The comparison reveals that the experimental mass flow rates are significantly higher than the choked mass flow rates. This points to the fact that the experimental flow is two-phase, i.e. containing some mercury in liquid form. Under the hypothesis that the difference between the experimentally determined mass flow rate and the simulation mass flow rate corresponds to the liquid proportion, the volumetric flow rate of the liquid can be estimated by dividing by the density of liquid mercury [202]. When further assuming that liquid and gas velocities at the nozzle throat are the same, the volumetric liquid fraction is less than 3×10^{-7} for all boiler powers. Thus, even if the liquid speed is significantly smaller than the vapor speed, the liquid fraction is so small that its influence on the vapor flow can be neglected.

Table 5.4.: Comparison of the mass flow rates between experiments and choked vapor flow according to Eq. (5.2) at the experimental vapor temperature TI02 and the stagnation temperature T_0 assumed in the DSMC simulations. The experimental values are averaged from several measurements (cf. Sec. 5.2.4).

Experiments		**Choked flow**			
Boiler power	$\dot{m}$	**TI02**	$\dot{m}$	$T_{0,\mathrm{DSMC}}$	$\dot{m}$
(in W)	**(in mg/s)**	**(in K)**	**(in mg/s)**	**(in K)**	**(in mg/s)**
184.5	229 ± 38	390.4 ± 0.9	151 ± 6	383.15	107
215.25	248 ± 34	396.4 ± 0.9	199 ± 8	389.15	142
246.0	321 ± 31	401.7 ± 1.0	252 ± 11	395.15	188
307.5	429 ± 35	409.7 ± 1.0	355 ± 15	403.15	268

This partially explains the debate in literature whether the flow is single- or two-phase: While condensation is unlikely to occur due to the expansion through the nozzle as discussed in Sec. 3.3.2, it is likely that the flow in real-world diffusion pumps is always slightly two-phase already upstream the nozzle due to condensation caused by heat losses in the tubing between boiler and nozzle (as also pointed out in [59]). However, due to the large difference between the vapor and liquid densities in case of the heavy species mercury, the liquid part can be neglected when modeling the flow. Likewise, it is plausible that very small volumetric fractions of condensate were not detected by the experimenters cited in Sec. 3.3.2.

6. Modeling and characterization of baffles for vapor trapping in the Tokamak exhaust system

Vapor diffusion pumps require the installation of a baffle to prevent the migration of mercury vapor to upstream systems (MFPs, divertor and ultimately torus). In a Tokamak the baffle is required for three reasons:

- Mercury belongs to the so-called *high-Z* elements, i.e. elements with a high number of protons in the nucleus (in case of mercury 80). The concentration of high-Z materials in the plasma core has to be kept low because they increase radiation losses significantly [3, 39, 40].
- Higher neutron flux densities occur closer to the plasma, which will lead to increased activation of mercury.
- The number of components in contact with mercury should be limited as much as possible to facilitate maintenance without requiring mercury decontamination.

In the present chapter, first the operating principle of baffles is discussed mainly in view of the special conditions in the pulsed Tokamak operation. Then, DSMC simulations of two commonly used baffle structures are presented with the goal to extract design guidelines as a function of the flow regime.

6.1. Baffles for Tokamak exhaust pumping

Gas or vapor particles impinging on the baffle plates are either reflected or *stick* to the plates. *Sticking* here refers to either ab- / adsorption or a phase change in the form of condensation or desublimation at sufficiently low temperatures. The *sticking coefficient* ξ describes the probability that an impinging particle sticks to the surface. Applied to diffusion pumps the temperature of the cooled plates has to be kept low enough to facilitate condensation or desublimation of mercury vapor. This concept can also be used to construct a two-stage baffle that combines a condensation and desublimation stage [11, 71]. In case of condensation, the sticking coefficient is equivalent to the previously introduced effective condensation coefficient $\alpha_{c,\mathrm{eff}}$.

By design, baffles also represent a flow obstacle even for gases with zero sticking coefficient. As baffle and diffusion pump have to be connected in a serial connection, the baffle inevitably reduces the effective pumping speed available upstream of the baffle. Hence, the baffle design always has to compromise between maximizing mercury containment efficiency and minimizing the impact on the effective pumping speed. The situation is complicated further in case of the pulsed operation in Tokamaks because the flow regime changes significantly between burn and dwell phases. Up to now systematic parametric studies of different baffle geometries have only been conducted in the free-molecular regime [210–213]. As the assumption of free-molecular flow is not necessarily justified in the burn phase, the study is extended to a wide range of Knudsen numbers. As even opaqueness will not guarantee perfect vapor removal even if the sticking coefficient is assumed as

unity outside the free-molecular regime, the containment efficiency is also investigated. Furthermore, even if the baffle is designed to be operated in the free-molecular regime during nominal burn conditions, the flow regime might change in off-normal or transient operating conditions (e.g. pump-down, sudden load spikes and shut-down [69]).

6.2. Simulation of baffles in different flow regimes

The focus of the present study is to develop an understanding of the change in baffle performance when changing the flow regime. The two investigated baffle design archetypes are depicted in Fig. 6.1 with their characteristic parameters. The *chevron* type is the most widely used and the second type is referred to as *offset* type following [212] and reportedly has a higher conductance (free-molecular simulation [212] and experimentally for a mercury diffusion pump [65]). Therefore,

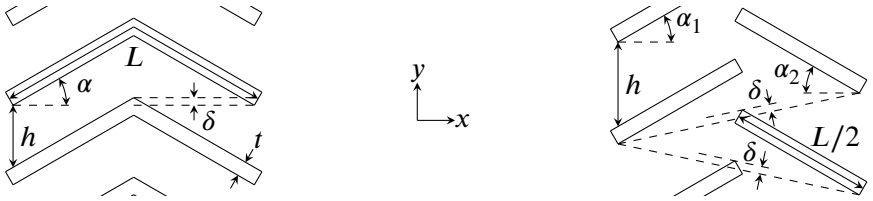

(a) (b)

Figure 6.1.: Illustration of the two investigated baffle archetypes ((a) chevron, (b) offset) and their geometrical parameters: the plate length L, the angles α_i, the opening gap height h, the plate thickness t and the overlap of the line of sight δ.

it is of interest to compare how the conductance and containment efficiency of the two designs compare outside the free-molecular regime. The results are presented in dimensionless form by translating the gas conductance into the *transmission probability* w (following the same rationale as for the translation of the pumping speed into the capture coefficient):

$$w = \frac{\dot{n}}{\dot{n}_{\mathrm{in}}}, \tag{6.1}$$

where $\dot{n}$ is the net flux of the gas and $\dot{n}_{\mathrm{in}}$ the molecular flux through the upstream interface (of which a part is reflected due to intermolecular and / or wall collisions). Similarly, the *containment efficiency* ψ of the vapor is defined as

$$\psi = 1 - \frac{\dot{n}}{\dot{n}_{\mathrm{in}}}. \tag{6.2}$$

6.2.1. Simulation setup

The flow geometry is depicted in Fig. 6.2. Similar to previous free-molecular simulations, the problem is reduced to two dimensions by assuming that the depth (in z-direction) of the baffle plates is a lot larger than its other dimensions, thus justifying the application of periodic boundary conditions in the third direction. This approach facilitates parametric studies with reasonable computational effort. Usually, the number of stacked baffle plates and the associated total height (in y-direction) is large compared to the dimensions of a single baffle plate. That is why periodic boundary conditions are also applied in the y-direction. The flow direction is from left to right. Particles sampled from a Maxwellian velocity distribution at prescribed number density n, temperature T and zero bulk velocity are injected at the left boundary. The distance between the boundary

and the baffle is chosen as 100λ, where λ is the mean free path calculated at the upstream conditions, to allow for an equilibration of the flow by collisions. The downstream boundary is placed in a fixed distance o to the right of the baffle. In the present work the distance was chosen as $o = 0$. The downstream boundary is considered as a perfect pump, thus all particles hitting this boundary are deleted from the simulation. The baffle plates are assumed to have a constant uniform temperature T_w. Isothermal flow is assumed in the present work, i.e. $T_w = T$. The Knudsen number is

Figure 6.2.: Simulation domain with the main geometrical parameters. The dashed lines represent periodic boundary conditions. The flow is directed from left to right.

defined here as

$$\mathrm{Kn} = \frac{\lambda}{h}, \tag{6.3}$$

with the upstream mean free path λ and the gap h between two plates (cf. Fig. 6.1). A three-level grid is chosen. The finest grid size is chosen as $\Delta x = \Delta y \leq \min\{0.05 \cdot h, 0.33 \cdot \lambda\}$ in the region in and directly around the baffle. Cells spaced further apart are coarser and spatial weighting factors are used to reduce the number of simulator particles based on the cell volume. The typical cell weighting factor between simulator and physical particles is calculated as $F_i \leq 0.002 \cdot nV_i$, with the upstream number density n. This leads to about 500 simulator particles per cell in the upstream cells and sufficient simulators in downstream cells. The DSMC time step is chosen as $\Delta t \leq 0.1 \cdot \min\{\tau, \Delta x/v_{\mathrm{mp}}\}$, where τ is the mean collision time and v_{mp} the most probable velocity (both based on the upstream conditions).

Two types of simulations are performed: Firstly, the transmission probability is determined for helium by considering the baffle plates as fully diffuse reflectors. Secondly, the containment efficiency for mercury vapor is determined by assigning a sticking coefficient to the plates. In the latter simulations lower cell weighting factors have to be used in order to ensure a sufficient number of particles per cell leading to about 5000 simulator particles in the upstream cells. In both simulations the VSS model is used to simulate the intermolecular collisions. The parameters for helium and mercury as reported in Tab. 3.1 are used. However, since the results are presented in dimensionless form they are transferable to other species. It is emphasized that both setups only consider a single species (either helium or mercury). While the flow of mixtures would also be of interest especially with respect to the vapor containment efficiency, it increases the number of free parameters, which is why it is not considered in the present work.

In dimensionless form three geometrical parameters can be varied. The two most important parameters are the angle α and the overlap to gap ratio δ/h. The third - less important - parameter is the plate thickness to gap ratio t/h. Some previous works have therefore assumed the thickness to be negligible, i.e. taken $t/h = 0$ [210, 212], whilst others have investigated the influence [213]. As different flow regimes are considered in the present work and the simulation of all combinations is computationally prohibitive the following strategy is pursued to reduce the number of simulations to manageable amounts:

- First $t/h = 0$, $\delta/h = 0$ and a sticking coefficient of unity are assumed and the baffle angle α is varied to identify the optimum angle range. The following parametric simulations are then performed only for the optimum angle range.

- This involves the variation of the overlap to gap ratio δ/h to quantify the trade-off between increase in vapor containment efficiency and decrease in gas transmission probability.

- Then, the thickness to gap ratio t/h is varied, as a non-zero t/h is required in view of manufacturability.
- Finally, the sensitivity of the containment efficiency to the sticking coefficient is quantified.

6.2.2. Variation of the baffle angle

In principle the offset type allows different angles for the up- and downstream baffles. However, in the present work only equiangular offset baffles are considered. The angle is varied in the range 10-80° in increments of 10°. Further simulations are performed in the range around the optimum angle. The results are depicted in Fig. 6.3. The results are verified in the free-molecular regime by comparison with those of Ross et al. [212]. The agreement between the literature results and the free-molecular results generated in the present work is within the uncertainty associated with the graphical extraction of the literature data, therefore the simulation setup can be considered validated in the free-molecular regime. For very small angles (10°, cf. insets in Fig. 6.3) the baffles start to behave as thin slits and the Knudsen minimum [97] is observed, i.e. the transmission probability is the lowest in the transitional regime ($\mathrm{Kn} = 0.5 - 1$). At higher angles this phenomenon is not observed and the transmission probability increases monotonically with decreasing Knudsen number. The maximum transmission probability is observed at about 30° for the chevron and 25° for the offset type baffles respectively.

The containment efficiency under the assumption of perfect sticking ($\xi = 1$) is depicted in Fig. 6.4 for $\mathrm{Kn} \leq 0.1$ and the angle range around the optimum angles found above. The containment efficiency is found to be $> 99\,\%$. Additionally, an almost linear increase of the containment efficiency with respect to the angle is observed. As expected the containment efficiency decreases with decreasing Knudsen number due to intermolecular collisions within the baffle that allow particles to pass the baffle without coming in contact with the baffle surfaces. When comparing the two baffle archetypes, the chevron baffle is found to be superior regarding the containment efficiency. At the respective optimum angle (chevron: 30°, offset: 25°) the vapor transmission probability (i.e. $1 - \psi$) is 66-82 % higher for the offset configuration.

6.2.3. Variation of the baffle overlap

The overlap to gap ratio δ/h can have physically sensible values in the range $-\infty < \delta/h < \infty$. Optical tightness is achieved at $\delta/h \geq 0$, which implies that the vapor containment efficiency is less than unity for all Knudsen numbers for negative δ/h. In the present work the overlap to gap ratio is varied in the range $-0.05 < \delta/h < 0.75$ for the optimum angles that have been determined for both baffle archetypes. In case of the transmission probability a close to linear scaling is observed (cf. Fig. 6.5). On the contrary, asymptotically bounded growth is observed for the vapor containment efficiency as visible in Fig. 6.6. The containment efficiency approaches unity irrespective of the Knudsen number for large values of δ/h. Above $\delta/h > 0.5$, nearly the same containment efficiency is observed for all Knudsen numbers investigated here. Physically speaking, increasing the overlap to gap ratio δ/h increases the number of wall collisions that particles undergo on average while traveling in the baffle structure. Consequently, it becomes less likely that intermolecular collisions enable vapor particles to pass the baffle without getting stuck to the baffle plates.

6.2.4. Variation of the baffle plate thickness

The sensitivity of the baffle performance metrics towards the plate thickness to gap ratio t/h is investigated in Figs. 6.7 & 6.8 for the respective optimum angles determined above. Both the transmission probability and the containment efficiency are found to be approximately linearly dependent on t/h. The transmission probability decreases almost linearly with increasing t/h,

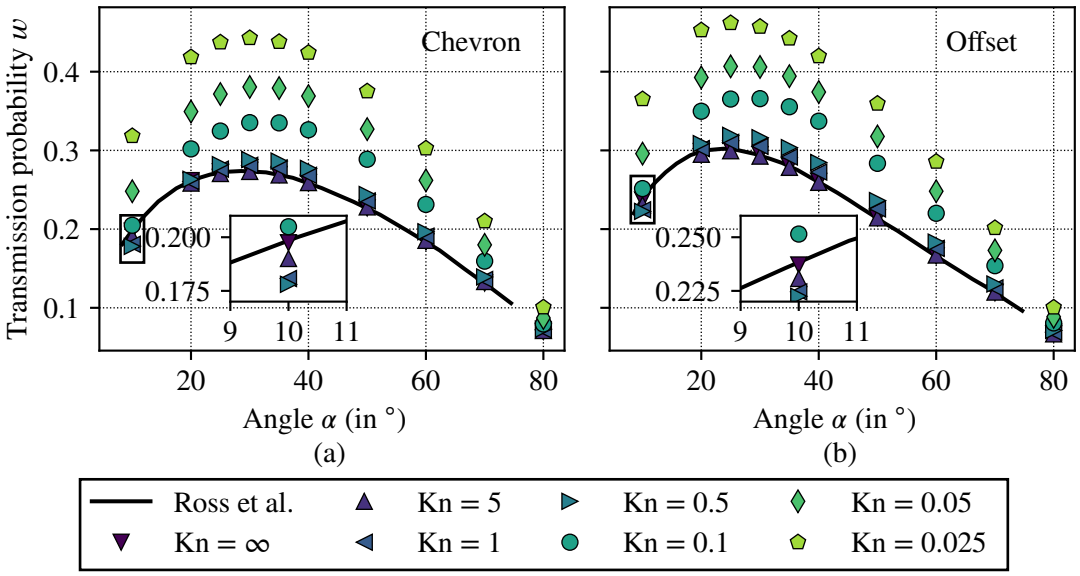

Figure 6.3.: Baffle transmission probability w as a function of the angle α for both baffle types ((a) chevron, (b) offset). The baffles are very thin, i.e. the thickness to gap ratio $t/h \approx 0$ and the overlap to gap ratio is $\delta/h = 0$. The lines correspond to free-molecular results from Ross et al. [212]. Symbols are results from the present work. Error bars (95% confidence interval) are smaller than the symbols.

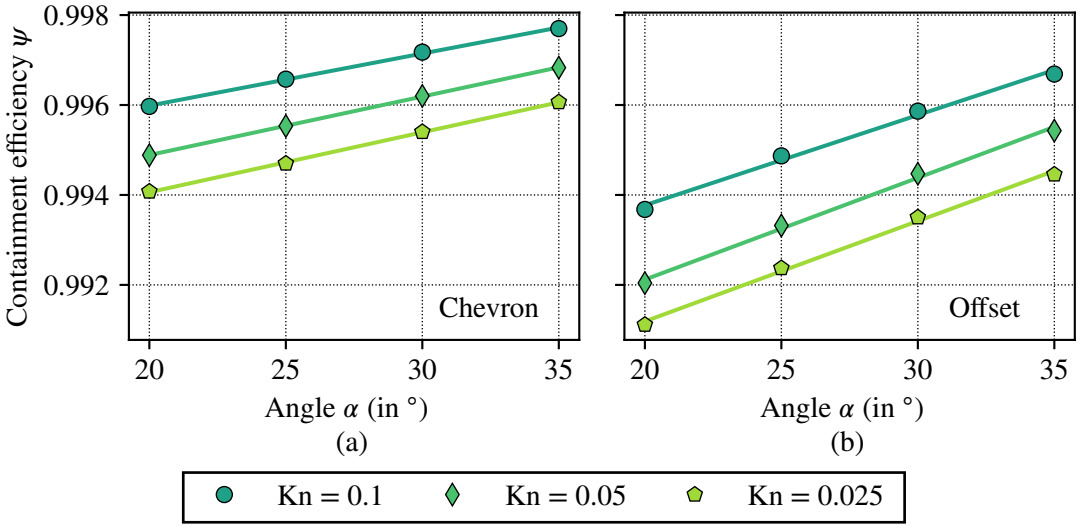

Figure 6.4.: Baffle vapor containment efficiency ψ as a function of the angle α for both baffle types ((a) chevron, (b) offset). The baffles are very thin, i.e. the thickness to gap ratio $t/h \approx 0$ and the overlap to gap ratio is $\delta/h = 0$. The vapor sticking coefficient is $\xi = 1$. Error bars (95% confidence interval) are smaller than the symbols. The lines correspond to linear regressions of the simulation results.

because the finite plate thickness leads to some particles being reflected on the front walls of the baffles with a probability in the order of magnitude of t/h. This is also in good agreement with the results of [213], who also find a nearly linear scaling over a wide range of t/h ratios. The

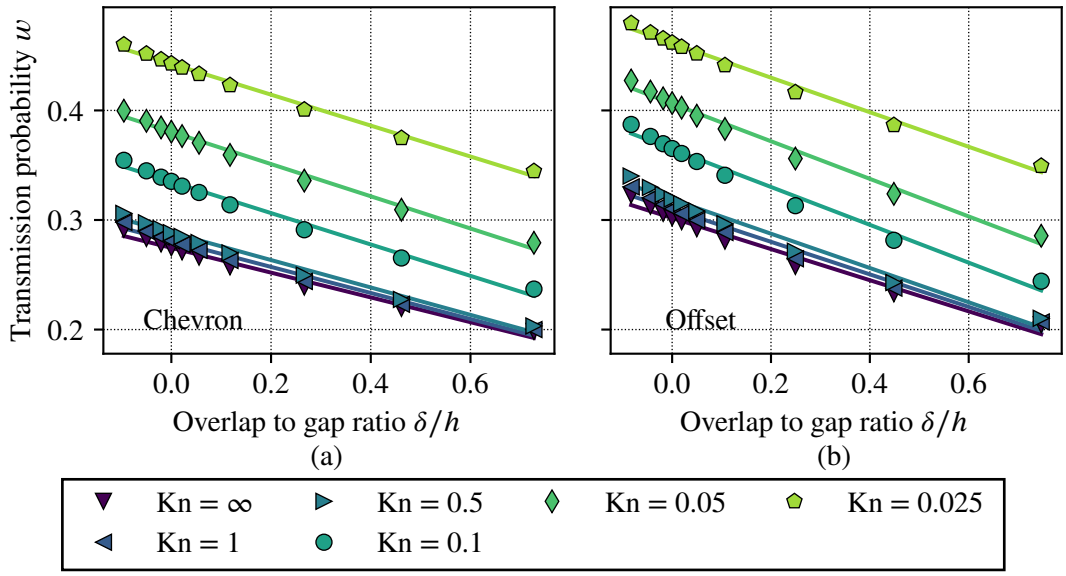

Figure 6.5.: Baffle transmission probability w as a function of the overlap to gap ratio δ/h for both baffle types ((a) chevron, (b) offset). The thickness to gap ratio is $t/h \approx 0$. The optimum angles of 30° for chevron and 25° for offset configurations are chosen. Error bars (95% confidence interval) are smaller than the symbols. The lines correspond to linear regressions of the simulation results.

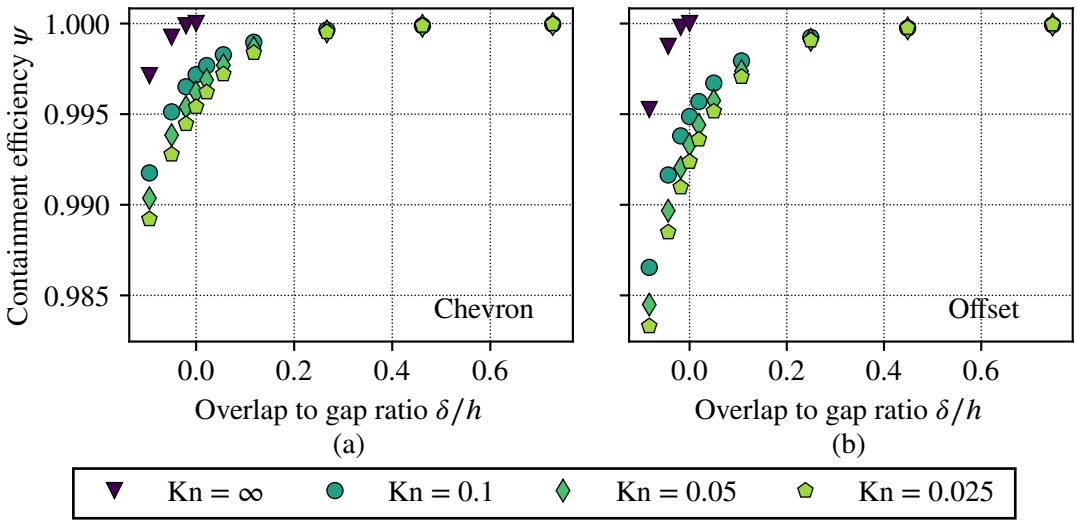

Figure 6.6.: Baffle vapor containment efficiency ψ as a function of the overlap to gap ratio δ/h for both baffle types ((a) chevron, (b) offset). The thickness to gap ratio is $t/h \approx 0$. The vapor sticking coefficient is $\xi = 1$. The optimum angles of 30° for chevron and 25° for offset configurations are chosen. Error bars (95% confidence interval) are smaller than the symbols.

vapor containment efficiency increases because vapor particles can also stick to the front walls. A finite baffle plate thickness is required for reasons of manufacturability. This also has to account for a means to actively cool the baffle plates, which can either be done by conductive cooling by

bringing the plates in direct contact with a heat sink or by introducing internal cooling channels in the baffle plates. Therefore, the ratio t/h cannot be chosen arbitrarily and, generally speaking, increases as the absolute physical dimensions of the baffle decrease. Therefore, the difficulty of constructing a baffle operating in the free-molecular regime with high conductance increases with the baffles intended operating pressure.

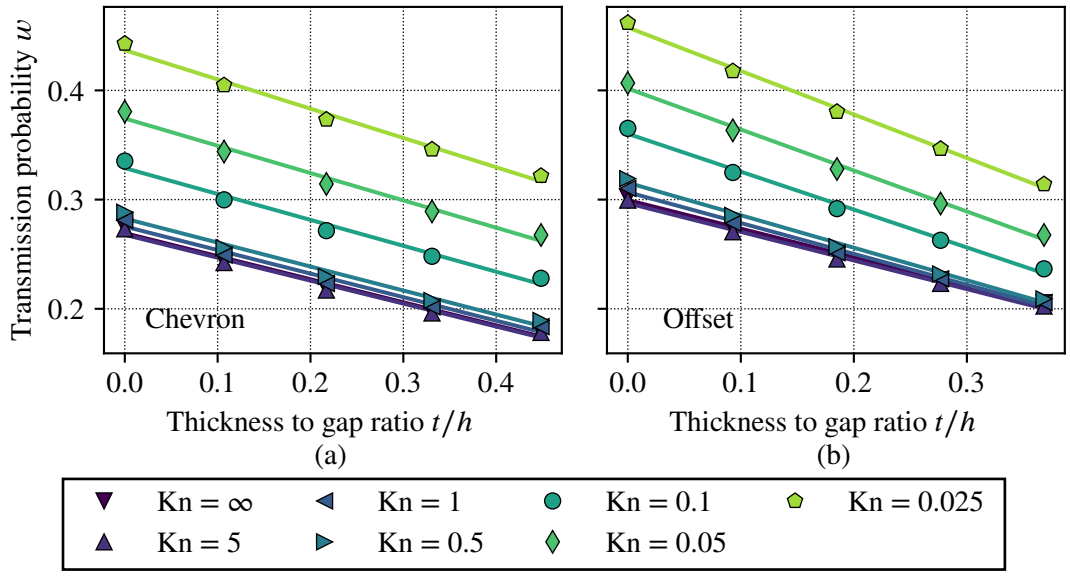

Figure 6.7.: Baffle transmission probability w as a function of the plate thickness to gap ratio t/h for both baffle types ((a) chevron, (b) offset). The overlap to gap ratio is $\delta/h = 0$. The optimum angles of 30° for chevron and 25° for offset configurations are chosen. Error bars (95% confidence interval) are smaller than the symbols. The lines correspond to linear regressions of the simulation results.

6.2.5. Variation of the vapor sticking coefficient

The sensitivity of the vapor containment efficiency to the sticking efficiency has been determined by a variation in the range $\xi \in [0.9, 1.0]$. The results are compared in Fig. 6.9. The containment efficiency is sensitive to the sticking coefficient. If the sticking coefficient is smaller than unity even an opaque baffle does not exhibit a containment efficiency of unity in the limit of free-molecular flow because particles have a chance to be reflected upon impinging the baffle plates. A linear relationship is found between the containment efficiency and the sticking coefficient. Irrespective of the design the scaling becomes stronger with decreasing Knudsen number. However, overall the scaling is significantly stronger for the offset configuration.

6.3. Implications for the application in Tokamak exhaust pumping

In view of the pulsed operation in Tokamaks three main design philosophies can be distinguished:

Firstly, the baffle can be designed to operate exclusively in the free-molecular regime, which guarantees the highest vapor containment efficiency. This, in turn requires that the conditions

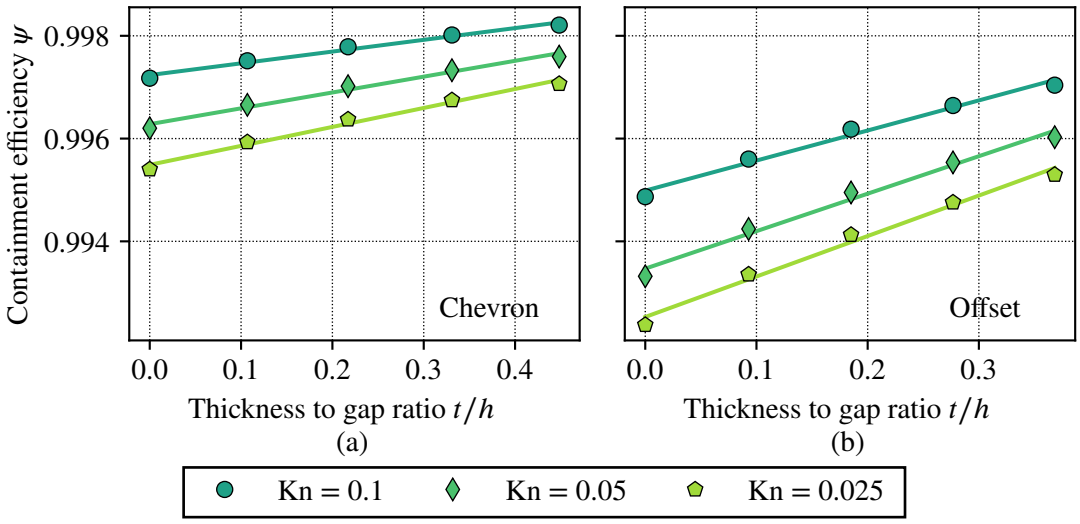

Figure 6.8.: Baffle vapor containment efficiency ψ as a function of the plate thickness to gap ratio t/h for both baffle types ((a) chevron, (b) offset). The overlap to gap ratio is $\delta/h = 0$. The vapor sticking coefficient is $\xi = 1$. The optimum angles of 30° for chevron and 25° for offset configurations are chosen. Error bars (95% confidence interval) are smaller than the symbols. The lines correspond to linear regressions of the simulation results.

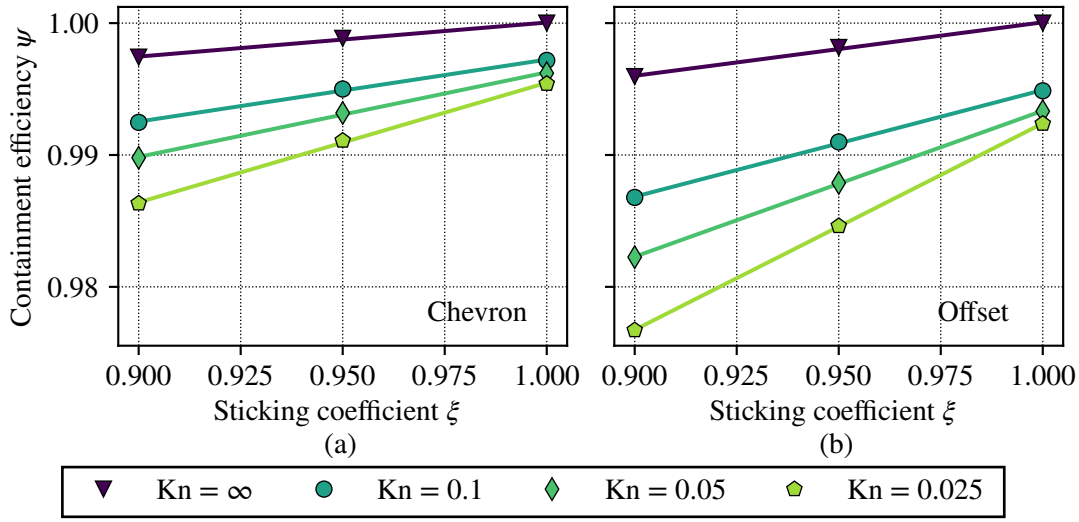

Figure 6.9.: Baffle vapor containment efficiency ψ as a function of the sticking coefficient ξ for both baffle types ((a) chevron, (b) offset). The baffles are very thin, i.e. the thickness to gap ratio $t/h \approx 0$ and the overlap to gap ratio is $\delta/h = 0$. The optimum angles of 30° for chevron and 25° for offset configurations are chosen. Error bars (95% confidence interval) are smaller than the symbols. The lines correspond to linear regressions of the simulation results.

(mainly pressure) at the baffle installation position are known a priori. The advantage of this approach is that the performance (i.e. transmission probability and vapor containment efficiency) during burn and dwell is almost similar. This is supported by the declining influence of the Knud-

sen number on the performance metrics for Knudsen numbers $\mathrm{Kn} \gtrapprox 1$. The disadvantage of this approach is that the manufacturability restricts the lower limit of the thickness to gap ratio t/h, which in turn impairs the transmission probability (Fig. 6.7). For example, when estimating the pressure level during burn phase to be approximately 1 Pa (corresponding to mean free paths of approx. 2 mm and 14 mm for pure mercury and helium respectively), the baffle dimensions have to be chosen in the order of magnitude of $L = 5.5\,\mathrm{mm}$ and $h = 1.5\,\mathrm{mm}$ to reach a Knudsen number of approximately 5 (assuming an average mean free path of 8 mm). It is estimated that the minimum thickness that can be manufactured with integrated cooling channels is in the order of magnitude of $t = 5\,\mathrm{mm}$. For this reason the thickness to gap ratio t/h has to exceed unity leading to an extremely low transmission probability (cf. Fig. 6.7, which is however limited to $t/h < 0.5$). Thus, such a design strategy is not feasible on a technical level.

Secondly, if permissible with respect to plasma radiation losses and other requirements, some mercury back flow can be tolerated and thus, the baffle can be operated outside the free-molecular regime during the burn phase. In this case, the design has to compromise between a lower mercury containment efficiency at higher transmission probability. At present no reliable estimation can be made on the permissible mercury flow rate to upstream systems. Thus, to still provide some reference dimensions to compare to, the largest technically realizable dimensions which are expected to be in the order of magnitude of $L = 200\,\mathrm{mm}$ are considered. This results in Knudsen numbers $\mathrm{Kn} > 5$ for pressures $\lessapprox 25\,\mathrm{mPa}$, which is one to two orders of magnitude higher than the pressure expected during the dwell phase. For these dimensions the Knudsen number during the burn phase ($\approx$1 Pa) corresponds to approximately $\mathrm{Kn} = 0.125$. The simulation results shown allow for the first time to estimate the mercury containment efficiency quantitatively if such a configuration is chosen.

Thirdly, the baffle geometry can be adjusted between burn and dwell phases. For example this can be achieved using the offset configuration by rotating the left and right baffle plates relative to each other. This way the baffle can be optimized to feature a high transmission probability during the dwell phase and the performance can be artificially "throttled" during the burn phase. While a rotation does not change the Knudsen number significantly due to an artifact of the chosen definition in the present chapter (cf. Eq. (6.3)), it changes the overlap to gap ratio δ/h, which has a significant impact on the transmission probability as well as vapor containment efficiency. The realization of such a configuration requires cryo-rotary joints that can be operated in the magnetic field close to the Tokamak. Since only two manipulations at very low rotation speeds are necessary per pulse this seems plausible. Cryo-rotary joints have been developed for the more challenging application in high-temperature superconductor motors and can be operated with different cooling fluids, among them gaseous and liquid nitrogen which are candidates for the baffle cooling [214]. A second plausible implementation of this concept lies in the introduction of additional, not actively cooled, rotatable plates that are installed in the gap between the regular baffle plates. During the dwell phase these can be oriented in parallel to the original plates, thus reducing the performance only slightly. During burn, they can be rotated to partially close the gap between the original baffle plates, thus increasing the number of collisions. Lastly, the basic idea can also be implemented using a high vacuum valve at the upstream side of the baffle. Partially closing this valve during the burn phase decreases the pressure inside the baffle thus increasing the Knudsen number. All of these approaches introduce further complexity in the form of moving parts as compared with a stationary baffle design. However, since the actuation speeds are slow compared to e.g. a turbomolecular pump, they are not considered problematic in view of the high magnetic fields close to the torus. Furthermore, moving parts provide more flexibility during the operation as they provide a means of adjusting the effective pumping speed of the diffusion pumps. Said flexibility might for example be required for the regulation of the MFP operating pressure. It is known that this pressure has a lower limit that is given by the ignition condition of the cold plasma [215]. Thus, a

valve on the upstream side of the baffle can be used to regulate the pressure in order to ensure that the MFPs are operable.

Based on the qualitative discussion above, a preliminary design of a diffusion pump vapor trap featuring two baffle stages and including a valve for the application in torus exhaust pumping is discussed in detail in Chap. 7.

7. Application to the EU-DEMO high vacuum pumping system

The purpose of this chapter is to derive a preliminary design of a high vacuum pumping system based on mercury-driven diffusion pumps for the European demonstration fusion power plant (EU-DEMO). This is accomplished in several steps: Firstly, the expected operating conditions of the high vacuum system and the requirements it needs to meet are summarized. Next, a preliminary design for a mercury-driven diffusion pump in EU-DEMO relevant scale is established using the developed and validated DSMC simulation model. The diffusion pump design is complemented with a mercury vapor trap design based on the parametric baffle studies. Finally, a simplified model is proposed to estimate the integrated system performance. This model is then used to compare against the requirements and to identify sensitivities of the involved subsystems.

7.1. Operating conditions and requirements

A Tokamak vacuum pumping system has to fulfill distinct functions during burn and dwell phases. Currently, the preliminary architecture of the high vacuum system of EU-DEMO comprises three main components arranged in the following order when following the pumping path of the exhaust gas mixture:

1. Metal foil pumps, which separate about 80 % of the unburnt D-T fuel to the DIRL during the burn phase by means of superpermeation,

2. mercury baffle adapter (MBA), which is responsible for condensing and desublimating residual mercury vapor,

3. mercury-driven vapor diffusion pumps featuring a linear design for pumping the MFP retentate in the INTL during burn and for dwell pumping.

In order to achieve the necessary performance several versions of the above configuration are installed in parallel in multiple pumping ports distributed around the Tokamak. The pumping ports are connected to the Tokamak torus below the divertor. The requirements and estimations of the associated operating conditions are summarized in Tab. 7.1. The layout and dimensions of the pumping ports are in large parts defined by the limited space close to the Tokamak. In the present work the configuration discussed in [216, 217] is considered. Furthermore, a preliminary MFP configuration is assumed in the present work [218]. The transmission probability $w_{\mathrm{duct+MFP}}$ corresponds to the combination of the vacuum duct and MFPs (in the assumed configuration). The operating pressures given in Tab. 7.1 correspond to the conditions expected in the divertor. For a lack of accurate data these pressures are also assumed at the inlet cross-section of the pumping ports, which are situated in the sub-divertor, in the present work. It is emphasized that these are subject to change due to uncertainties with respect to the divertor performance for which no final design exists as of yet. The pressure at the inlet of the VDPs is expected to be lower because of conductance losses in the pumping path comprised of pumping duct, MFPs (as given by $w_{\mathrm{duct+MFP}}$) and baffle adapter.

Table 7.1.: List of tentative operating conditions of the EU-DEMO torus high vacuum pumping system and pumping requirements. The sub-divertor pressures are subject to change due to uncertainties regarding the divertor performance.

Property	**Symbol**	**Value (range)**	**Reference**
System layout			
Number of pumping ports	N_{ports}	10 ± 2	[219]
Pumping duct inflow cross-section	$A_{\mathrm{duct,in}}$	$5.62\,\mathrm{m}^2$	[216, 218]
MFP to MBA cross-section	$A_{\mathrm{MBA,in}} = A_{\mathrm{MFP,out}}$	$3.04\,\mathrm{m}^2$	[218]
Transmission probability (incl. MFPs)	$w_{\mathrm{duct+MFP}}$	0.104	[218]
Burn phase			
(Sub-) divertor pressure	p_{burn}	3 Pa	[217]
(Sub-) divertor temperature	T_{DIV}	573.15 K	estimated
Max. total throughput	q_{burn}	$427\,\mathrm{Pa\,m^3\,s^{-1}}$	Sec. 2.1.2
Mole fractions Q_2 / inert	$x_{\mathrm{Q_2}}/x_{\mathrm{inert}}$	0.99 / 0.006	Sec. 2.1.2
MFP separation efficiency	η_{DIR}	0.8	[18, 19]
Max. INTL throughput	$q_{\mathrm{burn,INTL}}$	$88\,\mathrm{Pa\,m^3\,s^{-1}}$	Sec. 2.1.2
INTL mole fractions Q_2 / inert	$x_{\mathrm{Q_2,INTL}}/x_{\mathrm{inert,INTL}}$	0.97 / 0.03	Sec. 2.1.2
Dwell phase			
Final sub-divertor pressure	p_{dwell}	≤ 2 mPa	[217]
Pump-down time	$\Delta t_{\mathrm{dwell}}$	600 s	[19]
First wall protium outgassing	$q_{\mathrm{H_2}}$	$0.0715\,\mathrm{Pa\,m^3\,s^{-1}}$	[19]
Torus volume (including ports)	V_{torus}	$6400\,\mathrm{m}^3$	[220]

Based on the reported requirements the necessary effective capture coefficient can be estimated during both Tokamak phases. During burn this is a direct consequence of the maximum throughput in the INTL loop and the temperature and pressure expected in the sub-divertor region where the pumping system is connected. When assuming DT, which is the most abundant species in the exhaust gas mixture, the required capture coefficient can be estimated according to

$$\varsigma_{\mathrm{eff,burn}} = \frac{q_{\mathrm{burn,INTL}}}{N_{\mathrm{ports}}} \cdot \frac{T_{\mathrm{DIV}}}{273.15\,\mathrm{K}} \cdot \frac{1}{p_{\mathrm{burn}}} \cdot \frac{4}{\bar{v}_{\mathrm{DT}}(T_{\mathrm{DIV}}) A_{\mathrm{duct,in}}} = 0.00282. \tag{7.1}$$

During dwell the pumping system has to reduce the pressure inside the torus starting from the burn pressure in order to achieve the conditions required to initiate the next plasma ramp-up phase. The time to achieve this has to be kept as short as possible for economic reasons, which is challenging due to the large torus volume. The situation is aggravated by gas loads into the torus, constituted in large parts by outgassing from the first wall. As of now, only estimations of the outgassing rate are available. The rate reported in Tab. 7.1 corresponds to integral protium outgassing of tungsten, which is the projected first wall material of EU-DEMO. However, it does not consider plasma driven implantation of Q_2 and neutron induced damage to the wall material, which both are expected to alter the composition and magnitude of the outgassing rate over the lifetime of the first wall material [19, 221]. Therefore, the reported rate can be conceived only as a lower limit. Due to the uncertainty regarding the outgassing rate, the required capture coefficient during dwell is derived as a function of the outgassing rate from the transient pumping equation (Eq.

(2.10)). Combined with the other requirements and limitations this allows to identify a viable range of the effective capture coefficient as displayed in Fig. 7.1. If the protium outgassing rate of tungsten is considered as the lower limit of the dwell gas load, the workable effective capture coefficient is solely determined by the dwell pumping requirements. Additionally, comparison of the three included pump-down times reveals that the dwell requirements are only sensitive towards the pump-down time at outgassing rates lower than expected in a DEMO-scale fusion reactor. Thus, the dwell requirement can be simplified to the steady-state value (corresponding to the curve

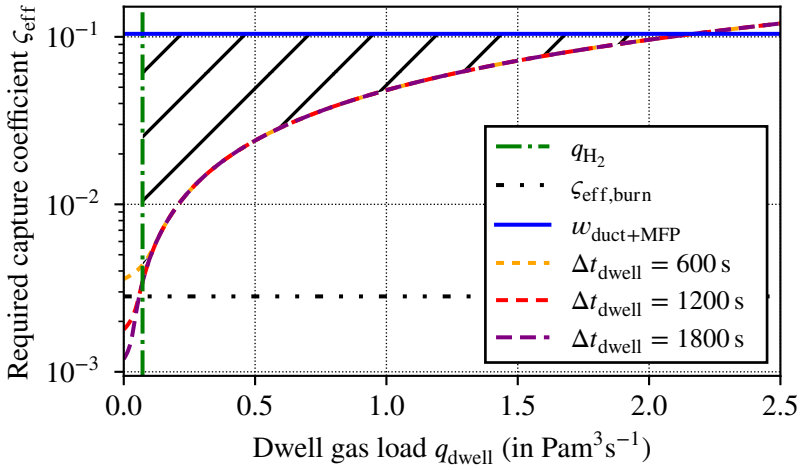

Figure 7.1.: Required effective capture coefficient ς_{eff} at the pumping duct inlet cross-section as a function of the dwell gas load q_{dwell} assuming $N_{\mathrm{ports}} = 10$ and DT as the pumped gas species for three different pump-down times $\Delta t_{\mathrm{dwell}} \in \{600, 1200, 1800\}$ s. The possible range of the effective capture coefficient of the integrated system is indicated by the hatched area as a result of the superposition of requirements of the burn phase, dwell phase, the upper limitation by the transmission probability of the duct and MFPs $w_{\mathrm{duct+MFP}} = 0.104$ and the estimation of the first wall protium outgassing $q_{\mathrm{H_2}}$.

to which all three $\Delta t_{\mathrm{dwell}}$ converge in Fig. 7.1):

$$\varsigma_{\mathrm{eff,dwell}} = \frac{q_{\mathrm{dwell}}}{N_{\mathrm{ports}}} \cdot \frac{T_{\mathrm{DIV}}}{273.15\,\mathrm{K}} \cdot \frac{1}{p_{\mathrm{dwell}}} \cdot \frac{4}{\bar{v}_{\mathrm{DT}}(T_{\mathrm{DIV}}) A_{\mathrm{duct,in}}} = q_{\mathrm{dwell}} \cdot 0.0481\,\mathrm{s\,Pa^{-1}\,m^{-3}}. \quad (7.2)$$

The next section introduces a concept that allows to estimate the effective high vacuum system performance, i.e. ς_{eff}, based on the individual performances of its components.

7.2. Estimation of the effective high vacuum system performance

The effective performance of vacuum systems can be modeled in two fundamentally different ways: Either the full system is incorporated and solved in a single model or the simulation results of dedicated sub-models for parts of the system can be combined by satisfying the particle balance between the systems. The approaches can be differentiated based on the quality of the results and the efficiency. The former approach yields higher-quality results because it involves fewer simplifications and assumptions. Because subsystem models are independent in the latter approach, it has the advantage that the most efficient method and tool can be chosen for each subsystem model.

Furthermore, changes in any of the subsystems only effect the respective model whereas the entire system has to be recomputed in the integrated approach. At the time of writing the high vacuum exhaust pumping system of EU-DEMO is in the concept design stage, which implies that changes to subsystems are frequent. For this reason the latter approach is currently pursued.

The *Ansatz of Oatley* provides a semi-empirical method to estimate the integrated performance of complex vacuum systems under the assumption of isothermal free-molecular flow [222–225]:

$$\begin{aligned}\frac{1}{A_{1,\mathrm{in}}}\left(\frac{1}{\varsigma_{\mathrm{eff}}}-1\right) =& \frac{1}{A_{N,\mathrm{in}}}\left(\frac{1}{\varsigma_N}-1\right)+\sum_{i=1}^{N-1}\frac{1}{A_{i,\mathrm{in}}}\left(\frac{1}{w_i}-1\right)\\ &+\sum_{i=2}^{N}\frac{1}{A_{i-1,\mathrm{out}}}\left(\max\left\{\frac{A_{i-1,\mathrm{out}}}{A_{i,\mathrm{in}}},1\right\}-1\right).\end{aligned} \tag{7.3}$$

Equation (7.3) allows estimating the effective system capture coefficient ς_{eff} of a vacuum system composed of N serial subsystems as a function of the subsystem properties. Conceptually, it has some similarities with the calculation of the electrical current in a serial connection subject to electrical resistances [223]. Subsystems $i \in [1, N-1]$ correspond to flow resistances (pipes, valves, etc.), whereas the final subsystem N represents the vacuum pump whose effective capture coefficient is to be estimated at the system inflow cross-section $A_{1,\mathrm{in}}$. Each subsystem $i \in [1, N]$ is characterized by three quantities: Its inflow cross-section $A_{i,\mathrm{in}}$, its outflow cross-section $A_{i,\mathrm{out}}$ and its transmission probability w_i or in case of the vacuum pump its capture coefficient ς_N. The first term on the r.h.s. of Eq. (7.3) describes the pumping action generated by the vacuum pump. The second term considers the reduction of the effective capture coefficient by the limited transmission probabilities of the involved subsystems. Finally, reductions of the cross-section between subsystems in flow direction are considered as additional orifices by means of the last term.

The Ansatz of Oatley as well as similar approaches are commonly used to model the integrated performance of complex vacuum systems. With regard to nuclear fusion, similar approaches have been used in the past. Some prominent examples are the software *ITERVAC* that was used to model the ITER vacuum systems [226] and recently the ones of the Russian DEMO project (*Tokamak with Reactor Technologies*, *TRT*) [227]. Both of these have in common that they describe the complex conductance of the vacuum system as an interconnection of simple elements for which semi-empirical analytical expression are available. In case of ITERVAC the solution is provided for all flow regimes, whereas the TRT model assumes free-molecular flow. The present work and a previous publication by the author [228] differ from the previously mentioned ones in that sophisticated simulation results of whole subsystems are used instead of modeling them as a composition of simpler, analytical elements.

Thus, in order to apply Eq. (7.3) to the EU-DEMO high vacuum pumping system, the transmission probabilities / capture coefficients and flow cross-sections of the individual subsystems are required. While these are available for the MFP configuration that is assumed in the present work (cf. Tab. 7.1), they have to be determined for VDPs (cf. Sec. 7.3) and MBA (cf. Sec. 7.4). Afterward, the integrated performance of the high vacuum system incorporating these designs is estimated using the Ansatz of Oatley in Sec. 7.5. The results are compared to the required performance to determine the feasibility.

7.3. Preliminary design and performance of the diffusion pumps

Currently, a *linear vapor diffusion pump (LDP)* design is favored for EU-DEMO because it is simpler to scale and reportedly features higher pumping speeds per inlet cross-sectional area than the conventional cylindrical design [52, 71]. It is noted that the design discussed in the following is preliminary. It serves as a practical demonstration of the applicability of the developed simulation

workflow and how the extracted results can be used to further advance the high vacuum system development. The design is based on previous published DSMC results of LDPs by the author. These comprise parametric simulation of small, single-stage LDPs [131] and simulations of the large, three-stage LDP from [52] that was operated in the 1950s [132].

7.3.1. Introduction and justification of the baseline design parameters and DSMC LDP model

The baseline design of the LDP proposed for EU-DEMO and the corresponding DSMC simulation domain are depicted in Fig. 7.2. Similar to the large mercury-driven LDP of Lind and Steinhaus [52], three linear nozzle stages are included in the baseline design. Of those, the uppermost stage is responsible for providing the high pumping speed at low pressures, whereas the lower stages generate the compression. The successive compression from inlet to outlet is supported by the tapered walls of the pump, which lead to an area ratio of 20:1 between pump inlet and outlet. Additionally, the opening angle of the nozzles stages is successively reduced from 40° (top) over 30° (mid) to 20° (bottom) to adapt the respective expansion ratio to the increasing pressure of the surrounding gas. The walls are actively cooled by external cooling coils to facilitate the condensation of mercury vapor. The dimensions of the baseline LDP design are chosen such that three LDPs can be installed in parallel in each available pumping port, to enlarge the effective pumping cross-section from $A_{\mathrm{LDP,in}} = 0.56\,\mathrm{m}^2$ (single LDP) to $1.68\,\mathrm{m}^2$ (per port).

The two-dimensional DSMC simulation domain corresponds to the symmetric half of a cut through the pump. A three-dimensional DSMC simulation of the domain is prohibitive with regard to computational resources when adhering to the recommended DSMC simulation parameter range. The necessity to adhere to the former rules was confirmed by Liao et al. [104], who simulated the pump of [52] using three-dimensional DSMC under violation of the DSMC discretization parameters. Based on a mesh variation study they conclude that the chosen parameters do not yield accurate results [104]. Additionally, it was confirmed in [132] by the author that two-dimensional DSMC simulations agree with acceptable accuracy with the experimentally measured pumping speeds of [52]. For these reasons only two-dimensional simulations are performed in the present work and the results should be understood in this context. Due to the inherently assumed periodicity in the third direction (along the linear length of the pump) boundary effects on the front and back housing walls are ignored in the two-dimensional model. Furthermore, the vapor flow in the nozzle pipes, which have to be fed from both sides, is not considered. Results are thus either reported in relation to the unit length or extrapolated to three-dimensions by scaling with the linear length $L = 1750\,\mathrm{mm}$ of the pump.

The following boundary conditions are applied at the interfaces indicated in Fig. 7.2 (b):

- ①, ② & ③ nozzle throats: Injection of mercury vapor particles according to a shifted Maxwell-Boltzmann distribution function. The nozzle throat corresponds to the critical nozzle cross-section where the flow chokes. Thus, the number density, temperature and speed at the boundary are estimated from the one-dimensional isentropic relationships (cf. Sec. 3.3.1) by assuming a Mach number of unity at the throat. The stagnation conditions are assumed to be saturated vapor and the saturation curve by Huber et al. [68] is used. Mercury vapor particles colliding with the throat are leaving the simulation domain. If not otherwise specified, the stagnation conditions $T_{\mathrm{Hg},0} = 413.15\,\mathrm{K}$ and $p_{\mathrm{Hg},0} = 247.8\,\mathrm{Pa}$ are assumed at these boundaries.

- ④ inlet: At this interface either the pressure or throughput of the gas are prescribed. In both cases the emitted gas particles are determined from a Maxwell-Boltzmann distribution function assuming zero bulk velocity. If the pressure is prescribed, gas particles colliding

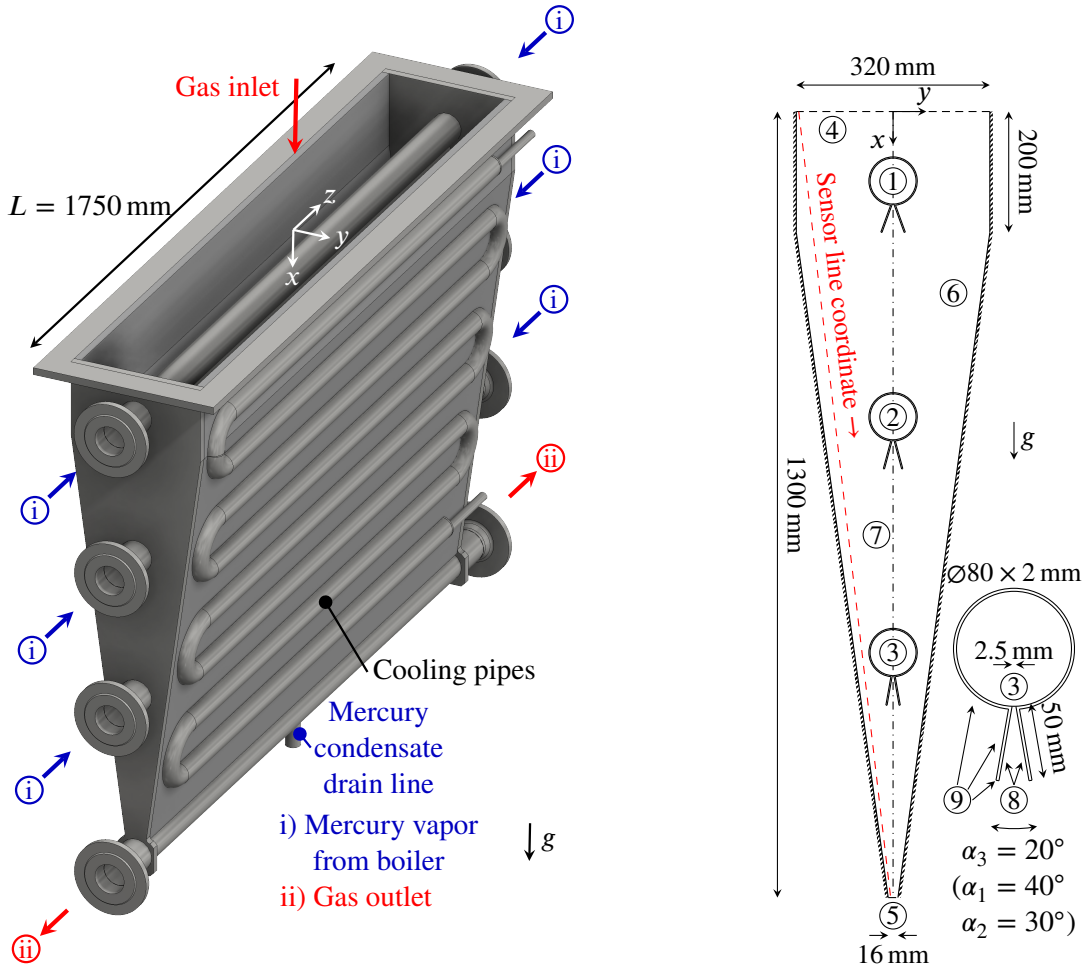

Figure 7.2.: (a) CAD drawing of the preliminary linear diffusion pump design. (b) Two-dimensional DSMC LDP model including the important dimensions and boundary conditions. The three nozzle stages have opening angles of 40, 30 and 20° respectively (from top to bottom). The boundaries are labeled: ①, ②, ③ throats of the three nozzle stages (each with width of 2.5 mm), ④ inlet (connection to mercury baffle adapter), ⑤ outlet (connection to backing pump), ⑥ outer, actively cooled wall of the pump, ⑦ symmetry axis, ⑧ inner wall of the nozzle skirts, ⑨ tip and outer wall of the nozzle skirts and nozzle pipe. The boundary conditions are described in the text. The dashed red line corresponds to a continuous, straight sensor line between inlet and outlet (in both cases spaced 4 mm from the pump wall) and is used to compare local flow quantities.

with the surface are leaving the simulation domain. However, if the throughput is prescribed, gas particles colliding with the surface are diffusely reflected. Mercury particles are leaving the simulation domain irrespective of the boundary condition type. The temperature at this interface is assumed to be $T_{\text{inlet}} = 240\,\text{K}$ in all simulations in agreement with the baffle that is installed upstream.

- ⑤ outlet: The pressure of the gas is prescribed, and outgoing gas particles leave the simulation domain. In the case of mercury vapor concurrent condensation and evaporation at the

assumed interface temperature is implemented assuming a condensation coefficient of unity and steady evaporation at saturation conditions (cf. Sec. 3.5.5). If not otherwise specified, the temperature at this interface is assumed to be constant at $T_{\mathrm{cool}} = 280.15\,\mathrm{K}$ corresponding to the cooled walls.

- ⑥ cooled wall: Gas particles colliding are diffusely reflected. Mercury vapor condenses at this surface and is partly re-evaporated at saturation conditions similar to the outlet. Additionally, the same temperature $T_{\mathrm{cool}} = 280.15\,\mathrm{K}$ as at the outlet is prescribed.

- ⑦ symmetry plane: A symmetry boundary conditions is assumed here to halve the simulation domain.

- ⑧ inner walls of the nozzle skirts: Adiabatic boundary conditions (cf. Sec. 3.5.5) are assumed for all particle collisions with the inner nozzle skirt walls.

- ⑨ tip and outer wall of the nozzle skirts and outer nozzle pipe walls: A constant temperature corresponding to the mercury vapor stagnation temperature is assumed for these surfaces and all particles are diffusely reflected upon collision. This overestimates the temperature but is conservative regarding the backstreaming rate.

The DSMC simulation setup is adapted from the setup used for the simulations of the NEMESIS experiment. In particular the domain is initialized with a structured, rectangular grid of $1{\times}1\,\mathrm{mm}^2$ cells. The same dynamic grid refinement based on the local mixture mean free path and number of simulator particles per cell described in 4.3 is used. Thus, the final grids (depending on boundary and flow conditions) typically contain about 1.2 million cells. A time step of $\Delta t = 2.5 \times 10^{-8}\,\mathrm{s}$ is chosen, which ensures that the mean collisions time is resolved and that particles travel less than one cell per time step on average. Depending on the gas compression ratio, species weighting zones are used to increase the number of gas simulator particles in the LDP volume above the lowest nozzle.

The DSMC simulations are started with an empty domain. Therefore, a certain amount of time steps are required to establish the stationary particle distribution in the system, which is characterized by a stabilized number of simulator particles per species. The attainment of steady-state is sped up by starting with a time step eight times higher than the final value and numerical weight four times higher than the final value. These settings are reduced step-wise after steady-state is reached for the previous setting. Afterwards, the collection of moment averaging samples is started to facilitate the calculation of the macroscopic quantities of interest. Samples are collected in every time step for 500,000 total time steps.

The DSMC settings summarized above ensure a balanced trade-off between accuracy and computational cost. It has been verified that the chosen setup yields DSMC parameter independent results by comparison with a refined case employing significantly more grid cells (7.9 million), a lower time step ($\Delta t = 1.25 \times 10^{-8}\,\mathrm{s}$) and more simulator particles (factor four). A detailed comparison of the standard and refined setups is available in Appendix A.7.1.

The next sections describe how the diffusion pump performance indicators are determined from the DSMC simulation results and how to interpret these results in the context of operation during burn and dwell phases of EU-DEMO. As the mixed isotopologue DT accounts for almost half of the exhaust gas mixture composition, most parametric studies are carried out assuming pure DT as the pumped gas and only selected simulations are performed for other constituents.

7.3.2. Pumping speed and capture coefficient

The pumping speed is determined as

$$S = \frac{\dot{N}_{\mathrm{gas,DSMC}}}{n_{\mathrm{gas,inlet}}}, \tag{7.4}$$

where $\dot{N}_{\mathrm{gas,DSMC}}$ is the net number flow rate of the gas through the inlet as determined by the DSMC simulation and $n_{\mathrm{gas,inlet}}$ the number density of the gas as prescribed by the boundary condition at the inlet. Because a resting gas is assumed in the boundary condition this corresponds to the conditions in an infinite reservoir upstream of the pump. This definition is chosen to be as compatible as possible with the recommended experimental pumping speed determination procedure laid out in [204]. Accordingly, the capture coefficient is determined by

$$\varsigma = \frac{4\dot{N}_{\mathrm{gas,DSMC}}}{n_{\mathrm{gas,inlet}}\bar{v}_{\mathrm{gas,inlet}}A_{\mathrm{inlet}}} = \frac{4S}{\bar{v}_{\mathrm{gas,inlet}}A_{\mathrm{inlet}}}, \tag{7.5}$$

where $\bar{v}_{\mathrm{gas,inlet}}$ corresponds to the mean thermal speed of the injected gas at the prescribed temperature.

The pump efficiency η_ς is obtained by comparison of the capture coefficient with the theoretical upper limit of the capture coefficient $\varsigma_{0,\mathrm{max}}$ given by the one-dimensional model, i.e.

$$\eta_\varsigma = \frac{\varsigma}{\varsigma_{0,\mathrm{max}}}, \tag{7.6}$$

where $\varsigma_{0,\mathrm{max}}$ is calculated from Eq. (4.9) under the assumption of infinite vapor expansion.

With regard to the pulsed Tokamak operation it is important to determine the pumping speed over a wide range of inlet pressures. For this reason several simulations assuming DT have been performed under the assumption of a constant outlet pressure and variation of the inlet pressure. The resulting normalized pumping speed curve for the baseline LDP design and operation is shown in Fig. 7.3 as a function of the inlet pressure. The pumping speed curve exhibits a plateau at low inlet pressures, which is a characteristic feature of vapor diffusion pumps. At inlet pressures above approximately $p_{\mathrm{DT,inlet}} = 0.01\,\mathrm{Pa}$ a decline of the pumping speed is observed and the operational range ends above approximately $p_{\mathrm{DT,inlet}} = 0.1\,\mathrm{Pa}$ as a result of the increasing number of vapor-gas collisions that start to weaken the upper stage vapor jet. During the burn phase, the LDPs have to handle the largest throughput, which is at most $q_{\mathrm{burn,INTL}} = 88\,\mathrm{Pa\,m^3\,s^{-1}}$ (cf. Tab. 7.1). Thus, assuming ten pumping ports and three parallel LDPs per port, the throughput each LDP has to handle is approximately $q_{\mathrm{burn,LDP}} \approx 3\,\mathrm{Pa\,m^3\,s^{-1}}$. The corresponding inlet pressure of $p_{\mathrm{DT,inlet}} = 0.081\,\mathrm{Pa}$ has been determined by first performing a simulation with fixed throughput as inlet boundary condition and then identifying and performing a matching simulation with prescribed inlet pressure.

The theoretical upper limit of the capture coefficient for the given pump operating conditions is $\varsigma_{0,\mathrm{DT,max}} = 0.69$. In combination with the simulated capture coefficient this results in a pump efficiency of approximately $\eta_\varsigma = 0.35$ in the plateau region. The comparatively low efficiency is a result of several influencing factors. Of these, the most crucial factor is the geometry of the pump, which inherently reduces the efficiency due to the limited conductance between the pump inlet and first stage vapor jet, which in turn is to a great extent determined by the nozzle pipe blocking part of the cross-section.

7.3.3. Superheating of the mercury vapor

One possibility to increase the pumping speed of diffusion pumps is to superheat the operating fluid vapor beyond the saturation state [59]. Superheating increases the capture coefficient because

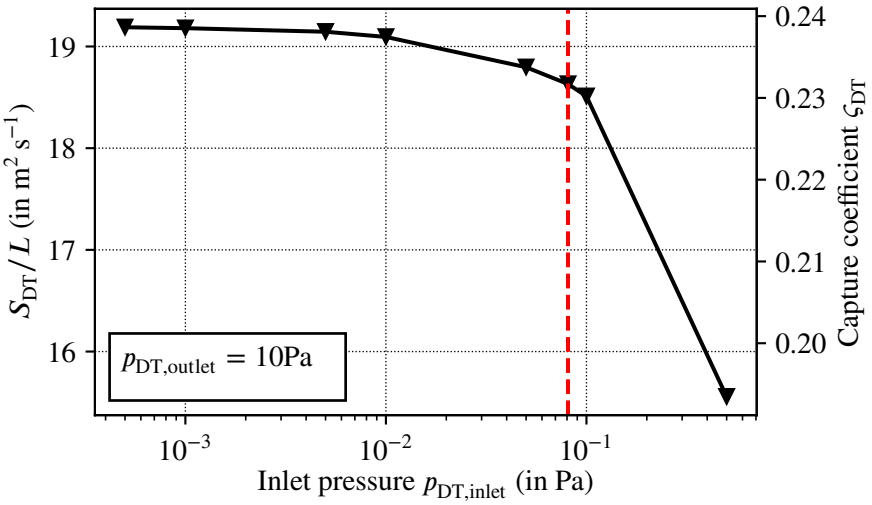

Figure 7.3.: LDP pumping speed per unit length S_{DT}/L and capture coefficient ς_{DT} as a function of the DT inlet pressure $p_{DT,inlet}$. Simulation results are indicated by the symbols and connected with straight lines to guide the eye. The dashed red line indicates the inlet pressure corresponding to the maximum throughput of $q_{burn,LDP} = 3\,\mathrm{Pa\,m^3\,s^{-1}}$ per LDP that is expected during the Tokamak burn phase (see derivation in text).

the speed of sound and thus the speed ratio between vapor velocity and thermal velocity of the pumped gas increase with the vapor stagnation temperature. The effectiveness of superheating the mercury vapor in LDPs has been determined by comparison of three cases: A baseline case using saturated mercury vapor, and two cases with superheating by 50 and 100 K, respectively. A comparison of the results is available in Tab. 7.2. Evidently, superheating does enhance the capture coefficient as theoretically expected. However, the relative improvement predicted by the DSMC simulations is less pronounced than the relative improvement given by the theoretical upper limit. The reason for this is the limited pump efficiency that has already been determined in the previous section. The decision on whether to install superheating has to be based on economic considerations. While the improvement is small, the same applies for the required additional power when compared with the boiler power. If the boiler is operated with fluid streams available in the power plant, superheating is trivial to realize in form of an additional heat exchanger. Besides the small performance improvement, it can have the added benefit of preventing or at least reducing vapor condensation in the feed lines (as likely observed in the NEMESIS experiment).

Table 7.2.: Effect of vapor superheating on the LDP capture coefficient by comparison of three cases: A baseline case assuming saturated vapor and two cases assuming vapor superheated by 50 and 100 K respectively. Numbers in parentheses indicate the relative change to the baseline case.

Property	**Symbol**	**Unit**	**Cases**		
			Baseline	**$\Delta T_{Hg,0}$ =50 K**	**$\Delta T_{Hg,0}$ =100 K**
Stagnation temperature	$T_{Hg,0}$	K	413.15	463.15	513.15
Stagnation pressure	$p_{Hg,0}$	Pa	247.8		
Capture coefficient	ς_{DT}	1	0.234	0.238 (+1.8%)	0.241 (+3.2%)
Theoretical –"–	$\varsigma_{0,DT,max}$	1	0.690	0.711 (+3.0%)	0.729 (+5.7%)

7.3.4. Reduced order model in the operational range

The efficiency of the design process can be enhanced by a combination of the DSMC and the dimensionless model. Such a reduced order model (ROM) can be constructed based on the Ansatz of Oatley (Sec. 7.2), in order to take into account the pump efficiency reduction due to the geometry. The reduced order model has the form

$$\varsigma_{\mathrm{ROM}} = \left[\frac{1}{c_2} \cdot \left(\frac{1}{c_1 \varsigma_{0,\max}} - 1 \right) + \frac{1}{c_3} \right]^{-1}, \tag{7.7}$$

where ς_{ROM} is the capture coefficient of the reduced order model at the LDP inlet and $\varsigma_{0,\max}$ the theoretical upper limit of the capture coefficient at the interface between vapor jet and gas (see dimensionless model in Sec. 4.1). Furthermore, three model parameters are introduced, which describe different physical aspects:

The parameter c_1 describes inefficiencies in the capture coefficient at the virtual pumping surface. Consequently, the valid range of this parameter is $c_1 \in [0, 1]$. This is influenced by various factors, like reflection of the gas due to backstreaming vapor and temperature changes between the LDP inlet (whose temperature is assumed in the calculation of $\varsigma_{0,\max}$) and the virtual pumping surface.

The parameter c_2 corresponds to the area ratio between the virtual pumping surface, i.e. the zone where gas and vapor jet interact and momentum is transferred from the jet to the gas, and the pump inlet cross-section. As the pumping surface is not parallel to the inlet surface but defined by the expansion of the upper nozzle stage vapor jet, the ratio can be larger than unity so that the sensible range is $c_2 \geq 0$.

The parameter c_3 represents the limited transmission probability between the pump inlet and virtual pumping surface, thus, its value range is defined as $c_3 \in [0, 1]$. In LDPs the transmission probability is reduced in particular by the cross-section reduction due to the pipe of the upper nozzle stage as already pointed out before.

The coefficients can be determined from at least three simulation results at different operating conditions. For example, the results of the previous section on vapor superheating can be used to determine $c_1 = 0.405$, $c_2 = 1.45$ and $c_3 = 0.401$. The high area ratio c_2 might seem odd at first sight, however, it corresponds remarkably well with a simple geometric comparison of the prolongation of the upper stage nozzle skirts to the cooled pump wall and the inlet width. The applicability of the model is verified in the next section that compares the capture coefficients for different gas species contained in the exhaust gas mixture. The reduced order model can be used twofold: Firstly, it can reduce the number of computationally demanding DSMC simulations as will be shown in the next section. Secondly, it can be employed in higher level simulation codes for the integrated fuel cycle.

7.3.5. Pumping speed for different exhaust gas constituents

Up to now the pumping speed has only been determined for DT. This is reasonable as hydrogen makes up for about 97 % of the INTL exhaust gas mixture. Therefore, in isotopic equilibrium, about 48 % of the entire mixture are DT and 24 % D_2 and T_2, respectively. Additionally, about 1 % of the hydrogen is H_2 and the mixed isotopologues HD and HT due to protium outgassing from structural materials. The remaining approximately 3 % are mostly helium and plasma enhancement gases like neon or argon. Furthermore, trace amounts of impurities like water Q_2O and hydrocarbons, e.g. CQ_4, are expected [19].

The species dependent pumping speed of high vacuum pumps can effectuate changes in the mixture composition. For this reason the LDP performance has been evaluated for all main constituents of the exhaust gas mixture. The results are compared in Tab. 7.3. It is evident, that the pumping speed depends strongly on the molecular mass of the pumped species. In rarefied conditions, where

no uniform bulk velocity can establish due to intermolecular collisions, the pumping speeds of the individual species closely follow the tabulated values. This is also fulfilled in the upper part of the LDP, which is in the transitional to rarefied regime (Kn $\approx$ 1 during burn and greater during dwell), so that no large deviations from the reported values are expected. This implies that heavy species with lower pumping speeds will enrich upstream of the LDPs. A more detailed discussion of this effect is given later when the integrated system is discussed in Sec. 7.5.2.

Table 7.3.: Comparison of the LDP performance for the main constituents of the fusion reactor exhaust gas mixture. The reported simulations were performed at a gas inlet temperature of 240 K, inlet pressure of 0.05 Pa and outlet pressure of 10 Pa. Additionally, the capture coefficients of the DSMC simulations are compared with the ones predicted by the reduced order model introduced in Sec. 7.3.4.

Species	**Pumping speed**	**Capture coefficient**	
	S **(in** $\mathbf{m^3\,s^{-1}}$**)**	$\varsigma_{\mathbf{DSMC}}$	$\varsigma_{\mathbf{ROM}}$
H_2	41.3	0.186	0.197 (+6.2%)
D_2	35.1	0.223	0.226 (+1.2%)
DT	32.9	0.234	0.234 (+0.038%)
T_2	31.1	0.242	0.240 (−0.86%)
He	36.1	0.229	0.225 (−1.5%)
Ne	20.4	0.291	0.272 (−6.6%)
Ar	14.1	0.282	0.280 (−0.41%)

Additionally, Tab. 7.3 confirms the validity of the reduced order model, which is capable of accurately predicting the capture coefficients of other species albeit the model parameters have been exclusively determined based on DT simulations. The largest deviation is less than 7 %, and the average deviation smaller than 2.5 %. Thus, the combination of the reduced order and DSMC models can be applied in order to significantly reduce the computational requirements of future LDP optimization simulations as these can then be performed for a single species - due to its abundance most reasonably DT - and extrapolated to all other species in the exhaust gas mixture.

7.3.6. Fore-vacuum tolerance and compression ratio

Usually, the fore-vacuum tolerance is measured at constant throughput by observing the pressure evolution at the pump inlet as a function of the fore-vacuum pressure. However, a different approach is taken here by assuming a constant pressure at the pump inlet and simulating the evolution of the throughput because this setup is easier to implement. While the pressure at the inlet starts to rise in the former method, the throughput starts to decline in the latter method when the fore-vacuum tolerance is approached. In order to retain consistency with the definitions of the pumping speed (Eq. (7.4)) and capture coefficient (Eq. (7.5)) the compression ratio is defined as

$$\kappa = \frac{p_{\text{gas,outlet}}}{p_{\text{gas,inlet}}}, \tag{7.8}$$

i.e. as the ratio of the prescribed pressures at in- and outlet boundaries. It is noteworthy that the pressures resulting from the DSMC simulation are slightly lower at the inlet and slightly higher at the outlet compared with the respective prescribed pressures. This is due to the fact that the flow has a non-zero bulk velocity and therefore the effect is more pronounced at the inlet where the bulk velocity is higher due to the lower density.

The fore-vacuum tolerance has been determined for an exemplary inlet pressure level of $p_{\mathrm{DT,inlet}} = 0.05\,\mathrm{Pa}$ by performing several simulations with different prescribed outlet pressures assuming the baseline LDP design and operating conditions. The resulting throughput is shown as function of the outlet pressure and compression ratio in Fig. 7.4. The fore-vacuum tolerance and corresponding maximum compression ratio are characterized by the sharp reduction of the throughput at approximately $p_{\mathrm{DT,outlet}} = 20\,\mathrm{Pa}$. Detailed insight into the breakdown process is provided in Fig. 7.5, which shows the DT pressure evolution along the line connecting LDP in- and outlet, which is indicated in Fig. 7.2 (b) and the inset in Fig. 7.5. It is evident that the mercury vapor jet of the third stage cannot sustain against backing pressures exceeding 10-15 Pa, which effectuates a pressure increase in the volume between second and third stage. Similarly, the second stage breaks down between 20-22.5 Pa. By taking into account the sharp reduction of the throughput visible in Fig. 7.4 it can be inferred that the first stage cannot operate at full load under these conditions.

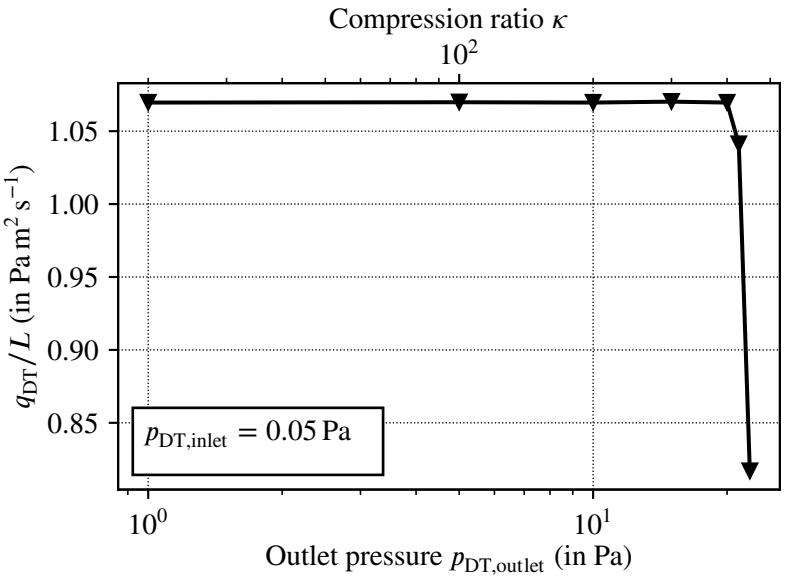

Figure 7.4.: Normalized LDP throughput per unit length q_{DT}/L as a function of the outlet pressure $p_{\mathrm{DT,outlet}}$ and compression ratio κ. Simulation results are indicated by the symbols and connected with straight lines to guide the eye.

Knowledge of the fore-vacuum tolerance is important because it determines the requirements on the backing pumps, which have to operate at the handover pressure.

7.3.7. Mercury backstreaming rate

The backstreaming rate is defined as the net mass flow rate of mercury leaving through the LDP inlet, i.e.

$$\dot{m}_{\mathrm{BS}} = \dot{N}_{\mathrm{Hg,inlet}} m_{\mathrm{Hg}}. \tag{7.9}$$

The mercury backstreaming rate has to be determined for two main reasons: Firstly, backstreaming reduces the pumping speed because it increases the chance that gas molecules are reflected in the volume between pump inlet and jet without being pumped. Secondly, it defines the load that the upstream baffle has to handle and consequently the baffle design which has to compromise between a high gas conductance and high mercury containment efficiency. DSMC simulations of the LDP backstreaming rate have been performed for varying inlet and outlet gas pressures as depicted in Fig. 7.6. Evidently, the mercury backstreaming rate decreases with increasing gas (here DT) inlet

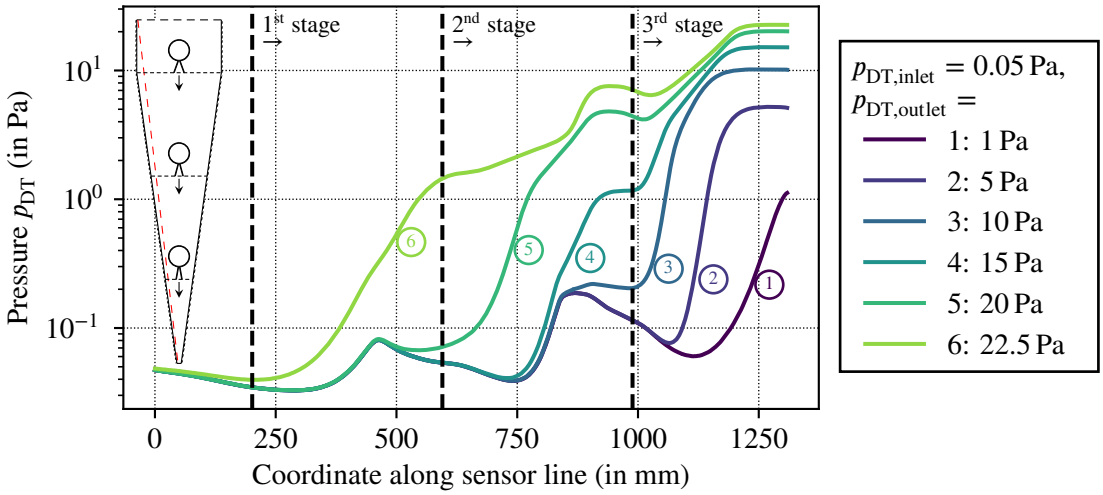

Figure 7.5.: Pressure evolution along the sensor line coordinate between inlet and outlet (dashed red line in the inset and Fig. 7.2) for a constant prescribed inlet pressure of $p_{DT,inlet} = 0.05\,Pa$ and six different prescribed outlet pressures $p_{DT,outlet}$ between 1 and 22.5 Pa. The dashed lines indicate the positions of the nozzle outlet cross-sections of the respective stages.

pressure. This is explicable by the increased amount of intermolecular collisions between gas and mercury vapor. These on the one hand reduce the pumping speed but on the other hand reduce the backstreaming rate as mercury atoms have a chance to be reflected into the pump body. The backstreaming rate is independent of the gas outlet pressure over a wide range and only starts to increase as the fore-vacuum tolerance of the LDP is approached. The backstreaming rate varies between 20 and 30 $mg\,s^{-1}$ per LDP (i.e. with length $L = 1.75\,m$) for burn and dwell conditions respectively.

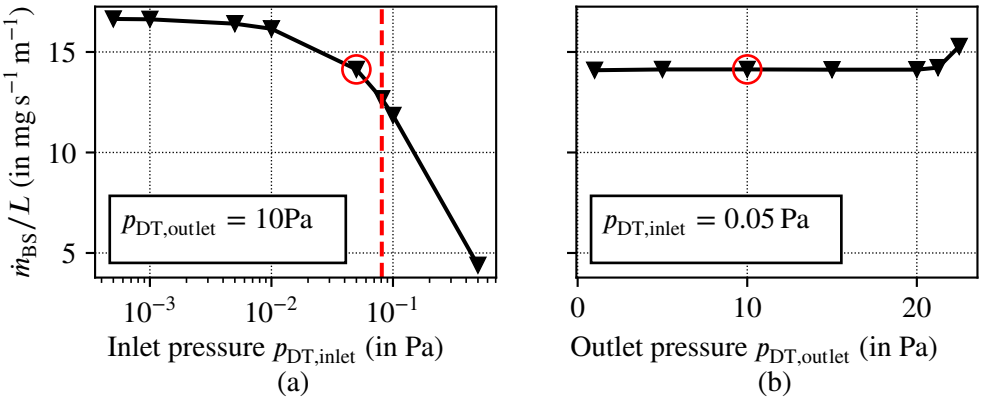

Figure 7.6.: Mercury vapor backstreaming rate per unit length $\dot{m}_{BS}/L$ as a function of (a) the inlet pressure for a fixed outlet pressure and of (b) the outlet pressure for a fixed inlet pressure. Simulation results are indicated by the symbols and connected with straight lines to guide the eye. The points circled in red in both figures correspond to the same case. The dashed red line indicates the inlet pressure corresponding to a throughput of $q_{burn,LDP} = 3\,Pa\,m^3\,s^{-1}$ per LDP as expected during the Tokamak burn phase.

The main reason for the high backstreaming rate is the concurrent condensation and evaporation on the cooled pump walls, which is for the first time modeled realistically in the present work and has been neglected in previous DSMC simulations of diffusion pumps. This is confirmed by a sensitivity study with respect to the wall cooling temperature in the next section.

7.3.8. Sensitivity of the wall cooling temperature

The temperature of the cooled walls determines how much condensed mercury is re-evaporated due to its saturation vapor pressure. Consequently, it is the most important source for mercury backstreaming. In order to quantify the impact, three different realistic wall-cooling temperatures (270.15, 280.15 (baseline) and 290.15 K) have been compared numerically. The results regarding the pumping speed, capture coefficient and backstreaming rate are collected in Tab. 7.4. The comparison underlines the significance of the wall temperature for the pumping speed (and capture coefficient) as well as the mercury vapor backstreaming rate. The pumping speed increases considerably at lower wall temperatures in particular when compared with the much smaller impact of vapor superheating as discussed in Sec. 7.3.3. This is in good agreement with the experimental results of the Livermore LDP [52]. The backstreaming rate scales even stronger with the cooling temperature and changes by a factor of 4.5 between 270.15 and 290.15 K. The primary reason for the observed scaling is the strong temperature dependency of the saturation pressure which changes by a factor of more than 6.5 over the investigated temperature range of 20 K. This is also the dominating factor in the relative change of the term $p_{\mathrm{Hg,sat}}/\sqrt{T_{\mathrm{cool}}}$, which characterizes the theoretical scaling of the evaporation flux (cf. Eq. (3.38)). Comparison between the relative change of this term and the backstreaming rate reveals that the latter scales weaker but in the same order of magnitude. The presumable reason is that the evaporation flux from the walls is also partially limited by the local condensation fluxes in case of the LDP especially at the vertical position of the first nozzle stage and above.

Table 7.4.: Sensitivity of the pump performance to the cooling temperature T_{cool} of the LDP walls. Values in parentheses indicate the relative change to the baseline configuration at 280.15 K. An inlet DT pressure of 0.05 Pa and outlet DT pressure of 10 Pa is assumed in all cases.

Property	**Unit**	**Wall cooling temperature T_{cool}**		
		270.15 K	280.15 K	290.15 K
Hg saturation pressure $p_{\mathrm{Hg,sat}}$	Pa	0.0200 (−62.4%)	0.0531	0.132 (+148%)
$p_{\mathrm{Hg,sat}}/\sqrt{T_{\mathrm{cool}}}$	$\mathrm{Pa}/\sqrt{\mathrm{K}}$	0.00121 (−61.7%)	0.00317	0.00775 (+144%)
Pumping speed S	$\mathrm{m^3\,s^{-1}}$	35.1 (+6.61%)	32.9	29.2 (−11.2%)
Capture coefficient ς	1	0.249 (+6.61%)	0.234	0.208 (−11.2%)
Backstreaming rate $\dot{m}_{\mathrm{BS}}$	$\mathrm{mg\,s^{-1}}$	11.3 (−54.2%)	24.7	51.1 (+107%)

7.3.9. Reduction of mercury backstreaming by guard plates

Backstreaming mitigation is essential for the optimization of diffusion pump designs. Beside the reduction of the wall cooling temperature discussed above, the so-called *cold cap* or *guard ring* [62, 64–67] is particularly effective. This component corresponds to an actively or passively cooled element that is arranged to condense the over-divergent vapor stream leaving the nozzle opposite to the pumping direction. These devices are claimed to be effective for oil- and mercury-driven diffusion pumps.

The concept has been transferred to LDPs in form of so-called *guard plates*, which are installed close to the upper stage nozzle skirts. An almost tenfold decrease of the backstreaming rate was observed under the assumption of perfect mercury vapor condensation on the guard plates and cooled walls in a previous work by the author [131]. Here, a more realistic boundary condition has been employed to analyze if and how this impacts the guard plate efficiency. For this purpose the performance of the baseline LDP is compared to two configurations featuring guard plates maintained at different temperature levels. The position and dimensions of the guard plates can be seen in Fig. 7.7, which also compares the pressure distribution of mercury vapor in the vicinity of the first nozzle stage. The direct comparison reveals that the mercury vapor pressure upstream of the first nozzle is reduced significantly by the installation of guard plates. Furthermore, a reduction of the guard plate temperature from 280.15 K to 240 K, leads to a further reduction in the backstreaming rate due to the lower saturation pressure. Considering that mercury desublimation on the guard plates has to be prevented, the temperature has to be maintained above the triple point 234.32 K [68]. Therefore, the simulation assuming a guard plate temperature of 240 K can be considered as the limiting case.

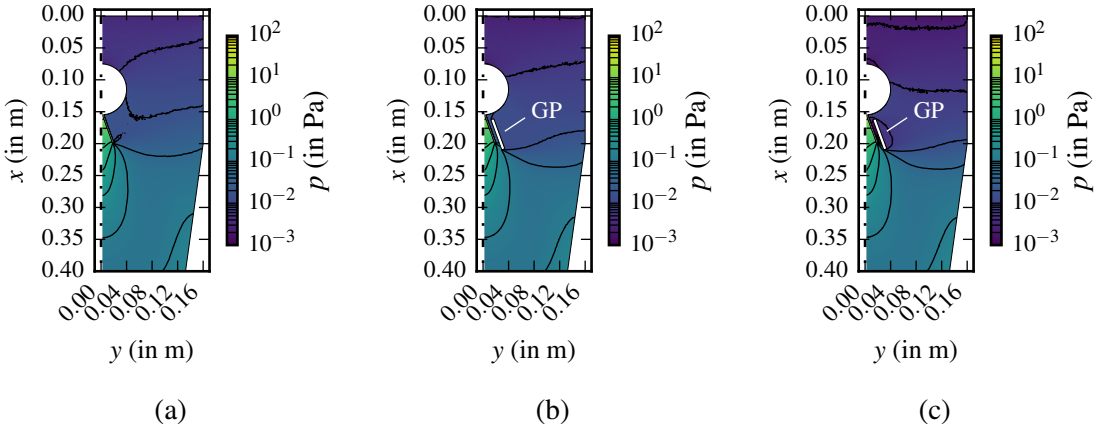

Figure 7.7.: Comparison of the mercury vapor pressure distribution around the upper nozzle stage for three different configurations. (a) Baseline configuration without guard plates; (b) guard plates cooled at 280.15 K; (c) guard plates cooled at 240 K. The temperature of the outer pump casing is 280.15 K in all configurations.

The performance of the three LDP configurations is compared in Tab. 7.5. Discernibly, the backstreaming rate is significantly reduced by the introduction of the guard plates. Compared with the baseline configuration, the backstreaming rate reduces by 25 % when cooling the guard plates to 280.15 K and by 57 % at the lower limit of 240 K. Moreover, the impact of the guard plates on the pumping speed and capture coefficient is negligible as shown in Tab. 7.5. A marginal decrease of the pumping speed is observed for the higher guard plate temperature, whereas the exact opposite is the case for the lower guard plate temperature. This can be attributed to the interplay of the reduction in flow cross-section (which reduces the transmission probability) and the reduction of the backstreaming rate (causing less gas particles to be reflected towards the inlet).

This investigation confirms that the backstreaming reduction predicted by the model employing the more realistic condensation-evaporation boundary condition is not as pronounced as is the case for the simpler model assuming perfect condensation without re-evaporation that has been previously used to simulate single-stage LDPs and predicted a reduction of the backstreaming rate by almost one order of magnitude when guard plates are introduced [131]. However, considering that the installation and cooling of guard plates requires minimal additional expense and infrastructure,

Table 7.5.: Impact of guard plates and their cooling temperature on the LDP performance. Values in parentheses indicate the relative change to the baseline configuration which does not feature guard plates. An inlet DT pressure of 0.1 Pa and outlet DT pressure of 10 Pa is prescribed. Irrespective of the guard plate temperature, the temperature of the outer pump casing is 280.15 K in all cases.

Property	**Unit**	**Baseline**	**Guard plates**	
			280.15 K	240 K
Pumping speed S	$m^3\,s^{-1}$	32.4	31.9 (−1.39%)	32.6 (+0.708%)
Capture coefficient ς	1	0.230	0.227 (−1.39%)	0.232 (+0.708%)
Backstreaming rate $\dot{m}_{BS}$	$mg\,s^{-1}$	20.7	15.4 (−25.5%)	11.8 (−43%)

it is still recommended to implement them in order to reduce the load on the upstream baffle.

7.3.10. Tritium inventory and activity

A key motivation for the research into mercury-driven diffusion pumps is that continuous operation reduces the tritium inventory compared to discontinuous pumping solutions like cryopumps. The steady inventory in the pumps can be determined from the simulations by integrating the local densities over the cell volumes of the simulation domain. The sensitivity with respect to the inlet and outlet gas pressures is depicted in Fig. 7.8. The simulations consider DT as the pumped gas species which is expected to provide a realistic estimation with respect to the tritium inventory. The inventory and activity are found to be insensitive to changes of the inlet pressure in the operational range and only starts to increase once the former is exceeded. The relationship with the outlet pressure is approximately linear up to the fore-vacuum tolerance and intensifies at higher outlet pressures. Based on the simulations the steady gaseous tritium inventory per LDP (i.e. with length $L = 1.75\,m$) is in the range of 25 to 750 µg depending on the pressures at the inlet and outlet of the pump. This tritium mass corresponds to an activity of 9 to 270 GBq. Hence, the total extrapolated tritium inventory in all 30 LDPs (10 pumping ducts, 3 LDPs per duct) is lower than 23 mg; corresponding to 8.3 TBq. It is emphasized that the cases discussed here do not cover all potential operating scenarios. Additionally, the reported inventory does only consider the pump body as shown in Fig. 7.9, which compares the activity density in the LDP for three different combinations of inlet and outlet pressures. The tritium inventory and activity are concentrated (note the logarithmic scale) in the volume below the third nozzle stage, which is responsible for the majority of the compression. This also explains the aforementioned insensitivity with respect to the inlet pressure. Another important contributor to the tritium inventory of the pumping system is therefore the necessary piping to the backing pumps, which is not considered here. For these reasons the reported inventories are considered indicative. For comparison the tritium inventory of the fuel in the ITER cryopumps is estimated to reach about 100 g [229]. Thus, even when considering the aforementioned uncertainties, it is clear that the tritium inventory can be reduced significantly by utilizing a continuous pumping system relying on diffusion pumps.

7.3.11. Summary of the linear diffusion pump development and next steps

The simulations discussed demonstrate the applicability of the developed models for designing and optimizing diffusion pumps for torus exhaust pumping. Although the discussed parametric studies are not exhaustive, they serve as a first step in the development and provide an indication of the anticipated performance. This section gives a brief summary of the main findings and

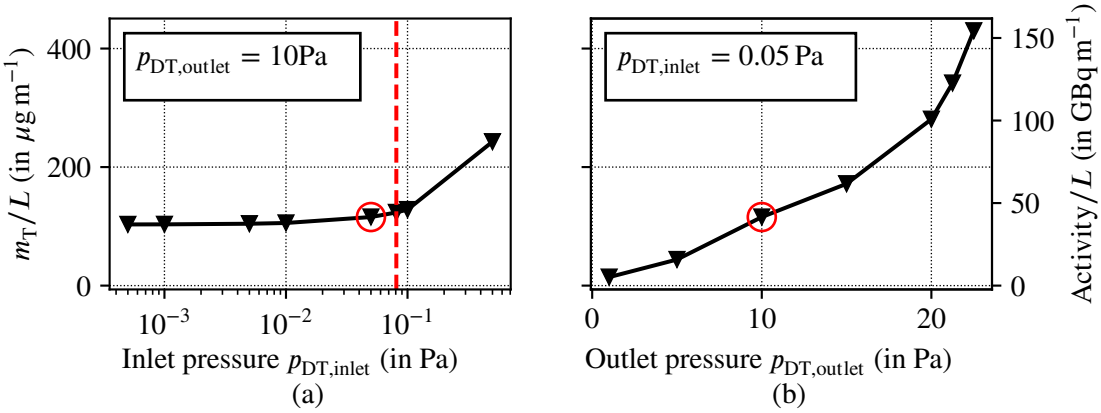

Figure 7.8.: (a) Tritium inventory per unit length m_T/L and tritium activity per unit length as functions of the inlet pressure for a fixed outlet pressure. (b) Tritium inventory per unit length m_T/L and tritium activity per unit length as functions of the outlet pressure for a fixed inlet pressure. Simulation results are indicated by the symbols and connected with straight lines to guide the eye. The points circled in red in both figures correspond to the same case. The dashed red line indicates the inlet pressure corresponding to a throughput of $q_{burn,LDP} = 3\,\mathrm{Pa\,m^3\,s^{-1}}$ per LDP as expected during the Tokamak burn phase.

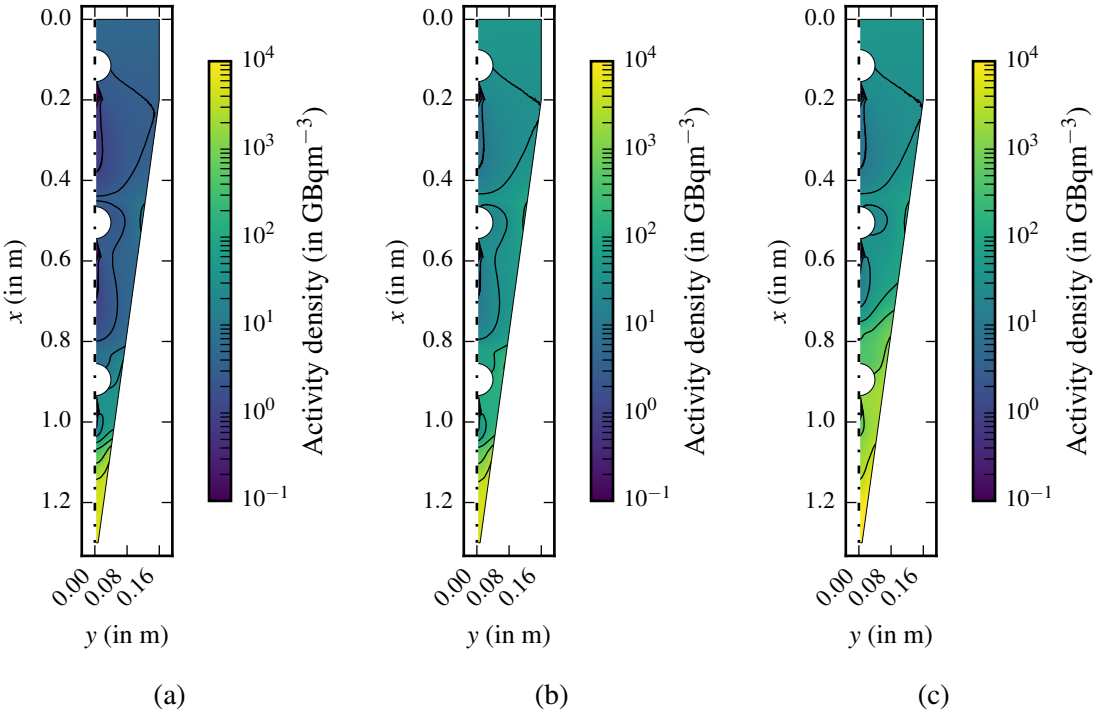

Figure 7.9.: Comparison of the local tritium activity density in the LDP for three different operating conditions: (a) $p_{DT,inlet} = 0.01\,\mathrm{Pa}$ & $p_{DT,outlet} = 10\,\mathrm{Pa}$, (b) $p_{DT,inlet} = 0.1\,\mathrm{Pa}$ & $p_{DT,outlet} = 10\,\mathrm{Pa}$ and (c) $p_{DT,inlet} = 0.1\,\mathrm{Pa}$ & $p_{DT,outlet} = 20\,\mathrm{Pa}$.

recommendations regarding the next development steps.

For the described baseline design and operating conditions, a pumping speed of $33.6\,\mathrm{m^3\,s^{-1}}$ (corresponding to a capture coefficient of 0.239) for DT has been evaluated in the operational range. The operational range is limited to inlet pressures of approximately 0.1 Pa and lower. The highest expected burn throughput results in an inlet pressure of approximately 0.081 Pa, which is close to the maximum inlet pressure but still in the operational range (approximately 3 % pumping speed reduction compared with the plateau value). A reduced order model can be used to extrapolate the capture coefficients of all other exhaust gas mixture constituents from DT simulation results of a given pump design, thereby reducing the required computational effort of parametric studies substantially. Under similar operating conditions the pumping speeds of the main exhaust gas species differ between $41.4\,\mathrm{m^3\,s^{-1}}$ (H_2) and $14.1\,\mathrm{m^3\,s^{-1}}$ (Ar). Superheating of the mercury vapor can improve the pumping speed only marginally, nonetheless it should be considered to prevent mercury condensation in the vapor feed line.

The highest tolerable fore-vacuum pressure is approximately 20 Pa at the assumed mercury vapor driving pressure of approximately 250 Pa, thus resulting in a maximum compression ratio of approximately 250 under burn conditions (but higher during dwell).

The backstreaming rate is approximately $30\,\mathrm{mg\,s^{-1}}$ per LDP and two methods of reducing backstreaming are compared. Firstly, reducing the cooling temperature of the pump casing responsible for condensing the mercury proofs to be very effective. A reduction of the cooling temperature by 10 K increases the pumping speed by 6.6 % while reducing the backstreaming rate by more than 50 %. Secondly, guard plates have been identified to be effective in reducing the backstreaming rate at negligible impact on the performance.

The steady gaseous tritium inventory inside the LDPs is estimated in the sub-gram range, confirming the advantages of a continuous over a discontinuous pumping system with respect to the tritium inventory.

The next steps in the LDP development program have to focus on the following aspects:

- Design, assembly and experimental exploitation of an easily modifiable test LDP in a relevant size. Based on the discussed simulation results, provisions should be made for the integration of guard plates and an adjustable cooling temperature of the pump walls. Furthermore, it is suggested to perform an in-depth experimental study of the condensation behavior of mercury vapor under the conditions prevalent in a LDP.

- A preliminary advanced nozzle pipe design has been developed with the aim to produce a uniform vapor distribution upstream the linear nozzle for arbitrary pipe lengths by integration of an intermediate throttling stage. A more detailed description is available in Appendix A.7.2. The final design choice should be based on an experimental comparison of the advanced to the regular nozzle pipe design in the test LDP.

- The LDP DSMC simulations require quantitative experimental validation to identify potential deficits related to their limitation to two dimensions. For example, the achievable fore-vacuum tolerance can be overestimated by the two-dimensional simulations that inherently neglect the boundary effects at the front and rear pump walls. Moreover, it is suggested to measure the pressure distribution along the nozzle pipes, which have not been modeled in the present work, for both the regular as well as the advanced design. This allows to adjust the assumptions on the vapor stagnation state that are used to calculate the boundary conditions at the nozzle throat of the two-dimensional DSMC LDP model and thus improve the results. Additionally, detailed experiments on the condensation behavior of mercury vapor in a LDP as described above can be used to adjust the condensation coefficient in the DSMC boundary condition.

- The developed simulation framework can be employed to continue the optimization of the pump design based on the preliminary results presented and discussed above. Examples of potential future parametric investigations include the mercury vapor stagnation conditions, the nozzle angles and the relative position of the nozzle pipes of the three stages.

The next section introduces the design of the baffle adapter to be installed upstream of the LDPs. Furthermore, its performance is discussed with regard to the LDP backstreaming rate determined in the present section.

7.4. Preliminary design and performance of the mercury baffle adapter

The migration of the backstreaming mercury vapor of the LDPs has to be limited. The LDP design introduced above permits the parallel installation of three LDPs per pumping port. For this reason it is space-saving to design a single, so-called *mercury baffle adapter (MBA)*, per port that is attached to all three LDPs in parallel. A preliminary design of the MBA is depicted in Fig. 7.10. This design includes three main components: Three parallel condensation baffle stages in the respective connectors to the LDPs, a second desublimation baffle stage and a linear high vacuum gate valve (sketched without actuator). The MBA is connected to the MFP retentate outlet on the upstream side, which is why its inlet cross-section area of $A_{\mathrm{MBA,in}} = 3.04\,\mathrm{m}^2$ corresponds to the MFP outlet area (cf. Tab. 7.1). The total outlet area of the three parallel connectors that are foreseen for the installation of the LDPs corresponds to $A_{\mathrm{MBA,out}} = 3 \cdot A_{\mathrm{LDP,in}} = 1.68\,\mathrm{m}^2$. The same baffle design is used for the condensation and desublimation baffle stages. The baffle configuration is chosen based on the parametric survey discussed in Chap. 6. In particular, the following parameters are selected: The offset configuration is implemented due to its higher transmission probability using the identified optimum angle of 25°. The smallest tolerable Knudsen number is specified to be $\mathrm{Kn}_{\mathrm{Hg}} \approx 0.05$ at a conservative maximum mercury vapor pressure of 1 Pa assumed during the burn phase. Based on this the gap between the baffle plates is chosen as $h \approx 36\,\mathrm{mm}$ (resulting in $\mathrm{Kn}_{\mathrm{Hg}} \approx 0.06$). To ensure a sufficient containment efficiency the overlap of the line of sight to gap ratio is chosen as $\delta/h \approx 0.4$, because Fig. 6.6 indicates negligible containment efficiency losses compared to the free-molecular regime above this value (in case of $\mathrm{Kn}_{\mathrm{Hg}} = 0.05$, the vapor transmission probability is 0.026 %). The baffle thickness is chosen as $t = 5\,\mathrm{mm}$ to ensure manufacturability of internal cooling channels. Based on Fig. 6.7, a transmission probability deterioration of about 10 % is to be expected at the resulting thickness to gap ratio of $t/h \approx 0.14$. These properties result in a conservative baffle design, serving as an appropriate starting point for potential future optimization. The cooling of the two baffle stages can for example be provided using gaseous nitrogen as proposed in [11, 23]. The design and successful operation of a similar system has been reported in [230]. The temperature of the three parallel first stage baffles should be kept above the triple point of mercury. The temperature of the second stage has to be lower to further reduce the mercury vapor backstreaming. The optimum temperature for this stage has to be determined in future experiments.

The gate valve has two main functions. It allows isolating the MBA and LDPs from the upstream pumping system for regeneration and maintenance. Further, it provides flexibility during operation as it can be used to adjust the effective pumping speed that the LDPs provide at the interface to the MFPs and to regulate the pressure. Partially closing the valve yields a pressure increase in the MFPs and a pressure reduction in the MBA, which in turn changes the MBA flow regime towards higher Knudsen numbers.

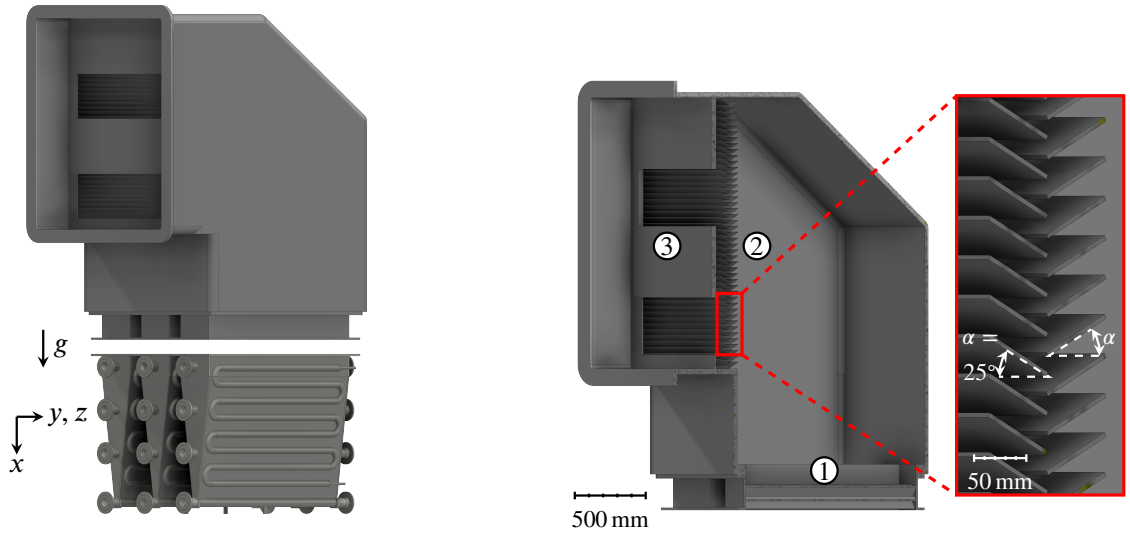

(a) (b)

Figure 7.10.: (a) CAD drawing of the preliminary mercury baffle adapter. Three LDPs are connected to the MBA in parallel via the bottom flanges (depicted in exploded view). (b) Half-section view of the MBA to reveal the inner components, which are labeled: ① three parallel first baffle stages and flanges to LDPs (see (a)), ② second baffle stage, ③ linear high vacuum gate valve. The cutout on the right provides a detailed view on the offset baffle configuration used in both stages.

7.4.1. Performance prediction in the free-molecular regime

A simulation of the complex, three-dimensional geometry of the baffle is computationally demanding outside the free-molecular regime. However, due to the extensive parametric studies upon which the design is based on it is not deemed necessary at the present stage of development. For this reason a TPMC simulation has been performed using the software MOLFLOW+ (version 2.9.0) [120, 121] to determine a conservative estimate of the MBA transmission probability in the free-molecular regime. The results are summarized in Tab. 7.6. Due to the conservative baffle design that is used for condensation and desublimation stages the transmission probability is only 4.8 %. The conductance depends on the thermal particle velocity and therefore scales $\propto m^{-0.5}$ with the particle mass m.

7.4.2. Mercury accumulation and baffle regeneration

The operating principle of the second baffle stage is based on the desublimation of mercury vapor. Thus, mercury in solid form accumulates in the baffle during operation and regeneration of the baffle is necessary in regular intervals. The mercury accumulation rate can be estimated based on the determined LDP backstreaming rate and the vapor transmission probability of the baffle. The former is largest during the dwell phase and in the order of magnitude of 30 mg s^{-1} per LDP for the baseline LDP design proposed above when operated with mercury vapor at a stagnation pressure of approximately 250 Pa. Regarding the latter, the vapor transmission probability is about 0.026 % (assuming a sticking coefficient of unity) for the minimum expected Knudsen number of $Kn_{Hg} = 0.05$. Combining these two figures results in an estimated mercury vapor load of 23 µg s^{-1} or 2 g d^{-1} on the second baffle stage[1]. Obviously, this is only a first ballpark estimate and sensitive

[1] 2 g of liquid mercury corresponds to a spherical droplet of ca. 6.5 mm diameter.

Table 7.6.: Free-molecular TPMC simulation results of the mercury baffle adapter.

Property		Unit	Value
Number of test particles		1	1×10^9
Number of pumped particles		1	48×10^6
Transmission probability		1	0.0480
Conductance (at 293.15 K)	He	$m^3\ s^{-1}$	45.45
	D_2		45.31
	DT		40.55
	T_2		37.03
	Ne		20.25
	Ar		14.39

to the actual sticking coefficient, which will have to be determined in dedicated experiments.

Regeneration can be performed by closing the high vacuum gate valve, shutting down the LDPs and then purging the baffle with hot gas in order to vaporize the desublimated mercury. Apart from mercury vapor, high boiling species, like tritiated water Q_2O, that are expected in the exhaust gas mixture [19] condense or desublimate in the baffle. While it is not expected that these increase the tritium inventory considerably and thus dominate the required regeneration frequency, it is necessary to separate them from the mercury vapor during the regeneration phase. As this precludes purely cryogenic separation, a separate purification system is required. A possible implementation could combine a condensation pre-separation stage (at temperatures where only mercury condenses) with a subsequent mercury amalgamation stage (e.g. metal packed column) consisting of gold, sodium, potassium, cadmium, zinc or their alloys, which have been used previously for mercury trapping [231–233].

7.4.3. Summary of the mercury baffle adapter development and next steps

A preliminary MBA design that incorporates two baffle stages for mercury vapor condensation and desublimation and a high vacuum valve to facilitate regeneration has been proposed. The design of the two baffle stages is based on the parametric simulations and can be regarded as a conservative starting point.

One of the central results of the present work is the importance of the baffle performance on the integrated system. This motivates the need for a dedicated experimental study of a mercury baffle adapter under DEMO relevant operating conditions. The two main outcomes of this study should be an experimental confirmation of the vapor containment efficiency and a determination of the onset of performance deterioration with respect to the accumulated amount of mercury. Regarding the vapor containment efficiency, the DSMC simulations indicate a strong scaling with the sticking coefficient. A smaller than unity effective sticking coefficient is expected due to surface conditions, inhomogeneous temperature distribution and re-evaporation, however it is not possible to determine an accurate value without experiments. The onset of performance deterioration with respect to the accumulation of mercury in the baffle will determine the required regeneration frequency. The outcomes of the experimental work can be used to tune the sticking factor assumed in the TPMC simulation to make this tool also useful for predicting the mercury containment efficiency and accumulation rate in the desublimation stage.

7.5. Estimation of the integrated performance of the EU-DEMO high vacuum pumping system

The performance of LDPs and MBA has been determined and these results are used here to estimate the integrated system performance by means of a hybrid model[2]. As indicated in Sec. 7.2, this hybrid model combines the simulation results obtained by the detailed subsystem models in the form of the following analytical expression by means of the Ansatz of Oatley:

$$\varsigma_{\mathrm{eff}} = \left[\frac{1}{w_{\mathrm{duct+MFP}}} + \frac{A_{\mathrm{duct,in}}}{A_{\mathrm{MBA,in}}} \left(\frac{1}{w_{\mathrm{MBA}}} - 1 \right) + \frac{A_{\mathrm{duct,in}}}{3A_{\mathrm{LDP,in}}} \left(\frac{1}{\varsigma_{\mathrm{LDP}}} - 1 \right) \right]^{-1} . \tag{7.10}$$

The cross-sections, transmission probabilities and capture coefficients have been determined above and are summarized in Tab. 7.7. Based on these parameters the system performance in the INTL loop can be determined to $\varsigma_{\mathrm{eff}} = 0.0174$, meaning that a gas particle entering the vacuum duct in the sub-divertor region has a 1.74 % chance to be pumped during dwell when the MFPs are not operated and all pumping is provided by the LDPs. This value exceeds the requirement of 0.00282 that was determined for burn conditions (Eq. (7.1)) significantly, and it is furthermore expected that Eq. (7.10) yields conservative results during burn due to the assumption of free-molecular flow. However, the requirements of the dwell performance are more stringent than the ones of the burn performance in EU-DEMO so that it is justified to focus on the dwell performance in the following.

Table 7.7.: Summary of the subsystem parameters used in the hybrid model of the EU-DEMO high vacuum pumping system. In case of the LDPs the capture coefficient of DT during burn determined in Sec. 7.3.2 has conservatively been assumed.

Property	Symbol	Value	Reference
Pumping duct inflow cross-section	$A_{\mathrm{duct,in}}$	$5.62\,\mathrm{m}^2$	[216, 218]
Transmission probability duct & MFPs	$w_{\mathrm{duct+MFP}}$	0.104	[218]
MBA inflow cross-section	$A_{\mathrm{MBA,in}}$	$3.04\,\mathrm{m}^2$	Sec. 7.4
MBA transmission probability	w_{MBA}	0.0480	
LDP inflow cross-section	$A_{\mathrm{LDP,in}}$	$0.56\,\mathrm{m}^2$	Sec. 7.3
LDP capture coefficient (for DT)	ς_{LDP}	0.232	

As no detailed information on the dwell load is available yet, it is only possible to determine a tolerable dwell gas load that can be processed by the pumping system. The tolerable dwell gas load follows as $q_{\mathrm{dwell}} \leq 0.36\,\mathrm{Pa\,m^3\,s^{-1}}$ (for an assumed terminal sub-divertor pressure of 2 mPa and with linear pressure scaling) from Fig. 7.1 or Eq. (7.2) and is about five times higher than the expected protium outgassing rate of $0.0715\,\mathrm{Pa\,m^3\,s^{-1}}$. At the tolerable load the inlet LDP pressure can be estimated to be of the order of 0.3 mPa. Future work has to show if outgassing rates within the tolerable limit are realistic for the first wall and divertor materials, also with regard to the increasing effects of irradiation over their lifetime in the reactor.

7.5.1. Sensitivity analysis of the subsystems

A mathematical sensitivity study of the integrated system to its subsystems can be performed due to the analytical nature of the hybrid model in Eq. (7.10). Under the assumption that the physical

[2]The same hybrid model, however for a different system configuration, has been introduced and discussed in a previous publication by the author [228].

layout of the system is fixed, i.e. that all interface cross-sections between the subsystems remain constant, the transmission probabilities and LDP capture coefficient are the only variables. It is therefore possible to derive the sensitivity of the system with respect to the property $\chi_i = \{w_i, \varsigma_i\}$ as the partial derivative,

$$\frac{\partial \varsigma_{\text{eff}}}{\partial \chi_i} = \frac{A_{\text{duct,in}}}{A_{i,\text{in}}} \cdot \left(\frac{\varsigma_{\text{eff}}}{\chi_i} \right)^2 . \tag{7.11}$$

Based on this the relative sensitivity Λ_i with respect to the baseline configuration can be obtained by normalizing the partial derivative according to

$$\Lambda_i = \left. \frac{\partial \varsigma_{\text{eff}}}{\partial \chi_i} \right|_0 \cdot \frac{\chi_{i,0}}{\varsigma_{\text{eff},0}} = \frac{A_{\text{duct,in}}}{A_{i,\text{in}}} \cdot \frac{\varsigma_{\text{eff},0}}{\chi_{i,0}}, \tag{7.12}$$

where the properties with subscript "0" correspond to the baseline configuration characterized by the values summarized in Tab. 7.7. The resulting relative sensitivities for the three subsystems are listed in Tab. 7.8. The relative sensitivity can be interpreted as a measure of how much the integrated system performance improves if a subsystem is improved. For example, if the LDP performance is improved by 5 %, the determined relative sensitivity of $\Lambda_{\text{LDP}} = 0.251$ implies that the integrated system performance improves by only 1.25 %. Therefore, the comparison of the relative sensitivities (right most column in Tab. 7.8) is helpful in identifying the bottlenecks at which optimization efforts should be focused. For example, the MFP design was found to be limiting the INTL performance in a previous study [228] and the design revised afterwards to the design with improved conductance considered in the present work [218]. Based on the results of the present analysis further optimization efforts have to concentrate on improving the MBA transmission probability.

Table 7.8.: Relative sensitivities of the integrated system performance to the performance of each subsystem. The right most column compares the sensitivities to each other to identify the relative importance of the subsystems during optimization.

Subsystem	Relative sensitivity	Value	Proportion
Pumping duct & MFPs	$\Lambda_{\text{duct+MFP}}$	0.168	15.4 %
Mercury baffle adapter	Λ_{MBA}	0.672	61.6 %
Linear diffusion pumps	Λ_{LDP}	0.251	23.1 %

7.5.2. Species dependent pumping speeds

The species dependency of the pumping speeds is only relevant in or close to free-molecular conditions. The expected effects therefore change between burn and dwell phases of the Tokamak.

During the dwell phase the flow is free-molecular in nearly the entire high vacuum pumping system. Therefore, the species effect is dominated by the species dependent conductance resulting from the thermal velocity, which is inversely proportional to the square root of the species mass. In fact, the LDP pumping speed exhibits a weaker scaling with the species mass. Hence, the concentration shift is most pronounced at the inlet of the duct and slightly reduces along the pumping path towards the LDPs. Additionally, a transient concentration shift is expected during the initial phase of pump-down as the lighter gases are pumped faster. The preceding discussion is supported by experimental and numerical findings in JET (which uses cryopumps), in which higher molecular pressures in the sub-divertor were observed for deuterium plasmas than for protium plasmas for the same throughput [234].

During the burn phase the flow in the duct between sub-divertor and MFPs is in the viscous regime. Therefore, no species effects are expected in the sub-divertor volume and an influence on the plasma operation is thereby effectively excluded. Inside the MFPs the active separation of the unburnt fuel due to superpermeation leads to an enrichment of all passive species in the retentate mixture that has to be pumped by the LDPs. A further, albeit much smaller species effect occurs inside the LDPs as the flow becomes transitional. Due to the higher pumping speed for lighter gases (cf. Tab. 7.3), the heavier constituents enrich in the volume upstream of the first nozzle stage.

7.6. Development state and implications for the rough pumping system

In this chapter, a preliminary high vacuum system layout featuring linear, mercury-driven diffusion pumps has been discussed. The required dwell performance is identified to be the limiting factor based on an analysis of the expected operating conditions and loads during burn and dwell. Furthermore, the dwell load likely is dominated by the outgassing rate from the plasma facing materials. Next, preliminary designs for LDP and MBA have been introduced and simulated using the developed models. Subsequently, a hybrid model including the obtained performance parameters has been implemented to estimate the integrated performance of the INTL high vacuum pumping system. The investigation shows that burn requirements can be met by the chosen components. Regarding the dwell performance an upper limit of approximately $0.36\,\mathrm{Pa\,m^3\,s^{-1}}$ is identified for the tolerable outgassing rate. Furthermore, a sensitivity study of the integrated pumping system performance to the individual subsystem performances reveals that the MBA features the highest optimization potential. Moreover, expected concentration shifts due to species dependent pumping speeds are qualitatively discussed, and no general issues are determined with respect to the Tokamak operation. Finally, the required pumping speed of the rough pumping system during burn can be estimated to be approximately 5-10 $\mathrm{m^3\,s^{-1}}$ based on the simulated LDP fore-vacuum tolerance of approximately 10-20 Pa. A promising combination of mercury-driven ejector pumps and mercury liquid ring pumps expected to be capable of providing this performance is currently under investigation.

Additionally, recommendations on future experimental work are provided. Regarding the LDP it is important to validate the two-dimensional DSMC results (especially the fore-vacuum tolerance) and their extrapolation to three dimensions. On the subject of the MBA it is important to firstly reconfirm the estimated mercury containment efficiency and secondly to determine the performance degradation with respect to the accumulated amount of mercury on the desublimation baffle stage in order to establish the regeneration frequency. It is currently foreseen to perform these experiments in the framework of the *DIPAK (Direct Internal Recycling Integrated Development Platform Karlsruhe)* platform, which will allow integrated testing of the vacuum pumping technologies.

8. Summary of results and recommendations for future work

8.1. Summary

This work contributes to advance the development of mercury-driven vapor diffusion pumps for the application in the exhaust pumping system of future nuclear fusion power plants. Vapor diffusion pumps are operating continuously and therefore are considered as a replacement for discontinuous high vacuum pumping technologies like cryopumps, which are currently used as a standard in nuclear fusion experiments.

The vapor diffusion pump operating principle is based on the momentum transfer from a supersonic vapor jet to the pumped gas. For reasons of tritium compatibility, the use of mercury is advantageous in fusion power plants. Mercury does not degrade under the tritium beta radiation, it does not undergo any chemical reactions and it has a low solubility for tritium. Furthermore, it has favorable neutron activation properties. Therefore, the main purpose of the present work is to develop and validate numerical simulation models that can be used to design and optimize mercury-driven vapor diffusion pumps for the application in a nuclear fusion reactor.

The objective is achieved by first identifying the design driving performance indicators of diffusion pumps on the basis of a literature research. By that, the requirements for dedicated models of the gas-vapor interaction inside the diffusion pump, the vapor trap upstream of the pump and the integrated vacuum system are established. Diffusion pumps operate in the rarefied gas flow regime, where neither a continuum nor a free-molecular descriptions of the flow is valid. Therefore, the kinetic theory of gases has to be employed for a description of the physical particle transport processes inside the diffusion pump and the vapor trap. Furthermore, the Direct Simulation Monte Carlo method (DSMC) is identified as adequate for modeling complex geometries. The available open source DSMC tool, SPARTA, has been extended with respect to the application to diffusion pump modeling. As highlights this involved the determination of parameters for modeling the intermolecular potential of mercury vapor via the Variable Soft Sphere (VSS) model, an implementation of a common species weighting algorithm to improve the computational efficiency and a new boundary condition that allows to describe the local, concurrent condensation and evaporation of mercury on the cooled walls of the pump.

Two models describing the interaction between the mercury vapor jet and gas inside the pump have been established. The first model is based on a model described in literature and purely analytical. It is formulated in dimensionless form and subsequently used to explain the main influencing factors on the diffusion pump operation with a focus on the application in fusion reactor vacuum systems. The second model is more detailed and involves the interaction of the mercury vapor jet with the mechanical structure of the pump. Simulations of this model are performed numerically by using the DSMC method and can be employed to describe realistic pump geometries.

The model assumptions have been validated by a detailed comparison with the experimental results obtained in the experimental NEMESIS setup. NEMESIS resembles a single-stage mercury diffusion pump which has been developed and successfully operated in the mercury laboratory at KIT. Measurements of the axial mercury vapor pressure distribution in the expanding jet, the forevacuum tolerance and the mercury mass flow rate have been performed at different boiler powers.

A vapor trap has to be installed upstream of the diffusion pumps. Vapor traps are based on

cooled baffle plates that condense or desublimate the impinging vapor molecules. A peculiarity with respect to the application in a pulsed Tokamak are the operating pressure differences between the burn and dwell phases. Therefore, free-molecular descriptions of baffles that are available in literature are not applicable. For this reason, the performance of two baffle geometries has been investigated over a wide gas rarefaction range in the present work based on a simplified DSMC model. Parametric studies of the main geometrical and operational baffle features have enabled to extract design guidelines.

Lastly, the developed models have been applied to derive preliminary designs of a linear vapor diffusion pump and mercury baffle adapter for the application in the European demonstration fusion power plant (EU-DEMO). Exemplary parametric studies for the chosen vapor diffusion pump design have allowed to quantify the influence of several operational parameters. Additionally, a reduced order model for predicting the diffusion pump capture coefficient under different operating conditions has been introduced on the basis of the analytical model and its applicability has been verified. The combination of the sophisticated DSMC pump model with the reduced order model allows to improve the efficiency of future parametric studies substantially. It is confirmed that stricter requirements are set on the high vacuum system by dwell than by burn specifications. Moreover, a hybrid model of the pumping train has been established by incorporating the simulation results of the subsystem performances. This has allowed to analyze the performance of the integrated EU-DEMO high vacuum pumping system for the first time. The sensitivities of the subsystems which are comprised of metal foil pumps, mercury baffle adapter and linear diffusion pumps have been derived and discussed. It has been shown that the system characterized by the combination of the considered preliminary subsystem designs delivers the required performance during burn and a tolerable dwell gas load has been derived.

8.2. Recommendations for future work

Recommendations for future work are grouped in three categories and discussed in the following.

Advancements of the vacuum system design should be based on the developed hybrid model of the integrated system and its results. Most importantly, the subsystem sensitivities of a given design provide guidance on the highest optimization potential. Additionally, it is recommended to consider a rearrangement of the subsystems if the found tolerable dwell gas load is exceeded. A significant improvement of the dwell performance is expected if the metal foil pumps are moved downstream of the linear diffusion pumps because they act as a passive flow resistance during dwell.

Future experimental work regarding the mercury-driven diffusion pumps is recommended to focus on two main aspects: Firstly, the validation of the applicability of the two-dimensional DSMC model for describing the linear diffusion pumps. It is expected that the fore-vacuum tolerance is the most sensitive regarding the inherent negligence of the boundary interactions on the front and rear pump walls in the two-dimensional model. Furthermore, the mercury vapor pressure distribution in the linear nozzle pipes should be measured. First theoretical studies of an advanced nozzle pipe design capable of providing uniform vapor conditions upstream of the linear nozzle by means of a throttling stage are promising but require experimental validation. Moreover, a detailed experimental study of the condensation behavior of the mercury vapor on the cooled walls of the pump could provide valuable input for further improvements of the DSMC model. Secondly, a parametric study of the mercury baffle adapter should be initiated. Experimental results are necessary in order to establish a database of the sticking factor as a function of the operating conditions. Additionally, it is mandatory to determine the performance degradation of the desublimation stage

with respect to the amount of accumulated mercury in order to derive the required regeneration frequency. To accomplish these objectives, work on designing a test linear diffusion pump and mercury baffle adapter in EU-DEMO relevant scales using the simulation models and results of the present work has been initiated. It is planned to integrate these in the framework of the DIPAK platform, which is foreseen for the integrated testing of the vacuum pumping technologies.

Further development of the simulation models can be supported by integrating experimental results once they are available, for example in the form of an efficiency factor. Moreover, experiments dedicated to the transport properties of mixtures featuring mercury and the other exhaust gas mixture constituents can be used to improve the Variable Soft Sphere model parameters of interspecies collisions, which are averaged from the properties of the pure substances in the present work. Furthermore, the advancement of kinetic models with respect to accurate modeling of gas mixtures should be monitored. Together with the recent progress regarding the parallelization of the Discrete Velocity Method on graphics processing units, these can evolve to a potentially more efficient alternative to the Direct Simulation Monte Carlo method employed in the present work. Accompanying the suggested experiments regarding the pressure distribution in the nozzle pipes continuum simulations could be performed and compared with the experimental results.

Bibliography

[1] A. Einstein, "Ist die Trägheit eines Körpers von seinem Energiegehalt abhängig? (in German)", *Annalen der Physik*, vol. 323, no. 13, pp. 639–641, 1905. DOI: 10.1002/andp.19053231314.

[2] A. S. Eddington, "The internal constitution of the stars", *Nature*, vol. 106, no. 2653, pp. 14–20, Sep. 1920. DOI: 10.1038/106014a0.

[3] G. McCracken and P. Stott, *Fusion - The energy of the universe* (Complementary Science Series). Amsterdam, Boston, Heidelberg, London, New York, Oxford, Paris, San Diego, San Francisco, Singapore, Sydney, Tokyo: Elsevier Academic Press, 2005, 186 pp., ISBN: 0-12-481851-X.

[4] A. M. Petros'yants, "A pioneer of nuclear power; Obninsk marks 30 years of nuclear power", *International Atomic Energy Agency Bulletin*, vol. 26, no. 4, pp. 42–46, Dec. 1984.

[5] A. Kohyama, A. Hishinuma, D. S. Gelles, R. L. Klueh, W. Dietz, and K. Ehrlich, "Low-activation ferritic and martensitic steels for fusion application", *Journal of Nuclear Materials*, vol. 233–237, pp. 138–147, Oct. 1, 1996. DOI: 10.1016/S0022-3115(96)00327-3.

[6] M. Rubel, "Fusion neutrons: Tritium breeding and impact on wall materials and components of diagnostic systems", *Journal of Fusion Energy*, vol. 38, pp. 315–329, Aug. 2019. DOI: 10.1007/s10894-018-0182-1.

[7] G. Federici *et al.*, "DEMO design activity in Europe: Progress and updates", *Fusion Engineering and Design*, vol. 136, no. A, pp. 729–741, Nov. 2018. DOI: 10.1016/j.fusengdes.2018.04.001.

[8] C. Day and T. Giegerich, "The Direct Internal Recycling concept to simplify the fuel cycle of a fusion power plant", *Fusion Engineering and Design*, vol. 88, no. 6–8, pp. 616–620, Oct. 2013. DOI: 10.1016/j.fusengdes.2013.05.026.

[9] C. Day, D. Murdoch, and R. Pearce, "The vacuum systems of ITER", *Vacuum*, vol. 83, no. 4, pp. 773–778, Nov. 2008. DOI: 10.1016/j.vacuum.2008.05.010.

[10] T. Giegerich and C. Day, "Conceptuation of a continuously working vacuum pump train for fusion power plants", *Fusion Engineering and Design*, vol. 88, no. 9–10, pp. 2206–2209, 2013. DOI: 10.1016/j.fusengdes.2013.05.019.

[11] T. Giegerich and C. Day, "The KALPUREX-process – A new vacuum pumping process for exhaust gases in fusion power plants", *Fusion Engineering and Design*, vol. 89, no. 7–8, pp. 1476–1481, Oct. 2014. DOI: 10.1016/j.fusengdes.2014.03.082.

[12] M. Siccinio *et al.*, "Impact of the plasma operation on the technical requirements in EU-DEMO", *Fusion Engineering and Design*, vol. 179, 113123, pp. 1–11, Jun. 2022. DOI: 10.1016/j.fusengdes.2022.113123.

[13] P. C. de Vries and Y. Gribov, "ITER breakdown and plasma initiation revisited", *Nuclear Fusion*, vol. 59, no. 9, 096043, pp. 1–27, Aug. 2019. DOI: 10.1088/1741-4326/ab2ef4.

[14] G. Granucci *et al.*, "Conceptual design of the EU DEMO EC-system: Main developments and R&D achievements", *Nuclear Fusion*, vol. 57, no. 11, 116009, pp. 1–8, Aug. 2017. DOI: 10.1088/1741-4326/aa7b15.

[15] M. Jakobs, "Fusion energy - Burning questions", Dissertation, Department of Applied Physics and Science Education, Eindhoven University of Technology, Eindhoven, Netherlands, Nov. 14, 2016, 150 pp. DOI: 10.13140/RG.2.2.20211.04646.

[16] R. Kembleton, J. Morris, M. Siccinio, and F. Maviglia, "EU-DEMO design space exploration and design drivers", *Fusion Engineering and Design*, vol. 178, 113080, pp. 1–9, May 2022. DOI: 10.1016/j.fusengdes.2022.113080.

[17] D. G. Whyte, R. Delaporte-Mathurin, S. E. Ferry, and S. Meschini, "Tritium burn efficiency in deuterium–tritium magnetic fusion", *Nuclear Fusion*, vol. 63, no. 12, 126019, pp. 1–10, Sep. 2023. DOI: 10.1088/1741-4326/acf3fb.

[18] M. Abdou *et al.*, "Physics and technology considerations for the deuterium–tritium fuel cycle and conditions for tritium fuel self sufficiency", *Nuclear Fusion*, vol. 61, no. 1, 013001, pp. 1–51, Nov. 2020. DOI: 10.1088/1741-4326/abbf35.

[19] C. Day *et al.*, "The pre-concept design of the DEMO tritium, matter injection and vacuum systems", *Fusion Engineering and Design*, vol. 179, 113139, pp. 1–26, Jun. 2022. DOI: 10.1016/j.fusengdes.2022.113139.

[20] J. C. Schwenzer, C. Day, T. Giegerich, and A. Santucci, "Operational tritium inventories in the EU-DEMO fuel cycle", *Fusion Science and Technology*, vol. 78, no. 8, pp. 664–675, Nov. 2022. DOI: 10.1080/15361055.2022.2101834.

[21] A. Kallenbach *et al.*, "Neutral pressure and separatrix density related models for seed impurity divertor radiation in ASDEX Upgrade", *Nuclear Materials and Energy*, vol. 18, pp. 166–174, Jan. 2019. DOI: 10.1016/j.nme.2018.12.021.

[22] C. Day, S. Varoutis, and Y. Igitkhanov, "Effect of the dome on the collisional neutral gas flow in the Demo divertor", *IEEE Transactions on Plasma Science*, vol. 44, no. 9, pp. 1636–1641, Sep. 2016. DOI: 10.1109/TPS.2016.2565727.

[23] T. Giegerich, "Novel vacuum pumping concepts for fusion power plants", Dissertation, Department of Chemical and Process Engineering, Karlsruhe Institute of Technology, Karlsruhe, Germany, May 24, 2016, 112 pp. DOI: 10.5445/IR/1000056126.

[24] C. Day and T. Giegerich, "Development of advanced exhaust pumping technology for a DT fusion power plant", *IEEE Transactions on Plasma Science*, vol. 42, no. 4, pp. 1058–1071, Apr. 2014. DOI: 10.1109/TPS.2014.2307435.

[25] H. Hackfort, "A selective pump for hydrogen isotopes based on the superpermeation effect in iron", *Fusion Engineering and Design*, vol. 10, pp. 293–297, 1989. DOI: 10.1016/0920-3796(89)90066-5.

[26] B. J. Peters and C. Day, "Analysis of low pressure hydrogen separation from fusion exhaust gases by the means of superpermeability", *Fusion Engineering and Design*, vol. 124, pp. 696–699, Nov. 2017. DOI: 10.1016/j.fusengdes.2017.05.124.

[27] B. J. Peters, "Development of a hydrogen-selective vacuum pump on the basis of superpermeation", Dissertation, Department of Mechanical Engineering, Karlsruhe Institute of Technology, Karlsruhe, Germany, May 2020. DOI: 10.5445/IR/1000122305.

[28] C. A. Foster, "High-throughput continuous cryopump", *Journal of Vacuum Science & Technology A*, vol. 5, no. 4, pp. 2558–2562, Jul. 1987. DOI: 10.1116/1.574421.

[29] C. A. Foster, D. E. Schechter, R. S. Willms, D. Dogruel, and L. Baylor, "A continuous cryogenic diffusion pump for fusion reactors", in *21st IEEE/NPS Symposium on Fusion Engineering SOFE 05*, (Knoxville, Tennessee, US, Sep. 26–29, 2005), 2005. DOI: 10.1109/FUSION.2005.252918.

[30] J. Krasznai, D. Mullins, and R. Mowat, “Tritiated waste management - Tritiated oil packaging and decontamination”, *Fusion Technology*, vol. 28, no. 3P2, pp. 1540–1545, Oct. 1, 1995. DOI: 10.13182/FST95-A30631.

[31] C. L. Folkers and V. P. Gede, “Transfer operations with tritium - A review”, in *Proceedings of the 23rd Conference On Remote Systems Technology*, (San Francisco, California, US, Nov. 16–21, 1975), 1975, pp. 219–227.

[32] R. T. Tsugawa, J. S. Bowers, J. A. Emig, R. S. Hafner, J. L. Maienschein, and A. S. Nicolosi, “Determination of tritium in mercury from Sprengel pumps”, *Journal of Nuclear Materials*, vol. 172, no. 2, pp. 239–240, Jul. 1990. DOI: 10.1016/0022-3115(90)90443-Q.

[33] R. A. Forrest, A. Tabasso, C. Danani, S. Jakhar, and A. K. Shaw, “Handbook of activation data calculated using EASY-2007”, EURATOM/UKAEA Fusion Association, Culham Science Centre, Abingdon, UK, Tech. Rep. UKAEA FUS 552, Mar. 2009, 660 pp.

[34] W. J. Lange, J. G. Gorman, D. Green, and D. A. Sink, “TFTR vacuum system considerations”, Fusion Power Systems Department, Westinghouse Electric Corporation, Pittsburgh, Pennsylvania, US, Tech. Rep. WFPS-TME-021, Nov. 1975, 42 pp. DOI: 10.2172/5425308.

[35] W. Gaede, “Die Diffusion der Gase durch Quecksilberdampf bei niederen Drucken und die Diffusionsluftpumpe (in German)”, *Annalen der Physik*, vol. 351, no. 3, pp. 357–392, 1915. DOI: 10.1002/andp.19153510304.

[36] W. W. Crawford, “The parallel jet high vacuum pump”, *Physical Review*, vol. 10, no. 5, pp. 557–563, Nov. 1917. DOI: 10.1103/PhysRev.10.557.

[37] I. Langmuir, “A high vacuum mercury vapor pump of extreme speed”, *Physical Review*, vol. 8, no. 1, pp. 48–51, Jul. 1916. DOI: 10.1103/PhysRev.8.48.

[38] I. Langmuir, “The condensation pump: An improved form of high vacuum pump”, *Journal of the Franklin Institute*, vol. 182, no. 6, pp. 719–743, Dec. 1916. DOI: 10.1016/S0016-0032(16)90056-5.

[39] N. Milleron, “Progress report on diffusion pump development”, *Vacuum*, vol. 13, no. 12, pp. 555–562, Dec. 1963. DOI: 10.1016/0042-207X(63)90543-8.

[40] E. Morse, *Nuclear fusion* (Graduate Texts in Physics), Series editor K. H. Becker *et al.* Cham, Switzerland: Springer International Publishing AG, 2018, 512 pp., ISBN: 978-3-319-98171-0. DOI: 10.1007/978-3-319-98171-0.

[41] T. M. Dowell, “Survey of pumps for tritium gas”, Canatom Inc. under contract to the Canadian Fusion Fuel Technology Project, Mississagua, Ontario, Canada, Tech. Rep. F83021, May 1983, 23 pp.

[42] M. H. Hablanian, “Diffusion pump technology”, *Japanese Journal of Applied Physics*, vol. 13, pp. 25–31, 1974. DOI: 10.7567/JJAPS.2S1.25.

[43] R. Jaeckel, *Kleinste Drucke und ihre Messung und Erzeugung (in German)* (Technische Physik 9), in collab. with H. Schwarz and E. Schüller. Berlin, Göttingen, Heidelberg: Springer-Verlag, 1950, 302 pp., ISBN: 978-3-662-01205-5. DOI: 10.1007/978-3-662-01204-8.

[44] M. Wutz, *Molekularkinetische Deutung der Wirkungsweise von Diffusionspumpen (in German)* (Sammlung Vieweg), H. Ebert, Ed. Braunschweig, Germany: Friedr. Vieweg + Sohn, 1969, vol. 130, 77 pp., ISBN: 978-3-663-03186-4. DOI: 10.1007/978-3-663-04375-1.

[45] M. H. Hablanian, *Diffusion pumps - Performance and operation* (AVS Monograph Series), 2nd ed. New York, New York, US: American Vacuum Society, 1994, 65 pp., ISBN: 1-56396-384-1.

[46] D. Latham, B. D. Power, and N. T. M. Dennis, "An assessment of some working fluids for diffusion pumps", *Vacuum*, vol. 2, no. 1, pp. 33–49, Jan. 1952. DOI: 10.1016/0042-207X(52)90221-2.

[47] J. Blears and R. W. Hill, "The speeds of diffusion pumps for gases of low molecular weight", *Review of Scientific Instruments*, vol. 19, no. 12, pp. 847–851, Dec. 1948. DOI: 10.1063/1.1741184.

[48] B. B. Dayton, "The speed of oil and mercury diffusion pumps for hydrogen, helium, and deuterium", *Review of Scientific Instruments*, vol. 19, no. 11, pp. 793–804, Nov. 1948. DOI: 10.1063/1.1741161.

[49] D. Fluke, "A comparison of mercury diffusion pumping speeds for five gases", *Review of Scientific Instruments*, vol. 19, no. 10, pp. 665–666, Oct. 1948. DOI: 10.1063/1.1741073.

[50] K. M. Simpson, "A rectangular diffusion pump", Technical Information Division, United States Atomic Energy Commission, Oak Ridge, Tennessee, US, Tech. Rep. AECD-2687, Sep. 13, 1945, 9 pp.

[51] K. M. Simpson, "Vacuum pumping apparatus", U.S. Patent 2,691,481, Oct. 12, 1954.

[52] E. R. Lind and J. F. Steinhaus, "Development of a large, linear jet, mercury diffusion pump having high pumping speeds in the 10^{-6} mm mercury absolute pressure range", Livermore Research Laboratory, Livermore, California, US, Tech. Rep. MTA-14, Jan. 13, 1953, 44 pp.

[53] M. J. Copley, O. C. Simpson, H. M. Tenney, and T. E. Phipps, "A study of the speed of divergent nozzle pumps", *Review of Scientific Instruments*, vol. 6, no. 9, pp. 265–267, Sep. 1935. DOI: 10.1063/1.1752002.

[54] T. L. Ho, "Multiple nozzle diffusion pumps", *Review of Scientific Instruments*, vol. 3, no. 3, pp. 133–135, Mar. 1932. DOI: 10.1063/1.1748915.

[55] R. M. Zabel, "A simple high speed oil diffusion pump", *Review of Scientific Instruments*, vol. 6, no. 2, pp. 54–55, Feb. 1935. DOI: 10.1063/1.1751930.

[56] T. L. Ho, "Speed, speed factor and power input of different designs of diffusion pumps, and remarks on measurements of speed", *Physics*, vol. 2, pp. 386–395, May 1932. DOI: 10.1063/1.1745064.

[57] N. A. Florescu, "The theoretical development of the vapour vacuum pump", *Vacuum*, vol. 10, no. 3, pp. 250–259, Jun. 1960. DOI: 10.1016/0042-207X(60)90147-0.

[58] K. C. D. Hickman and C. R. Sanford, "A study in condensation pumps", *Review of Scientific Instruments*, vol. 1, no. 3, pp. 140–163, Mar. 1930. DOI: 10.1063/1.1748679.

[59] H. R. Smith, "Relationship of diffusion pump performance to the thermodynamics of the pumping fluid", in *Vacuum technology transactions*, C. R. Meissner, Ed., Oxford, New York, Paris, Frankfurt am Main: Pergamon Press, 1960, pp. 140–145, ISBN: 978-1-4831-9852-1. DOI: 10.1016/B978-1-4831-9852-1.50033-5.

[60] H. F. Stimson, "A two-stage mercury vapor pump", *Journal of the Washington Academy of Sciences*, vol. 7, no. 15, pp. 477–482, 1917.

[61] C. S. Bull and O. Klemperer, "The suppression of the evaporation of mercury from diffusion pumps", *Journal of Scientific Instruments*, vol. 20, no. 11, pp. 179–181, Nov. 1943. DOI: 10.1088/0950-7671/20/11/303.

[62] B. D. Power and D. J. Crawley, “Sources, measurement and control of backstreaming: In oil vapour vaccum pumps”, *Vacuum*, vol. 4, no. 4, pp. 415–437, Oct. 1954. DOI: 10.1016/0042-207X(54)90003-2.

[63] N. S. Harris, “Diffusion pump back-streaming”, *Vacuum*, vol. 27, no. 9, pp. 519–530, 1977. DOI: 10.1016/S0042-207X(77)80419-3.

[64] M. Morand, “Vacuum pump”, U.S. Patent 2,508,765, May 23, 1950.

[65] S. A. Vekshinsky, M. I. Menshikov, and I. S. Rabinovich, “High-vacuum pumps and units for accelerators”, *Vacuum*, vol. 9, no. 3–4, pp. 201–206, Jul.–Sep. 1959. DOI: 10.1016/0042-207X(59)90192-7.

[66] M. H. Hablanian, “Pumping fluid condensation in oil diffusion pumps”, *Journal of Vacuum Science & Technology*, vol. 9, no. 1, pp. 421–424, Jan. 1972. DOI: 10.1116/1.1316641.

[67] M. H. Hablanian and J. C. Maliakal, “Advances in diffusion pump technology”, *Journal of Vacuum Science & Technology*, vol. 10, no. 1, pp. 58–64, Jan. 1973. DOI: 10.1116/1.1318043.

[68] M. L. Huber, A. Laesecke, and D. G. Friend, “The vapor pressure of mercury”, National Institute of Standards and Technology, US Department of Commerce, Boulder, Colorado, US, Tech. Rep. NISTIR 6643, Apr. 2006, 56 pp. DOI: 10.6028/NIST.IR.6643.

[69] D. W. Jones and C. A. Tsonis, “Theoretical investigation of oil backstreaming through a vacuum trap”, *Journal of Vacuum Science & Technology*, vol. 1, no. 1, pp. 19–22, Sep. 1964. DOI: 10.1116/1.1377229.

[70] D. J. Santeler, “The use of diffusion pumps for obtaining ultraclean vacuum environments”, *Journal of Vacuum Science & Technology*, vol. 8, no. 1, pp. 299–307, Jan. 1971. DOI: 10.1116/1.1316316.

[71] H. R. Smith, “The technology of large mercury-pumped vacuum systems”, Radiation Laboratory, University of California, Berkeley, California, US, Tech. Rep. UCRL-3194, Nov. 9, 1955, 41 pp.

[72] D. A. Sink and M. Sniderman, “The TFTR ultrahigh-vacuum pumping system incorporating mercury diffusion pumps”, Fusion Power Systems Department, Westinghouse Electric Corporation, Pittsburgh, Pennsylvania, US, Tech. Rep. WFPS-TME-034, Jun. 1976, 112 pp. DOI: 10.2172/5438585.

[73] N. Milleron and L. L. Levenson, “Discussion on optimization of large oil-pumped ultra high vacuum systems”, Lawrence Radiation Laboratory, University of California, Livermore, California, US, Tech. Rep. UCRL-5597, Sep. 12, 1960, 20 pp. DOI: 10.2172/4100899.

[74] N. Milleron and L. L. Levenson, “Vacuum trap and valve combination”, U.S. Patent 3,077,712, Feb. 19, 1963.

[75] T. I. Gombosi, *Gaskinetic theory* (Cambridge Atmospheric and Space Science Series). Cambridge, UK: Cambridge University Press, 1994, ISBN: 978-0-521-43966-4. DOI: 10.1017/CBO9780511524943.

[76] F. Sharipov, *Rarefied gas dynamics: Fundamentals for research and practice*. Weinheim, Germany: Wiley-VCH Verlag GmbH & Co. KGaA, 2016, 305 pp., ISBN: 978-3-527-68507-3. DOI: 10.1002/9783527685523.

[77] G. A. Bird, *Molecular gas dynamics and the direct simulation of gas flows* (Oxford Engineering Science Series 42). Oxford, UK: Clarendon Press, 1994, 458 pp., ISBN: 0-19-856195-4.

[78] K. Koura and H. Matsumoto, "Variable soft sphere molecular model for inverse-power-law or Lennard-Jones potential", *Physics of Fluids A: Fluid Dynamics*, vol. 3, no. 10, pp. 2459–2465, Oct. 1991. DOI: 10.1063/1.858184.

[79] K. Jousten, "Gasgesetze und kinetische Gastheorie (in German)", in *Handbuch Vakuumtechnik*, K. Jousten, Ed., 12th ed., Wiesbaden, Germany: Springer Vieweg, 2018, pp. 33–61, ISBN: 978-3-658-13386-3.

[80] H. Haberland, U. Buck, and M. Tolle, "Velocity distribution of supersonic nozzle beams", *Review of Scientific Instruments*, vol. 56, no. 9, pp. 1712–1716, Sep. 1985. DOI: 10.1063/1.1138129.

[81] L. J. Norrby, "Why is mercury liquid? Or, why do relativistic effects not get into chemistry textbooks?", *Journal of Chemical Education*, vol. 68, no. 2, pp. 110–113, Feb. 1991. DOI: 10.1021/ed068p110.

[82] M. E. Wieser *et al.*, "Atomic weights of the elements 2011 (IUPAC technical report)", *Pure and Applied Chemistry*, vol. 85, no. 5, pp. 1047–1078, Apr. 29, 2013. DOI: 10.1351/PAC-REP-13-03-02.

[83] O. F. Hagena, "Scaling laws for condensation in nozzle flows", *Physics of Fluids*, vol. 17, no. 5, pp. 894–896, May 1974. DOI: 10.1063/1.1694827.

[84] O. F. Hagena, "Condensation in free jets: Comparison of rare gases and metals", *Zeitschrift für Physik D - Atoms, Molecules and Clusters*, vol. 4, pp. 291–299, Sep. 1987. DOI: 10.1007/BF01436638.

[85] N. Y. Bykov and Y. E. Gorbachev, "Cluster formation in copper vapor jet expanding into vacuum: The direct simulation Monte Carlo", *Vacuum*, vol. 163, pp. 119–127, May 2019. DOI: 10.1016/j.vacuum.2019.02.007.

[86] N. Y. Bykov and Y. E. Gorbachev, "Cluster formation process in metal vapor plume", *AIP Conference Proceedings*, vol. 2132, no. 1, 030005, pp. 1–7, Aug. 5, 2019. DOI: 10.1063/1.5119530.

[87] H.-G. Nöller, "Die physikalischen Vorgänge in Diffusions- und Dampfstrahl-Pumpen - I. Die Strömungseigenschaften des Treibstrahles und die Vorvakuumfestigkeit (in German)", *Zeitschrift für angewandte Physik*, vol. 7, no. 5, pp. 218–225, 1955.

[88] A. Hoareau, B. Cabaud, and P. Melinon, "Time-of-flight mass spectroscopy of supersonic beam of metallic vapours; Intensities and appearance potentials of M_x aggregates", *Surface Science*, vol. 106, no. 1–3, pp. 195–203, May 1981. DOI: 10.1016/0039-6028(81)90201-6.

[89] B. Cabaud, A. Hoareau, and P. Melinon, "Time-of-flight spectroscopy of a supersonic beam of mercury. Intensities and appearance potentials of Hg_x aggregates", *Journal of Physics D: Applied Physics*, vol. 13, no. 10, pp. 1831–1834, Oct. 1980. DOI: 10.1088/0022-3727/13/10/011.

[90] C. Cai and I. D. Boyd, "Collisionless gas expanding into vacuum", *Journal of Spacecraft and Rockets*, vol. 44, no. 6, pp. 1326–1330, 2007-11/2007-12. DOI: 10.2514/1.32173.

[91] C. Cai, K. R. A. Khasawneh, H. Liu, and M. Wei, "Collisionless gas flows over a cylindrical or spherical object", *Journal of Spacecraft and Rockets*, vol. 46, no. 6, pp. 1124–1131, Nov.–Dec. 2009. DOI: 10.2514/1.44071.

[92] C. Cai, Q. Sun, and A. Vanderwyst, "Analytical exact solutions for unsteady collisionless plume flows in a vacuum", *Acta Astronautica*, vol. 91, pp. 218–227, Oct.–Nov. 2013. DOI: 10.1016/j.actaastro.2013.06.019.

[93] C. Cai and X. He, "Detailed flowfield and surface properties for high Knudsen number planar jet impingement at an inclined flat plate", *Physics of Fluids*, vol. 28, no. 5, 056103, pp. 1–30, May 2016. DOI: 10.1063/1.4948365.

[94] A. K. Rebrov, P. A. Skovorodko, S. V. Nedosekova, and J. J. Roig, "Numerical simulation of pumping process in the diffusion pump", in *Rarefied gas dynamics: Experimental techniques and physical systems*, ser. Progress in Astronautics and Aeronautics, D. Weaver, Ed., Series editor A. R. Seebass, vol. 158, American Institute of Aeronautics and Astronautics, Inc., Jan. 1994, pp. 143–151. DOI: 10.2514/5.9781600866302.0143.0151.

[95] N. V. Iliasova, S. V. Nedosekova, A. K. Rebrov, P. A. Skovorodko, and J. J. Roig, "Computational optimization of diffusion pump parameters", *Vacuum*, vol. 44, no. 5–7, pp. 745–747, May–Jul. 1993. DOI: 10.1016/0042-207X(93)90139-2.

[96] A. K. Rebrov, "New principles of improvements of diffusion pumps", *Vacuum*, vol. 44, no. 5–7, pp. 741–743, May–Jul. 1993. DOI: 10.1016/0042-207X(93)90138-Z.

[97] M. Knudsen, "Die Gesetze der Molekularströmung und der inneren Reibungsströmung der Gase durch Röhren (in German)", *Annalen der Physik*, vol. 333, no. 1, pp. 75–130, 1909. DOI: 10.1002/andp.19093330106.

[98] G. A. Bird, "Approach to translational equilibrium in a rigid sphere gas", *Physics of Fluids*, vol. 6, no. 10, pp. 1518–1519, Oct. 1963. DOI: 10.1063/1.1710976.

[99] G. A. Bird, "Direct simulation and the Boltzmann equation", *Physics of Fluids*, vol. 13, no. 11, pp. 2676–2681, Nov. 1970. DOI: 10.1063/1.1692849.

[100] G. A. Bird, "Monte Carlo simulation in an engineering context", in *Rarefied gas dynamics, Parts I and II*, ser. Progress in Astronautics and Aeronautics, S. S. Fisher, Ed., vol. 74, American Institute of Aeronautics and Astronautics, Inc., Jan. 1981, pp. 239–255. DOI: 10.2514/5.9781600865480.0239.0255.

[101] Y. K. Lee and J. W. Lee, "Analysis of the compression characteristics of vapor jet injected into high vacuum", *KSME Journal*, vol. 10, no. 1, pp. 72–85, 1996. DOI: 10.1007/BF02953946.

[102] Y. K. Lee and J. W. Lee, "Direct simulation of pumping characteristics for a model diffusion pump", *Vacuum*, vol. 47, no. 3, pp. 297–306, Mar. 1996. DOI: 10.1016/0042-207X(95)00230-8.

[103] C.-l. Zhao, S.-f. Mao, P. Liu, S.-j. Qin, Y. Yu, and M.-y. Ye, "DSMC simulation study of influence of nozzle angle on pumping performance of mercury diffusion pump (in Chinese)", *VACUUM (Chinese)*, vol. 57, no. 2, pp. 8–12, Mar. 2020. DOI: 10.13385/j.cnki.vacuum.2020.02.02.

[104] Z. Liao, S. Mao, C. Zhao, and M. Ye, "Study of the linear mercury diffusion pump with the fixed mass-flow-rate model by direct simulation Monte Carlo method", *Fusion Engineering and Design*, vol. 173, 112796, pp. 1–7, Dec. 2021. DOI: 10.1016/j.fusengdes.2021.112796.

[105] F. Sharipov, "Numerical simulation of turbomolecular pump over a wide range of gas rarefaction", *Journal of Vacuum Science & Technology A*, vol. 28, no. 6, pp. 1312–1315, Nov. 2010. DOI: 10.1116/1.3484139.

[106] G. A. Bird, "Effect of inlet guide vanes and sharp blades on the performance of a turbomolecular pump", *Journal of Vacuum Science & Technology A*, vol. 29, no. 1, 011016, pp. 1–6, Jan. 2011. DOI: 10.1116/1.3521313.

[107] M. Rose, "Simulation of a complete triple turbo molecular pumping stage using direct simulation Monte Carlo in 3D", *AIP Conference Proceedings*, vol. 1628, no. 1, pp. 212–219, Dec. 9, 2014. DOI: 10.1063/1.4902595.

[108] T. J. Scanlon, E. Roohi, C. White, M. Darbandi, and J. M. Reese, "An open source, parallel DSMC code for rarefied gas flows in arbitrary geometries", *Computers & Fluids*, vol. 39, no. 10, pp. 2078–2089, Dec. 2010. DOI: 10.1016/j.compfluid.2010.07.014.

[109] C. White *et al.*, "dsmcFoam+: An OpenFOAM based direct simulation Monte Carlo solver", *Computer Physics Communications*, vol. 224, pp. 22–43, Mar. 2018. DOI: 10.1016/j.cpc.2017.09.030.

[110] H. G. Weller, G. Tabor, H. Jasak, and C. Fureby, "A tensorial approach to computational continuum mechanics using object-oriented techniques", *Computers in Physics*, vol. 12, no. 6, pp. 620–631, 1998-11. DOI: 10.1063/1.168744.

[111] M. A. Gallis, J. R. Torczynski, S. J. Plimpton, D. J. Rader, and T. Koehler, "Direct simulation Monte Carlo: The quest for speed", *AIP Conference Proceedings*, vol. 1628, no. 1, pp. 27–36, Dec. 9, 2014. DOI: 10.1063/1.4902571.

[112] M. A. Gallis, T. P. Koehler, and S. J. Plimpton, "SPARTA - stochastic Particle Real Time Analyzer - Validation and verification suite", Sandia National Laboratories, Albuquerque, New Mexico, US, Tech. Rep. SAND2014-19198, Sep. 2014. DOI: 10.2172/1324252.

[113] A. G. Klothakis, I. K. Nikolos, T. P. Koehler, M. A. Gallis, and S. J. Plimpton, "Validation simulations of the DSMC code SPARTA", *AIP Conference Proceedings*, vol. 1786, no. 1, 050016, pp. 1–8, Nov. 15, 2016. DOI: 10.1063/1.4967566.

[114] J. E. Broadwell, "Study of rarefied shear flow by the discrete velocity method", *Journal of Fluid Mechanics*, vol. 19, no. 3, pp. 401–414, Jul. 1964. DOI: 10.1017/S0022112064000817.

[115] A. B. Huang and D. L. Hartley, "Nonlinear rarefied Couette flow with heat transfer", *Physics of Fluids*, vol. 11, no. 6, pp. 1321–1326, Jun. 1968. DOI: 10.1063/1.1692103.

[116] P. L. Bhatnagar, E. P. Gross, and M. Krook, "A model for collision processes in gases. I. Small amplitude processes in charged and neutral one-component systems", *Physical Review*, vol. 94, no. 3, pp. 511–525, May 1954. DOI: 10.1103/PhysRev.94.511.

[117] E. M. Shakhov, "Generalization of the Krook kinetic relaxation equation", *Fluid Dynamics*, vol. 3, pp. 95–96, Sep. 1968. DOI: 10.1007/BF01029546.

[118] M. Groppi, S. Monica, and G. Spiga, "A kinetic ellipsoidal BGK model for a binary gas mixture", *Europhysics Letters*, vol. 96, no. 6, 64002, pp. 1–6, Dec. 2011. DOI: 10.1209/0295-5075/96/64002.

[119] L. Zhu, C. Songze, and G. Zhaoli, "dugksFoam: An open source OpenFOAM solver for the Boltzmann model equation", *Computer Physics Communications*, vol. 213, pp. 155–164, Apr. 2017. DOI: 10.1016/j.cpc.2016.11.010.

[120] R. Kersevan and J.-L. Pons, "Introduction to MOLFLOW+: New graphical processing unit-based Monte Carlo code for simulating molecular flows and for calculating angular coefficients in the compute unified device architecture environment", *Journal of Vacuum Science & Technology A*, vol. 27, no. 4, pp. 1017–1023, Jul. 2009. DOI: 10.1116/1.3153280.

[121] M. Ady, "Monte Carlo simulations of ultra high vacuum and synchrotron radiation for particle accelerators", Dissertation, School of Basic Sciences, École Polytechnique Fédérale de Lausanne (EPFL), Lausanne, Switzerland, 2016, 183 pp.

[122] G. A. Bird, "Perception of numerical methods in rarefied gasdynamics", in *Rarefied gas dynamics: Theoretical and computational techniques*, ser. Progress in Astronautics and Aeronautics, D. P. Weaver, C. D. H., and M. E. P., Eds., vol. 118, American Institute of Aeronautics and Astronautics, Inc., Jan. 1989, pp. 211–226. DOI: 10.2514/5.9781600865923.0211.0226.

[123] S. Stefanov and C. Cercignani, "Monte Carlo simulation of Bénard's instability in a rarefied gas", *European Journal of Mechanics - B/Fluids*, vol. 11, no. 5, pp. 543–553, 1992.

[124] F. J. Alexander, A. L. Garcia, and B. J. Alder, "Cell size dependence of transport coefficients in stochastic particle algorithms", *Physics of Fluids*, vol. 10, no. 6, pp. 1540–1542, Jun. 1998. DOI: 10.1063/1.869674.

[125] M. S. Green, "Markoff random processes and the statistical mechanics of time-dependent phenomena. II. Irreversible processes in fluids", *The Journal of Chemical Physics*, vol. 22, no. 3, pp. 398–413, Mar. 1954. DOI: 10.1063/1.1740082.

[126] R. Kubo, "Statistical-mechanical theory of irreversible processes. I. General theory and simple applications to magnetic and conduction problems", *Journal of the Physical Society of Japan*, vol. 12, no. 6, pp. 570–586, Jun. 1957. DOI: 10.1143/JPSJ.12.570.

[127] N. G. Hadjiconstantinou, "Analysis of discretization in the direct simulation Monte Carlo", *Physics of Fluids*, vol. 12, no. 10, pp. 2634–2638, Oct. 2000. DOI: 10.1063/1.1289393.

[128] G. Chen and I. D. Boyd, "Statistical error analysis for the direct simulation Monte Carlo technique", *Journal of Computational Physics*, vol. 126, no. 2, pp. 434–448, Jul. 1996. DOI: 10.1006/jcph.1996.0148.

[129] D. J. Rader, M. A. Gallis, J. R. Torczynski, and W. Wagner, "Direct simulation Monte Carlo convergence behavior of the hard-sphere-gas thermal conductivity for Fourier heat flow", *Physics of Fluids*, vol. 18, no. 7, 077102, pp. 1–16, Jul. 2006. DOI: 10.1063/1.2213640.

[130] G. J. LeBeau, "A parallel implementation of the direct simulation Monte Carlo method", *Computer Methods in Applied Mechanics and Engineering*, vol. 174, no. 3–4, pp. 319–337, May 1999. DOI: 10.1016/S0045-7825(98)00302-8.

[131] T. Teichmann and C. Day, "Particle simulation of linear diffusion pumps for DEMO torus exhaust pumping", *Fusion Engineering and Design*, vol. 169, 112694, pp. 1–11, Aug. 2021. DOI: 10.1016/j.fusengdes.2021.112694.

[132] T. Teichmann, T. Giegerich, and C. Day, "Simulation of mercury-driven diffusion pumps for torus exhaust pumping", *IEEE Transactions on Plasma Science*, vol. 50, no. 11, pp. 4459–4464, Nov. 2022. DOI: 10.1109/TPS.2022.3202083.

[133] L. F. Epstein and M. D. Powers, "Liquid metals. I. The viscosity of mercury vapor and the potential function for mercury", *The Journal of Physical Chemistry*, vol. 57, no. 3, pp. 336–341, Mar. 1953. DOI: 10.1021/j150504a019.

[134] J. O. Hirschfelder, C. F. Curtiss, and R. B. Bird, *Molecular theory of gases and liquids*. New York, New York, US: John Wiley & Sons, Inc., 1954, 1219 pp.

[135] K. A. Stephani, "Development of a hybrid DSMC/CFD method for hypersonic boundary layer flow over discrete surface roughness", Dissertation, Faculty of the Graduate School, University of Texas, Austin, Texas, US, May 2012.

[136] A. B. Weaver, "Assessment of high-fidelity collision models in the direct simulation Monte Carlo method", Dissertation, Graduate School, Purdue University, West Lafayette, Inidiana, US, May 2015, 148 pp.

[137] J. A. Nelder and R. Mead, "A Simplex method for function minimization", *The Computer Journal*, vol. 7, no. 4, pp. 308–313, Jan. 1965. DOI: 10.1093/comjnl/7.4.308.

[138] P. Virtanen *et al.*, "SciPy 1.0: Fundamental algorithms for scientific computing in Python", *Nature Methods*, vol. 17, pp. 261–272, Mar. 2020. DOI: 10.1038/s41592-019-0686-2.

[139] P. D. Neufeld, A. R. Janzen, and R. A. Aziz, "Empirical equations to calculate 16 of the transport collision integrals $\Omega^{(l,s)^*}$ for the Lennard-Jones (12–6) potential", *The Journal of Chemical Physics*, vol. 57, no. 3, pp. 1100–1102, Aug. 1972. DOI: 10.1063/1.1678363.

[140] M. Klein and F. J. Smith, "Tables of collision integrals for the (m,6) potential function for 10 values of m", *Journal of Research of the National Bureau of Standards - A. Physics and Chemistry*, vol. 72A, no. 4, pp. 359–423, Jul.–Aug. 1968. DOI: 10.6028/jres.072A.033.

[141] J. Kestin, S. T. Ro, and W. A. Wakeham, "Viscosity of the isotopes of hydrogen and their intermolecular force potentials", *Journal of the Chemical Society, Faraday Transactions 1: Physical Chemistry in Condensed Phases*, vol. 68, no. 0, pp. 2316–2323, 1972. DOI: 10.1039/F19726802316.

[142] M. J. Assael, S. Mixafendi, and W. A. Wakeham, "The viscosity of normal deuterium in the limit of zero density", *Journal of Physical and Chemical Reference Data*, vol. 16, no. 2, pp. 189–192, Apr. 1987. DOI: 10.1063/1.555778.

[143] M. J. Assael, S. Mixafendi, and W. A. Wakeham, "The viscosity and thermal conductivity of normal hydrogen in the limit of zero density", *Journal of Physical and Chemical Reference Data*, vol. 15, no. 4, pp. 1315–1322, Oct. 1986. DOI: 10.1063/1.555764.

[144] A. van Itterbeek and A. Claes, "Measurements on the viscosity of hydrogen- and deuterium gas between 293°K and 14°K", *Physica*, vol. 5, no. 10, pp. 938–944, Dec. 1938. DOI: 10.1016/S0031-8914(38)80036-7.

[145] P. J. Gardner, P. Pang, and S. R. Preston, "Binary gaseous diffusion coefficients of mercury and of zinc in hydrogen, helium, argon, nitrogen, and carbon dioxide", *Journal of Chemical & Engineering Data*, vol. 36, no. 3, pp. 265–268, Jul. 1991. DOI: 10.1021/je00003a003.

[146] B. Clément *et al.*, "Determination of diffusion coefficients of mercury atoms in various gases from longitudinal spin relaxation in magnetic gradients", *Physical Review A*, vol. 106, no. 6, 062815, pp. 1–8, Dec. 19, 2022. DOI: 10.1103/PhysRevA.106.062815.

[147] K. Nakayama, "An accurate measurement of the mercury vapour drag effect in the pressure region of transition flow", *Japanese Journal of Applied Physics*, vol. 7, no. 9, pp. 1114–1119, Sep. 1968. DOI: 10.1143/JJAP.7.1114.

[148] H. B. Spencer, J. M. Toguri, and J. A. Kurtis, "Diffusivity measurements of the argon-mercury vapor system", *Canadian Journal of Chemistry*, vol. 47, no. 12, pp. 2197–2203, Jun. 1969. DOI: 10.1139/v69-357.

[149] A. Frezzotti, "Non-equilibrium structure of the vapor-liquid interface of a binary fluid", *AIP Conference Proceedings*, vol. 1333, no. 1, pp. 161–166, May 20, 2011. DOI: 10.1063/1.3562642.

[150] J. Delhommelle and P. Millié, "Inadequacy of the Lorentz-Berthelot combining rules for accurate predictions of equilibrium properties by molecular simulation", *Molecular Physics*, vol. 99, no. 8, pp. 619–625, 2001. DOI: 10.1080/00268970010020041.

[151] S. Sharma, *Thermal and statistical physics - Concepts and applications*. Cham, Switzerland: Springer Nature Switzerland AG, 2022, 393 pp., ISBN: 978-3-031-07685-5. DOI: 10.1007/978-3-031-07685-5.

[152] R. T. Jacobsen and R. B. Stewart, "Thermodynamic properties of nitrogen including liquid and vapor phases from 63 K to 2000 K with pressures to 10,000 bar", *Journal of Physical and Chemical Reference Data*, vol. 2, no. 4, pp. 757–922, Oct. 1973. DOI: 10.1063/1.3253132.

[153] L. Haar, A. S. Friedman, and C. W. Beckett, *Ideal gas thermodynamic functions and isotope exchange functions for the diatomic hydrides, deuterides, and tritides* (NBS Monograph 20). Washington D.C., US: National Bureau of Standards, US Department of Commerce, May 1961, 271 pp. DOI: 10.2172/4067290.

[154] C. Borgnakke and P. S. Larsen, "Statistical collision model for Monte Carlo simulation of polyatomic gas mixture", *Journal of Computational Physics*, vol. 18, no. 4, pp. 405–420, Aug. 1, 1975. DOI: 10.1016/0021-9991(75)90094-7.

[155] F. Robben and L. Talbot, "Experimental study of the rotational distribution function of nitrogen in a shock wave", *Physics of Fluids*, vol. 9, no. 4, pp. 653–662, Apr. 1966. DOI: 10.1063/1.1761730.

[156] K. J. Higdon, B. A. Cruden, A. M. Brandis, D. S. Liechty, D. B. Goldstein, and P. L. Varghese, "DSMC shock simulation of Saturn entry probe conditions", in *46th AIAA Thermophysics Conference*, (Washington D.C., US, Jun. 13–17, 2016), 2016. DOI: 10.2514/6.2016-3840.

[157] S. Montero and J. Pérez-Ríos, "Rotational relaxation in molecular hydrogen and deuterium: Theory versus acoustic experiments", *The Journal of Chemical Physics*, vol. 141, no. 11, 114301, pp. 1–13, Sep. 17, 2014. DOI: 10.1063/1.4895398.

[158] K. Kern, R. David, and G. Comsa, "Low temperature measurements of the rotational relaxation in D_2 free jets", *The Journal of Chemical Physics*, vol. 82, no. 12, pp. 5673–5676, Jun. 15, 1985. DOI: 10.1063/1.448554.

[159] C. Galitzine and D. Boyd, "Development of an adaptive weighting scheme for DSMC and its application to an axisymmetric jet", *AIP Conference Proceedings*, vol. 1501, no. 1, pp. 587–594, Nov. 27, 2012. DOI: 10.1063/1.4769595.

[160] C. Galitzine and I. D. Boyd, "An adaptive procedure for the numerical parameters of a particle simulation", *Journal of Computational Physics*, vol. 281, pp. 449–472, Jan. 15, 2015. DOI: 10.1016/j.jcp.2014.10.044.

[161] K. Nanbu, "Probability theory of electron-molecule, ion-molecule, molecule-molecule, and Coulomb collisions for particle modeling of materials processing plasmas and cases", *IEEE Transactions on Plasma Science*, vol. 28, no. 3, pp. 971–990, Jun. 2000. DOI: 10.1109/27.887765.

[162] I. D. Boyd, "Conservative species weighting scheme for the direct simulation Monte Carlo method", *Journal of Thermophysics and Heat Transfer*, vol. 10, no. 4, pp. 579–585, Oct.–Dec. 1996. DOI: 10.2514/3.832.

[163] S. Rjasanow and W. Wagner, "A stochastic weighted particle method for the Boltzmann equation", *Journal of Computational Physics*, vol. 124, no. 2, pp. 243–253, Mar. 15, 1996. DOI: 10.1006/jcph.1996.0057.

[164] S. J. Araki and R. S. Martin, "Interspecies fractional collisions", *Physics of Plasmas*, vol. 27, no. 3, 033504, pp. 1–11, Mar. 2020. DOI: 10.1063/1.5143145.

[165] G. Oblapenko, D. Goldstein, P. Varghese, and C. Moore, "Hedging direct simulation Monte Carlo bets via event splitting", *Journal of Computational Physics*, vol. 466, 111390, pp. 1–17, Oct. 1, 2022. DOI: 10.1016/j.jcp.2022.111390.

[166] S. Varoutis, F. Bonelli, C. Day, and Y. Igitkhanov, "Optimization of pumping efficiency and divertor operation in DEMO", *Nuclear Materials and Energy*, vol. 12, pp. 668–673, Aug. 2017. DOI: 10.1016/j.nme.2017.04.001.

[167] C. Gleason González, "Modelling and validation of neutral particle flow by means of stochastic algorithms using the example of a fusion divertor", Dissertation, Department of Mechanical Engineering, Karlsruhe Institute of Technology, Karlsruhe, Germany, Sep. 29, 2022, 199 pp. DOI: 10.5445/IR/1000152187.

[168] M. Knudsen, "Das Cosinusgesetz in der kinetischen Gastheorie (in German)", *Annalen der Physik*, vol. 353, no. 24, pp. 1113–1121, 1916. DOI: 10.1002/andp.19163532409.

[169] R. Feres and G. Yablonsky, "Knudsen's cosine law and random billiards", *Chemical Engineering Science*, vol. 59, no. 7, pp. 1541–1556, Apr. 2004. DOI: 10.1016/j.ces.2004.01.016.

[170] A. Mohammadzadeh, A. Rana, and H. Struchtrup, "DSMC and R13 modeling of the adiabatic surface", *International Journal of Thermal Sciences*, vol. 101, pp. 9–23, Mar. 2016. DOI: 10.1016/j.ijthermalsci.2015.10.007.

[171] A. Frezzotti and T. Ytrehus, "Kinetic theory study of steady condensation of a polyatomic gas", *Physics of Fluids*, vol. 18, no. 2, 027101, pp. 1–12, Feb. 2006. DOI: 10.1063/1.2171231.

[172] A. Frezzotti, "A numerical investigation of the steady evaporation of a polyatomic gas", *European Journal of Mechanics - B/Fluids*, vol. 26, no. 1, pp. 93–104, Jan.–Feb. 2007. DOI: 10.1016/j.euromechflu.2006.03.007.

[173] A. Frezzotti, "Boundary conditions at the vapor-liquid interface", *Physics of Fluids*, vol. 23, no. 3, 030609, pp. 1–9, Mar. 2011. DOI: 10.1063/1.3567001.

[174] M. Knudsen, "Die maximale Verdampfungsgeschwindigkeit des Quecksilbers (in German)", *Annalen der Physik*, vol. 352, no. 13, pp. 697–708, 1915. DOI: 10.1002/andp.19153521306.

[175] J. N. Brönsted and G. Hevesy, "The separation of the isotopes of mercury", *Nature*, vol. 106, no. 2657, pp. 144–144, Sep. 1920. DOI: 10.1038/106144c0.

[176] M. Volmer and I. Estermann, "Über den Verdampfungskoeffizienten von festem und flüssigem Quecksilber (in German)", *Zeitschrift für Physik*, vol. 7, pp. 1–12, Dec. 1921. DOI: 10.1007/BF01332773.

[177] M. N. Ivanovskii, Y. V. Milovanov, and V. I. Subbotin, "Condensation coefficient of mercury vapor", *Soviet Atomic Energy*, vol. 24, pp. 176–181, Feb. 1968. DOI: 10.1007/BF01114185.

[178] U. Narusawa and G. S. Springer, "Measurement of the condensation coefficient of mercury by a molecular beam method", *Journal of Heat Transfer*, vol. 97, no. 1, pp. 83–87, Feb. 1975. DOI: 10.1115/1.3450294.

[179] S. P. Sukhatme and W. M. Rohsenow, "Heat transfer during film condensation of a liquid metal vapor", Department of Mechanical Engineering, Massachusetts Institute of Technology, Cambridge, Massachusetts, US, Tech. Rep. 9167-27 / MIT-2995-1, Apr. 1964, 68 pp.

[180] S. Necmi and J. W. Rose, "Film condensation of mercury", *International Journal of Heat and Mass Transfer*, vol. 19, no. 11, pp. 1245–1256, Nov. 1976. DOI: 10.1016/0017-9310(76)90076-4.

[181] J. Niknejad and J. W. Rose, "Interphase matter transfer: An experimental study of condensation of mercury", *Proceedings of the Royal Society of London. A. Mathematical and Physical Sciences*, vol. 378, pp. 305–327, Oct. 26, 1981. DOI: 10.1098/rspa.1981.0154.

[182] S. Taguchi, K. Aoki, and S. Takata, "Vapor flows condensing at incidence onto a plane condensed phase in the presence of a noncondensable gas. II. Supersonic condensation", *Physics of Fluids*, vol. 16, no. 1, pp. 79–92, Jan. 2004. DOI: 10.1063/1.1630324.

[183] A. Polikarpov and I. Graur, "Evaporation and condensation of rarefied gas between two parallel condensed phases", *Journal of Physics: Conference Series*, vol. 925, 012013, pp. 1–4, Nov. 2017. DOI: 10.1088/1742-6596/925/1/012013.

[184] K. Ohashi, K. Kobayashi, H. Fujii, and M. Watanabe, "Evaporation coefficient and condensation coefficient of vapor under high gas pressure conditions", *Scientific Reports*, vol. 10, no. 1, 8143, pp. 1–10, May 18, 2020. DOI: 10.1038/s41598-020-64905-5.

[185] A. P. Kryukov, V. V. Zhakhovsky, and V. Y. Levashov, "Condensation of subsonic and supersonic gas flows on a flat surface", *International Journal of Heat and Mass Transfer*, vol. 198, 123390, pp. 1–11, Dec. 1, 2022. DOI: 10.1016/j.ijheatmasstransfer.2022.123390.

[186] T. Ytrehus and S. Østmo, "Kinetic theory approach to interphase processes", *International Journal of Multiphase Flow*, vol. 22, no. 1, pp. 133–155, Feb. 1996. DOI: 10.1016/0301-9322(95)00056-9.

[187] M. Kollera and U. Grigull, "Untersuchungen zur Kondensation von Quecksilberdampf (in German)", *Wärme- und Stoffübertragung*, vol. 4, no. 4, pp. 244–258, Dec. 1971. DOI: 10.1007/BF01002479.

[188] K. Khasawneh, C. Cai, and H. Liu, "Rarefied compressible two-dimensional jet plume impingement on a flat plate", in *49th AIAA Aerospace Sciences Meeting including the New Horizons Forum and Aerospace Exposition*, ser. Aerospace Sciences Meetings, Orlando, Florida, US: American Institute of Aeronautics and Astronautics, Jan. 4–7, 2011. DOI: 10.2514/6.2011-761.

[189] G. Tóth, "Eine Übersicht über die Theorie der Diffusionspumpen, Teil 1 (in German)", *Vakuum-Technik*, vol. 16, no. 3, pp. 41–47, Mar. 1967.

[190] L. Wertenstein, "Contribution to the theory of the diffusion pump", *Mathematical Proceedings of the Cambridge Philosophical Society*, vol. 23, no. 5, pp. 578–583, Jan. 1927. DOI: 10.1017/S0305004100011713.

[191] M. Matricon, "Etude sur la vitesse d'extraction des pompes à condensation (in French)", *Journal de Physique et Le Radium*, vol. 3, no. 3, pp. 127–144, Mar. 1932. DOI: 10.1051/jphysrad:0193200303012700.

[192] R. Jaeckel, "Zur Theorie der Diffusionspumpe (in German)", *Zeitschrift für Naturforschung A*, vol. 2, no. 11–12, pp. 666–677, 1947. DOI: 10.1515/zna-1947-11-1211.

[193] C. H. Kruger, "The axial-flow compressor in the free-molecule range", Dissertation, Department of Mechanical Engineering, Massachusetts Institute of Technology, Cambridge, Massachusetts, US, 1960, 90 pp.

[194] J. S. Maulbetsch and A. H. Sharipo, "Free-molecule flow in the axial-flow turbo-vacuum pump", Fluid Mechanics Laboratory, Department of Mechanical Engineering, Massachusetts Institute of Technology, Cambridge, Massachusetts, US, Tech. Rep. DSR 7-8120, Mar. 1963, 45 pp.

[195] K.-H. Bernhardt, "Calculation of the pumping speed of turbomolecular vacuum pumps by means of simple mechanical data", *Journal of Vacuum Science & Technology A*, vol. 1, no. 2, pp. 136–139, Apr. 1983. DOI: 10.1116/1.572058.

[196] K. Jousten, "Molekular- und Turbomolekularpumpen (in German)", in *Handbuch Vakuumtechnik*, K. Jousten, Ed., 12th ed., Wiesbaden, Germany: Springer Vieweg, 2018, pp. 487–534, ISBN: 978-3-658-13386-3.

[197] M. A. Branch, T. F. Coleman, and Y. Li, "A subspace, interior, and conjugate gradient method for large-scale bound-constrained minimization problems", *SIAM Journal on Scientific Computing*, vol. 21, no. 1, pp. 1–23, Jan. 1999. DOI: 10.1137/S1064827595289108.

[198] T. Teichmann, C. Tantos, and C. Day, "Analytical, stochastic and deterministic modeling of diffusion pumps", *AIP Conference Proceedings*, vol. 2996, no. 1, 180002, pp. 1–12, Feb. 2024. DOI: 10.1063/5.0187495.

[199] T. Teichmann, T. Giegerich, M. Jäger, and C. Day, "Experimental and numerical investigation of expanding mercury vapor jets", *IEEE Transactions on Plasma Science*, 2024, Manuscript accepted for publication (Apr. 2024). DOI: 10.1109/TPS.2024.3394756.

[200] H. Kutscher, "Die physikalischen Vorgänge in Diffusions- und Dampfstrahl-Pumpen - IV. Eine Methode zur Druckmessung in Überschall-Dampfströmungen bei niedrigen Drucken, ihre Ergebnisse und ihr Vergleich mit den Strömungsbildern (in German)", *Zeitschrift für angewandte Physik*, vol. 7, no. 5, pp. 234–240, 1955.

[201] T. Giegerich, K. Battes, J. C. Schwenzer, and C. Day, "Development of a viable route for lithium-6 supply of DEMO and future fusion power plants", *Fusion Engineering and Design*, vol. 149, 111339, pp. 1–10, Dec. 2019. DOI: 10.1016/j.fusengdes.2019.111339.

[202] H. Bettin and H. Fehlhauer, "Density of mercury - measurements and reference values", *Metrologia*, vol. 41, no. 2, pp. 16–23, Mar. 2004. DOI: 10.1088/0026-1394/41/2/S02.

[203] BIPM, IEC, IFCC, ILAC, ISO, IUPAC, IUPAP and OIML (Joint Committee for Guides in Metrology). "Evaluation of measurement data - Guide to the expression of uncertainty in measurement (JCGM 100:2008)". (2010), [Online]. Available: https://www.bipm.org/documents/20126/2071204/JCGM_100_2008_E.pdf (visited on Dec. 9, 2022).

[204] Normenausschuß Vakuumtechnik (NAV) im DIN Deutsches Institut für Normung e.V, *DIN 28427: Abnahmeregeln für Diffusionspumpen und Dampfstrahlvakuumpumpen für Treibmitteldampfdrücke kleiner 1 mbar (in German)*. Berlin, Germany: Beuth Verlag GmbH, Feb. 1983, 10 pp.

[205] A. Savitzky and M. J. E. Golay, "Smoothing and differentiation of data by simplified least squares procedures", *Analytical Chemistry*, vol. 36, no. 8, pp. 1627–1639, Jul. 1964. DOI: 10.1021/ac60214a047.

[206] G. Tóth, "The pumping theory of diffusion pumps", *Acta Physica Academiae Scientiarum Hungaricae*, vol. 20, pp. 99–114, Feb. 1966. DOI: 10.1007/BF03157048.

[207] B. D. Power, N. T. M. Dennis, and D. J. Crawley, "Aspects of the technology of mercury vapour pumping systems", in *Transactions of the Eighth National Vacuum Symposium combined with the Second International Congress on Vacuum Science and Technology*, (Washington, D.C., US, Oct. 16–19, 1961), vol. 2, 1962, pp. 1218–1223.

[208] B. E. Poling, G. H. Thomson, D. G. Friend, R. L. Rowley, and W. V. Wilding, "Physical and chemical data (Section 2)", in *Perry's chemical engineers' handbook*, D. W. Green and R. H. Perry, Eds., 8th ed., New York, Chicago, San Francisco, Lisbon, London, Madrid, Mexico City, Milan, New Delhi, San Juan, Seoul, Singapore, Sydney, Toronto: McGraw-Hill, 2008, ISBN: 0-07-154209-4.

[209] J. N. Tilton, "Fluid and particle dynamics (Section 6)", in *Perry's chemical engineers' handbook*, D. W. Green and R. H. Perry, Eds., 8th ed., New York, Chicago, San Francisco, Lisbon, London, Madrid, Mexico City, Milan, New Delhi, San Juan, Seoul, Singapore, Sydney, Toronto: McGraw-Hill, 2008, ISBN: 0-07-154213-2.

[210] C. Benvenuti, D. Blechschmidt, and G. Passardi, "Molecular and radiation transmissivities of chevron type baffles for cryopumping", *Journal of Vacuum Science & Technology*, vol. 19, no. 1, pp. 100–103, May 1981. DOI: 10.1116/1.570996.

[211] N. Saho, T. Uede, Y. Yamashita, O. Kaneko, and Y. Takeiri, "Monte Carlo simulation of transmission probability in cryopumps for neutral beam injectors", in *Fusion technology 1990*, B. E. Keen, M. Huguet, and R. Hemsworth, Eds., Oxford, UK: Elsevier, 1991, pp. 317–321, ISBN: 978-0-444-88508-1. DOI: 10.1016/B978-0-444-88508-1.50046-3.

[212] A. W. Ross, M. Fink, and H. F. Wellenstein, "Monte Carlo simulation of chevron baffle performance", *Journal of Vacuum Science & Technology A*, vol. 11, no. 3, pp. 723–725, May 1993. DOI: 10.1116/1.578798.

[213] S. R. In and M. Y. Park, "Transmission probability of the chevron baffle", *Journal of the Korean Vacuum Science & Technology*, vol. 5, no. 1, pp. 25–32, 2001.

[214] M. Miki, B. Felder, K. Tsuzuki, M. Izumi, and H. Hayakawa, "Development of the cryo-rotary joint for a HTS synchronous motor with Gd-bulk HTS field-pole magnets", *Journal of Physics: Conference Series*, vol. 234, no. 3, 032039, pp. 1–7, Jun. 2010. DOI: 10.1088/1742-6596/234/3/032039.

[215] Y. Kathage *et al.*, "Experimental progress in the development of a metal foil pump for demo", *Plasma*, vol. 6, no. 4, pp. 714–734, 2023. DOI: 10.3390/plasma6040049.

[216] C. Gliss *et al.*, "Initial integration concept of the DEMO lower horizontal port", *Fusion Engineering and Design*, vol. 146, no. B, pp. 2667–2670, Sep. 2019. DOI: 10.1016/j.fusengdes.2019.04.078.

[217] T. Giegerich *et al.*, "Preliminary configuration of the torus vacuum pumping system installed in the DEMO lower port", *Fusion Engineering and Design*, vol. 146, no. B, pp. 2180–2183, Sep. 2019. DOI: 10.1016/j.fusengdes.2019.03.147.

[218] X. Luo, Y. Kathage, T. Teichmann, S. Hanke, T. Giegerich, and C. Day, "Assessment of metal foil pump configurations for EU-DEMO", *Energies*, vol. 17, no. 16, 3889, pp. 1–12, Aug. 2024. DOI: 10.3390/en17163889.

[219] T. Haertl *et al.*, "Design and feasibility of a pumping concept based on tritium direct recycling", *Fusion Engineering and Design*, vol. 174, 112969, pp. 1–9, Jan. 2022. DOI: 10.1016/j.fusengdes.2021.112969.

[220] M. D'Onorio and G. Caruso, "Pressure suppression system influence on vacuum vessel thermal-hydraulics and on source term mobilization during a multiple first wall – blanket pipe break", *Fusion Engineering and Design*, vol. 164, 112224, pp. 1–7, Mar. 2021. DOI: 10.1016/j.fusengdes.2020.112224.

[221] R. Arredondo, K. Schmid, F. Subba, and G. A. Spagnuolo, "Preliminary estimates of tritium permeation and retention in the first wall of DEMO due to ion bombardment", *Nuclear Materials and Energy*, vol. 28, 101039, pp. 1–9, Sep. 2021. DOI: 10.1016/j.nme.2021.101039.

[222] C. W. Oatley, "The flow of gas through composite systems at very low pressures", *British Journal of Applied Physics*, vol. 8, no. 1, pp. 15–19, Jan. 1957. DOI: 10.1088/0508-3443/8/1/305.

[223] L. Füstöss and G. Tóth, "The problem of the compounding of transmission probabilities for composite systems", *Journal of Vacuum Science & Technology*, vol. 9, no. 4, pp. 1214–1217, Jul. 1972. DOI: 10.1116/1.1317015.

[224] L. Füstöss and G. Tóth, "The resistance concept and the dynamical characterization of molecular gas flow", *Vacuum*, vol. 40, no. 1–2, pp. 43–46, 1990. DOI: 10.1016/0042-207X(90)90115-F.

[225] K. Jousten, "Molekulare Strömung von Gasen (in German)", in *Handbuch Vakuumtechnik*, K. Jousten, Ed., 12th ed., Wiesbaden, Germany: Springer Vieweg, 2018, pp. 171–193, ISBN: 978-3-658-13386-3.

[226] V. Hauer and C. Day, "Conductance modelling of ITER vacuum systems", *Fusion Engineering and Design*, vol. 84, no. 2–6, pp. 903–907, Jun. 2009. DOI: 10.1016/j.fusengdes.2008.12.115.

[227] D. A. Karpov, A. G. Ivanov, A. I. Livshits, and A. N. Dranichnikov, "Vacuum pumping system of TRT", *Plasma Physics Reports*, vol. 47, no. 12, pp. 1267–1284, Dec. 2021. DOI: 10.1134/S1063780X21120023.

[228] T. Teichmann, X. Luo, T. Giegerich, and C. Day, "Study of the effective torus exhaust high vacuum pumping system performance in the Inner Tritium Plant Loop of EU-DEMO", *Fusion Science and Technology*, vol. 80, no. 3-4, pp. 399–410, Apr.–May 2024. DOI: 10.1080/15361055.2023.2229679.

[229] C. Day, A. Mack, M. Glugla, and D. K. Murdoch, "Tritium inventories in the high vacuum pumps of ITER", *Fusion Science and Technology*, vol. 41, no. 3P2, pp. 602–606, May 2002. DOI: 10.13182/FST02-A22659.

[230] T. Giegerich *et al.*, "Conceptual design of the Mechanical Tritium Pumping System for JET DTE2", *Fusion Science and Technology*, vol. 68, no. 3, pp. 630–634, Oct. 2015. DOI: 10.13182/FST14-950.

[231] F. E. Poindexter, "A substitute for liquid air in low pressure work", *Journal of the Optical Society of America*, vol. 9, no. 5, pp. 629–634, Nov. 1924. DOI: 10.1364/JOSA.9.000629.

[232] A. L. Hughes and F. E. Poindexter, "XLII. Potassium as a mercury-vapour trap", *The London, Edinburgh, and Dublin Philosophical Magazine and Journal of Science*, vol. 50, no. 296, pp. 423–439, 1925. DOI: 10.1080/14786442508634754.

[233] K. W. Hunten, G. A. Woonton, and E. C. Longhurst, "On the use of alkali metal alloys for trapping mercury vapor", *Review of Scientific Instruments*, vol. 18, no. 11, pp. 842–844, Nov. 1947. DOI: 10.1063/1.1740858.

[234] V. Solokha *et al.*, "Isotope effect on the detachment onset density in JET ohmic plasmas", *Physica Scripta*, vol. 2020, no. T171, 014039, pp. 1–5, Mar. 2020. DOI: 10.1088/1402-4896/ab4bed.

[235] S. Chapman and T. G. Cowling, *The mathematical theory of non-uniform gases - An account of the kinetic theory of viscosity, thermal conduction, and diffusion in gases*, reprinted 2nd ed. Cambridge, UK: Cambridge University Press, 1953, 431 pp.

[236] P. Sharipov, “Analytical and numerical calculations of rarefied gas flows”, in *Handbook of vacuum technology*, K. Jousten, Ed., 2nd ed., Weinheim, Germany: Wiley-VCH Verlag GmbH & Co. KGaA, 2016, pp. 167–228, ISBN: 978-3-527-68825-8. DOI: 10.1002/9783527688265.ch5.

[237] S. Kosuge, “Model Boltzmann equation for gas mixtures: Construction and numerical comparison”, *European Journal of Mechanics - B/Fluids*, vol. 28, no. 1, pp. 170–184, Jan.–Feb. 2009. DOI: 10.1016/j.euromechflu.2008.05.001.

[238] E. Roohi and S. Stefanov, “Collision partner selection schemes in DSMC: From micro/nano flow to hypersonic flows”, *Physics Reports*, vol. 656, pp. 1–38, Oct. 25, 2016. DOI: 10.1016/j.physrep.2016.08.002.

[239] S. K. Stefanov, “On the basic concepts of the direct simulation Monte Carlo method”, *Physics of Fluids*, vol. 31, no. 6, 067104, pp. 1–17, Jun. 2019. DOI: 10.1063/1.5099042.

[240] C. R. Harris *et al.*, “Array programming with NumPy”, *Nature*, vol. 585, pp. 357–362, Sep. 2020. DOI: 10.1038/s41586-020-2649-2.

[241] *MKS Baratron® type AA02A absolute pressure transducer with process relay option*, 1073365-001 Rev. 001, MKS Instruments, Inc., Andover, Massachusetts, US, Dec. 2016.

[242] DKE Deutsche Kommission Elektrotechnik Elektronik Informationstechnik im DIN und VDE, *DIN EN 60751: Industrielle Platin-Widerstandsthermometer und Platin-Temperatursensoren (IEC 60751:2008) (in German)*. Berlin, Germany: Beuth Verlag GmbH, May 2009, 24 pp.

[243] DKE Deutsche Kommission Elektrotechnik Elektronik Informationstechnik im DIN und VDE, *DIN EN 60584-1: Thermoelemente – Teil 1: Thermospannungen und Grenzabweichungen (IEC 60584-1:2013) (in German)*. Berlin, Germany: Beuth Verlag GmbH, Jul. 2014, 65 pp.

[244] *Hardware-Handbuch ProfiMessage (in German)*, Delphin Technology AG, Bergisch Gladbach, Germany, Jan. 2018.

[245] *SIMATIC S7 / S7-1200 Automatisierungssystem - Systemhandbuch (in German)*, V4.2.3, Siemens AG, Nürnberg, Germany, Aug. 2018.

[246] *JUMO safetyM STB/STW Betriebsanleitung 70115000T90Z003K000 (in German)*, V4.00/DE/00540087, JUMO GmbH & Co. KG, Fulda, Germany.

[247] *MINI MCR-2-RTD - Installation notes for electricians*, MNR 9063887, PHOENIX CONTACT GmbH & Co. KG, Blomberg, Germany, Jul. 6, 2015.

[248] *MINI MCR-2-RPSS-I-I - Installation notes for electricians*, MNR 9063885, PHOENIX CONTACT GmbH & Co. KG, Blomberg, Germany, May 3, 2017.

[249] L. R. Fokin, V. N. Popov, and S. P. Naurzakov, “Equation of state and thermodynamic properties of saturated and superheated mercury vapors up to 1650 K and 125 MPa”, *High Temperature*, vol. 49, no. 6, pp. 832–840, Dec. 2011. DOI: 10.1134/S0018151X11050075.

A. Appendices

A.1. Mathematical expressions

A.1.1. Error function

The *error function* is defined as (cf. [75, 77])

$$\mathrm{erf}(x) = \frac{2}{\sqrt{\pi}} \int_0^x \exp\left\{-t^2\right\} \mathrm{d}t. \tag{A.1}$$

A.1.2. Gamma function

The *gamma function* is defined as (cf. [77])

$$\Gamma(x) = \int_0^\infty t^{x-1} \exp\left\{-t\right\} \mathrm{d}t. \tag{A.2}$$

A.2. Fundamentals of gas kinetics

A.2.1. Phase space distribution function

Phase-space refers to the six dimensional space that is spanned by the three spatial coordinates $\vec{x} = [x, y, z]^\mathrm{T}$ and the three velocity coordinates $\vec{v} = [v_x, v_y, v_z]^\mathrm{T}$ - here both in the Cartesian coordinate system. At a given time t_0 any particle p in the system can be identified with a discrete, six dimensional position in phase space $(\vec{x}_p, \vec{v}_p)$. It is infeasible for most real world systems to consider all involved particles individually. Therefore, the continuous, six dimensional particle velocity distribution function $f(\vec{x}, \vec{v})$ is introduced, which describes the statistical distribution of particles in phase space. The value of the distribution function f at a given point $(\vec{x}_i, \vec{v}_i)$ in phase space is equivalent to the particle phase density (dimensions $\mathrm{s}^3/\mathrm{m}^6$) at $\vec{x}_i$ and with velocity $\vec{v}_i$. For most real-world applications averaged, macroscopic properties like the pressure or temperature are more relevant. The derivation of these from the microscopic distribution function is described in Appendix A.2.3.

A.2.2. The Boltzmann equation

The Boltzmann equation describes the temporal evolution of the particle velocity distribution function $f(t, \vec{x}, \vec{v})$, short f, and can be expressed as a seven dimensional integro-differential equation:

$$\frac{\partial f}{\partial t} = \underset{a)}{-\frac{\partial f}{\partial \vec{x}} \vec{v}} \underset{b)}{- \frac{\partial f}{\partial \vec{v}} \frac{\vec{F}}{m}} + \underset{c)}{C(f)}. \tag{A.3}$$

Exhaustive mathematical derivations of this equation can be found in various textbooks covering the kinetic theory of gases [75, 235]. Therefore, a more descriptive derivation is provided here: For a six-dimensional volume $\mathrm{d}\vec{x}\mathrm{d}\vec{v}$ around point $(\vec{x}_i, \vec{v}_i)$ in phase space the average number of

particles residing in this element at time t is given by $f(t, \vec{x}_i, \vec{v}_i)\,\mathrm{d}\vec{x}\mathrm{d}\vec{v}$. This count of particles can change with time (l.h.s. of Eq. (A.3)) by three mechanisms (r.h.s. of Eq. (A.3)): Firstly and most intuitively, particles that have a velocity in $\mathrm{d}\vec{v}$ around $\vec{v}_i$ can move in and out of the element $\mathrm{d}\vec{x}$ around $\vec{x}_i$ in physical space by crossing its bounding surface (term a) in Eq. (A.3)). Secondly, particles that are located in $\mathrm{d}\vec{x}$ around $\vec{x}_i$ can undergo a change in velocity so that they either join or leave the element $\mathrm{d}\vec{v}$ around $\vec{v}_i$. Such a change in velocity can happen in two ways: Particles can either be accelerated by an external force $\vec{F}$ acting on their mass m (term b) in Eq. (A.3)) or their velocity is changed by intermolecular collisions with other particles (term c) in Eq. (A.3)). The collision operator $C(f)$ introduces most of the complexity in the equation because - unlike the other terms - it requires integrating over the distribution function as collisions always involve at least two particles. Ludwig Boltzmann derived an expression for this operator under the main assumptions of molecular chaos and the restriction to dilute gases by considering only binary collisions [75, 76, 236]:

$$C(f(\vec{v})) = \iiint_{-\infty}^{+\infty} \int_0^{2\pi} \int_0^{\pi} \left(f'(\vec{v}')f'(\vec{v}_2') - f(\vec{v})f(\vec{v}_2) \right) \sin(\chi)\sigma(c_r, \chi)c_r \,\mathrm{d}\chi \,\mathrm{d}\epsilon \,\mathrm{d}\vec{v}_2. \tag{A.4}$$

In Eq. (A.4) $\vec{v}$ and $\vec{v}_2$ correspond to the velocities of the binary collision partners before the collision. Similarly, $\vec{v}'$ and $\vec{v}_2'$ are the velocities after the collision. The magnitude of the relative velocity is abbreviated as $c_r = \left|\vec{v}_2 - \vec{v}\right| = \left|\vec{v}_2' - \vec{v}'\right|$. σ is called the differential collision cross-section, which depends on the molecular potential that is assumed for the particles [76, 77]. Finally, χ and ϵ are the deflection and azimuthal angles of the collision. One of the most important properties of $C(f)$ is that it conserves mass, momentum and energy, which are therefore called *collision invariants* [76].

A.2.3. Converting the microscopic to the macroscopic state

The microscopic description of the gas via the particle velocity distribution function f can be converted to all relevant macroscopic properties by calculating *moments* of f at a given point $\vec{x}_i$ in physical space. The moments of f are calculated by integrating the product of any chosen particle property (e.g. the speed) with f over the entire velocity space at the given point $\vec{x}_i$. The most important macroscopic gas properties are the number density,

$$n(\vec{x}_i) = \iiint_{-\infty}^{+\infty} f(\vec{x}_i, \vec{v})\,\mathrm{d}\vec{v}, \tag{A.5}$$

the bulk velocity,

$$\vec{u}(\vec{x}_i) = \frac{1}{n(\vec{x}_i)} \iiint_{-\infty}^{+\infty} \vec{v}(\vec{x}_i) f(\vec{x}_i, \vec{v})\,\mathrm{d}\vec{v}, \tag{A.6}$$

the mean particle velocity magnitude or speed,

$$\overline{v}(\vec{x}_i) = \frac{1}{n(\vec{x}_i)} \iiint_{-\infty}^{+\infty} \left|\vec{v}(\vec{x}_i)\right| f(\vec{x}_i, \vec{v})\,\mathrm{d}\vec{v}, \tag{A.7}$$

the pressure,

$$p(\vec{x}_i) = \frac{m}{3} \iiint_{-\infty}^{+\infty} \left|\vec{v}(\vec{x}_i) - \vec{u}(\vec{x}_i)\right|^2 f(\vec{x}_i, \vec{v})\,\mathrm{d}\vec{v}, \tag{A.8}$$

and the translational temperature,

$$T(\vec{x}_i) = \frac{m}{3k_B}\frac{1}{n(\vec{x}_i)} \iiint_{-\infty}^{+\infty} \left|\vec{v}(\vec{x}_i) - \vec{u}(\vec{x}_i)\right|^2 f(\vec{x}_i, \vec{v})\, \mathrm{d}\vec{v}. \tag{A.9}$$

Other quantities - for example the heat flux - can be obtained as *higher order* moments of f. They are omitted here for the sake of brevity but can be found in literature (e.g. [76, 237]). It is also noted that the expressions above are only valid in case the gas is composed of a single species. In case the gas is composed of several different species the above expressions are only valid by replacing the distribution function $f(\vec{x}_i, \vec{v})$ with the distribution function $f_s(\vec{x}_i, \vec{v})$ of the particles of species s, e.g.

$$n_s(\vec{x}_i) = \iiint_{-\infty}^{+\infty} f_s(\vec{x}_i, \vec{v})\, \mathrm{d}\vec{v}. \tag{A.10}$$

The average properties of a gas mixture composed of N_s constituents follow from the macroscopic properties of the involved species (see e.g. [77, 237]):

$$n_{\mathrm{mix}}(\vec{x}_i) = \sum_{s=1}^{N_s} n_s(\vec{x}_i), \tag{A.11}$$

$$\rho_{\mathrm{mix}}(\vec{x}_i) = \sum_{s=1}^{N_s} \rho_s(\vec{x}_i) = \sum_{s=1}^{N_s} m_s n_s(\vec{x}_i), \tag{A.12}$$

$$\vec{u}_{\mathrm{mix}}(\vec{x}_i) = \frac{1}{\rho_{\mathrm{mix}}} \sum_{s=1}^{N_s} \rho_s(\vec{x}_i)\vec{u}_s(\vec{x}_i), \tag{A.13}$$

$$p_{\mathrm{mix}}(\vec{x}_i) = k_B n_{\mathrm{mix}}(\vec{x}_i) T_{\mathrm{mix}}(\vec{x}_i) = \sum_{s=1}^{N_s} \left[p_s(\vec{x}_i) + \frac{1}{3}\rho_s(\vec{x}_i) \left|\vec{u}_s(\vec{x}_i) - \vec{u}_{\mathrm{mix}}(\vec{x}_i)\right|^2 \right]. \tag{A.14}$$

A.2.4. Intermolecular potentials

In order to derive inter-particle collisional quantities it is necessary to describe the binary collision cross-section σ, which is part of the Boltzmann collision operator in Eq. (A.4), more closely. The collision cross-section depends on the assumed intermolecular potential, i.e. the force field by which the particles interact with each other. The simplest model is the *Hard Sphere (HS)* model, in which the particles are assumed to be rigid spheres so that the total cross-section[1] is simply

$$\sigma_{T,\mathrm{HS}} = \pi d_{\mathrm{HS}}^2, \tag{A.15}$$

where d_{HS} is the particle diameter. This model however, is not able to accurately represent transport properties like viscosity, thermal conductivity and diffusion coefficient of actual gases at different temperatures. In order to remedy these shortcomings more complex intermolecular potentials have been introduced over the years. A group of models that is attractive for the use in numerical computations because of their relative simplicity at acceptable accuracy are the so-called *Variable Hard Sphere (VHS)* [100] and *Variable Soft Sphere (VSS)* [78] models, which feature identical total cross-sections that include a dependency on the collision energy [100]:

$$\sigma_{T,\mathrm{VSS}} = \sigma_{T,\mathrm{VHS}} = \pi d_{\mathrm{ref}}^2 \left(\frac{c_{r,\mathrm{ref}}^2}{c_r^2}\right)^{\omega-0.5}, \tag{A.16}$$

[1] The total cross-section σ_T is related to the differential cross-section σ by $\sigma_T = 2\pi \int_0^\pi \sigma \sin\chi\, \mathrm{d}\chi$, where χ is the deflection angle.

where c_r corresponds to the relative velocity of the collision partners, ω is the viscosity coefficient and "ref" indicates constant, gas specific reference values. The HS model is recovered for the special case of $\omega = 0.5$. If the gas is in thermal equilibrium, i.e. if the velocity distribution is Maxwellian, the mean collision energy is directly related to the temperature so that Eq. (A.16) can be expressed as

$$\sigma_{T,\mathrm{VSS,eq}} = \sigma_{T,\mathrm{VHS,eq}} = \pi d_{\mathrm{ref}}^2 \left(\frac{T_{\mathrm{ref}}}{T}\right)^{\omega-0.5} \frac{(2.5-\omega)^{0.5-\omega}}{\Gamma(2.5-\omega)}, \tag{A.17}$$

where $\Gamma(...)$ is the *Gamma function* (cf. Appendix A.1.2). The latter factor depends only on the viscosity coefficient ω and is a constant for a specific gas (mixture)[2]. The gas specific reference properties have to be derived from either quantum mechanical calculations or experimental measurements of the gas transport properties. Parameters for common gases are available in tabulated form in [77].

A.2.5. Mean free path and mean collision time of gas mixtures

The equilibrium mean free path and mean collision time of VHS and VSS gas mixtures are identical and derived in [77]. For a mixture composed of N_s species the mean collision time follows as:

$$\tau_{\mathrm{VHS,eq,mix}} = \left[\sum_{i=1}^{N_s} \frac{n_i}{n} \left(\sum_{j=1}^{N_s} \sqrt{\frac{8k_B T_{\mathrm{ref},ij}\pi}{m_{r,ij}}} d_{\mathrm{ref},ij}^2 n_j \left(\frac{T}{T_{\mathrm{ref},ij}}\right)^{1-\omega_{ij}}\right)\right]^{-1}, \tag{A.18}$$

where $m_{r,ij}$ is the reduced mass defined as

$$m_{r,ij} = \frac{m_i m_j}{m_i + m_j}. \tag{A.19}$$

Similarly, the mean free path follows as

$$\lambda_{\mathrm{VHS,eq,mix}} = \sum_{i=1}^{N_s} \frac{n_i}{n} \left[\sum_{j=1}^{N_s} \pi d_{\mathrm{ref},ij}^2 n_j \sqrt{1+\frac{m_i}{m_j}} \left(\frac{T_{\mathrm{ref},ij}}{T}\right)^{\omega_{ij}-0.5}\right]^{-1}. \tag{A.20}$$

In both expressions (Eqs. (A.18) & (A.20)) the VHS properties in case $i = j$ correspond to the ones of the pure species. The mixed properties (i.e. $i \neq j$) have to be either measured experimentally or estimated. As dedicated experimental measurements for mixtures are scarce they are commonly estimated as the average of the involved species, e.g. $\omega_{ij} = 0.5 \cdot (\omega_i + \omega_j)$ [77]. The latter approach is also used in the present work as discussed in Sec. 3.5.2.

A.3. Implementation details of the Direct Simulation Monte Carlo method

A.3.1. The *No Time Counter* method

DSMC differs from molecular dynamics simulations in that its simulator particles represent numerous real particles. Thus, intermolecular collisions cannot be computed rigorously as in a

[2]The complexity of this term results from the choice of the reference value definition as $c_{r,\mathrm{ref}} = \left(\overline{c_r^{2\omega-1}}\Big|_{\mathrm{ref}}\right)^{1/(2\omega-1)}$, which simplifies derived quantities [77].

molecular dynamics simulation which considers every real particle and its interactions with all other particles. Instead, intermolecular collisions are treated in a stochastic manner in the DSMC method. Consider two DSMC particles (1, 2) each representing F_N physical particles with velocities $\vec{v}_1, \vec{v}_2$ and relative velocity $\vec{c}_{r,12}$ (magnitude $c_{r,12}$) that reside in the same computational cell with volume V. Given their collision cross-section $\sigma_{T,12}$ their binary collision probability P_{12} within a time of Δt is given by the ratio of the volume swept out by the cross-section moving at the relative speed and the volume of the computational cell [77]:

$$P_{12} = \frac{F_N \sigma_{T,12} c_{r,12} \Delta t}{V}. \tag{A.21}$$

If there are more than two particles in the computational cell the naive approach is to calculate the individual collision probabilities of all $0.5 \cdot N_p(N_p - 1)$ particle pairs. Therefore, the naive approach features a computational complexity of $O(N_p^2)$ and thus becomes less effective the smaller the average P_{12}. In order to improve the efficiency of the collision step, Bird introduced the so-called *No Time Counter (NTC)* method [122, 123]: The computational complexity is reduced by a priori calculating the maximum number of potential collision pairs $N_{c,\max}$ to check by means of

$$N_{c,\max} = \frac{N_p(N_p - 1)}{2} \cdot \frac{F_N (\sigma_T c_r)_{\max} \Delta t}{V}, \tag{A.22}$$

where $(\sigma_T c_r)_{\max}$ is the maximum product of cross-section and relative velocity in the respective cell. At the start of the simulation this value is initialized to a reasonably large number and then kept up to date during the simulation in case a larger product is encountered in a collision [122]. During a time step $N_{c,\max}$ collision pairs[3] are chosen at random from the particles residing in the computational cell and each collision is accepted with the probability

$$P_{12} = \frac{\sigma_{T,12} c_{r,12}}{(\sigma_T c_r)_{\max}}. \tag{A.23}$$

The computational complexity of Eq. (A.22) & (A.23) is $O(N_p)$ as $N_p \propto F_N^{-1}$, therefore making the NTC method more efficient than the naive approach discussed above [238, 239].

The NTC algorithm can either be applied to all particles within the cell or to groups of particles. In the latter case, the algorithm is performed for each group pairing including the groups paired with themselves. For example if the simulation considers two species A and B, collisions are computed for the group pairings $A - A$, $A - B$ and $B - B$. The product $0.5 \cdot N_p(N_p - 1)$ in Eq. (A.22) is then replaced by $0.5 \cdot N_{p,A}(N_{p,A} - 1)$, $N_{p,A} N_{p,B}$ and $0.5 \cdot N_{p,B}(N_{p,B} - 1)$ respectively. While this requires more computational storage as the product $(\sigma_T c_r)_{\max}$ has to be stored for each group pairing, it improves the efficiency of the algorithm for high mass ratios between the species [77]. The reason for this is that the product $(\sigma_T c_r)_{\max}$ is otherwise dominated by the light species due to its wider velocity distribution function (cf. Fig. 3.1), which results in a high number of collision attempts at a very low probability for the heavier species as per Eq. (A.23). As mercury vapor has a significantly higher mass than all the exhaust gas species (up to factor ~ 50 for helium and deuterium) collision groups are used in the present work.

A.4. One-dimensional DSMC diffusion pump simulation

The purpose of this appendix is to provide in-depth information about the case setup discussed in Sec. 4.2 of the main text.

[3] As $N_{c,\max}$ is usually a floating point number, it is truncated, and the remaining fraction is carried over to the next time step.

The simulation domain of the DSMC model is depicted in Fig. A.1. At the upstream boundary ($x = 0$) mercury vapor and gas particles are injected based on the assumption of equilibrium Maxwell-Boltzmann distribution functions. In case of the gas the conditions are given by the reservoir conditions at number density $n_{\mathrm{G,r}}$ and temperature $T_{\mathrm{G,r}}$. The mercury vapor jet enters with bulk velocity u_{V}, number density n_{V} and temperature T_{V} following a shifted Maxwell-Boltzmann distribution function. Particles of both species leaving the domain through the upstream boundary are removed from the simulation. At the downstream boundary ($x = L$) mercury vapor particles are allowed to freely leave the domain (sticking coefficient $\xi_{\mathrm{V}} = 1$), whereas the limited uptake capacity of the backing pump for the gas is modeled by a sticking coefficient $\xi_{\mathrm{G}} < 1$. Gas particles not considered to be pumped (probability $1 - \xi_{\mathrm{G}}$) are reflected diffusely assuming a temperature of the outlet of $T_L = T_{\mathrm{G,r}}$.

All case parameters and results for the cases shown in Fig. 4.4 are collected in Tab. A.1. As the comparison is performed in the operational range of the diffusion pump the capture coefficient is not sensitive to both the upstream gas density $n_{\mathrm{G,r}}$ and the outlet sticking coefficient ξ_{G}. This is verified by halving as well as doubling both of these parameters separately, which does not change the computed capture coefficient by more than 1 %. Additionally, it is verified that the results are not sensitive towards the chosen species weights by altering the ratio between neon and mercury vapor particles $F_{N,\mathrm{Ne}}/F_{N,\mathrm{Hg}}$ from 0.0375 (standard cases) to 0.075 and 0.15, while keeping the number of gas particles in the domain roughly the same (thus doubling / quadrupling the number of mercury vapor particles in the domain). Comparing the three setups confirms that the choice of the species weights do not change the computed capture coefficient by more than 1 %.

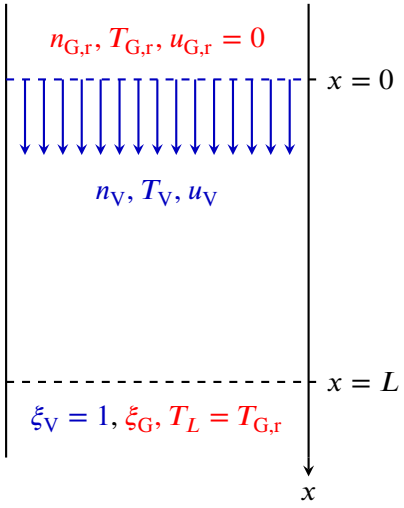

Figure A.1.: DSMC model of a simplified one-dimensional diffusion pump (resembling the problem in Fig. 4.1). Indices "G" and "V" refer to the gas and vapor respectively. The simulation domain spans $x = 0$ ("upstream") to $x = L$ ("downstream").

Table A.1.: Overview of the simulation parameters, the resulting speed ratio Φ and the DSMC and analytical capture coefficients $\varsigma_{\mathrm{DSMC}}$ and ς_0. The other simulation parameters are held constant and are: $L = 0.4\,\mathrm{m}$, $n_{\mathrm{G,r}} = 2.41 \times 10^{19}\,\mathrm{m}^{-3}$ and $\xi_{\mathrm{G}} = 0.1$. The DSMC parameters are chosen as $\Delta x = 50\,\mu\mathrm{m}$, $\Delta t = 5 \times 10^{-9}\,\mathrm{s}$ and $F_{N,\mathrm{Hg}} = 1 \times 10^{15}$. Additionally, the species weights $F_{N,\mathrm{Ar}} = 2.5{\times}10^{13}$, $F_{N,\mathrm{Ne}} = 3.75{\times}10^{13}$ and $F_{N,\mathrm{He}} = 5 \times 10^{13}$ are used to improve the ratio of simulated gas to mercury vapor particles. Finally, it has been verified that each computational cell contains more than 10 gas as well as mercury vapor simulator particles.

Gas	**Gas temp.**	**Mercury vapor jet**			**Speed ratio**	**Capture coefficient**	
-	$T_{\mathrm{G,r}}$	n_{V}	T_{V}	u_{V}	Φ	$\varsigma_{\mathrm{DSMC}}$	ς_0
-	(in K)	(in m^{-3})	(in K)	(in ms^{-1})	-	-	-
Ar	200	4.53×10^{20}	58.9	255	0.884	0.974	0.961
	300	3.95×10^{20}	147	202	0.570	0.907	0.872
		4.53×10^{20}	58.9	255	0.722	0.961	0.927
		4.12×10^{20}	18.5	286	0.809	0.974	0.948
	400	4.53×10^{20}	58.9	255	0.625	0.946	0.895
Ne	200	4.53×10^{20}	58.9	255	0.629	0.927	0.897
	300	3.95×10^{20}	147	202	0.405	0.814	0.765
		4.53×10^{20}	58.9	255	0.513	0.897	0.841
		4.12×10^{20}	18.5	286	0.575	0.924	0.874
	400	4.53×10^{20}	58.9	255	0.444	0.871	0.796
He	200	4.53×10^{20}	58.9	255	0.280	0.677	0.631
	300	3.95×10^{20}	147	202	0.181	0.518	0.473
		4.53×10^{20}	58.9	255	0.229	0.618	0.556
		4.12×10^{20}	18.5	286	0.256	0.663	0.598
	400	4.53×10^{20}	58.9	255	0.198	0.577	0.505

A.5. NEMESIS DSMC Simulations

This appendix supplements the description of the numerical DSMC model of the NEMESIS diffusion pump, which is introduced in Sec. 4.3 of the main text and the simulations that have been performed with this model.

A.5.1. Verification of the DSMC simulation parameters

The choice of the DSMC parameters (time step, number of particles per cell and grid) have been verified by comparison with simulations using a refined set of parameters. Representative cases for both setups of the boundary ③ in Fig. 4.5 have been considered and the results are summarized in the following paragraphs.

Open inlet, boundary condition ③ a) Helium and argon have been considered as the pumped gas species. The comparison of the cases with standard DSMC setup and refined parameters are summarized in Tab. A.2. Comparison of the results between standard and refined setups reveals

that the largest deviation is found for the helium pumping speed S and capture coefficient ς and amounts to approximately 2 %. The case considering argon is considerably less sensitive towards the DSMC parameters. Due to the approximately 3.2 times higher thermal velocity of helium as compared with argon it is expected that the deviation is mainly a result of the time discretization.

Table A.2.: Comparison of DSMC simulations with standard and refined parameters for representative cases with mercury vapor stagnation temperature 403.15 K and considering helium and argon as the pumped gas respectively. The critical time for each species is calculated as $\Delta t_{\mathrm{crit},i} = \frac{\Delta x}{|\vec{u}_i| + v_{\mathrm{mp},i}}$ in each cell.

Category	Property	Unit	Case setup			
			Helium		Argon	
			Standard	Refined	Standard	Refined
Setup	Δt	s	2.5×10^{-8}	1×10^{-8}	2.5×10^{-8}	1×10^{-8}
	N_p	1×10^6	≈ 38	≈ 77	≈ 36	≈ 73
	N_c	1	897,277	2,319,536	924,553	2,408,902
	N_{sample}	1	200,000	400,000	200,000	400,000
DSMC criteria	$N_p/\mathrm{cell} < 10$	% of N_c	0.01	0.01	0.01	0.01
	$N_p/\mathrm{cell} < 20$	% of N_c	26.63	31.93	27.04	31.85
	$\Delta x/\lambda_{\mathrm{mix}} > 1$	% of N_c	0.02	0.00	0.02	0.00
	$\Delta x/\lambda_{\mathrm{mix}} > 1/3$	% of N_c	49.27	15.02	47.99	14.48
	$\Delta t/\tau_{\mathrm{mix}} > 1$	% of N_c	0.00	0.00	0.00	0.00
	$\Delta t/\tau_{\mathrm{mix}} > 1/3$	% of N_c	0.00	0.00	0.00	0.00
	$\Delta t/\Delta t_{\mathrm{crit,Hg}} > 1/3$	% of N_c	0.00	0.00	0.00	0.00
	$\Delta t/\Delta t_{\mathrm{crit,gas}} > 1/3$	% of N_c	0.00	0.00	0.00	0.00
Results	$\bar{\Phi}$	1	0.2216	0.2218	0.7078	0.7080
	S	$\mathrm{m^3\,s^{-1}}$	1.577	1.546	0.6424	0.6423
	ς	1	0.2920	0.2862	0.3755	0.3754
Cost	Relative run time	1	1.0	4.255	0.9273	4.505

Closed top flange, boundary condition ③ b) The experimental setup that is used to validate the DSMC model as discussed in Chap. 5 is approximated by considering a closed top flange. The case with the highest vapor stagnation temperature of 403.15 K as given by Tab. 5.3 has been chosen because this corresponds to the densest mercury vapor jet. Moreover, a fairly high gas pressure of 4.5 Pa, which is close to the fore-vacuum tolerance has been chosen. The setup, DSMC criteria, results and an estimation of the relative computational cost are compared in Tab. A.3 for three cases: The first case features the standard setup which was used for all simulations in Chap. 5. The second case uses identical DSMC parameters except for a tenfold increase of the number of sampling time steps N_{sample}. Finally, a refined set of DSMC parameters is used in the last case. Evidently, the most sensitive quantity is the nitrogen pressure $p_{\mathrm{HV,N_2}}$ at the upper boundary, which shows a deviation between 1-2 %. Due to the low pressure, which corresponds to a low simulator particle sample size, this is likely a result of poor statistics. This hypothesis is supported by the good agreement between the case employing default DSMC parameters except for the increased sample size and the case using refined parameters.

Table A.3.: Comparison of DSMC simulations with three different case setups for a representative case with mercury vapor stagnation temperature 403.15 K and prescribed nitrogen pressure 4.5 Pa. The first case setup corresponds to the standard setup used for all simulations in Chap. 5. The second setup uses the same DSMC parameters but with a tenfold increased number of sampling time steps. Finally, the third setup uses refined DSMC parameters. The critical time for each species is calculated as $\Delta t_{\mathrm{crit},i} = \frac{\Delta x}{|\vec{u}_i| + v_{\mathrm{mp},i}}$ in each cell.

Category	Property	Unit	Case setup		
			Standard	**Statistics**	**Refined**
Setup	Δt	s	2.5×10^{-8}	2.5×10^{-8}	1×10^{-8}
	N_p	1×10^6	≈ 44	≈ 44	≈ 177
	N_c	1	846,454	844,549	6,082,187
	N_{sample}	1	200,000	2,000,000	400,000
DSMC criteria	$N_p/\mathrm{cell} < 10$	% of N_c	0.01	0.01	0.00
	$N_p/\mathrm{cell} < 20$	% of N_c	19.22	19.25	17.95
	$\Delta x/\lambda_{\mathrm{mix}} > 1$	% of N_c	0.03	0.03	0.00
	$\Delta x/\lambda_{\mathrm{mix}} > 1/3$	% of N_c	47.70	47.90	5.73
	$\Delta t/\tau_{\mathrm{mix}} > 1$	% of N_c	0.00	0.00	0.00
	$\Delta t/\tau_{\mathrm{mix}} > 1/3$	% of N_c	0.00	0.00	0.00
	$\Delta t/\Delta t_{\mathrm{crit,Hg}} > 1/3$	% of N_c	0.00	0.00	0.00
	$\Delta t/\Delta t_{\mathrm{crit,N_2}} > 1/3$	% of N_c	0.00	0.00	0.00
Results	$p_{\mathrm{FV,N_2}}$	Pa	4.530	4.529	4.529
	$p_{\mathrm{HV,N_2}}$	Pa	0.1750	0.1781	0.1770
	$p_{\mathrm{FV,Hg}}$	Pa	0.4013	0.4027	0.4033
	$p_{\mathrm{HV,Hg}}$	Pa	0.1114	0.1121	0.1121
Cost	Relative run time	1	1.0	9.56	10.22

A.5.2. Sensitivity of modeling assumptions

The sensitivity of the DSMC pump model towards the main modeling assumptions and numerical parameters is assessed. All the simulations in the present section are performed under the assumption of a closed top flange, i.e. boundary condition ③ b), which corresponds to the experimental setup discussed in Chap. 5. Additionally, the fore-vacuum tolerance is chosen to test the sensitivity because this has been used for the validation of the DSMC pump model with the experimental data.

Vapor liquid boundary condition The influence of the vapor liquid boundary condition that was assumed for mercury on the cooled outer walls of the pump has been assessed by performing comparable simulations under the assumption of perfect condensation, i.e. an effective condensation coefficient of $\alpha_{c,\mathrm{eff}} = 1$. This corresponds to the assumption of all previously reported DSMC diffusion pump models in literature [94, 95, 101–104, 132, 199] with the exception of a previous work by the author which discusses the sensitivity of the effective condensation coefficient [131]. Furthermore, the temperature assumed on the cooled surfaces (cylindrical outer walls and

top flange) is changed from 288.15 K (standard setup) to 283.15 K (for the simulations assuming $\alpha_{c,\mathrm{eff}} = 1$). The simulation results of the model assuming $\alpha_{c,\mathrm{eff}} = 1$ have been compared to the experimental results in an accepted manuscript [199] by the author.

Here, the simulation results of the two models are compared to determine the sensitivity with respect to the fore-vacuum tolerance of the mercury vapor jet at different vapor stagnation temperatures, which is determined as described in Sec. 5.3.1. Figure A.2 depicts the high vacuum pressure as a function of the fore-vacuum pressure assuming nitrogen as the pumped gas. Furthermore, the extracted fore-vacuum tolerances are listed in Tab. A.4. The simulations with both boundary conditions are performed at the same four stagnation conditions. It is evident that the fore-vacuum tolerance is not sensitive towards the implemented boundary condition as the maximum deviation between the two implementations is 6.4 %.

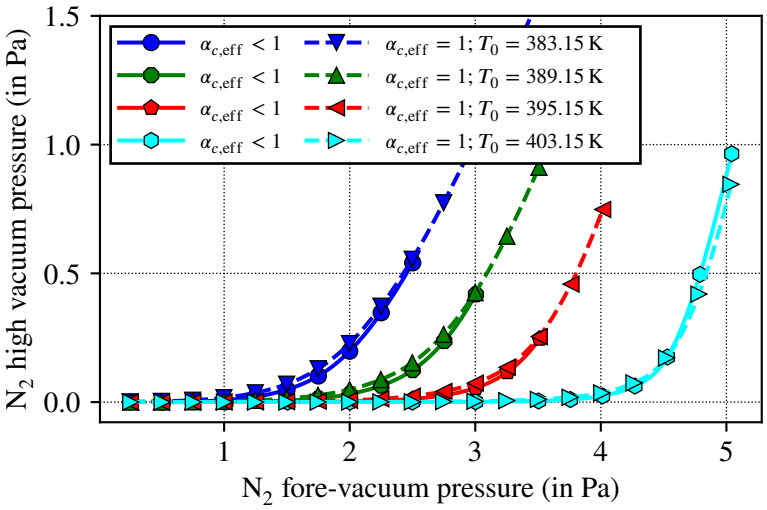

Figure A.2.: High vacuum nitrogen pressure as a function of the fore-vacuum nitrogen pressure comparing the two vapor liquid boundary conditions for four vapor stagnation conditions (individual: symbols, fit: lines).

Table A.4.: Comparison of the fore-vacuum tolerance at four stagnation temperatures between DSMC simulations assuming concurrent condensation and evaporation at saturation conditions at 288.15 K ($\alpha_{c,\mathrm{eff}} < 1$, standard setup) and perfect condensation ($\alpha_{c,\mathrm{eff}} = 1$) at 283.15 K (the latter have been published in a previous work by the author [199]).

T_0	$\alpha_{c,\mathrm{eff}} < 1$	$\alpha_{c,\mathrm{eff}} = 1$
	p_{FT}	p_{FT}
(in K)	**(in Pa)**	**(in Pa)**
383.15	1.33	1.25
389.15	2.02	1.93
395.15	2.84	2.77
403.15	4.04	4.01

Effective condensation coefficient In addition to the comparison in the last paragraph, the sensitivity of the fore-vacuum tolerance to the boundary condition describing the mercury vapor

condensation has been analyzed by varying the effective condensation coefficient of the mercury vapor. Four simulations are compared that assume values for $\alpha_{c,\mathrm{eff}}$ between 1.0 (as compared to the standard setup in the previous paragraph) and 0.5 (which is much lower than expected based on the literature review on this matter in Sec. 3.5.5). A visual comparison of the nitrogen pressure in the high vacuum compartment above the jet as function of the fore-vacuum pressure is depicted in Fig. A.3. A large deviation is only observed for the lowest effective condensation coefficient of $\alpha_{c,\mathrm{eff}} = 0.5$, whereas the cases for effective condensation coefficients between 0.8 and 1.0 are in very good agreement. Notably, the determined values for the fore-vacuum tolerance varies between 2.77 and 2.80 Pa for all cases, i.e. within 1 %, despite the visual differences. Thus, it is concluded that the fore-vacuum tolerance is not sensitive to the assumption of the effective condensation coefficient.

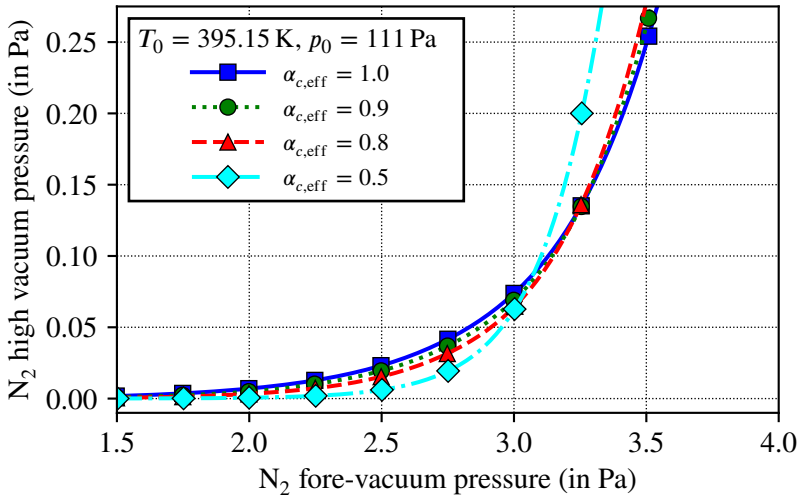

Figure A.3.: High vacuum nitrogen pressure as a function of the fore-vacuum nitrogen pressure comparing four DSMC simulation setups (individual: symbols, fit: lines). The DSMC simulations feature similar setups apart from the effective condensation coefficient which is varied from $\alpha_{c,\mathrm{eff}} = 1.0$ to $\alpha_{c,\mathrm{eff}} = 0.5$. The same mercury vapor stagnation temperature 395.15 K is assumed in all cases.

Rotational degrees of freedom The implementation of the rotational degrees of freedom in the present work assumes a temperature independent, constant rotational relaxation number. To investigate the sensitivity of the results to this assumption, a comparative simulation is performed that neglects the rotational degrees of freedom of the nitrogen molecules entirely (i.e. assuming $z_{\mathrm{rot},\mathrm{N}_2} = 0$). Apart from the modeling of the rotational degrees of freedom the DSMC simulation setup is identical. The results of the comparison are available in Tab. A.5. The pressures in the high and fore-vacuum compartments are found to deviate less than 1 % between the case with default setup ($z_{\mathrm{rot},\mathrm{N}_2} = 2$) and the case neglecting the rotational degrees of freedom. Thus, the simulation results are not sensitive to the modeling of the rotational degrees of freedom. This conclusion can be extended towards the hydrogen isotopologues because their rotational relaxation number is almost 35 times higher than that of nitrogen, which implies a less frequent energy exchange.

Table A.5.: Comparison of DSMC simulations including the rotational degrees of freedom of the nitrogen molecules (standard setup) and neglecting them for a representative case with mercury vapor stagnation temperature 403.15 K and prescribed nitrogen pressure 4.5 Pa.

Property	**Unit**	$z_{\mathrm{rot,N_2}} = 2$ (default)	$z_{\mathrm{rot,N_2}} = 0$
$p_{\mathrm{FV,N_2}}$	Pa	4.530	4.537
$p_{\mathrm{HV,N_2}}$	Pa	0.1750	0.1764
$p_{\mathrm{FV,Hg}}$	Pa	0.4013	0.3977
$p_{\mathrm{HV,Hg}}$	Pa	0.1114	0.1111

VSS parameters in interspecies binary collisions Due to the absence of exhaustive experimental data for the transport properties of mercury vapor gas mixtures the interspecies VSS collision parameters ($d_{12,\mathrm{ref}}$, $T_{12,\mathrm{ref}}$, ω_{12} and α_{12}) are averaged from the properties of the pure substances (cf. Tab. 3.1). The comparisons of the binary diffusion coefficients predicted by the VSS model and experimental data discussed in Sec. 3.5.2 has revealed that the qualitative agreement is good, however, quantitative differences are observed foremost for the Hg-He mixture (cf. Fig. 3.8). In order to analyze the sensitivity of the DSMC simulation results with respect to the VSS parameters comparative simulations for helium are performed in which the binary scattering coefficient α_{12} is adjusted to achieve a better agreement between the binary diffusion coefficient predicted by the VSS model and the experimental data. The remaining interspecies VSS parameters are determined as averages. It is noted that a change of the scattering coefficient also changes the mixture viscosity, however to a smaller degree than the binary diffusion coefficient. The results of the comparison between the default cases using averaged parameters and the considered cases with modified scattering coefficient α_{12} are depicted in Fig. A.4 for two different mercury vapor stagnation conditions. The qualitative and quantitative agreement of the high vacuum pressure evolution between the cases at identical mercury vapor stagnation conditions is good. As expected the increase of the binary diffusion coefficient by approximately 20 % effectuates higher high vacuum pressures at the same fore-vacuum pressures and a steeper gradient. This in turn leads to significantly lower fore-vacuum tolerances compared with the default setups. The relative deviation is more pronounced at the lower mercury vapor stagnation temperature of 395.15 K where the fore-vacuum tolerance reduces by 18 % from 1.67 Pa (default setup) to 1.37 Pa. At the higher mercury vapor stagnation temperature of 403.15 K a reduction by 12 % from 3.36 Pa (default setup) to 2.96 Pa is observed. However, two aspects are emphasized: Firstly, the VSS binary diffusion coefficients for the mixtures of mercury vapor with other gases show a much better agreement with experimental data than the investigated Hg-He mixture (cf. Fig. 3.8). Therefore, smaller deviations are expected for the other gas species in the exhaust gas mixture. Secondly, the fore-vacuum tolerance is expected to be the most sensitive diffusion pump performance indicator with respect to the binary diffusion coefficient. Nonetheless, future work dedicated to the determination of the transport properties of mercury vapor gas mixtures could be used to improve the VSS parameters by deriving collision specific parameters in better agreement with the experimental data.

Species weighting As outlined in Sec. 3.5.4 species weighting can lead to random walk effects that can in turn result in errors in the DSMC simulations. While species weights have not been used in the simulations of the NEMESIS pump, they are mandatory for the simulation of multistage diffusion pumps. For this reason the one-dimensional verification shown in Fig. 3.11 is substantiated by the present sensitivity study for the two-dimensional axisymmetric NEMESIS domain. Three cases are compared: The first case conforms to the default setup (i.e. without species weighting)

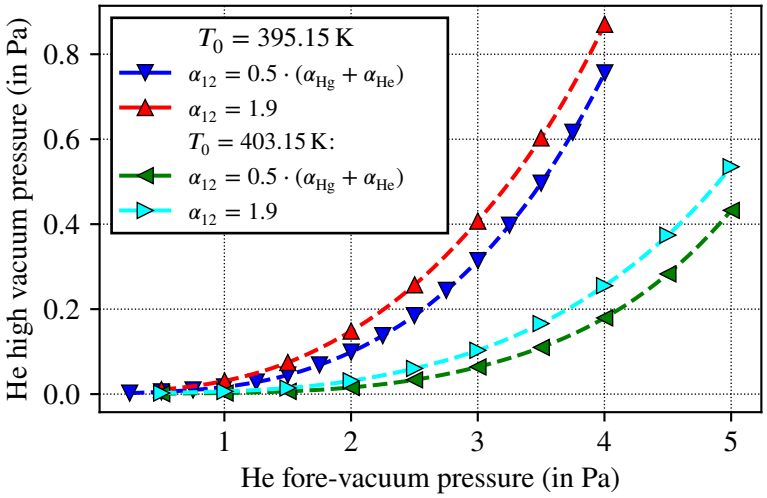

Figure A.4.: High vacuum helium pressure as a function of the fore-vacuum helium pressure comparing four DSMC simulations (individual: symbols, fit: dashed lines). The DSMC simulations feature identical setups apart from the interspecies VSS scattering coefficient α_{12}, which is varied from the averaged value of $\alpha_{12} = 0.5 \cdot (\alpha_{Hg} + \alpha_{He}) = 1.3547$ (default setup) to $\alpha_{12} = 1.9$, which leads to a binary diffusion coefficient close to the experimental value shown in Fig. 3.8. Two different mercury vapor stagnation conditions are compared.

and species weights are used in the other two cases to double the number of nitrogen and mercury simulator particles respectively. The results are collected in Tab. A.6. The comparison of the resulting high and fore-vacuum pressures of nitrogen and mercury confirms that these are not sensitive to species weighting, as the observed deviations are smaller than 0.5 %, which is within the statistical error resulting from the limited sample size as estimated in Appendix A.5.1.

Table A.6.: Comparison of DSMC simulations without species weighting ($F_{N,N_2} = F_{N,Hg} = F_{N,0}$, default setup) and with active species weighting for nitrogen ($F_{N,N_2} = 0.5 \cdot F_{N,0}$, $F_{N,Hg} = F_{N,0}$) as well as mercury ($F_{N,Hg} = 0.5 \cdot F_{N,0}$, $F_{N,N_2} = F_{N,0}$). A representative case with mercury vapor stagnation temperature 403.15 K and prescribed nitrogen pressure 4.5 Pa is considered.

Property	**Unit**	**Default setup**	**More N_2 simulators**	**More Hg simulators**
F_{N,N_2}	1	1	0.5	1
$F_{N,Hg}$	1	1	1	0.5
p_{FV,N_2}	Pa	4.530	4.531	4.531
p_{HV,N_2}	Pa	0.1750	0.1752	0.1746
$p_{FV,Hg}$	Pa	0.4013	0.4008	0.3996
$p_{HV,Hg}$	Pa	0.1114	0.1119	0.1115

A.6. NEMESIS experiment

A.6.1. Sensors and data acquisition system

NEMESIS is monitored and controlled by a mobile control cabinet equipped with a *SIMATIC S7-1200* controller by *Siemens AG*. Data from the various sensors that are installed in the experiment is acquired by a *ProfiMessage* unit by *Delphin Technology AG*. For the majority of the sensors this unit is also responsible for performing analog to digital conversion (ADC) of the analog sensor signals (usually 0-10 V or 4-20 mA) to digital values. The types of utilized sensors are described here briefly including the respective measurement chain. This is important for the following uncertainty estimate (cf. Appendix A.6.3).

Capacitance pressure transducers (PI01-04) include a diaphragm that forms one side of a capacitor. The pressure deforms the diaphragm and the change in capacitance is measured and transformed into the pressure signal. The key benefit of this direct measurement principle is that it is gas type independent. In NEMESIS condensation of mercury vapor in the manometers has to be prevented. Additionally, temperature stability is very important when measuring low pressures using capacitance manometers. For these reason *Baratron AA02A* units with built-in temperature-control to 100 °C by *MKS instruments, Inc.* are used in NEMESIS. The transducers output a linear signal in the range 0-10 V, which is converted to a digital signal by the *ProfiMessage* ADC.

Resistance temperature detectors (RTDs / TI01-02) rely on measuring the electrical resistance of a platinum wire, that changes with temperature. Several *Pt100* (i.e. with a nominal resistance of 100 Ω at 0 °C) by *TC Mess- und Regeltechnik GmbH* are installed in NEMESIS. The resistance is measured and converted to a linear analog signal through a calibration curve by *MINI MCR-2-RTD* transmitters by *PHOENIX CONTACT GmbH*. Finally, the analog signals are converted by the *ProfiMessage* ADC.

Thermocouples (TCs / TI03-05) operate on the principle of the Seebeck effect, i.e. the formation of an electric potential between the two junction points of two metals wires, which are held at different temperatures. Therefore, besides the measured voltage, precise knowledge of the reference junction temperature is required. All thermocouples in the NEMESIS setup are of type K. Some of these thermocouples are connected to *SM1231 TC* modules of the Siemens *SIMATIC S7-1200*. The signal is then communicated digitally from the *SIMATIC S7-1200* to the *ProfiMessage* via fieldbus (*Profibus*). The remaining thermocouples are connected to the *ProfiMessage* directly. In both cases the respective units measure the voltage and the temperature of the reference junction and then perform an ADC.

Guided wave radar sensors (LI01) can measure the level of liquid surfaces by the reflection of microwave pulses. In NEMESIS a *VEGAFLEX 81* by *VEGA Grieshaber KG* is installed in the boiler to measure the level of liquid mercury. The sensor outputs a linear analog signal between 4-20 mA. The signal is repeated by the power supply unit *MINI MCR-2-RPSS-I-I-PT* by *PHOENIX CONTACT GmbH* and then converted to an analog voltage signal by a calibrated resistance (nominal value of 500 Ω). Finally, the *ProfiMessage* is responsible for ADC. The measured liquid level is then converted to a volume by a calibration curve (recorded using water). The determined calibration curve is available in Appendix A.6.2. Additionally, the liquid mercury mass can be calculated from the volume using the temperature-dependent density correlation valid between -20-300 °C taken from [202].

A.6.2. Mercury boiler volume calibration

As the mercury boiler in NEMESIS is a custom design manufactured as a welded construction, no calibration curve that relates the liquid level to the liquid volume exists. For this reason, a calibration curve using demineralized water has been recorded. The boiler has been mounted on a scale as similar as possible to its final mounting inclination. The temperature of the water has been recorded several times over the duration of the calibration. Since the variations have been small (<0.5 K) a single, averaged temperature of 19.7 °C has been used to determine the water density of 998.2 kg m^{-3} by linear interpolation from the tabulated data in [208]. Water has been poured into the boiler in 35 small increments while noting down the mass and the measurement current of the VEGAFLEX 81 sensor. Afterwards, the same incremental process has been performed while draining the boiler in 25 steps in order to increase the number of individual measurement points to 60. Finally, a 10 degree polynomial has been fitted to the data using a least-squares algorithm as implemented in *numpy* [240]. The identified calibration function is

$$\begin{aligned} V(l) =& 12.42 - 0.1765 \cdot l^1 + 2.772 \cdot l^2 - 0.4155 \cdot l^3 + 0.02926 \cdot l^4 \\ & - 0.001151 \cdot l^5 + 2.74 \cdot 10^{-5} \cdot l^6 - 4.044 \cdot 10^{-7} \cdot l^7 + 3.619 \cdot 10^{-9} \cdot l^8 \\ & - 1.8 \cdot 10^{-11} \cdot l^9 + 3.816 \cdot 10^{-14} \cdot l^{10}, \end{aligned} \tag{A.24}$$

where V is the liquid volume in mL and l is the liquid level in %, which can be calculated from the measurement current I (4-20 mA) by

$$l = \frac{I - 4}{20 - 4} \cdot 100\,\%. \tag{A.25}$$

A.6.3. Uncertainty estimation

The uncertainties of the various measured quantities are estimated following the *Guide to the expression of uncertainty in measurement* [203], specifically the *Type B* uncertainty estimation detailed in section 4.3 therein. The combined uncertainties of all sensors (cf. Appendix A.6.1) are estimated by considering all uncertainties in the respective measurement chain from the sensor to the data acquisition system. The combined uncertainties can be approximated by a first-order Taylor series approximation. Furthermore, it is assumed that all the contributing error sources are uncorrelated. The combined error $\varepsilon(y)$ of a measured quantity $y = f(x_1, x_2, ..., x_N)$ can then be estimated according to

$$\varepsilon(y) = \sqrt{\sum_{i=1}^{N} \left(\frac{\partial f}{\partial x_i} \right)^2 \varepsilon^2(x_i)}, \tag{A.26}$$

where the x_i correspond to the individual inputs (e.g. measured voltage) with respective individual errors $\varepsilon(x_i)$ [203]. The error contributions of the involved components are listed in Tab. A.7. As no further information on the distribution of these errors is provided, the distribution functions are assumed to be rectangular as advised in [203]. For reasons of brevity, the detailed error analysis of all measurement chains is not included here, but the process instead demonstrated exemplarily for the measurement chain of RTD TI02. This measurement chain consists of three components, namely the *Pt-100* RTD, the *MINI MCR-2-RTD* transmitter and the ADC of the *ProfiMessage*. According to the tabulated uncertainties of the components (cf. Tab. A.7), the RTD uncertainty $\varepsilon_{\mathrm{RTD}}$ is composed of a relative (0.5 % of reading) as well as a constant part (0.3 K), the transmitter uncertainty $\varepsilon_{\mathrm{trans}}$ has a relative uncertainty of 0.1167 % and the ADC a constant uncertainty $\varepsilon_{\mathrm{ADC}}$ of 0.01 % of the max. value, which is set to 300 °C for TI02. Thus, the combined uncertainty can be estimated according to

$$\varepsilon_{\mathrm{TI02}} = \sqrt{\varepsilon_{\mathrm{RTD}}^2 + \varepsilon_{\mathrm{trans}}^2 + \varepsilon_{\mathrm{ADC}}^2}. \tag{A.27}$$

If the indicated temperature is for example 150 °C, the estimated uncertainty according to Eq. (A.27) is ±1.1 K. An overview of the estimated combined uncertainties of all sensors is provided in Tab. 5.1 in the main text for representative upper and lower values.

Table A.7.: List of components utilized in the NEMESIS data acquisition system and their respective uncertainties. Most of the uncertainties are taken from the referenced component data sheets.

ID	Component name	Uncertainty		Ref.
Pressure sensors				
PI01	0.1 Torr Baratron AA02A	0.4 % of reading + 2×10^{-6} Torr		[241]
PI02	0.1 Torr Baratron AA02A	0.4 % of rdg. + 2×10^{-6} Torr		[241]
PI03	0.1 Torr Baratron AA02A	0.4 % of rdg. + 2×10^{-6} Torr		[241]
PI04	10 Torr Baratron AA02A	0.2 % of rdg. + 2×10^{-4} Torr		[241]
Temperature sensors				
TI01	Pt-100 RTD, class B	0.5 % of abs. rdg. in °C + 0.3 K		[242]
TI02	Pt-100 RTD, class B	0.5 % of abs. rdg. in °C + 0.3 K		[242]
TI03	Type K TC, class 2	2.5 K		[243]
TI04	Type K TC	2.5 K		est.
TI05	Type K TC, class 2	2.5 K		[243]
Level sensor				
LI01	VEGAFLEX 81	Signal noise	0.1 % of rdg.	est.
		Volume calibration	1 % of rdg.	
Sensor signal conditioning and conversion				
-	ProfiMessage analog in	0.01 % of signal range (10 V)		[244]
-	ProfiMessage TC in	1.6 K		[244]
-	S7-1200 SM1231 TC in	1.9 K		[245]
-	safetyM 70.1150	Input	7.6 K	[246]
		Output	0.5 % of signal	
-	MINI MCR-2-RTD	0.12 % of signal (in range 0-300 °C)		[247]
-	MINI MCR-2-RPSS-I-I	0.01 mA		[248]
-	500 Ω Resistor	0.5 Ω		spec.
Manufacturing and assembly uncertainties				
-	Critical nozzle diameter	0.1 mm		spec.
-	Pressure probe position	2 mm		est.

A.6.4. Measured static pressure distribution in the mercury vapor jet

This appendix supplements Sec. 5.2.1 of the main text. Table A.8 summarizes all static pressure measurements performed at the three axial positions $x_1 = 84.52$ mm, $x_2 = 134.52$ mm and

$x_3 = 184.52$ mm and four boiler powers 184.5, 215.25, 246.0 and 307.5 W. The readings of PI03 and PI04, which are connected in parallel to the pressure probe, agree within uncertainty for all measurements. Due to the different measurement ranges the uncertainty of PI03 is significantly lower and therefore only readings of PI03 are included in Fig. 5.5.

Table A.8.: Static pressure measurements at different axial probe positions x_i and boiler powers.

Axial position x_i	**Boiler power**	**Static pressure**	
(in mm)	**(in W)**	**PI03 (in Pa)**	**PI04 (in Pa)**
84.52	184.5	0.528 ± 0.00273	0.630 ± 0.136
		0.605 ± 0.00300	0.697 ± 0.136
	215.25	0.781 ± 0.00364	0.866 ± 0.136
		0.899 ± 0.00409	0.985 ± 0.136
		0.927 ± 0.00419	1.00 ± 0.136
	246.0	1.46 ± 0.00626	1.52 ± 0.137
		1.34 ± 0.00578	1.40 ± 0.137
		1.26 ± 0.00548[1]	1.24 ± 0.136[1]
		1.17 ± 0.00513[1]	1.16 ± 0.136[1]
	307.5	2.46 ± 0.0102	2.51 ± 0.137
		2.16 ± 0.00903[1]	2.12 ± 0.137[1]
		2.27 ± 0.00945[1]	2.25 ± 0.137[1]
134.52	184.5	0.241 ± 0.00181	0.282 ± 0.136
	215.25	0.282 ± 0.00193	0.322 ± 0.136
	246.0	0.386 ± 0.00225	0.428 ± 0.136
		0.388 ± 0.00225	0.428 ± 0.136
	307.5	0.574 ± 0.00289	0.616 ± 0.136
		0.582 ± 0.00292	0.617 ± 0.136
184.52	184.5	0.298 ± 0.00198	0.326 ± 0.136
	215.25	0.258 ± 0.00186	0.289 ± 0.136
	246.0	0.262 ± 0.00187	0.291 ± 0.136
		0.267 ± 0.00189	0.296 ± 0.136
	307.5	0.328 ± 0.00207	0.354 ± 0.136
		0.326 ± 0.00206	0.353 ± 0.136

[1]The pressure probe was rotated by 180° for these measurements.

A.7. EU-DEMO linear diffusion pumps

A.7.1. Verification of the DSMC simulation parameters

The standard DSMC setup of the LDP simulation cases has been verified by comparing with two refined setups for a representative case under burn-like operating conditions. All three case setups and results are compared in Tab. A.9. The comparison confirms that the standard setup yields DSMC parameter independent results. Consequently, it has been used for all simulations discussed in Sec. 7.3.

Table A.9.: Comparison of DSMC simulations with standard and two sets of refined parameters for a representative case. The chosen case corresponds to a simulation of DT under burn conditions (cf. Sec. 7.3.2) with $p_{\mathrm{DT,inlet}} = 0.1\,\mathrm{Pa}$ and $p_{\mathrm{DT,outlet}} = 10\,\mathrm{Pa}$. All three nozzle stages are operated with mercury vapor at a stagnation temperature of $T_{\mathrm{Hg},0} = 413.15\,\mathrm{K}$ and corresponding saturated vapor pressure of $p_{\mathrm{Hg},0} \approx 248\,\mathrm{Pa}$. The critical time for each species is calculated as $\Delta t_{\mathrm{crit},i} = \frac{\sqrt{\Delta x^2+\Delta y^2}}{|\vec{u}_i|+v_{\mathrm{mp},i}}$ in each cell.

Category	Property	Unit	Case setup		
			Standard	**Refined 1**	**Refined 2**
Setup	Δt	s	2.5×10^{-8}	1.25×10^{-8}	1.25×10^{-8}
	N_p	1×10^6	≈ 92	≈ 184	≈ 367
	N_c	1	1,169,694	2,062,390	7,894,486
	N_{sample}	1	500,000	1,000,000	1,500,000
DSMC criteria	$N_p/\mathrm{cell} < 10$	% of N_c	0.04	0.03	0.02
	$N_p/\mathrm{cell} < 20$	% of N_c	15.84	18.03	14.81
	$\Delta x/\lambda_{\mathrm{mix}} > 1$	% of N_c	0.12	0.01	0.00
	$\Delta x/\lambda_{\mathrm{mix}} > 1/3$	% of N_c	21.10	9.36	0.38
	$\Delta t/\tau_{\mathrm{mix}} > 1$	% of N_c	0.00	0.00	0.00
	$\Delta t/\tau_{\mathrm{mix}} > 1/3$	% of N_c	0.00	0.00	0.00
	$\Delta t/\Delta t_{\mathrm{crit,Hg}} > 1/3$	% of N_c	1.30	0.00	2.50
	$\Delta t/\Delta t_{\mathrm{crit,DT}} > 1/3$	% of N_c	0.39	0.00	0.00
Results	S/L	$\mathrm{m^2\,s^{-1}}$	18.51	18.53	18.54
	ς	1	0.2302	0.2305	0.2306
	$\dot{m}_{\mathrm{Hg,BS}}/L$	$\mathrm{mg\,s^{-1}\,m^{-1}}$	11.84	11.83	11.84
Cost	Relative run time	1	1	4.2	14

A.7.2. Advanced nozzle pipe design with integrated throttling stage

The regular nozzle pipe in the LDP has the distinct disadvantage that the vapor pipe diameter depends on the linear length of the nozzle pipe. The reason is the requirement that the two circular cross-sectional areas of the nozzle pipe have to be larger than the area of the critical cross-section of the linear nozzle because the flow would otherwise choke there. This is disadvantageous for two reasons:

- The nozzle pipe blocks a part of the theoretical pumping surface and thus reduces the efficiency of the LDP.
- As a consequence of the previous point it is beneficial to choose the diameter of the nozzle pipe so that the two circular cross-sections are only slightly larger than the nozzle throat area. However, this has the direct consequence that the horizontal vapor speed along the pipe is not negligible compared to the vertical speed in the nozzle. Therefore, the vapor jet has a horizontal and vertical component which change along the nozzle pipe length. As the pumping effect is achieved mainly by the vertical jet velocity component this reduces the LDP efficiency further.

Thus, in order to eliminate these disadvantages, an advanced nozzle pipe design has been developed in the present work. The underlying idea is to include a throttling stage between the vapor supply to the nozzle pipe and the linear nozzle. A throttle corresponds to a flow constriction that reduces the pressure and density of the flow by acceleration. A uniform vapor distribution is achieved by distributing several individual throttle bores along the nozzle pipe length as shown in the CAD sketch in Fig. A.5. Thermodynamically, throttles are approximated as isenthalpic. Mercury vapor has a compressibility factor larger than 0.9992 below 550 K [249] and can therefore be considered as an ideal gas, for which the throttling process is isothermal. Consequently, throttling of saturated mercury vapor produces superheated mercury vapor, which has the positive side effect of improving the pump performance as demonstrated in Sec. 7.3.3 and proposed in [59]. In this setup the flow chokes first in the throttles and then a second time in the linear nozzle. The vapor stagnation conditions in the reservoir upstream of the linear nozzle are then dictated by mass conservation.

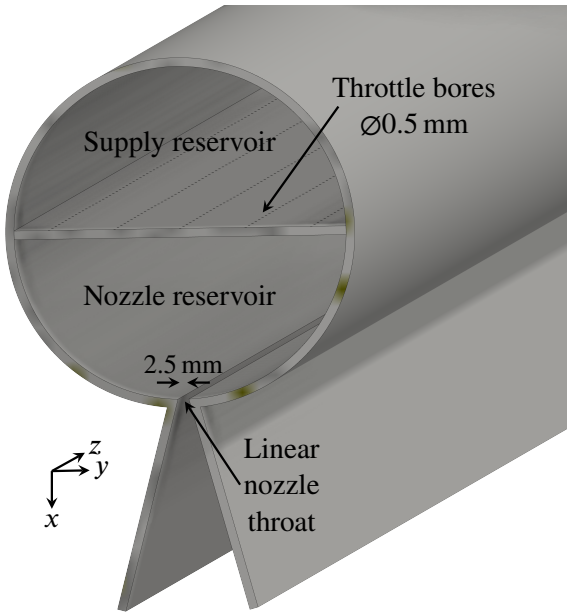

Figure A.5.: CAD sketch of the preliminary advanced nozzle pipe design featuring an intermediate throttling stage.

In the preliminary design of the nozzle pipe shown in Fig. A.5 the cross-sectional area of the throttle bores that separate the supply reservoir and the nozzle reservoir correspond to approximately 4.6 % of the linear nozzle throat area. Therefore, in order to achieve a similar stagnation pressure of 250 Pa in the nozzle reservoir as considered in the simulations discussed in Sec. 7.3 the boiler has to be operated at 500.9 K and corresponding saturation pressure of 5383 Pa. Isenthalpic throttling results in the stagnation pressure of 247.6 Pa at the same temperature, which corresponds

to a superheating by 87.75 K. The shown design is a drop-in replacement of the conventional nozzle pipes as the same pipe diameter of 80 mm is retained. However, it is noted that the intermediate throttling stage also allows for smaller diameters which could further improve the pump performance as noted above.